ParisTech
INSTITUT DES SCIENCES ET TECHNOLOGIES
PARIS INSTITUTE OF TECHNOLOGY

TELECOM ParisTech

2014-ENST-0074

EDITE ED 130

Doctorat ParisTech

T H È S E

pour obtenir le grade de docteur délivré par

Télécom ParisTech

Spécialité “Electronique et Communications”

présentée et soutenue publiquement par

Mark Donny CLEMENTE ARENAS

le 28 Novembre 2014

Application de la transformation d'espace à la conception d'antennes à diagramme de rayonnement contrôlé

Jury

M. Eric LHEURETTE, Professeur, IEMN, Université Lille 1	Rapporteur
M. Ala SHARAIHA, Professeur, IETR, Université de Rennes 1	Rapporteur
M. Gérard Pascal PIAU, Senior Expert, Airbus Group Innovations	Examinateur
M. Said ZOUHDI, Professeur, LGEP SUPELEC	Examinateur
M. Xavier BEGAUD, Professeur, Télécom ParisTech	Directeur de thèse
Mme Anne Claire LEPAGE, Maître de Conférences, Télécom ParisTech	Directeur de thèse
M. André DE LUSTRAC, Professeur, IEF, Université Paris Sud	Directeur de thèse

THÈSE

I dedicate this thesis to

my mother and my sisters for their support and unconditional love and especially for my father, because he was the only one that saw a doctor in me when I was a child

.

Acknowledgments

The list of the people I need to thank will not fit to a single Acknowledgement section. I just mention some people whose contribution is obvious.

It is my pleasure to thank my supervisors, Prof. Xavier BEGAUD and Dr. Anne Claire LEPAGE, who have offered me the opportunity to work on a very interesting subject. I acknowledge my deepest gratitude and appreciation to them for their guidance and help throughout my PhD studies. Many thanks go to Prof. André DE LUSTRAC and Dr. Shah Nawaz BUROKUR for their useful help in many opportunities.

Many thanks also to the jury president: Prof. Said ZOUHDI, Prof. Eric LHEURETTE, Prof. Ala SHARAIHA and Dr. Gérard Pascal PIAU, for coming from the different corners of France to serve on my thesis committee, and for sparing their invaluable time reviewing the manuscript.

I thank all Doctors and PhD students in the RFM laboratory, Aita, Lana, Lila, Taghrid, Nga, Reda, Christopher, José, Rupesh, Abdou, Mohammad, Yunfei and Chetan. I am always indebted to all my friends in France and Peru, Jinmi, Avid, Cesar, Oscar, Patricia, Naira, Katy y Miguel for their friendship.

I owe a lot to my family, who encouraged and helped me at every stage of my personal and academic life and longed to see this achievement come true. A special gratitude and love goes to my family for their unfailing support. My hard-working parents, Irene and Donato, have sacrificed their lives for my sisters and me and provided unconditional love and care. My sisters, Edith y Alejandra have been always my best friends. I love them so much and thank them for all their affections, advices, encouragement and support. Finally a special recognition to the woman that helped me through all kind of good and difficult times: Cynthia, recuerda que te adoro.

Mark CLEMENTE ARENAS

Résumé

Introduction

La transformation d'espace (TE) a été développée par J. B. Pendry et U. Leonhardt en 2006 et suscite un énorme intérêt depuis la démonstration expérimentale de la première cape d'invisibilité en micro-ondes. Cette technique permet de contrôler la propagation des ondes en modifiant les propriétés électromagnétiques de l'espace. Malgré quelques limitations liées à la bande passante ou aux pertes consécutives à l'utilisation de métamatériaux pour les dispositifs TE, cette technique a attiré l'attention de nombreux domaines (optique, microondes, acoustique, etc).

L'objectif de cette thèse est de développer des applications de la TE dans le domaine antennaire à l'aide de matériaux conventionnels lorsque cela est possible et aussi d'ouvrir de nouvelles voies dans le contrôle du rayonnement des antennes. Trois applications ont été étudiées: le réflecteur « parabolique plat »; un superstrat tout diélectrique pour contrôler l'ouverture angulaire d'une antenne patch; et finalement un superstrat permettant de modifier drastiquement le rayonnement d'une antenne.

Ce travail a été financé par les agences de défense du Royaume Uni et de la France (DSTL et DGA respectivement), dans le cadre du projet MIMiCRA (Metamaterial Inspired Microwave Conformal Radar Antennas).

Chapitre 1: Etat de l'art de la Transformation d'Espace.

En 2006 lorsque l'article de Pendry[1] sur la Transformation d'Espace est publié il attire l'attention de la communauté scientifique. C'est une découverte importante, car elle énonce la possibilité de contrôler la propagation des ondes en modifiant les propriétés électromagnétiques de l'espace. Cette flexibilité dans la conception en électromagnétisme a ensuite pu être mise en pratique avec l'utilisation des métamatériaux et des matériaux composites dont on peut modifier la permittivité et/ou la perméabilité. L'application la plus connue est la cape d'invisibilité. Cependant plusieurs problèmes ont été soulignés lors de l'utilisation des métamatériaux comme par exemple la faible largeur de bande, la vitesse de phase infinie ainsi que les pertes qui peuvent être excessives.

[1] J. B. Pendry, D. Schurig, and D. R. Smith, Controlling electromagnetic fields, Science, Vol. 312, pp. 1780–1782 (2006).

Ces problèmes font que la cape d'invisibilité et d'autres applications de la TE ne sont pas opérationnelles sur de larges plages de fréquences.

La première partie de ce manuscrit est dédiée à une revue de l'état de l'art de la TE où on décrira le principe, les points importants de la méthodologie de conception, les avantages et les limitations de son utilisation, ainsi que les différentes applications dans le domaine antennaire.

La Transformation d'Espace est une méthode très intéressante pour la conception des dispositifs optiques et microondes car elle permet de contrôler le rayonnement des ondes comme jamais auparavant. La Transformation d'Espace est inspirée du principe de Fermat qui gouverne l'optique géométrique. La lumière suit un chemin optique stationnaire entre deux points. La plupart du temps, elle suit le chemin le plus court. Dans certains cas, elle emprunte le chemin le plus long. Ce chemin optique est défini par la relation (1), où *n* est l'indice de réfraction qui peut dépendre des coordonnées spatiales et *dl*, un élément de distance.

$$S = \int n.dl \quad dl = \sqrt{dx^2 + dy^2 + dz^2} \quad (1)$$

La méthode de conception des dispositifs à base de TE est basée sur deux points importants représentés par les deux équations suivantes: l'invariance des équations de Maxwell par rapport au changement d'espace (3), et la dépendance entre les systèmes de coordonnées et les paramètres des matériaux:

$$\nabla \times E = -j\omega\mu H \qquad \nabla \times H = j\omega\varepsilon E \qquad (2)$$

$$\nabla' \times E' = -j\omega\mu' H' \qquad \nabla' \times H' = j\omega\varepsilon' E' \qquad (3)$$

$$\mu' = \frac{A\mu A^T}{\det(A)}, \quad \mu' = \frac{A\mu A^T}{\det(A)} \qquad (4)$$

Où J est le tenseur Jacobien qui représente le passage entre deux systèmes de coordonnées; dans notre cas entre: un système réel où l'espace est transformé, et un système virtuel où l'espace reste le même. L'équation 4 permet le calcul du profil spatial de permittivité et perméabilité. Ce profil sera ensuite nécessaire pour produire la structure finale.

Pour la méthode de conception, on peut définir plusieurs étapes:

- Définir l'interaction onde-matériau dans l'espace réel,
- Choisir un volume dans l'espace original et son espace transforme associé,
- Définir des équations analytiques que permettent de relier les deux espaces (réel et transformé),
- Calculer les paramètres constitutifs du matériau en utilisant les équations (3),

- Interpréter ces paramètres constitutifs du matériau dans l'espace original,
- Choisir ou concevoir les matériaux nécessaires pour le profil souhaité.

Habituellement la conception débute en 2D pour des raisons de simplicité pour ensuite passer à une structure 3D. Cela s'explique par le fait qu'en 2D, on réduit le nombre de variables à calculer. Une fois que la conception est complète, le dispositif est transformé en 3D (rotation, extrusion) pour construire le prototype final.

Dans la conception des dispositifs TE, il y a deux approches du point de vue de l'ingénierie: l'approche analytique et l'approche quasi-conforme. Dans le cas de l'approche analytique, toutes les composantes des équations de Maxwells sont utilisées ainsi que les composantes des tenseurs des paramètres constitutifs. Cette approche est très utilisée notamment pour les transformations les plus exotiques. De plus cette approche est la plus simple pour distinguer les différentes étapes de la méthode de conception ainsi que pour se familiariser avec la TE.

Dans le cas de l'approche quasi-conforme (Figure 0.1), la transformation est basée sur une transformation des coordonnées graphique en utilisant des maillages pour discrétiser l'espace à transformer. Le but est de calculer l'indice de réfraction n à partir de l'indice de réfraction initial n_0 et des variations spatiales Δx et Δy comme dans l'équation (5). Il est important de garder les critères d'orthogonalité nécessaires pour que les approximations faites dans cette approche restent toujours valables.

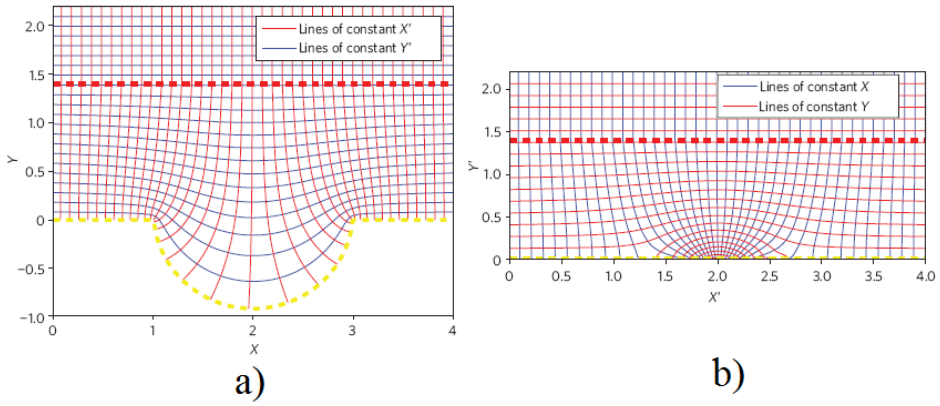


Figure 0.1 Exemple d'une transformation quasi-conforme.

$$n' = n_0 \sqrt{\frac{\Delta x_0 \Delta y_0}{\Delta x'_0 \, \Delta y'_0}} \quad (5)$$

Où: Δx_0, Δy_0,$\Delta x'_0$, et $\Delta y'_0$, sont les dimensions du maillage dans le système de coordonnées x, y, x' et y', respectivement. Cette approche est idéale lorsque l'on souhaite concevoir des dispositifs tout diélectrique, parce qu'il permet d'obtenir des faibles variations de la permittivité. Par contre, lorsque

l'on souhaite changer complètement la propagation électromagnétique, il peut être difficile à mettre en œuvre.

En ce qui concerne les applications, le manuscrit décrit les dispositifs utilisant le «cloaking» comme la cape et la couche d'invisibilité. La cape d'invisibilité est utilisée pour illustrer le principe de la TE; ensuite une description de la propagation souhaitée, définition des équations analytiques nécessaires pour la conception, et étapes de calcul et interprétation des tenseurs de permittivité et perméabilité.

L'application la plus connue de la transformation d'Espace est la cape d'invisibilité parce qu'elle montre la possibilité de modifier la trajectoire des ondes au tour d'un objet. Cela signifie que les ondes ne traversent pas l'objet mais les contournent et retrouvent ensuite leurs trajectoires initiales.

La couche d'invisibilité par contre est une application plus simple qui tente de cacher un objet d'une illumination incidente en utilisant une couche conçue avec la TE et un miroir PEC (Perfect Electric Conductor). Les paramètres constitutifs nécessaires pour cette application sont des matériaux standards et homogènes. Le dispositif est réalisé par pulvérisation avec notamment des poudres de titanates.

Une autre application particulièrement intéressante dans le cadre de ce manuscrit est «l'invisibilité des antennes», qui est un concept qui permet d'augmenter l'isolation ou découplage entre deux antennes voisines. Le principe est relativement simple: deux antennes qui fonctionnent à des fréquences différentes sont entourées par deux capes d'invisibilité qui sont actives chacune à la fréquence de l'autre antenne. Donc, si la première antenne émet, ses performances ne sont pas perturbées par la seconde qui n'est plus visible.

Des applications de la TE dans le domaine des dispositifs rayonnants sont aussi décrites dans le manuscrit en explorant des dispositifs de manipulations de source, de compression de dispositifs et d'antennes très directives et multifaisceaux.

A la fin du chapitre, un tableau (Table 0.1) récapitule les performances des différents dispositifs présentées. Les dimensions par rapport à la longueur d'onde, les paramètres constitutifs, les méthodes de conception et de réalisation sont comparées et présentes pour chaque famille d'applications.

Application	**Approche**	**Taille en λ**	**Matériau**	**Propriété du matériau**
"Cylindrical Cloaking"	Analytique	5-11	Métamatériau	Dispersif

"Invisibility carpet"	Quasi-conforme	2	Dielectrique	Non-Dispersif
"Antenna cloaking"	Les deux	3	Uniquement simulation/ Dielectrique	Les deux
"High directivity "	Les deux	2.5, 5, 10	Métamatériau / Dielectrique	Dispersif
"Multibeam Antenna "	Analytique	5	Métamatériau	Dispersif
"Multibeam Lens"	Quasi-conforme	2	Métamatériau	Dispersif

Table 0.1 Tableau récapitulatif des performances et des caractéristiques des applications TE.

Chapitre 2: Réflecteur plat tout diélectrique.

Ce chapitre présente une méthode de conception d'un réflecteur plat calculé par Transformation d'Espace (TE). Il débute par l'énoncé du principe mathématique et décrit ensuite toutes les étapes du processus de conception du dispositif utilisant la TE. Les problèmes de réalisation sont mis en évidence puis des approximations et compromis sont appliqués pour rendre la structure réalisable. Ainsi, un réflecteur plat élaboré uniquement à partir de diélectriques standards est proposé, en utilisant une méthode originale pour réaliser la variation de permittivité souhaitée.

Le réflecteur plat[2] est une application intéressante pour mettre en valeur les potentialités de la Transformation d'Espace dans le domaine des antennes. Ainsi, le réflecteur plat fonctionne comme un réflecteur parabolique et il présente entre autres, une taille réduite. Pour la conception de ce dispositif, l'équation d'une parabole est utilisée dans la mise en équation de l'espace transformé et le calcul du matériau requis. Sur la Figure 0.2, les espaces virtuels et réels sont présentés: l'espace

[2] F. Kong, B-I. Wu, J. A. Kong, J. Huangfu, S. Xi and H. Chen, Planar focusing antenna design by using coordinate transformation technology, Appl. Phys. Lett., Vol. 91, pp. 253509 (2007).

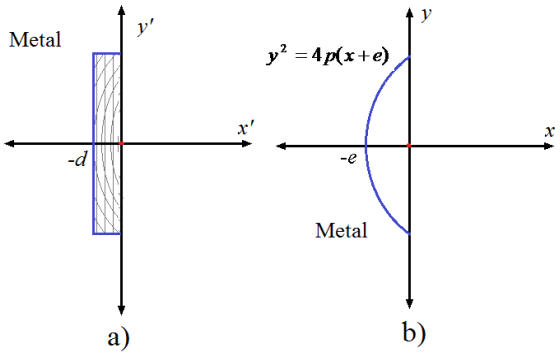


Figure 0.2 Section droite des réflecteurs a) Espace réel souhaité, b) Espace parabolique virtuel.

virtuel est représenté par le réflecteur décrit par une équation parabolique et l'espace réel souhaité est représenté par une structure plate, qui aurait les mêmes propriétés que la structure parabolique. Le passage des coordonnées est donné par (6), où *p* est la distance au foyer de la parabole. La seule composante du système de coordonnées qui est affectée par la transformation est *x*:

$$x' = \frac{4pdx}{4pe - y^2}; y' = y; z' = z \quad (6)$$

En utilisant l'équation 5 pour la Transformation d'Espace, on obtient les expressions qui permettent de calculer le profil des paramètres ε_r et μ_r dans la nouvelle structure. Le profil de permittivité et perméabilité est présenté sur la Figure 0.3. Plusieurs simplifications ont été appliquées dans le but de réduire le nombre de composantes dans les tenseurs de permittivité et perméabilité. Ainsi seules trois composantes de ces tenseurs (μ_{xx}, μ_{yy}, ε_{zz}) sont le résultat de ce processus de calcul. Les valeurs calculées varient entre 0 et 100 pour μ_{xx}, entre 0 et 1 pour μ_{yy}, et entre 0 et 1.45 pour ε_{zz}. Il est important de noter ici que ces valeurs peuvent être réalisées mais uniquement à l'aide de métamatériaux.

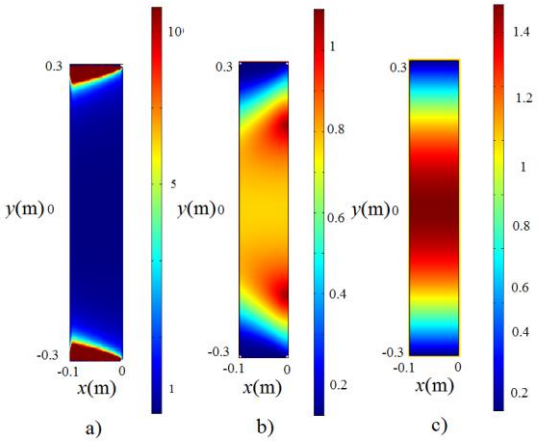


Figure 0.3 Profil des composantes des tenseurs de permittivité et de perméabilité avec e=0.15 m, d=0.1 m and p=0.15 m, a) μ_{xx} b) μ_{yy} et c) ε_{zz}.

Sur la Figure 0.3 les distributions de la composante *Ez* du champ électrique de trois structures sont présentées: la première structure est une parabole métallique classique, la deuxième distribution est un réflecteur plat où le matériau dans le rectangle est calculé par la Transformation d'Espace avec des parois métalliques, et la dernière est un réflecteur plat métallique. Chaque réflecteur à un diamètre de 60 cm et le calcul est réalisé à 5 GHz. Le réflecteur est éclairé par une source ponctuelle. Dans le deuxième cas, le matériau présente les variations spatiales des tenseurs de permittivité et perméabilité représentés sur la Figure 0.4.

On constate aisément que le réflecteur plat calculé par TE produit une distribution de champ semblable à celui de la parabole et que le plan métallique ne produit pas un rayonnement exploitable.

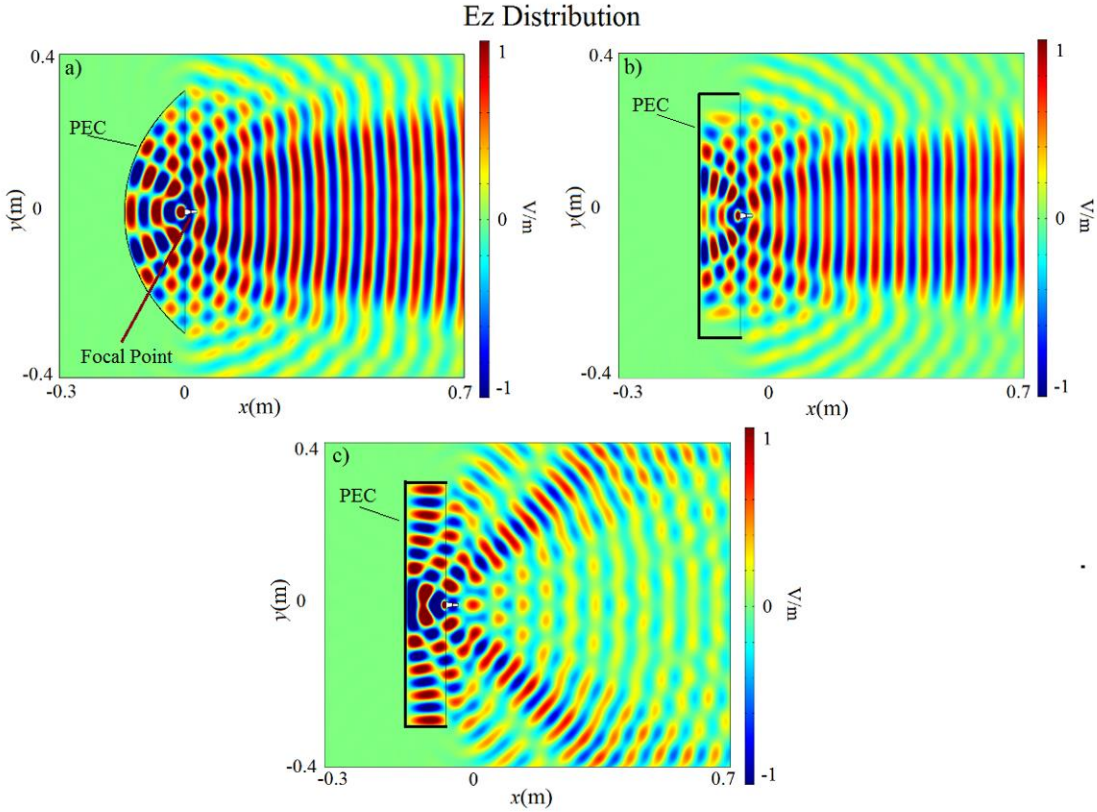


Figure 0.4 Distribution du champ électrique Ez normalisé à 5 GHz, a) Réflecteur parabolique b) Réflecteur plat avec parois métalliques c) Réflecteur métallique plat.

Dans cette étude, nous souhaitons simplifier la réalisation et n'utiliser que des matériaux standards. Ainsi, la discrétisation du matériau en 32 blocs (anneaux concentriques) diélectriques, permettant de réaliser la TE est proposée sur la Figure 0.5.

Des approximations sont également appliquées pour simplifier les valeurs de perméabilité et pour que la structure ne soit définie que par rapport à la permittivité (la perméabilité relative est ainsi fixée à 1). La permittivité relative varie entre 0,2 et 1,45 comme dans le cas présenté en théorie. Comme

les valeurs dispersives (inférieures à l'unité) ne correspondent pas à des matériaux standards, elles sont remplacées simplement par une permittivité relative de 1.

La réalisation de la structure diélectrique à permittivité variable est possible en ajustant le nombre de trous dans un matériel homogène.

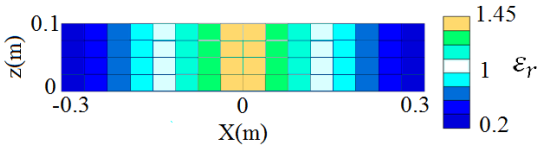


Figure 0.5 Profil de la structure calculée par TE. Les zones colorées représentent les valeurs de permittivité.

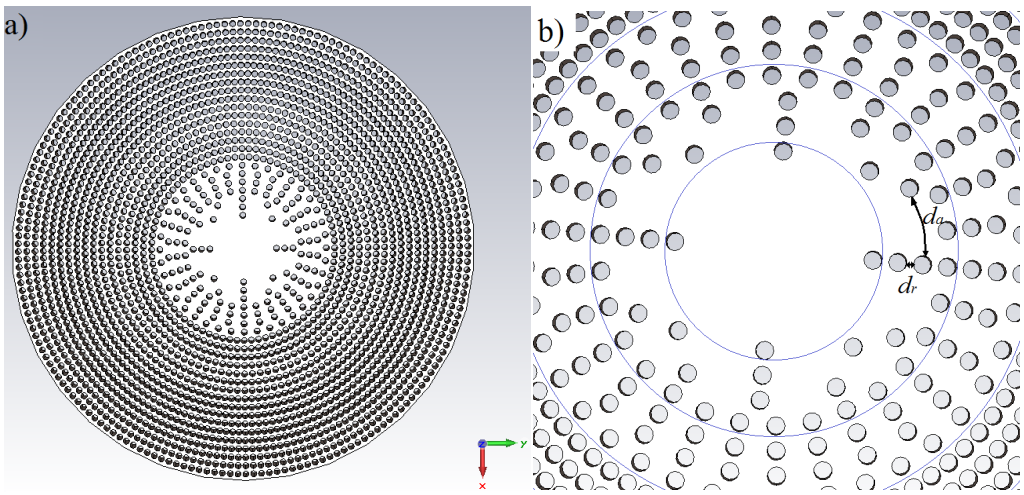


Figure 0.6. a) Vue de dessus du diélectrique (Téflon) avec les trous, b) Zoom

La densité des trous dans les différentes régions varie pour obtenir la variation de permittivité souhaitée. La densité des trous varie en changeant la distance angulaire d_a entre trous et en conservant la distance radiale d_r comme le montre la Figure 0.6. Les trous ont un diamètre de 4 mm ou 0.067λ à f= 5 GHz. L'équation 6 permet de calculer les valeurs de permittivité synthétisées ε_{synth} dans les différentes régions à partir de deux permittivités (ε_d et ε_a).

$$\varepsilon_{synth} = \varepsilon_d f_d + \varepsilon_a f_a = \varepsilon_d - (\varepsilon_d - \varepsilon_a) f_a \qquad (7)$$

Le facteur f_d est le rapport entre le volume de diélectrique perforé dans le matériel et le volume initial de la structure avant que les trous soient réalisés. Ensuite, le facteur f_a est le rapport entre le volume qui a été extrait et le volume initial. En résumé, f_a représente le volume de l'air présent dans la structure et f_d représente le volume du diélectrique. Dans notre étude nous avons choisi un bloc de téflon de permittivité égale à 2.2 disponible au laboratoire pour réaliser le diélectrique à trous.

Sur la Figure 0.7 est présenté le diagramme de rayonnement du réflecteur plat réalisé avec les anneaux concentriques homogènes (y compris avec les valeurs inférieures à l'unité ou dispersives)

de la Figure 0.5, comparé au diagramme d'un réflecteur plat où les valeurs de permittivité relative inférieures à 1 (réflecteur non dispersif) ont été remplacées par l'unité, puis à celui d'un réflecteur plat métallique. Le réflecteur est éclairé par un cornet situe dans le point du foyer, ou dans ce cas la source est mis à la même distance que l'épaisseur de la structure.

La structure avec une permittivité variant de 0,2 à 1,45 présente un diagramme de rayonnement directif comme attendu pour un réflecteur parabolique. Lorsque les valeurs inférieures à l'unité sont remplacées par l'unité le diagramme reste tout à fait convenable et présente un gain supérieur de 5 dB à celui du réflecteur plat métallique. Enfin le diagramme de la structure non dispersive présente un gain légèrement plus élevé en comparaison avec celui de la structure dispersive.

La comparaison des ouvertures à 3dB des structures dispersive et non dispersive, est présentée sur la Figure 0.8. Le diagramme du réflecteur dispersif est plus large avec une ouverture à 3dB de 20,1°, alors que celle du réflecteur non dispersif est de 16°.

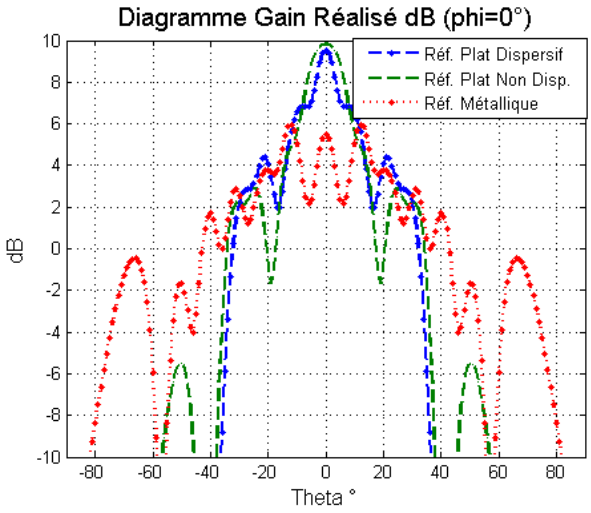


Figure 0.7 Comparaison des diagrammes de rayonnement (gain réalisé) entre 3 réflecteurs à 5 GHz.

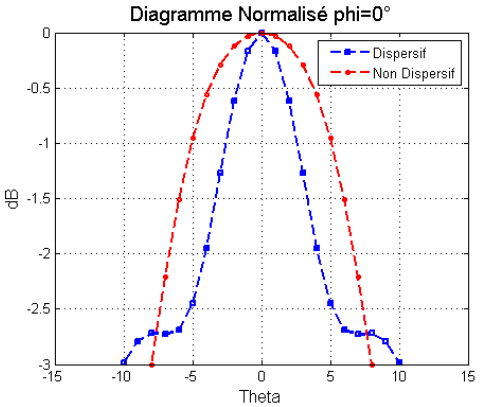


Figure 0.8. Comparaison des diagrammes de rayonnement normalisés des réflecteurs dispersif et non dispersif à 5 GHz.

Dans la Figure 0.7 les diagrammes obtenus avec les réflecteurs plats dispersifs et composés de Téflon à trous sont présentés. Même si les allures de deux diagrammes sont différentes, les ouvertures de diagramme à -3dB sont voisines (ouverture de 21,4° pour le réflecteur du Téflon et 21° pour le réflecteur dispersif). Le gain varie entre 8,9 dB pour le réflecteur avec trous et 9,5 dB pour le réflecteur dispersif dans la direction θ =0°.

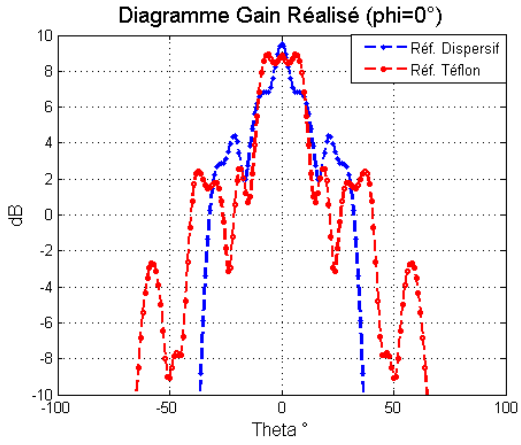


Figure 0.9. Comparaison des diagrammes du réflecteur dispersif et du réflecteur en Téflon à trous à 5 GHz.

Conclusion:

Dans ce chapitre, nous avons présenté la conception d'un réflecteur plat composé uniquement d'un matériau diélectrique standard et inspiré des principes de la Transformation d'Espace. Les performances obtenues avec ce réflecteur sont proches de celles utilisant des métamatériaux.

Les différentes valeurs de permittivité sont réalisées en faisant varier la densité des trous dans les différentes régions de la structure. Cette méthode peut donc être utilisée pour la réalisation des structures à permittivité variable mais doit encore être améliorée.

Chapitre 3: Superstrat tout diélectrique pour augmenter l'ouverture à 3dB d'une antenne.

Dans ce chapitre un superstrat tout diélectrique utilisé pour contrôler l'ouverture à 3dB d'une antenne à double polarisation est présenté. L'antenne à double polarisation est conçue pour travailler dans la bande [1.164-1.239] GHz. Le superstrat tout diélectrique initial est extrait du travail de Tang en 2010 qui a été conçu à l'origine pour augmenter la directivité d'un élément rayonnant en utilisant la Transformation d'Espace. Dans cette application la configuration des couches dans le profil de paramètres constitutifs a été changée pour augmenter l'ouverture à 3 dB. De plus, ce superstrat initialement conçu pour utiliser des métamatériaux a été modifié pour n'utiliser que des matériaux

standards tout en conservant les performances du dispositif. Les variations de la permittivité sont synthétisées en utilisant la méthode de diélectrique homogène avec trous présentée précédemment.

Les antennes patch sont utilisées dans le domaine aéronautique pour leurs propriétés géométriques et électromagnétiques intéressantes. Elles sont notamment adaptées pour être installées sur la structure d'un porteur. Néanmoins, l'ouverture angulaire à 3 dB est trop faible pour certaines applications. Pour l'antenne GPS utilisée en aéronautique, une ouverture angulaire importante du diagramme de rayonnement est donc requise pour que l'antenne puisse maintenir le lien avec les satellites en permanence sans que ce lien soit perturbé par un changement d'orientation ou de position de l'avion. Pour cela, une antenne à double polarisation linéaire (permettant de générer tous types de polarisations) est proposée comme antenne de référence. Un coupleur hybride -3dB est utilisé pour alimenter les deux accès avec un déphasage de 90°, générant ainsi la polarisation circulaire droite de l'antenne. Cette antenne fonctionne sur la bande [1,164-1,239] GHz qui correspond aux bandes L5 et L2 du GPS. Le substrat est de l'Arlon AD250 de dimensions 100x100 mm² et de 15mm d'épaisseur. Le plan de masse aux mêmes dimensions que le substrat et celles du patch sont 71x71 mm². L'antenne présente un gain de 6 dB dans l'axe et une isolation entre accès supérieure à 15 dB. L'ouverture angulaire à 3dB est de 93° pour les deux plans. Le but de notre étude est d'augmenter cette valeur.

Le superstrat doit permettre d'augmenter l'ouverture angulaire avec un moindre impact sur les performances initiales de l'antenne de référence. La largeur de la bande qui est relativement importante constitue la difficulté majeure. Ainsi, l'utilisation de structures résonantes comme les SRR (Split Ring Resonators) est délicate et complexe. Les matériaux diélectriques standards sont donc une alternative plus convenable. Dans la Figure 0.10, le profil du superstrat est présenté avec ses valeurs de permittivité relative [3]. Quatre configurations sont analysées (Figure 0.11 a-d) afin de chercher celle qui permet d'élargir le lobe principal du diagramme de l'antenne de référence

- Cas 1: L'antenne sans superstrat (Figure 0.11-a) appelée antenne de référence.
- Cas 2: La structure originale conçue pour augmenter la directivité [3] est placée directement au-dessus du patch de référence. Ce cas est étudié afin de démontrer que la transformation d'espace peut fonctionner indépendamment de la fréquence et de la distance entre la source et le superstrat (Figure 0.11-b).
- Cas 3: Les valeurs de permittivité relative ont ici été inversées horizontalement par rapport au cas 2: les valeurs du centre ont été déplacées sur les côtés (Figure 0.11-c).

[3] W. Tang, C. Argyropoulos, E. Kallos, W. Song and Y. Hao, Discrete coordinate transformation for designing all-dielectric flat antennas, IEEE Trans. on Antennas and Propagation, Vol. 58, pp. 3795-3804 (2010).

- Cas 4: Les valeurs de permittivité ont été déplacées verticalement comme dans la Figure 0.11-d

Pour les cas 2 et 4, la structure TE est en contact direct avec l'antenne. La conséquence est qu'il y a un décalage de la bande de fréquence d'adaptation, mais ce dernier reste convenable. Pour le cas 3, on a ajouté une couche diélectrique pour conserver l'adaptation entre le patch et le superstrat. Cette couche diélectrique a une épaisseur de 5 mm et une permittivité relative de 2.

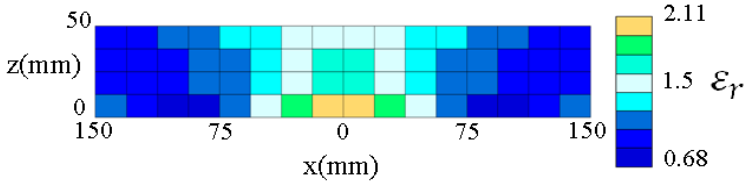


Figure 0.10. Profil initial de la structure TE.

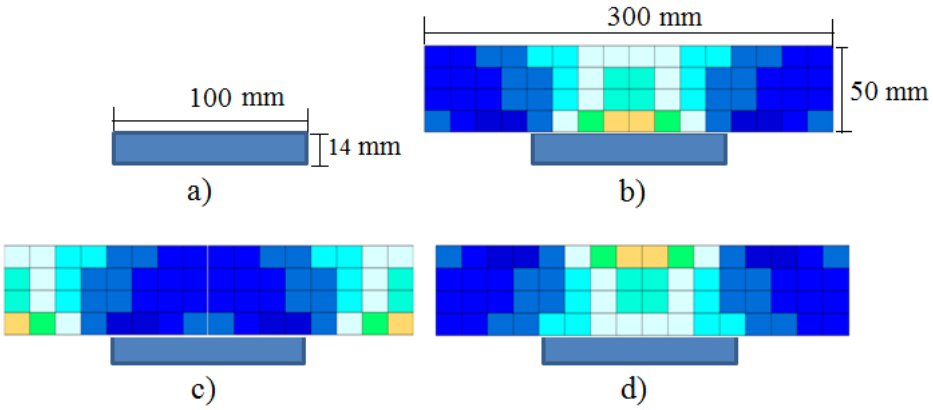


Figure 0.11. a) Antenne seule, b) Antenne avec superstrat initial (solution directive), c) Antenne avec superstrat modifié (symétrie horizontale), d) Antenne avec superstrat modifié (symétrie verticale).

Dans le cas 2, les résultats de simulation montrent le comportement d'une structure TE fonctionnant dans une bande de fréquence différente de celle pour laquelle elle a été conçue. En effet, la lentille plate originale fonctionne à 8 GHz. Dans notre cas, les simulations ont été effectuées à 1.2 GHz et la structure est plus directive comme attendu (l'ouverture angulaire à 3 dB est de 82°). La structure TE fonctionne donc à 1.2 GHz car le diamètre est de 300 mm et donc supérieur à une longueur d'onde.

La plage de variation des profils de permittivité relative est maintenant décalée de [1-2.11] vers [1.6-2.2], pour n'utiliser qu'un seul matériau pour le prototype final de superstrat. Trois couches de Téflon PTFE (ε_r=2.2) sont alors utilisées pour construire les différentes régions. La première et la troisième couche ont la même épaisseur (12.5 mm) et la deuxième couche a une épaisseur double (25 mm) (voir Figure 0.12). Finalement, chaque couche a 8 régions horizontales de différentes permittivités.

Les valeurs des différentes permittivités dans les régions horizontales sont synthétisées en changeant la densité de trous de chaque région. Les différentes densités de trous dans les régions horizontales sont obtenues en faisant varier la distance angulaire entre trous tout en conservant la distance radiale et le diamètre.

La quantité de trous et leurs positions sont déterminées par les valeurs spécifiques de permittivité nécessaires [4].

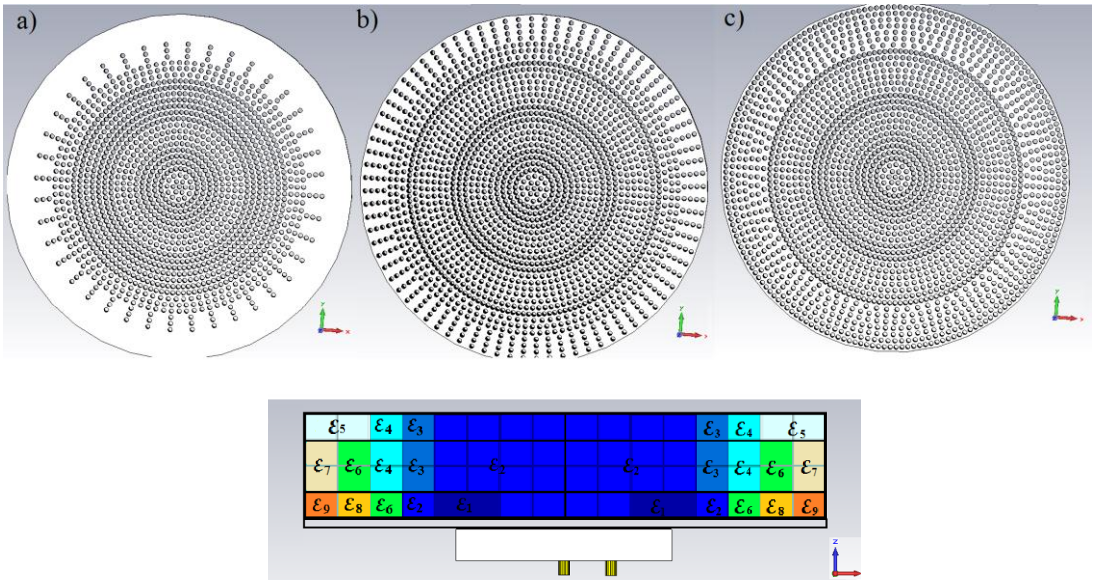


Figure 0.12 Vue de face du superstrat de permittivité variable, a) 1er couche (bas), b) 2ème couche (au milieu), c) 3ème couche (supérieure), d) Vue de profil de la structure: Antenne et superstrat avec la permittivité des différentes régions horizontales et verticales.

Dans le processus de conception, neuf valeurs de permittivité sont calculées pour les 3 couches différentes et sont présentées dans la Table 0.2. Le processus prend en compte l'équation 7, où les différentes valeurs peuvent être obtenues en utilisant deux matériaux de permittivités différentes. Dans notre cas, la permittivité dans le diélectrique est ε_r=2.2 et pour l'air est ε_r=1 pour les trous. Le diamètre des trous est 3.34 mm qui correspond a 0.013λ.

ε_{r1}	ε_{r2}	ε_{r3}	ε_{r4}	ε_{r5}	ε_{r6}	ε_{r7}	ε_{r8}	ε_{r9}
1.6	1.62	1.7	1.72	1.79	1.84	1.9	2.12	2.2

Table 0.2 Valeurs de permittivités synthétisées.

[4]. L. Schulwitz, L. Mortazawi, A new low loss rotman lens design using a graded dielectric substrate, IEEE Transactions on Microwave Theory and Techniques, Vol. 56, No.12, pp. 2734-2741 (Dec. 2008).

Le gain normalisé obtenu par simulation pour chaque configuration est présenté sur la Figure 0.13. Comme notre objectif est d'observer l'ouverture à mi-puissance on représente uniquement le lobe principal. Dans cette application, les simulations ont été réalisées à 1.2 GHz et la structure TE augmente la directivité légèrement. A 1.2 GHz, le diamètre de la structure (300 mm) est supérieure à la longueur d'onde et donc la TE peut opérer.

Le résultat du cas c présente un élargissement du faisceau d'environ 20% (Ouverture à 3dB égale à 112.5°). Dans ce cas, les valeurs les plus élevées de la permittivité ont été déplacées vers les couches extérieures. Il élargit rayonnement en dirigeant les ondes sur les côtés extérieurs au lieu d'aller dans le centre de la structure. Dans les cas b et d, la structure TE ne semble pas avoir d'effet sur le rayonnement parce que la largeur angulaire reste relativement proche du cas de référence.

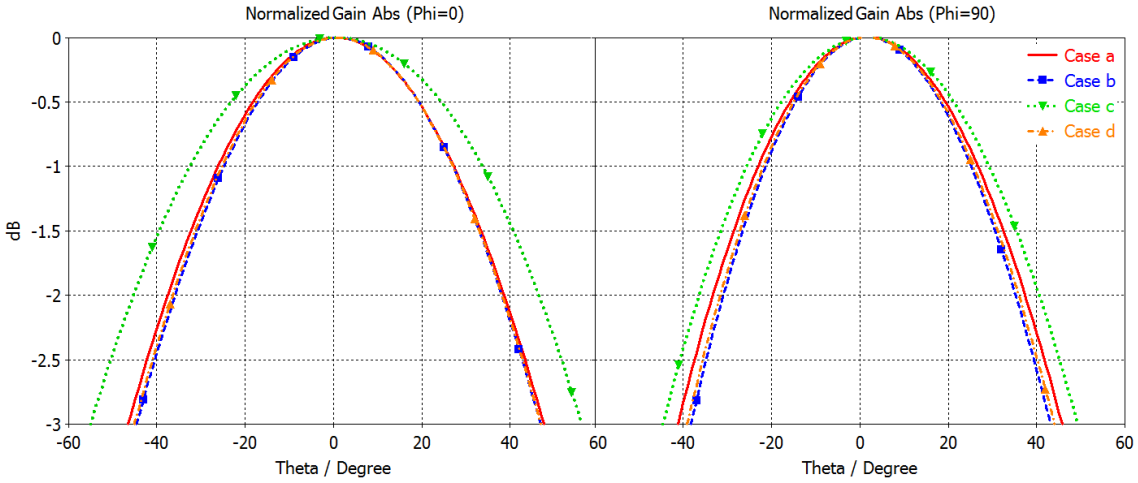


Figure 0.13 Gain normalisé à la fréquence centrale de la bande (1.2 GHz), dans les deux plans pour les diffèrent cas (polarisation linéaire).

La Figure 0.14-b présente le gain normalisé (lobe principal du diagramme de rayonnement en champ lointain dans deux plans orthogonaux) dans différentes configurations à 1.2 GHz. La première configuration est sans superstrat (Antenne de référence). Les deuxièmes et troisièmes configurations sont le matériau théorique avec et sans les valeurs de permittivité inférieure à l'unité (dispersif et non dispersif). Le dernier est superstrat composé du Téflon avec trous.

Avec les matériaux dispersifs ou non dispersifs, le superstrat augmente l'ouverture à 3dB de 20%. La solution avec des trous périodiques montre une augmentation intéressante de 26% de l'ouverture à 3dB (118 °). Ceci peut s'expliquer par le fait que nous avons modifié les valeurs d'origine de la permittivité et que des valeurs plus élevées ont été utilisées. Le fait de remplacer les valeurs inférieure à un par l'unité n'affecte pas les résultats, ce qui est la raison qui rend possible l'utilisation d'un seul matériau pour les trois couches.

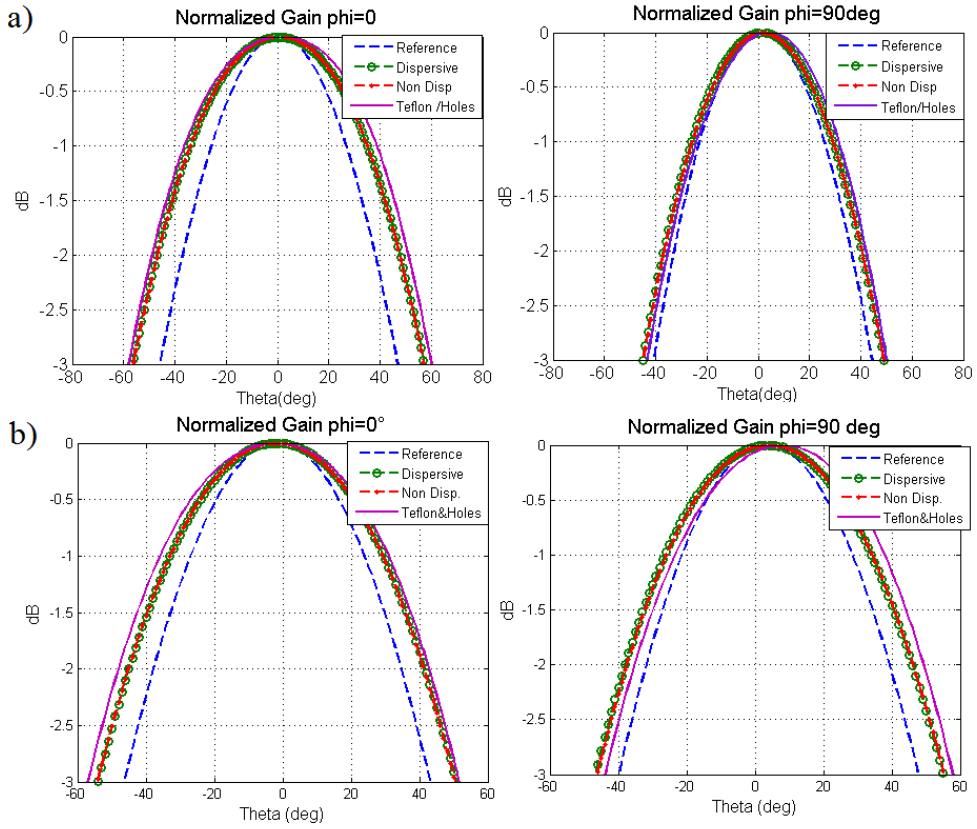


Figure 0.14. Gain normalise à la fréquence centrale (1.2 GHz), a) Polarisation linéaire, b) Polarisation circulaire.

Un superstrat tout-diélectrique peut donc être conçu en utilisant des structures modifiées inspirés par la TE. Une augmentation d'environ 26% de l'ouverture à 3dB a ainsi été démontrée.

Le processus pour réaliser une permittivité variable dans le diélectrique est très efficace car nous pouvons voir l'action de la TE sans compromettre les performances de l'antenne d'origine. Habituellement, quand un diélectrique homogène est placé au-dessus d'une antenne patch, il modifie l'ensemble des caractéristiques de rayonnement de l'antenne. Ensuite, un seul diélectrique peut être utilisé pour réaliser le superstrat qui permet d'élargir le faisceau. La prochaine étape est de valider ce travail par une réalisation et des mesures. Ensuite, notre objectif sera de réduire toutes les dimensions de la lentille afin d'avoir une antenne à faible encombrement.

L'objectif de cette validation n'est pas d'obtenir les meilleures performances mais de faire la preuve du concept. Une nouvelle couche supérieure a ainsi été conçue, afin de réduire la taille globale, avec un diamètre extérieur de 250 mm et une épaisseur de 40 mm au lieu d'un diamètre de 300 mm et une épaisseur de 50 mm pour la conception optimale. Ce diamètre (250 mm) a été choisi parce que c'est le diamètre maximal admis par l'imprimante 3D et aussi parce que parmi les optimisations en taille et en performances, cette structure offre le meilleur compromis. La géométrie mise à jour du superstrat est présentée sur la Figure 0.15. Afin de maintenir l'antenne bien adaptée,

l'écart entre l'antenne et le superstrat est maintenant de 5 mm et elle est remplie d'une couche en nid d'abeilles avec 300 mm de diamètre.

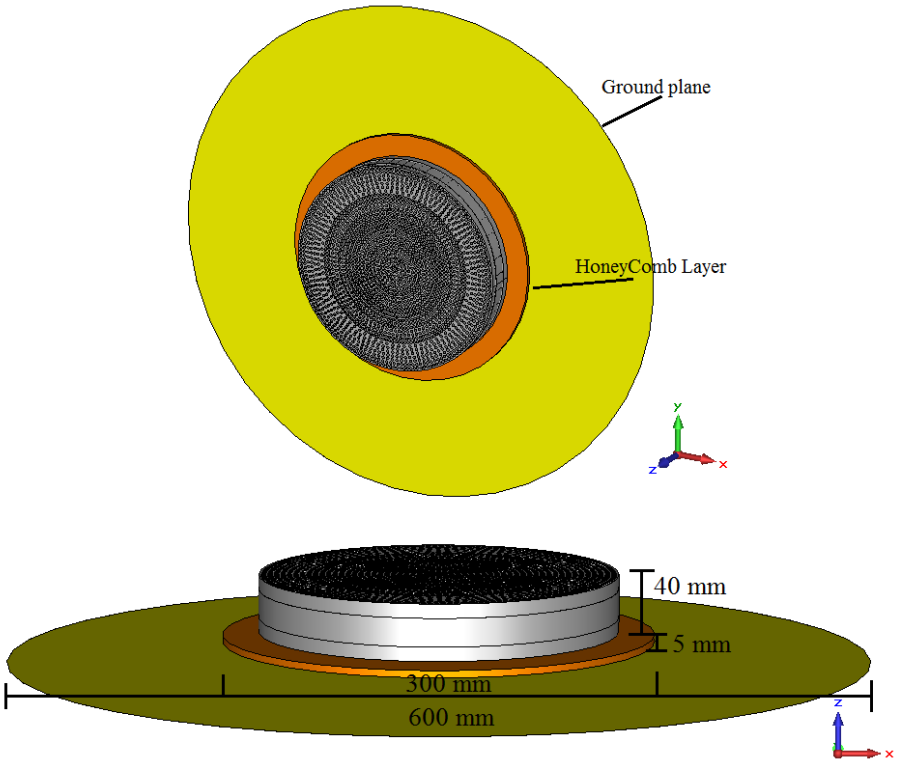


Figure 0.15 Vue de Perspective et vue de cote de l'antenne de référence avec un superstrat réalisé en FullCure avec un diamètre de 250 mm et une couche de nid d'abeille de 5 mm d'épaisseur et de 300 mm de diamètre.

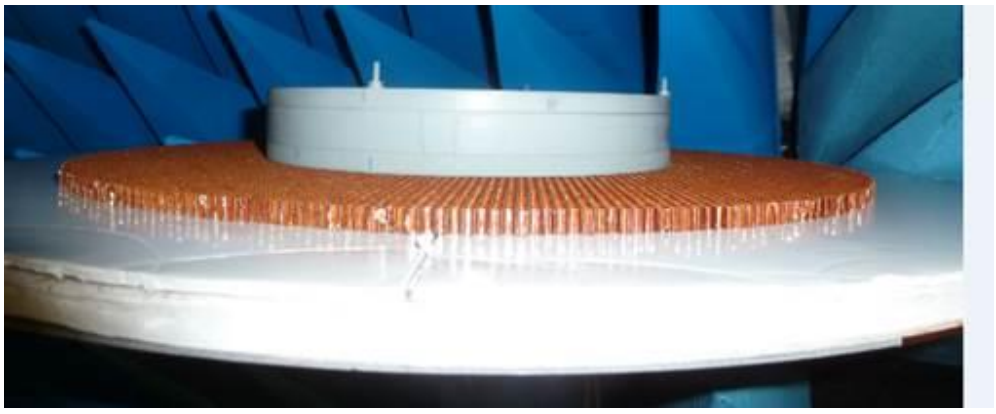


Figure 0.16 Antenne de référence associée avec le superstrat fabriqué.



Figure 0.17 Superstrat réalisé composé des 3 couches présentées sur la Figure 0.12.

L'impression 3D (ou fabrication additive) est une méthode polyvalente et incroyable pour la réalisation de nombreuses pièces mécaniques. Elle permet de s'affranchir d'opérations mécaniques complexes et difficiles à mettre en œuvre. Une photo de la structure complète est présentée sur la Figure 0.17. Cette structure a été fabriquée et mesuré dans les installations du groupe Airbus Innovations à Suresnes en Mars 2014 dans la configuration présentée Figure 0.15.

Les résultats de mesure et simulation (CST Microwave Studio, solveur temporel «transient») du prototype sont présentés ci-dessous. Les performances sont obtenues lorsque l'antenne est alimentée avec un coupleur hybride (3dB 90°) et avec le superstrat de FullCure de 250 mm de diamètre.

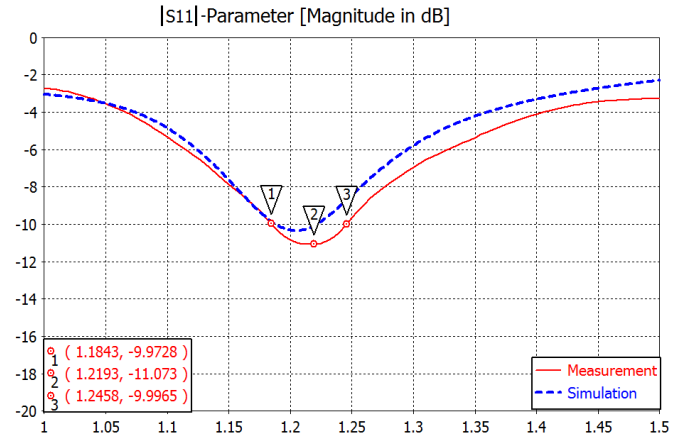


Figure 0.18 Comparaison mesure / simulation du module du coefficient de réflexion en fonction de la fréquence.

La comparaison entre modules des coefficients de réflexion (Figure 0.18) montre une légère différence entre la mesure et les résultats de simulation. Dans les résultats de la simulation, la bande

de fréquence est réduite à [1.18 au 1.22] GHz tandis que dans le cas de la mesure, la bande de fonctionnement va de [1.18 au 1.24] GHz. Ces valeurs de fréquences maximale et minimale sont utilisées pour la mesure du diagramme de rayonnement.

Les diagrammes de rayonnement sont présentés dans deux plans orthogonaux (*phi* = 0° et *phi* = 90°) à trois fréquences (1.184 GHz, 1.21 GHz, 1.245 GHz) de la bande passante nécessaire pour chaque composantes du diagramme de rayonnement E_{theta} et E_{phi}. Les résultats de la mesure et de simulation sont normalisés et comparés de la Figure 0.19 jusqu'à la Figure 0.24. Les deux plans sont comparés pour E_{theta} et E_{phi}.

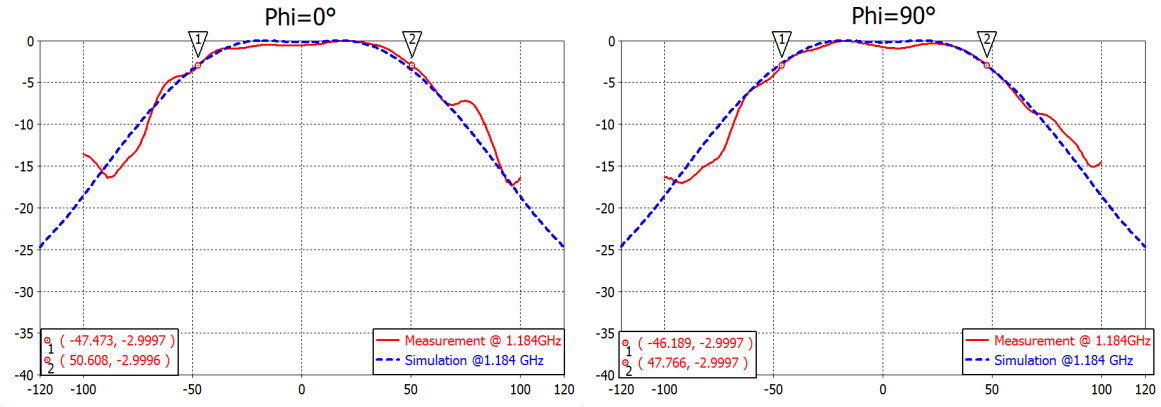


Figure 0.19 |E_{phi}| Mesuré vs Simulé à 1.184 GHz.

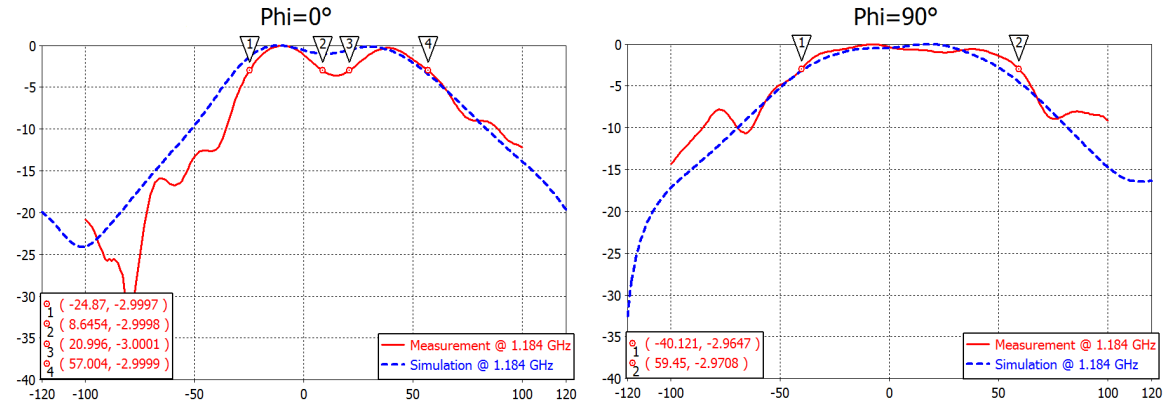


Figure 0.20 |E_{theta}| Mesuré vs Simulé à 1.184 GHz.

À la fréquence minimale (1,18 GHz), il existe un accord intéressant entre la simulation et la mesure pour les deux composantes. Néanmoins dans le plan phi = 0 ° pour la composante E_{theta}, une ondulation inattendue apparaît dans les résultats de mesure.

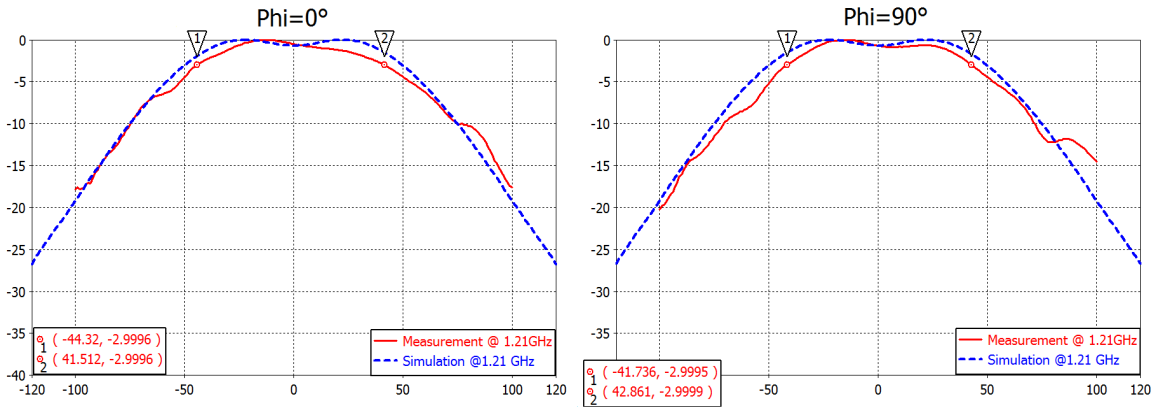


Figure 0.21 |E$_{phi}$| Mesuré vs Simulé à 1.21 GHz.

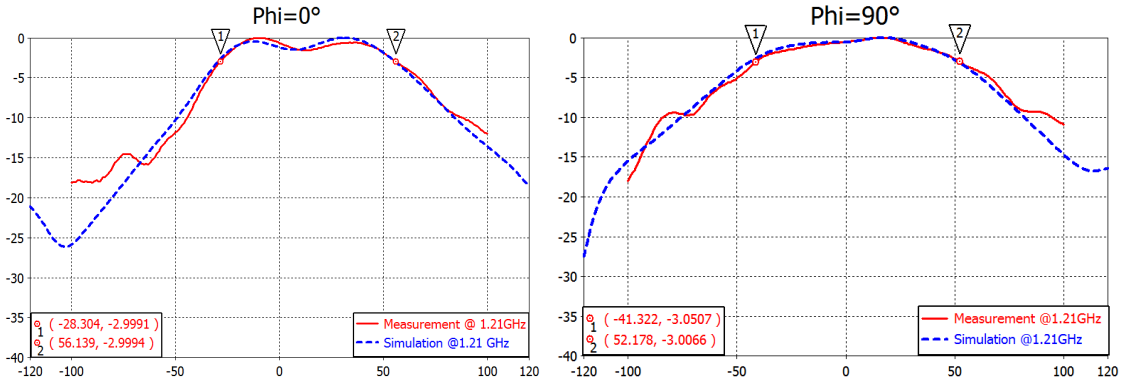


Figure 0.22 |E$_{theta}$| Mesuré vs Simulé à 1.21 GHz.

A la fréquence centrale, le HPBW est de 99° pour la composante E_{phi} dans les deux plans orthogonaux et de 84° et 94° pour la composant E_{theta} pour les deux plans phi = 0° et phi = 90° . L'écart entre les résultats des mesures et de simulations ne dépasse pas 3°. Pour les quatre figures, l'accord simulation mesure est tout à fait remarquable.

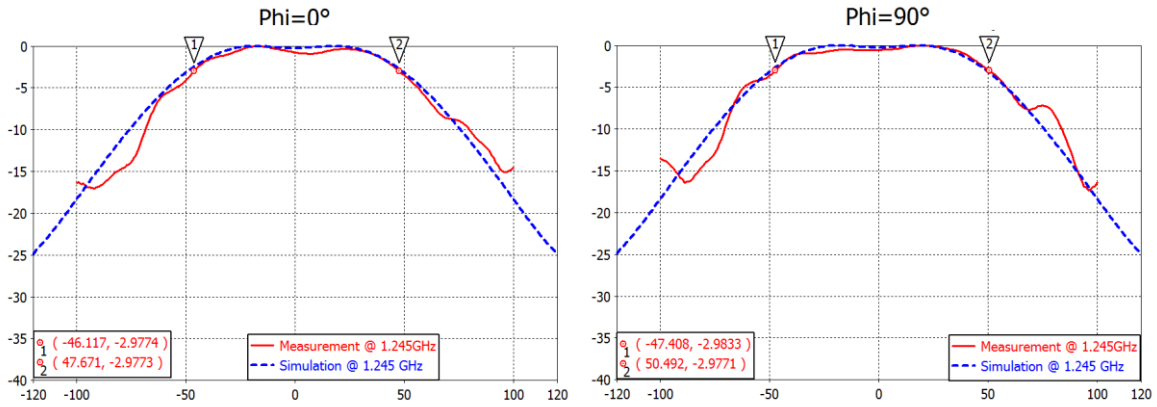


Figure 0.23 |E$_{phi}$| Mesuré vs Simulé à for 1.245 GHz.

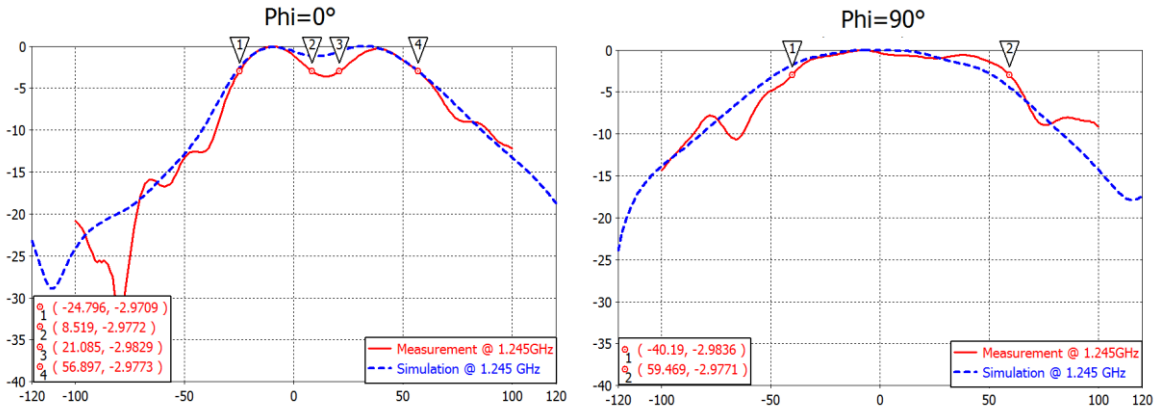


Figure 0.24 $|E_{theta}|$ Mesuré vs Simulé à for 1.245 GHz.

Enfin, à la fréquence maximum de la bande de fonctionnement, les résultats des quatre figures montrent un bon accord entre mesure et simulation. De plus les ouvertures à 3 dB sont à peu près identiques en mesure et en simulation sauf peut-être pour les valeurs de E_{theta} dans les plans *phi* = 0° et *phi* = 90° où les valeurs de mesure présentent des valeurs inférieures. En ce qui concerne le gain réalisé, une différence de 2 dB est toujours observée entre la mesure et les résultats de simulation dans la bande de fonctionnement [1.184 à 1.245] GHz.

L'ouverture à 3dB est augmentée de 18% par rapport à l'antenne de référence. L'ensemble de ces résultats valide le principe de la conception.

Bien que la couche supérieure soit une structure complexe, un bon accord entre résultats de simulation et de mesure des résultats est visible. La compatibilité entre les fichiers de simulation et l'imprimante 3D est tout à fait remarquable. Les fichiers de géométrie sont directement lisibles par l'imprimante 3D.

Conclusions :

Dans ce chapitre, un superstrat tout diélectrique a été décrit afin d'augmenter l'ouverture à 3dB d'une antenne planaire de faible encombrement. Ce superstrat est une modification d'un superstrat-lentille développé pour augmenter la directivité. Une fois que le profil modifié a été converti en une structure 3D, l'influence des valeurs dispersives sur les performances de l'antenne a été analysée. L'influence de la variation des valeurs de permittivité a aussi été analysée. Un premier objectif a été de synthétiser une permittivité variable avec un matériau unique (Téflon) et différentes densités de trous. Un deuxième objectif était de montrer la faisabilité de cette structure avec une imprimante 3D et d'adapter la conception aux exigences de l'imprimante. L'influence des dimensions et du plan de masse sur les performances de ce superstrat réalisé en matériau FullCure a été étudiée. Enfin le superstrat de dimensions 250x40 mm² a été réalisé avec l'imprimante 3D et a été mesurée pour prouver la validité du concept. Un bon accord entre mesure et de simulation des résultats a été observé.

Chapitre 4: Contrôle du rayonnement d'une antenne patch

Lors des premier et deuxième chapitres, les applications présentées permettaient de concentrer le rayonnement d'une antenne ou d'augmenter la largeur d'un faisceau directif. Mais comment peut-on changer complètement le diagramme de rayonnement d'une antenne planaire?

La Transformation d'Espace est une technique puissante qui permet de déformer l'espace à volonté afin d'imposer une trajectoire aux ondes électromagnétiques dans un milieu. Alors, dans ce chapitre on va maintenant utiliser la TE pour changer complètement le diagramme de rayonnement d'une antenne patch, en le combinant avec un superstrat.

On souhaite que le rayonnement s'éloigne de l'axe *Ox* (car aille vers les côtés du superstrat) (Figure 0.25). Pour cela on utilise deux quadri-ellipses opposées comme sur la Figure 0.25. Chaque une des parties transforme un espace cartésien en un plan «elliptique». L'antenne de référence utilisée précédemment est disposée comme sur la figure 0.25.

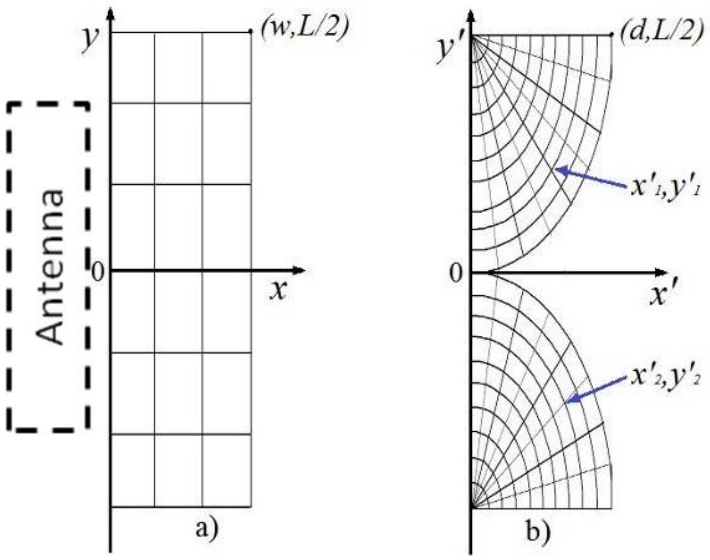


Figure 0.25 a) Espace réel. b) Espace virtuel. *L* = 200 mm, *d* = 37.5 mm, w = 37.5 mm, *a* = 2 (facteur de compression).

Les équations analytiques qui permettent de lier les deux espaces (virtuel et réel) sont présentées dans l'équation 8. Dans ce cas les deux coordonnées *x* et *y* sont transformées et permettent de diriger le rayonnement vers les antipodes.

$$x'_{1,2} = \frac{w}{d}\sqrt{(ax)^2 + \left(y \mp \frac{L}{2}\right)^2} \quad , \quad y'_{1,2} = \frac{L}{\pi}\tan^{-1}\left(\frac{y \mp \frac{L}{2}}{ax}\right) \qquad (8)$$

Ces deux transformations quadri-ellipses sont des modifications de deux quarts de cercles compressés dans la direction *x*. Les centres des cercles compressés sont localisées à $y=\pm L/2$. Chaque structure présente $L/2$ comme axe majeur et *d* comme axe mineur tandis que la structure cartésienne présente une épaisseur de *w* est une longueur *L*.

On utilise ensuite la technique de la TE pour calculer les paramètres constitutifs en utilisant l'équation 10 et 11 où: A représente la matrice Jacobienne.

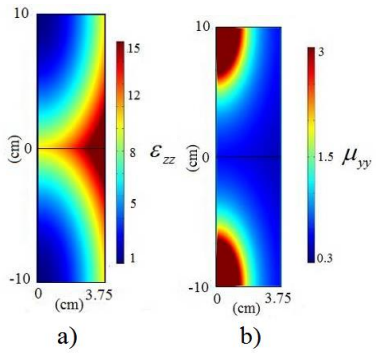
$$\varepsilon'_{1,2} = \frac{A\varepsilon_0 A}{\det(A)}; \qquad \mu'_{1,2} = \frac{A\mu_0 A}{\det(A)} \tag{9}$$

$$A = \begin{pmatrix} \frac{\partial x'}{\partial x} & \frac{\partial x'}{\partial y} & \frac{\partial x'}{\partial z} \\ \frac{\partial y'}{\partial x} & \frac{\partial y'}{\partial y} & \frac{\partial y'}{\partial z} \\ \frac{\partial z'}{\partial x} & \frac{\partial z'}{\partial y} & \frac{\partial z'}{\partial z} \end{pmatrix} \tag{10}$$

Apres réductions et simplifications des paramètres constitutifs calculés, et en considérant que $a=2$ et $d=w$, les composantes réduites des tenseurs de permittivité et de perméabilité sont donnés dans l'équation 11.

$$\mu_{xx}^{1,2} = 1 \qquad \mu_{yy}^{1,2} = \left(\frac{L}{\pi . x'_{1,2}}\right)^2 \qquad \varepsilon_{zz}^{1,2} = 4\left(\frac{\pi}{L} x'_{1,2}\right)^2 \tag{11}$$

Apres le calcul des paramètres constitutifs et la réduction jusqu'a $\mu'=diag(\mu_{xx}, \mu_{yy}, 1)$ et $\varepsilon'=diag(1,1\ \varepsilon_{zz})$, on trace leur profil spatial sur la Figure 0.26. On constate que la permittivité relative varie entre 1 et 15 tandis que la perméabilité relative varie entre 0.3 et 3. Les valeurs extrêmes ont été évitées pour ne garder que des valeurs réalisables (les valeurs extrêmes sont localisées dans de petites régions de la structure).



a) b)

Figure 0.26 a) Composante ε_{zz} du tenseur de permittivité relative. b) Composante μ_{yy} du tenseur de perméabilité relative.

Pour évaluer le comportement électromagnétique du dispositif, il est nécessaire de l'analyser en étudiant la propagation du champ électrique à l'intérieur de ce superstrat à 1.2GHz. On utilise Comsol Multiphysics pour réaliser ces simulations car avec ce simulateur il est possible de définir un matériau inhomogène et non-isotrope.

Une antenne patch est modélisée par une distribution de courant au-dessus d'un diélectrique lui-même au-dessus d'un plan de masse. Les distributions de la composante de champ électrique *Ez* avec le modèle d'antenne seul et avec le superstrat sont présentées dans les Figure 0.27 et Figure 0.28.

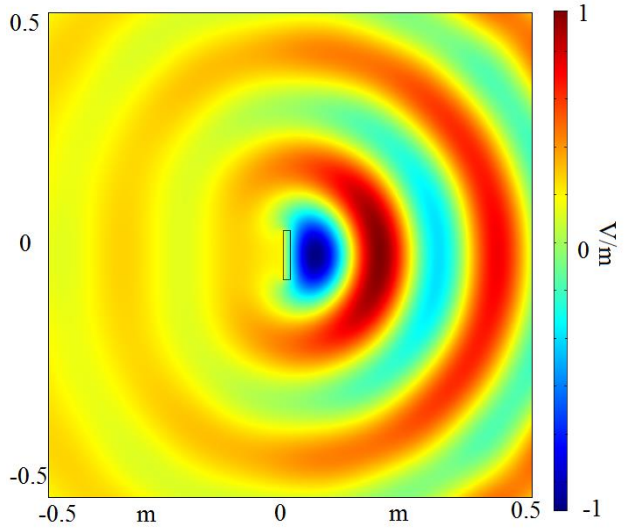


Figure 0.27 Distribution du champ électrique *Ez* à 1.2 GHz pour l'antenne seule.

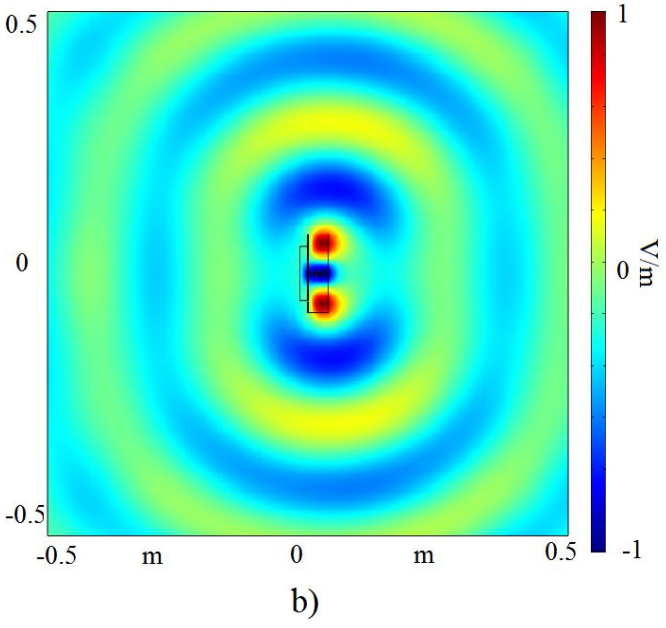


Figure 0.28 Distribution du champ électrique *Ez* à 1.2 GHz pour l'antenne avec le superstrat.

On observe sur la Figure 0.27 la distribution classique du champ électrique produit par une antenne patch, c'est à dire dirigé vers la direction «broadside» (phi=0°). Dans le cas du Figure 0.28 le superstrat combiné avec l'antenne produit maintenant une propagation du champ électrique radicalement différente, vers les directions ± 90°.

On utilise l'antenne patch de référence décrite dans les annexes fonctionnant entre [1.16-1.24] GHz associée au superstrat. Pour construire le superstrat, il est nécessaire de suivre les étapes intermédiaires de discrétisation et de rotation qui vont permettre de réaliser une structure en anneaux concentriques possédant des valeurs de permittivité et perméabilité homogènes.

L'antenne patch alimentée par deux ports a été conçue pour travailler dans la bande L avec le superstrat. Cette antenne ressemble à l'antenne de référence utilisée dans le chapitre trois (détaillées dans les annexes). La taille du patch a été modifiée afin de conserver la bande de fonctionnement de l'antenne avec le superstrat à la fréquence ciblée. Dans ce cas, le substrat de l'antenne est un carré de 100 * 100 mm² avec 15,5 mm d'épaisseur et de la taille du patch est 65,5 * 65,5 mm². Le substrat est de l'Arlon AD 250 (ε_r = 2,5) et le plan de masse a les mêmes dimensions latérales que le substrat.

En présence du superstrat, l'adaptation de l'antenne est perturbée. Une étape intermédiaire est donc prévue (Figure 0.29) pour retrouver la bande de fonctionnement de l'antenne. Plusieurs configurations sont étudiées : l'antenne et le superstrat sont en contact direct (pas de couche intermédiaire); l'antenne et le superstrat sont séparés de 10 mm; une couche intermédiaire de diélectrique homogène de 5 mm et 10 mm d'épaisseur est insérée entre l'antenne et le superstrat.

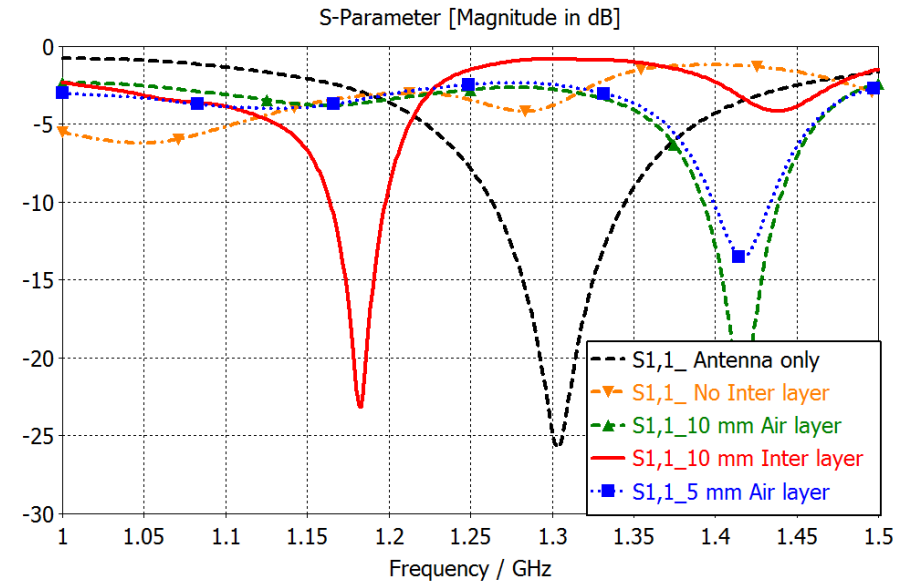
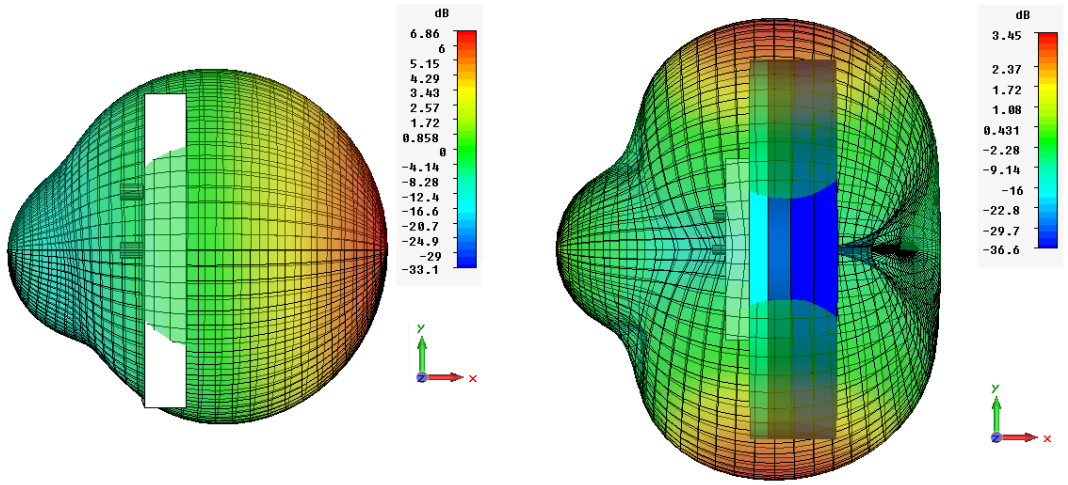


Figure 0.29 Coefficient de réflexion de la structure complète avec les différentes configurations.

L'ajout d'une couche d'air entre l'antenne et le superstrat permet de récupérer une largeur de bande d'exploitation, mais elle est décalée vers les fréquences plus élevées. Il faut donc ajouter une couche de transition de 10 mm d'épaisseur et de permittivité relative $\varepsilon_r = 4$ entre l'antenne et le superstrat pour obtenir la bande de fréquences souhaitée. Cette couche augmente l'épaisseur de l'ensemble du dispositif de 53 mm à 63 mm pour la structure finale. Afin de souligner les performances de la structure complète, les diagrammes de rayonnement 3D obtenus à partir de CST Microwave Studio sont présentés sur la Figure 0.30 avec et sans superstrat. Sur la Figure 0.30-b, on constate que l'antenne patch associée au superstrat produit bien un rayonnement antipodal avec un gain réalisé maximal de 3.5 dB dans la direction ± 89°, alors que dans la direction 0°, le gain est égal à -14.5 dB. La Figure 0.30-a montre que le gain réalisé de l'antenne patch seule est égal à 6.8 dB dans la direction 0°.



a) b)

Figure 0.30 Gain réalisé pour: a) Patch seul à 1.3 GHz et b) Patch avec le superstrate TE à 1.2 GHz.

Les performances présentées ont été calculées avec une polarisation linéaire (un seul accès de l'antenne est alimenté, l'autre est connecté à une charge 50 Ohms) et ces performances montrent la possibilité d'obtenir un diagramme de rayonnement antipodal dans un plan. Cependant, l'antenne possède deux accès qui doivent être connectés à un coupleur hybride lorsque l'on souhaite émettre en polarisation circulaire. Etudions maintenant le comportement de l'antenne si les deux ports de cette antenne sont alimentés simultanément en phase (polarisation linéaire) et avec la même amplitude (configuration 1). Dans un second temps, les ports sont alimentés avec une différence de phase de 90° avec la même amplitude (polarisation circulaire, configuration 2).La configuration 2 présente un rayonnement quasi omnidirectionnel dans un plan, formé par quatre larges faisceaux et présentant un maximum de 3.4 dB.

Deux lobes principaux sont formés dans la configuration 1 présentant un maximum de gain réalisé de 4.5 dB dans la direction thêta = 46°. Comme mentionné précédemment, le rayonnement antipodal

est observé dans un plan lorsque l'antenne est alimentée uniquement par un port et l'autre étant connecté à une charge de 50 Ohms. Avec ces deux configurations d'alimentation, le rayonnement antipodal est obtenu dans les deux plans (*thêta* = 90 ° et *phi* = 0°) (Figure 0.31 a et b). Dans le plan *thêta* = 90°, le gain réalisé dans les directions ± 90° est de 2.0 dB pour la configuration 2 et de 1.9 dB pour la configuration 1. Bien que le diagramme de rayonnement comporte trois lobes (Figure 0.31), le rayonnement antipodal est toujours bien présent. La plus grande différence entre ces configurations est observée dans le plan *phi* = 90 ° de la Figure 0.31c.

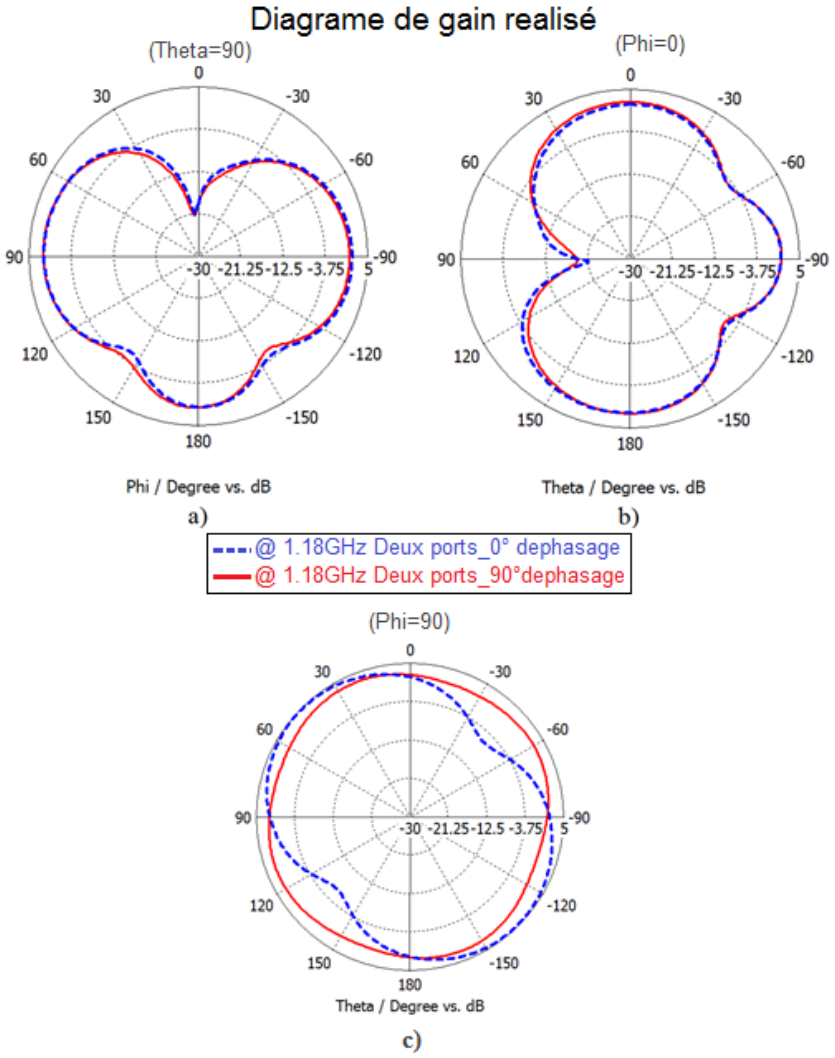


Figure 0.31 Gain réalisé dans les plans *thêta=90°*, *phi=0°* et *phi=90°* de l'antenne avec le superstrat pour les différentes configurations d'alimentation à 1.18 GHz (rouge avec 90° de déphasage et bleu sans déphasage entre accès).

Conclusions :

Nous avons présenté les potentialités d'un superstrat conçu grâce à la TE. Ce superstrat de faible épaisseur (0,15 λ à la fréquence de travail) change radicalement le diagramme d'une antenne patch en produisant un rayonnement antipodal avec un gain réalisé de 3.5 dB dans les directions ± 89°.

En utilisant les deux accès de l'antenne à double polarisation, le rayonnement antipodal apparaît pour les deux plans (thêta = 90° et phi = 0°). Lorsque l'antenne est alimentée avec la même amplitude et un déphasage de 90° entre accès, elle produit en présence du superstrat un diagramme quasi omnidirectionnel.

Conclusion générale

La technique de la Transformation d'Espace est un moyen puissant et performant pour contrôler la propagation des ondes. Toutefois, pour réaliser ces performances, il est nécessaire d'utiliser des matériaux complexes ou des matériaux qui ne sont pas disponibles dans la nature (métamatériaux) et aussi de définir un espace dont la taille est plus grande que la longueur d'onde.

Le présent travail a deux objectifs. Le premier est de vérifier qu'il est possible de réduire l'espace nécessaire à la transformation tout en conservant la propriété souhaitée par la conception d'antenne. Le deuxième objectif est de proposer différentes modifications des matériaux en agissant sur la permittivité relative et la perméabilité relative afin de faciliter la fabrication de prototypes avec des matériaux standards.

Nous avons notamment montré que dans le cas du superstrat développé pour élargir le faisceau, il était possible de réaliser directement ce superstrat en matériau FullCure à l'aide d'une imprimante 3D.

Pour résumer, trois applications qui visent à contrôler ou à modifier le diagramme de rayonnement d'une antenne classique ont été présentés. Soit pour concentrer le rayonnement dans la direction broadside, pour augmenter l'ouverture à 3dB et même pour créer deux lobes orientés vers les antipodes, l'objectif de ce travail était de démontrer au travers de ces applications qu'il était possible de simplifier la méthode de conception. Cette méthodologie est également compatible avec un processus industriel et peut être appliquée ou utilisée dans des domaines tels que les applications aéroportées.

Acronyms

Abbreviation	Meaning
HPBW	Half Power Beam Width
TE	Transformation Electromagnetic
MIMiCRA	Metamaterial Inspired Microwave Conformal Radar Antennas
PEC	Perfect Electric Conductor
MP	Material Parameters (permittivity and permeability)
SRR	Split Ring Resonator
FDTD	Finite-Difference Time-Domain
HFSS	High Frequency Structure Simulator- Commercial software package
ELC	Electric Coupled Resonator
FT	Field Transformation
CS	Coordinate System
RG	Realized Gain

Table of Contents

Acknowledgments 5

Resume 7

Acronyms 35

Table of Contents 37

Introduction 41

2. Background 41

3. Objectives 42

Chapter 1 Transformation Electromagnetics: State of the Art 43

1. Principle 43

2. Different approaches on TE 46

2.1. Analytical transformations 46

2.2. Quasi Conformal transformation 47

2.3. Comparison between analytical transformations and quasi Conformal transformation 48

3. TE Applications at microwave frequencies 49

3.1. Cloaking devices 49

3.1.1. Invisibility cloak 49

3.1.2. Invisibility coat 52

3.1.3. Electromagnetic cloaking of antennas 54

3.2. Radiating devices 55

3.2.1. High directive antennas 56

3.2.3. Multibeam antenna 60

3.2.4. Multibeam lensing by conformal mappings 61

3.3. Limitations and drawbacks of Transformation Electromagnetics applications 63

4. Conclusions 64

Chapter 2 All Dielectric Flat Reflector 66

1. TE Principle 67

1.1. 2D study 67

1.1.1. Analytical transformation 68

1.1.2. Near field analysis 70

2. Synthesis of the structure. 71

2.1. Solutions to synthesise CP values 72

2.1.1. All dielectric solutions for TE devices 72

2.1.2. Graded dielectric methodology 73

2.2. Constitutive parameter simplifications 74

2.3. Influence of varying constitutive parameters 75

2.4. Profile discretization 78

2.5. Permittivity synthesis 80

3. Complete structure 81

3.1. Geometry and performance of the device 81

3.2. Optimisations in size and performance 83

3.2.1. Optimizations in size 84

3.2.2. Farfield analysis at different frequencies 85

2.2.3. Comparison with similar devices 86

4. Conclusions 88

Chapter 3 All Dielectric Superstrate to Increase HPBW of an antenna 90

1. TE Inspired superstrate 91

1.1. From permittivity profile to superstrate (2D to 3D extension) 92

1.1.1. Profile Rotation 93

1.1.2. Rectangular blocks 94

1.2. Influence of dispersive values of permittivity 96

1.3. Influence of permittivity variation 98

1.4. Permittivity synthesis 100

1.5. Comparison with classical superstrates 103

2. Optimisation of size and performances of drilled structure 105

2.1. Geometry and performance of the device 105

2.2. Optimisations in size and performance 108

2.2.1. Influence of diameter and thickness. 108

2.2.3. Influence of ground plane 110

3. Validation by measurements 112

3.1. S parameters 114

3.2. Farfield pattern analysis 115

4. Conclusions. 118

Chapter 4 Antipodal Radiation from Superstrate and a Patch Antenna 120

1. Device description 121

1.1. Analytical Transformations 121

1.2. 2D structure 123

2. Impedance matching 125

3. Complete structure study 126

3.1. Radiation Pattern Analysis 127

3.2. Influence of the feeding configuration. 128

4. Sensitivity to the value of the maximal relative permittivity 131

5. Sensitivity to the value of the minimal relative permittivity 133

6. Conclusions 134

Conclusions and Future Work 136

Conclusions 136

Future Work 137

References 140

List of Figures 149

List of Publications 157

Publications 157

Appendices 159

Appendix A: Reference Antenna Specifications 159

1-Introduction 159

2-Description of Case 1 antenna 159

Geometry 159

3-Simulated performances of Case 1 Antenna with square 100 mm² ground plane results 161

4.Simulated performances of Case 1 Antenna with circular 600 mm diameter ground plane 165

Appendix B: Design tools 170

1-Defining the targeted transformation 170

2-Defining the mathematical expressions 170

3-Testing the electromagnetic behaviour of the device. 171

4-Synthesizing the material needed to produce the TE behaviour 172

Introduction

2. Background

The present work started in October 2011, in the framework of the MIMiCRA project and was performed in the RFM (RF & Microwave) group of Comelec department at Télécom ParisTech. This project was managed and funded by France and UK, within the framework of the European Defence Agency. The work was carried out by a wide consortium of different companies and universities: Airbus, Dassault Aviation, Thales, Telecom ParisTech, Institut d'Électronique Fondamentale, BAE Systems, MBDA (UK), Queen Mary College London, and Oxford University.

The MIMiCRA project intends to evaluate the contribution and viability of use of new techniques such as Metamaterials and Transformation Electromagnetics on airborne applications. One of the specific objectives of the project is to design and test GPS antennas with ambitious specifications. Then, in order to achieve the requirements; Metamaterials are used for many purposes such as thickness reduction, dual band behaviour, etc. Transformation Electromagnetics are also used in order to control the propagation and the radiation pattern of these antennas, which is the main purpose of this work.

Transformation Electromagnetics appeared in 2006 with two ground breaking papers [1],[2] written by J. Pendry et al. and U. Leonhardt. Then, a third paper [3] as proof of concept validated experimentally the initial theorethical work. Since then, this technique has become an emerging research field in physics and engineering in the last few years. The application that described the technique was the cloaking device, which obviously caught the imagination of many scientists in the microwave and optics community.

Apart from the fact that scientists claimed the possibility of achieving invisibility, the interest in these publications is due to the theoretical principle behind this work, which is remarkably complex and robust. This work claims the possibility of an unprecedented technique to control electromagnetic waves interaction with engineered materials to achieve exotic electromagnetic behaviour. This powerful technique allows accurate control of electromagnetic waves. This control is based on an appropriate interpretation of anisotropic and inhomogeneous compression and

stretching of the material and it takes into account the reinterpretation of Maxwell's equations in a transformed media.

3. Objectives

The final purpose of this work is to explore and propose applications of Transformation Electromagnetics in order to control the radiation pattern of an antenna. More precisely, to explore different configuration of radiation pattern control such as, achieving high directivity, increasing the half power beamwidth, directing the propagation to the sides of an antenna, etc. It is also intended to propose a simple methodology. It should also be compatible with industrial process in order to be applied or used in fields such as airborne applications.

Therefore, the document is organized in 4 chapters: In chapter one, the state of the art on Transformation Electromagnetics and some applications are explored. A full description of the theoretical principle is presented in order to show the main aspects that the reader needs to know about the technique. Both design approaches (analytical transformation and conformal mappings) are presented, discussed and compared. Next, many applications are summarized. In order to evaluate and discuss their potentials for antenna design, main trends on TE applications at microwave frequencies such as the invisibility cloak and some related applications are described and discussed. Then, applications on antenna design are presented for summarizing the efforts of the community on this field, as well as analysing and comparing the limitations and drawbacks.

Chapter two is dedicated to explore an application that intends to achieve high directivity while showing how TE can be used to design a device that can replace a classic electromagnetic device. A flat reflector is designed to perform as a parabolic reflector, decreasing the size and geometry using TE. Simplicity for the design and the realisation process is highly kept in mind while methodology of achieving variant values for constitutive parameters is presented as well.

In chapter three, a TE superstrate placed over a patch antenna is presented. This TE application intends to increase or enlarge the Half Power Beam Width (HPBW) of a planar antenna. Some simplifications and reductions are introduced in the transformation in order to simplify the realisation to obtain of a real prototype.

In chapter four, the antipodal radiation from a patch antenna combined with a superstrate is described from the analytical transformation down to the farfield results and optimizations in size and performance. Finally, the perspectives for future work and conclusions are summarized at the end of the manuscript.

Chapter 1
Transformation Electromagnetics: State of the Art

In past few years, an intense activity on the Transformation Electromagnetics (TE) has been developed around many fields such as optics, microwave, acoustics, etc. This activity is due to the refreshing new ideas and potential applications that TE brings to these fields among others. An unprecedented way to control the interaction wave-material focuses the attention of many research groups on the TE. Therefore, this chapter will be dedicated to explaining the principle of the TE technique and different applications that we can find in the literature, especially at microwave frequencies. The advantages and challenges of using TE to design electromagnetic devices are highlighted. Then, the applicability of TE for antenna design, as well as the issues related to the realisation of wideband and practical applications, are discussed at the end.

1. Principle

This part of the chapter is dedicated to explain the important points to understand the TE technique. Some key points are needed to be detailed in this part such as: invariance of Maxwell's equation and interpretation of constitutive parameters in transformed media, as well as a complete explanation of the TE technique. However for a full understanding of TE, it is almost mandatory to explain the theory behind the geometry of light [4] because, it is from this geometrical approximation of light trajectory that spatial transformation comes from. TE is also known as spatial transformation because we replace a regular space with a modified or transformed space where the light or waves trajectories are governed by mathematical expressions. These wave trajectories are explained by geometry of light, which we intend to describe.

As said before, the principle of TE is based on the theory of geometry of light [4] introduced by Fermat. It is applicable to almost all media as an approximation of geometrical optics. This principle explains the curved trajectories of light in inhomogeneous media and how waves see media as an effective geometry. Then, as curved trajectories are mentioned, we need to define the path length *S*.

The shortest optical path length *S* is described by the Fermat's principle (Eq. 1.1), where *n* is the refractive index and *dl* is the line element.

$$S = \int n.dl \quad dl = \sqrt{dx^2 + dy^2 + dz^2} \qquad \textbf{(1.1)}$$

If the refractive index *n* corresponds to a homogeneous medium the shortest path *S* follows a straight line. However, if *n* corresponds to inhomogeneous media, *S* follows a curved trajectory. More precisely, if *n* is a function of the coordinate system, and if this coordinate system is curved, then we have a curved optical path or trajectory. These curved trajectories are the first step to understand the technique of Transformation Electromagnetics and consequently to understand what happens when waves pass through a transformed medium.

Once the idea of a curved optical/wave trajectory is familiar to us, the next step is to describe the Transformation Electromagnetics technique itself. In Figure 1.1-a, the Cartesian grid with a straight ray passing through this system is shown. Any point *P* in this space is expressed in terms of: *x, y* and *z*. Then, it is transformed into a virtual space where the ray trajectory is curved (Figure 1.1-b), and where the coordinates are: *x'*, *y'* and *z'*. The link between the two spaces or Coordinate Systems (CS) is a mathematical expression that defines the wave material interaction, as Equation 1.2:

$$\begin{pmatrix} x' \\ y' \\ z' \end{pmatrix} = \begin{pmatrix} x'(x,y,z) \\ y'(x,y,z) \\ z'(x,y,z) \end{pmatrix} \qquad \textbf{(1.2)}$$

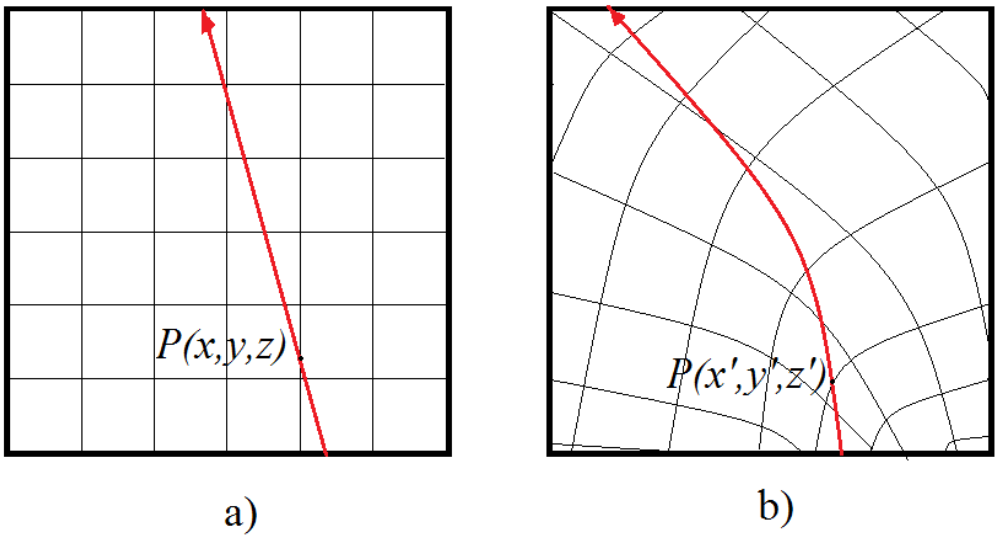


Figure 1.1 a) Cartesian coordinate system and b) Transformed coordinate system.

Transformation Electromagnetics, as aforementioned, is a method to control wave propagation under a transformed space. Two key points are relied upon for TE. These points are:

a) Invariance of the Maxwell's equations under any coordinate transformation [1],[2].

In general, these equations in harmonic regime and using the complex notation at a fixed frequency can be written as follows.

$$\nabla \times E = -j\omega\mu H \qquad \nabla \times H = j\omega\varepsilon E \qquad \textbf{(1.3)}$$

If Equation 1.2 is used in 1.3, then Maxwell's equations maintain the same form because the physical quantities (*E*, *H* and *w*) are independent from the coordinate system:

$$\nabla' \times E' = -j\omega\mu' H' \qquad \nabla' \times H' = j\omega\varepsilon' E' \qquad \textbf{(1.4)}$$

b) Interpretation of electric permittivity and magnetic permeability in the transformed CS as a set of transformed parameters of the original coordinate system.

The Equations 1.5 and 1.6 are the results of the mathematical development of the Maxwell's equation in transformed coordinate (Equation1.4). Then, the material parameters MP (ε' and μ') can be expressed as a function of the CS. Where: *A* and A^T in Equation 1.7 are: the Jacobian matrix and its transposed matrix respectively. They are used for the transformation between the real space and virtual space.

$$\mu' = \frac{A\mu A^T}{\det(A)} \qquad \textbf{(1.5)}$$

$$\varepsilon' = \frac{A\varepsilon A^T}{\det(A)} \qquad \textbf{(1.6)}$$

$$A = \begin{pmatrix} \frac{\partial x'}{\partial x} & \frac{\partial x'}{\partial y} & \frac{\partial x'}{\partial z} \\ \frac{\partial y'}{\partial x} & \frac{\partial y'}{\partial y} & \frac{\partial y'}{\partial z} \\ \frac{\partial z'}{\partial x} & \frac{\partial z'}{\partial y} & \frac{\partial z'}{\partial z} \end{pmatrix} \qquad \textbf{(1.7)}$$

The final step is to express the material parameters in terms of the transformed CS. Then, the resulting profile of every component of the permeability and permittivity tensor is calculated. Usually, the range of variation of the MP profile can be quite wide, which may be a problem for the realisation and manufacture of the resulting devices. However, these issues can be overcome using simplifications and reductions carefully. This key point will be discussed in the following sections.

Thus, in summary, the design process requires the following steps:

- Determining a known wave-material interaction in the real space. For example, changing the trajectory of a plane wave by using a curved geometry.
- Choosing a volume of space in the original system and its associated volume in the transformed system.
- Defining an analytical coordinate transformation that links both spaces (virtual and real).
- Computing the MP in the transformed space using Equations 1.5 and 1.6.
- Interpreting these MP and obtaining the material profile in the original space. For example, calculated MPs tensor could include some components needing some approximations, reductions or some particular orientation. These intermediate steps are needed to simplify the model and the resulting material.
- Choosing or designing a material with the desired profile.

Usually, for the purpose of simplicity the design process starts considering a two dimensional case, in order to minimize the quantity of variables for MP tensors. If 2D analysis is used, then only five components are calculated for the MP tensors, instead of nine (3D analysis), which obviously makes the design process simpler in each step. Once the 2D design is completed, it is possible to extend to a 3D device taking into account some considerations that are explained in next chapters.

2. Different approaches on TE

From the engineering point of view, there are two approaches for designing TE devices. These are: analytical transformation and the conformal mappings. These approaches on TE are described in this section. Both of them present some advantages and limitations. A full description, analysis and comparison between them are also presented.

2.1. Analytical transformations

This approach takes into account all the components in Maxwell's equations as well as all the components of the constitutive parameters in the transformed medium. Many applications are designed with this approach, mostly simulations where exotic electromagnetic behaviour is explored, including [1] which is considered as the reference contribution in this field. In literature, it is possible to find contributions on the theoretical development of the approach and rigorous descriptions of the principle are presented in [5]. In [6] many applications are proposed (tapper, antennas, cloaks) using this approach while in [7] and [8], reviews of the principle and some TE applications using this approach are summarized.

This approach is the simplest to become familiar with the TE technique, because from the mathematical transformation through the MP calculation it is possible to follow the different steps required for the technique. However, this approach leads to complicated tensors (in terms of difficulty for simplifying) for the MPs which can limit the realisation of the designed device, as the quantity of unknown variables in the calculation are important. To overcome this issue, some simplified methods of realisation are developed and synthesized using metamaterials [9], because calculated MP profiles are quite complicated and require dispersive (permittivity and permeability are less than one) materials and anisotropy. Dispersive materials are hard to handle in terms of realization. They represent a big compromise in terms of bandwidth and losses as usually resonant structures are involved to obtain the expected behaviour.

2.2. Quasi Conformal transformation

The discrete transformation is based on graphical coordinate transformation [10]. This approach for TE uses a 2D space to calculate the refractive index *n*. This calculation is also based on the Fermat principle (see Equation 1.1), where the transformed coordinates (*x'*, *y'*) are expressed in function *x* and *y*. Then, *n(x,y)* can be calculated using the trajectories *dS* and considering *dl* as in Equation 1.1. Keeping some conditions in terms of orthogonally in the curved grid, it is possible to express *n* as in Equation 1.8. The transformation is based on areas (not on shapes) as it is possible to see in Figure 1.2. It should be noted that it does not take into considerations non-linear effects.

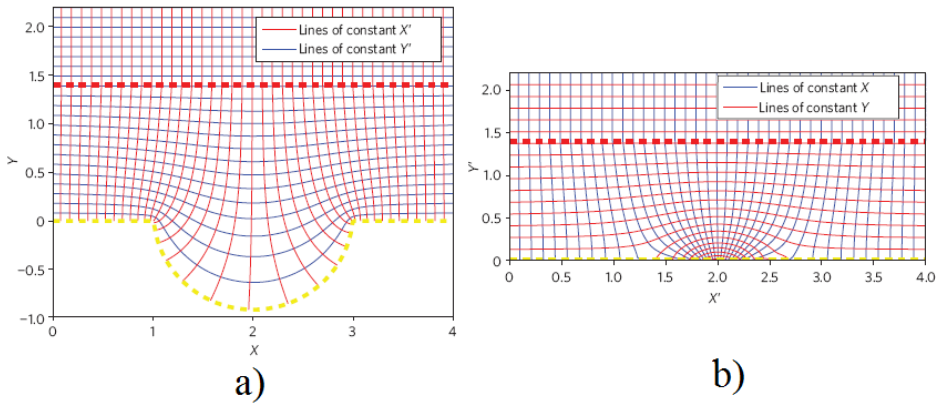


Figure 1.2 Example of Discrete Transformation [11].

The refractive index in the new coordinate system *n'* is related to initial refractive index n_0 by:

$$n' = n_0 \sqrt{\frac{\Delta x_0 \Delta y_0}{\Delta x'_0 \, \Delta y'_0}} \qquad \textbf{(1.8)}$$

Where: Δx_0, Δy_0,$\Delta x'_0$, and $\Delta y'_0$, are the mesh sizes along *x, y, x'* and *y'*, respectively.

Depending on the geometry, the required refractive index for the new map may have some regions with values of refractive index lower than one, which requires the use of metamaterials. For example, in [12] invisibility cloaks are proposed with a method of conformal mappings for arbitrary shaped objects and in [13] a non-Euclidean invisibility cloak in broadband regime is proposed using also conformal mappings.

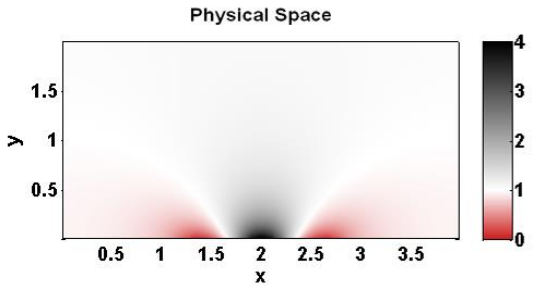


Figure 1.3 Maps of index in the physical and virtual spaces [11].

In Figure 1.3 it is possible to see a example of conformal mapping, the physical space intends to replace or behave as the virtual space. The physical space is a flat structure with a variable refractive index, while the real space is a curved structure. The mesh in Figure 1.2-b allows calculating an isotropic refractive index map. This map is usually translated to an only permittivity profile by keeping the permeability constant *(μ_r=1)*. Using only permittivity variation allows the use all dielectric methods for realization, and also a broadband behaviour, because resonant structures are usually avoided for synthesizing ε. Then, to run simulations usually Finite Difference Time Domain FDTD algorithms are used, because of its convenience to generate curved conformal mappings and calculate electromagnetic behaviour with it.

2.3. Comparison between analytical transformations and quasi Conformal transformation

As said before, there are two available approaches for the TE technique. The analytical transformation and the quasi-conformal transformation (discrete transformation), both of them exhibit several features that make them appropriate for different kind of applications and devices.

While the analytical transformation is based on perfect transformation using Maxwell Equations and analytical equations that describe the wave-material interaction, the quasi conformal transformation is based on graphical approximations of curved geometries using some considerations about orthogonality in the curved meshes.

The analytical transformations require anisotropic materials because of the complicated tensors (sometimes non diagonal μ and ε) that result from the calculation of the MP profile while in the case

of the quasi-conformal transformation, approximation on anisotropy are assumed with a graphical approximation, proposing a design process based on variable index (only diagonal) with no permeability variation.

As the analytical transformation requires anisotropic materials, this approach also introduces dispersive materials because some of the resulting material parameters can be negative or present a value below to one. In the case of the quasi conformal mappings, only non-dispersive materials are used because of the simplifications made through the process.

3. TE Applications at microwave frequencies

Since the first papers [1], [2] about TE that came out in 2006, many contributions at microwave frequencies have been proposed. As a way to present the design process of a TE device and also to familiarize with potential uses, limitations and current works on TE, some of the most know applications are reviewed. Including some of this application are described and presented in this section. More precisely, two types of applications are presented: cloaking devices and TE applications on antenna design.

3.1. Cloaking devices

Pendry, Shurig and Smith showed the principle of cloaking in a publication in 2006 [3]. This work explains the method to hide a cylindrical volume illuminated by a polarized electric field at a particular incidence by bending the waves around the volume. As it is known, this application causes a huge impact in many fields. Therefore, several contributions followed the initial work such as: notes about time delay and reflection on conformal invisibility cloaks [14], analysis of the different interactions between the cloak device and the electromagnetic waves [15], studies about the perfect cloak and its sensitivity to small perturbations [16], studies on the cloak limitations [17], the cloaking of active devices [18], etc. In the following sections, we have chosen to describe two main applications: invisibility cloak and the invisibility coat.

3.1.1. Invisibility cloak

The most intriguing application of TE is the invisibility cloak, because it claims the possibility of modifying the trajectory of light (or waves) around an object. It means that waves do not pass through the object, but skirt the object and recover their original path. Metamaterials were used to realise the first invisibility cloak [3] in the microwave domain, see Figure 1.4-a.

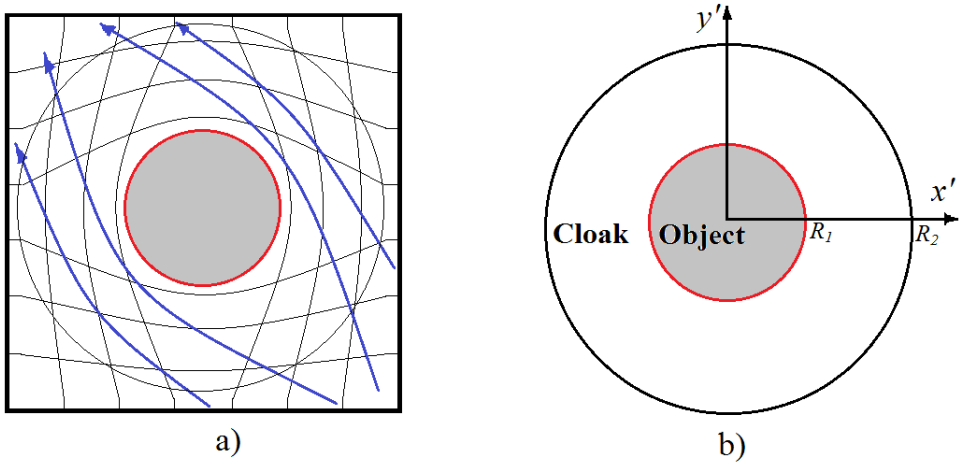


Figure 1.4 a) Wave's trajectory turned around an object. b) Layout for cloaking. Transformed space is the region between R_1 and R_2, the cylinder's section between 0 and R_1 is metallic.

In Figure 1.4-b, two regions are identified. A cylindrical region: $0 \leq \rho \leq R_1$, where the object is placed to be hidden, and an annular circular region: $R_1 \leq \rho' \leq R_2$, which corresponds to the cloaking device and where the transformation takes place. In this case, the analytical expression for the coordinate transformation is Equation 1.9:

$$\rho' = R_1 + \frac{R_2 - R_1}{R_2}\rho \qquad \varphi' = \varphi \qquad z' = z \qquad \textbf{(1.9)}$$

Then, the Jacobean is obtained using Equation1.10:

$$A = diag\left(\frac{R_2 - R_1}{R_2}, \frac{\rho'}{\rho}, 1\right) \qquad \textbf{(1.10)}$$

Using this Jacobean in Equations 1.5 and 1.6, the MPs (ε' and μ') are:

$$\varepsilon' = \mu' = diag\left(\frac{\rho' - R_1}{\rho'}, \frac{\rho'}{\rho' - R_1}, \left(\frac{R_2 - R_1}{R_2}\right)\frac{\rho' - R_1}{\rho'}\right) \qquad \textbf{(1.11)}$$

From Equation 1.11, it is clear that both permittivity and permeability are inhomogeneous and anisotropic. They present a continuous variation along the coordinate system. As aforementioned, the range of variation of the MPs of this profile can be very extreme. These continuous profiles of ε' and μ' cannot be directly used in the realization process, they need to be simplified and converted into realistic parameters. This key point will be discussed in following chapters of the manuscript.

In some cases, this mathematical development can be very tedious, but in general, the design is assisted by mathematical tools like Mathematica or MathCad, which are very helpful in cases where the transformation is not as elegant as the cloaking case just presented.

The next step is to verify the physics (field distribution) by running an electromagnetic simulator. However, this kind of anisotropic and inhomogeneous material requires particular simulation software that allows expressing permittivity and permeability in form of variant space tensors. Comsol Multiphysics satisfies this condition, as it allows declaring both permeability and permittivity as tensors depending on the coordinate system. Therefore, a full wave electromagnetic simulation can be conducted. To run the simulation, boundary condition and perfect matched layers are defined to avoid reflections between the volumes (simulation set up).

Figure 1.5-a shows the electric field distribution when a PEC (Perfect Electric Conductor) cylinder (R_1=4λ see Figure 1.4-b) is subjected to a Transverse Magnetic mode plane illumination from $-x$ direction. In Figure 1.5, one can see that when the PEC cylinder is inside the cloak, the field distribution outside the cloak (R_2 = 10.6 λ see Figure 1.4-b) is the same as if the cloak and the PEC cylinder would not be present.

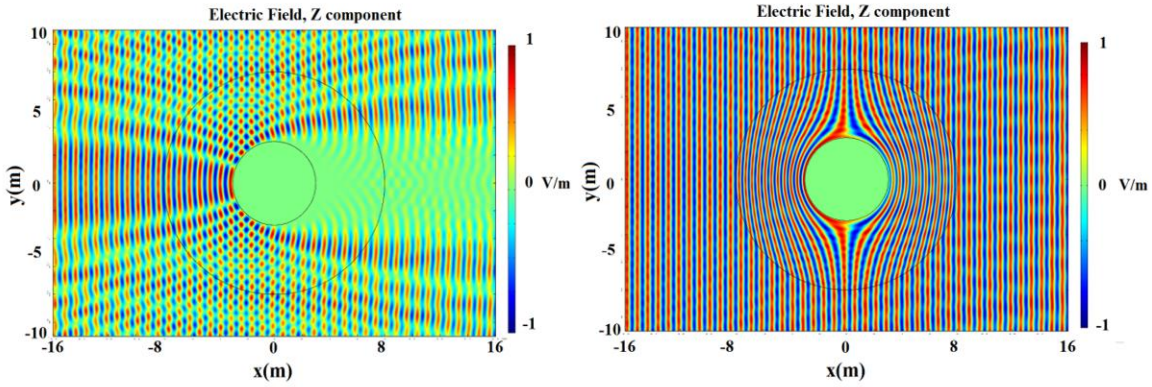


Figure 1.5 Comsol Multiphysics simulations at 400MHz, a) Effects of a TM illumination over a PEC cylinder, b) 2D annular cloak.

This result is similar to the cloaking device presented in [3], [8]. However, in other work such as [19], the cloaking device is designed choosing a polarization different from the previous analysis, which makes a different non-zero components of the tensors. In the previous case, ε_z, μ_ρ and μ_Θ were used, and only the value of μ_r varies along the device, keeping constant ε_z and μ_Θ. In contrast, in [19], [17] μ_z, ε_Θ and ε_ρ are the non-zero components of the tensor because of the change in polarization. The values for μ_z and ε_Θ are kept constant and ε_ρ varies. This explains the different setup for the realized cloaks in Figure 1.6.

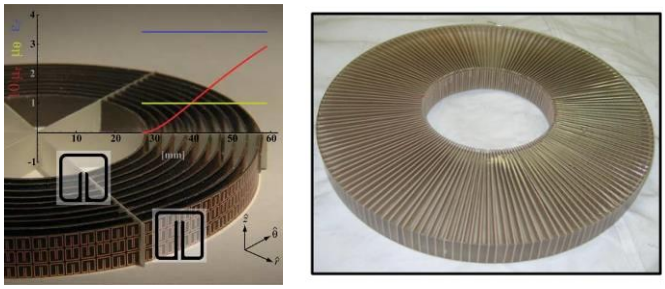


Figure 1.6 Experimental devices of invisibility cloak a) 2D microwave cloaking structure from [3] with a plot of the metamaterial cell and dimensions b) Assembling of the cloaking device from [17].

As this application is very popular, it is possible to find many works on invisibility cloaks with different shapes like: elliptic [20], square [21], polygonal [22], or arbitrary cross section [23] with different analysis methods [24]. In other contributions such as [25], the Huygens principle is applied to evaluate the electromagnetic behaviour in irregular cross section cloaks and including non-conformal boundaries in [26]. Cloaks with uniform thickness for hiding cylindrical and elliptical objects are presented in [27]. Other works intend to simplify and reduce the complexity of the device by using a non-magnetic approach in [28], while in [29] the scattering characteristics and issues are addressed. A bunch of other efforts intend to address the problem of the bandwidth in the cloaking device [30] in simplified cloaks models [31]. In [32] the bandwidth problem is related to delay losses while in [33] this issue is also analyzed in lenses using the Field Transformation FT algorithm. It is even applied at lower frequencies, acoustic [34], elastic [35] or seismic [36],[37], as well as in other fields [38], such as acoustics [39], thermodynamics [40].

3.1.2. Invisibility coat

This application is interesting to explore, because it is a TE application that achieves quasi invisibility using only non-dispersive materials. A method of drilling holes in a dielectric is proposed for the realisation of an invisibility coat that includes a PEC mirror. This contribution is proposed in [10] and validated with realisations at microwave [41] and optical frequencies [42].

First, this new type of cloaking proposes to conceal an object placed between a TE carpet and a PEC mirror, as shown in Figure 1.7. The basic principle is that an incident plane wave (with a certain incidence angle) crosses the rectangular invisibility carpet and it gets reflected (keeping the angle) by the PEC mirror as if the object (bump) would be completely plane.

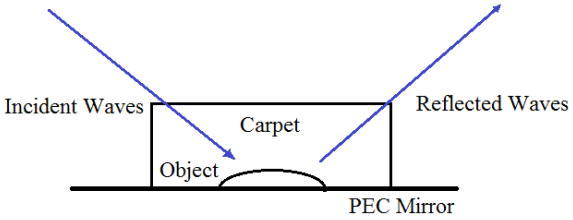


Figure 1.7 Principle of invisibility carpet.

This application is developed using the quasi-conformal transformation. As a result, the material parameters are kept homogeneous and isotropic; therefore this device can perform in a broadband range. The range of variation for the permittivity is 1 to 4.4, which makes possible the idea of realization with a dielectric such as silica glass with holes to vary the permittivity.

FDTD method is used to run simulations at 750 nm in order to obtain the electric field distribution. In Figure 1.8, it is possible to differentiate how the concealed object does not create perturbation in the wave front, it is smoothly reflected from left side to right side. This work also proposes size optimizations analysis with other dielectrics. In Figure 1.9, realisations in microwave optical regimes are shown from [41] and [42].

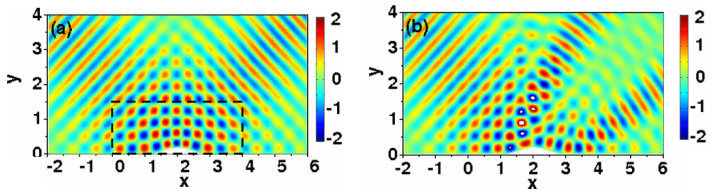


Figure 1.8 E-Field distribution at 750 nm. a) Cloacked object with a 45° illumination, b) The object only.

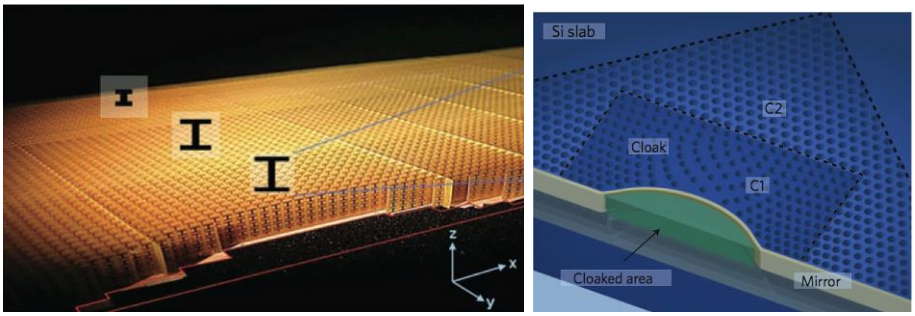


Figure 1.9 Two realisations of the carpet cloak: microwave regime (left) and optical regime (right).

Others groups explored other shapes of carpet instead of the rectangular one presented in this case. For example, in [43] the same principle is applied in a corner, keeping the simplicity in terms of material parameters for realization, but changing the approach for the designing process. In this case, the analytical transformation approach is used, then the commercial finite element software

Comsol Multiphysics is used for running the simulations and different angles of incidence are also analysed. It is interesting how both approaches can be applied to one similar objective.

Another interesting variation of this work is presented in [44], because, not only the same principle with a different shape (triangular) is proposed, but with a much sophisticated method of realization. It is used as a "smart metamaterial" to achieve invisibility, where elastic deformation is also considered for its properties to perform as a gradient index material. Another version of this work explores the use of negative index materials [45], which intends to create perfect invisibility.

3.1.3. Electromagnetic cloaking of antennas

Nowadays in modern wireless communication, systems use many antennas to reach many standards and antennas become more complex. They need to be more isolated because other antennas, platforms, and metallic surfaces surround them. This might affect their radiation patterns. The idea is to isolate two antennas from each other by cloaking them at different frequencies [46], [47]. In other words, to hide an antenna when the other one operates, and vice versa. Consequently, the antennas cannot affect each other in terms of performance (i.e. isolation and radiation pattern).

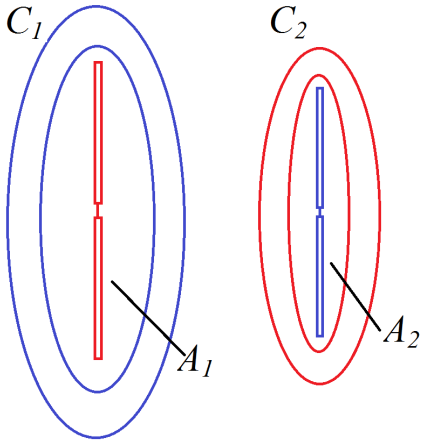


Figure 1.10 Two antennas A_1 and A_2 with narrow bands cloaks C_1 and C_2.

Two narrow bands antennas as in Figure 1.10 are used to illustrate this concept: A_1 and A_2. They operate close to each other (20 cm). Each one operates at f_1 and f_2. Both A_1 and A_2 are also enclosed in cloaks C_1 and C_2 respectively. In this application it is assumed that C_1 and C_2 perform perfect cloaking for f_2 and f_1 respectively. In conclusion, it means that an external observer waiting for communication with A_1 at f_1 does not sense the presence of A_2.

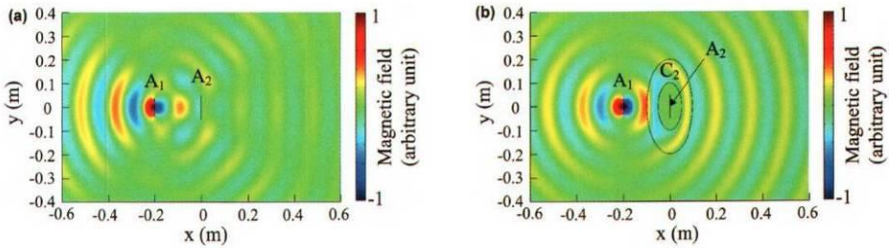


Figure 1.11 Magnetic field distribution of A_1 antenna at 2 GHz [46] in presence of: a) an uncloaked A_2 antenna, b) Cloaked A_2 antenna.

To simulate this model, two dipoles of 75 mm and 100 mm working at 2 GHz and 1.5 GHz respectively, are used to evaluate performances and radiation patterns. The sizes of both cloaks are larger than one wavelength. In Figure 1.11, the magnetic field distribution in free space is shown. First, in Figure 1.11-a, the antenna A_1 is radiating and antenna A_2 is not enclosed into a cloak. As a result, both near and far field are disturbed and scattered by the presence of A_2, due to coupling and blockage. However, in Figure 1.11-b, antenna A_2 is enclosed into cloak C_2, (which is elliptic) and A_1 works correctly, as the radiation pattern is not disturbed and is reconstructed after traversing the cloak C_2. Radiation patterns and input impedance are also analysed in [47] for a full understanding of the concept.

As mentioned before, Comsol Multiphysics is a full wave finite element simulation tool, which is used to evaluate the response to different cloaks and scattering configurations for this application. Towards realization, the use of metamaterials with multiband properties is suggested. They propose the use of a multiband metamaterial design optimization methodology similar to [48] to realize the cloaks for this application.

Another interesting example of invisibility for antennas is presented in [49] and [18]. The difference with the application in [46] is that in this case, the invisibility is achieved by using the carpet cloak with the PEC mirror and authors use the conformal mapping approach.

3.2. Radiating devices

In this section, some antenna applications using TE are explored. Devices such as source manipulation [50], surface and line sources [51], flat Luneburg lenses where the TE is used to compress the device [52], directive radiation [53] of a slab source inside a TE device, directive emission with thickness variation in [54], lens compression in [55], high directive antennas with virtual apertures [56], multibeam antennas are part of this category. However, this part is focused on high directive antennas, in order to explore some variations of high directive TE devices, their importance and degree of achievement in beam controlling devices.

3.2.1. High directive antennas

Most applications of TE on antenna design aim at increasing directivity on antennas as in [52] to [57]. One interesting example of them is an ultra directive antenna, presented in [58] and realized in [59], where high directivity is achieved using TE and metamaterials. The objective of this work is to show that permittivity and permeability tensors of a metamaterial are able to transform an isotropic radiating source into a high directive antenna using TE technique.

The coordinate transformation for this model, as Equation 1.12 shows, is in fact a transformation of cylindrical coordinates into rectangular ones. The geometry of the transformation is shown in Figure 1.12. Furthermore, it is possible to see in this transformation that stretching and compression can be achieved by varying parameters: *e*, *L* and *d*.

$$x' = \frac{2L}{d}\sqrt{x^2 + y^2}, \quad y' = \frac{e}{\pi}\arctan\left(\frac{y}{x}\right), \qquad z' = z \quad \text{with } -\frac{\pi}{2} \le \arctan\left(\frac{y}{x}\right) \le \frac{\pi}{2} \tag{1.12}$$

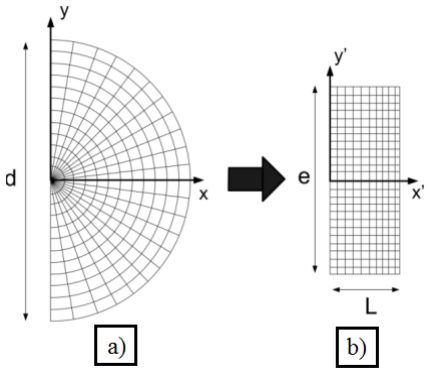


Figure 1.12 Transformation needed to achieve directivity from a) Initial to b) Transformed space [59].

After using the TE design process detailed before and taking into account Equation 1.12, permittivity and permeability tensors can be obtained. Then, they are reduced in order to obtain only diagonal values, which are:

$$\varepsilon_{xx}(x', y') = \mu_{xx}(x', y') = \frac{\pi}{e}x' \tag{1.13}$$

$$\varepsilon_{yy}(x', y') = \mu_{yy}(x', y') = \frac{1}{\varepsilon_{xx}(x', y')} \tag{1.14}$$

$$\varepsilon_{zz}(x', y') = \mu_{zz}(x', y') = \frac{d^2\pi}{4eL^2}x' \tag{1.15}$$

An *x'* dependency in Equations 1.13-1.15, is clearly identified for all non-zero values of MP tensors. It is also clear that ε_{yy} and μ_{yy} have a tendency towards infinite values. Some approximations

are applied later in order to minimize the design complexity. Such approximations as reducing the number of non zero component in the MP tensors and expressing all components of the tensors in terms of one component. The dimensions of the metamaterial used in [59] for *d*, *e* and *L* are: 15 cm, 15 cm, 5 cm. At 5 GHz, the length *L* = 5 cm is close to a wavelength and *d* and *e* are close to three wavelengths. The idea that device dimensions larger than the wavelength are important in order to see the TE effects over microwaves devices is explained later.

As aforementioned, Comsol Multiphysics software is used to perform simulations in order to verify the physical behaviour. In Figure 1.13-a, the right side of the rectangle space becomes the radiating plane. The excitation is applied at the left side of the structure. A perfect electric conductor PEC in the upper, lower and left sides limits this transformed space. The dimensions of the structure are 15 cm × 5 cm. Three frequencies are considered for the simulations: 5, 10 and 20 GHz, corresponding respectively to e/λ = 2.5, 5 and 10.

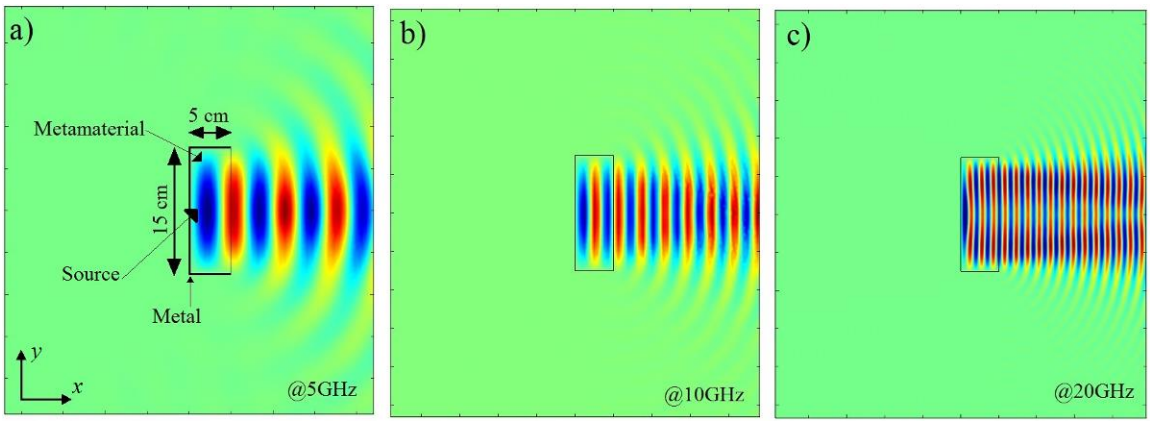


Figure 1.13 Normalised Electric Field distribution in Transverse Electric polarisation at different frequencies to test directivity variations [58]. a) 5 GHz, b) 10 GHz and c) 20 GHz.

The results at 5 GHz show a directivity of 23.6 dB with a half-power beamwidth HPBW of 13.5°. This directivity is compared to a regular parabolic reflector with the same dimensions with similar results. Directive is calculated under the $4\pi S/\lambda^2$ formule. A simulation at higher frequencies allows us to see how directivity increases, from 23.6 dB at 5 GHz to 29.5 dB at 10 GHz [58]. These results are interesting because the directivity increases when the simulations are performed at higher frequencies.

The previous material has a continuous variation of permittivity along the x-axis (the propagation direction). But some values of permittivity and permeability are below one. Then, the suitable solution to realise this material is to use Metamaterials. The experimental demonstration is realised in [60], the same theoretical transformation is kept and material parameters are adjusted to become realisable. More simplifications are made to achieve a material profile with low variations:

dimensions are adjusted to achieve $d^2/4L^2=4$ and to obtain achievable values. In addition, the electric field is set in *z* direction. An interesting aspect of this realisation is that both, permittivity and permeability are varying in the profile (μ_{yy} and ε_{zz}) (see Figure 1.14-b). The resulting MPs remain as a function of ε_{xx}, which is a simplification of Equations 1.13-1.15.

$$\varepsilon_{xx} = \left(\frac{\pi x}{e}\right)^2 ; \ \mu_{xx} = 1 ; \ \mu_{yy} = \frac{1}{\varepsilon_{xx}^2} ; \ \varepsilon_{zz} = 4(\varepsilon_{xx})^2 \quad \textbf{(1.16)}$$

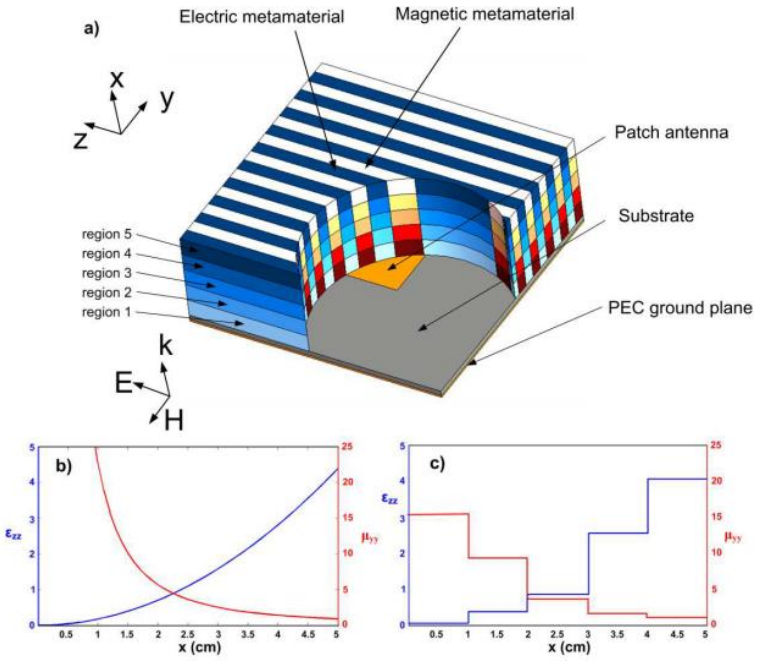


Figure 1.14 a) Schematic of the metamaterial structure with a microstrip path as source. The structure is composed of alternating permittivity and permeability vertical layers. b) Continuous variation of ε_{zz} and μ_{yy}c) Discrete values of MP of ε_{zz} and μ_{yy} [60].

The Equation 1.16 shows continuous functions. Therefore, a discretization of these values is needed. This discretization for μ_{yy} and ε_{zz} must be made to guarantee experimental results comparable to theoretical ones. Discretized values are set for 5 layers of 1cm of thickness (Figure 1.14). Each layer is composed of unit cells (SRR Split Ring Resonator) and their physical dimensions and orientation in the space are carefully configured. It is also interesting to note that unit cells are not regular and periodic (Figure 1.15). Equations in 1.16 show that to achieve the desired behaviour it is important to consider: μ_{xx} =1 and a longitudinally variation of μ_{yy} and ε_{zz}. In the resulting profile of the discretization, μ_{yy} varies from 1.58 to 15.3 and ε_{zz} takes values varying from 0.12 to 4.15. This variation is quite acceptable for a metamaterial realization as in Figure 1.15. The magnetic and electrical resonating layers are alternate in order to achieve the profile desired for the TE device. A patch antenna is used in this case as the feed. The metamaterial is composed of 5 regions and 56

layers, with 28 layers of magnetic resonant layers, and 28 electric resonant layers. Each layer has 5 regions corresponding to discrete values of permittivity or permeability.

The design of both magnetic and electric resonant structures (Split Ring Resonators (SRR) [61], and (Electric-LC) ELC [62][63]) comes from Pendry's and Smith's publications. Simulations with Ansoft HFSS are performed with normal incidence on unit cells to evaluate the S parameters. After a careful inversion procedure [63], the effective values of relative permeability and permeability are obtained.

As previously shown [58] Comsol Multiphysics simulations are performed to validate the metamaterial behaviour and measurements have validated the simulation [60]. Measurements are performed with a dual polarised horn antenna as receiver and the metamaterial antenna as transmitter.

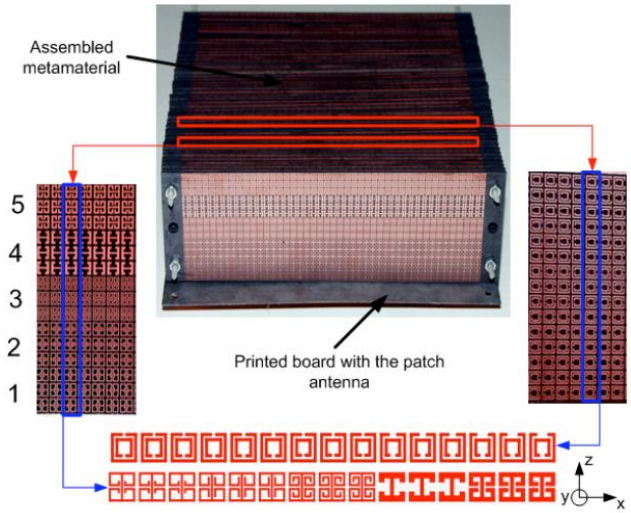


Figure 1.15 Detailed view of the assembled metamaterial over the antenna with the succession of permittivity and permeability metamaterial layers. Variations in unit cells is also in detail for SRR among the structure of the antenna. 5 regions in detail where each magnetic and dielectric layer of the metamaterial is presented along the propagation direction. Details of the resonators used in the magnetic (right) and electric (left) metamaterial layers. Three rows of identical resonators made each level [60].

The antenna presents a maximum radiated power at 10.6 GHz with a directive main beam and low side lobes level under -15 dB. The main lobe presents a HPBW of 13° in the E-plane (x-y plane). This narrow beam width is shorter than the one of a parabolic reflector antenna having similar dimensions (diameter equal to 15 cm). The HPBW of this parabolic reflector is around 16 degrees. Measurements are found to be consistent with the predicted radiation patterns shown in Figure 1.16-b.

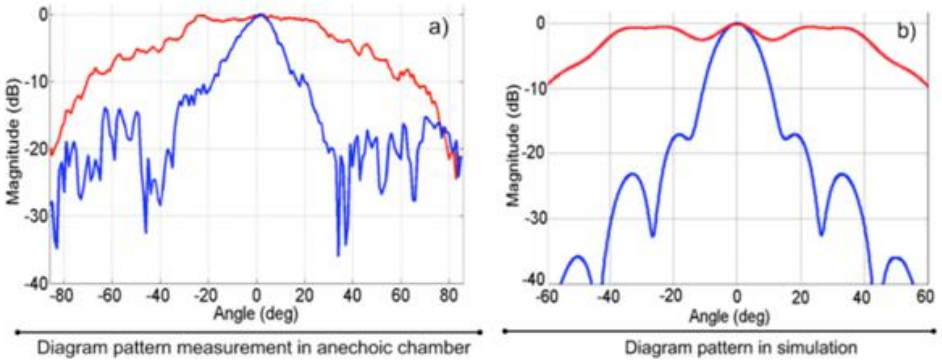


Figure 1.16 Farfield results at 10.6 GHz: antenna alone (red) and antenna and metamaterial layers (blue), a) Measurements, b) Simulations [60].

3.2.3. Multibeam antenna

The analytical transformation of the multibeam antenna [64] is presented, which is an extension of the high directive antenna presented before. In this application, TE design technique is applied to anti-collision radar systems. The technique is used to achieve multi beam antennas, where an isotropic line source is transformed into plane waves through a metamaterial layer, which has a circular shape in the inside and a polygon shape at the outside. This concept is similar to the high directive antenna aforementioned, because it intends to achieve multidirectional directivity. Both, the source and the metamaterial, construct a high-performance multi-beam antenna. The number of sides in polygon controls the number of beams for the antenna. In this work, several structures are analyzed such as device for three, four, five, six, seven, eight and twelve beams. In Figure 1.17-a, a hexagon for 6 directive beams is presented, as well as a triangle, which is one sector of the multi-beam antenna in Figure 1.17-b.

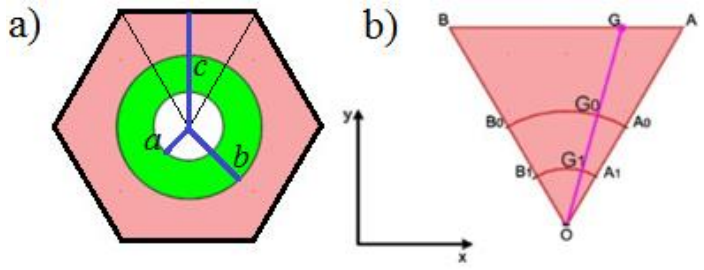


Figure 1.17 a) Configuration of the antenna. The green region is the original space and the red one is the transformed space, b) One sector of the multi beam antenna in the Cartesian coordinate system [64].

Equation 1.17 defines the coordinate transformation:

$$x' = \frac{(cr - by)(r - a)x}{(b - a)ry} + \frac{bx}{r}; \qquad y' = \frac{(cr - by)(r - a)x}{(b - a)r} + \frac{by}{r}; \quad z' = z \quad \textbf{(1.17)}$$

The inner and outer circles radius are: *a* and *b* and the height of the triangle is *c*. Simulations (finite-element method) are performed with transverse electric cylindrical waves. The structure is excited by line current source at 6 GHz in the centre. Perfect matching conditions and absorbing boundary conditions are assumed. An inhomogeneous and anisotropic material is the result of the transformation as expected.

E-Field distributions and performances in Figure 1.18 show a high gain and directivity in each lobe of the radiation pattern. Nevertheless, an increasing side lobe effect is observed as the number of beams increases. However, it is possible to control the number of beams by designing the outer outlines of the metamaterial layer.

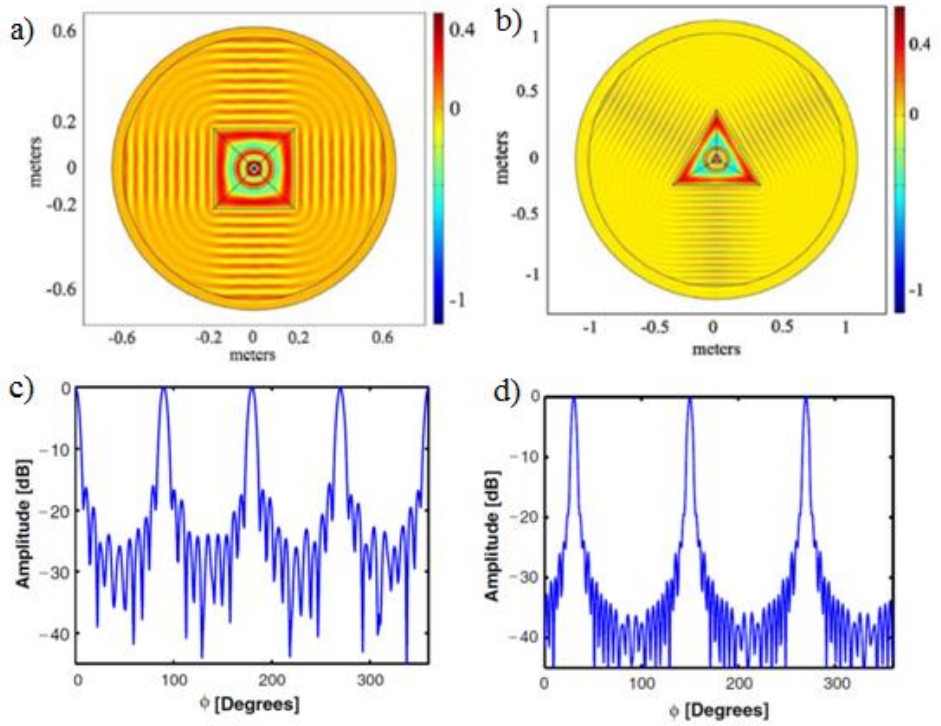


Figure 1.18 a) E-Field distribution for the four beam antenna, b) E Field distribution for the three beam antenna c) Normalised far field radiation for four beam antenna, d) Normalized far field radiation for the three beam antenna [64].

3.2.4. Multibeam lensing by conformal mappings

In the previous application, the model was validated by simulations and does not present a practical approach towards realisation of the anisotropic and inhomogeneous media needed. However, in [48], [65] and [66], other multi-beam antenna examples using TE with the conformal mappings approach are presented. The practical realisation is achieved using metamaterials.

Conformal mappings are defined as transformations in the complex plane. They can operate by using unaxial or isotropic materials, which means they are simple to construct with available metamaterial technology. Conformal mappings must satisfy Cauchy–Riemann equations: A mapping $w=u(x,y)+jv(x,y)=f(z)=f(x+jy)$ is said to be conformal if only and only if:

$$\frac{du}{dx}=\frac{dv}{dx} \text{ and } \frac{du}{dy}=-\frac{dv}{dy} \qquad \textbf{(1.18)}$$

Equation 1.19 defines the coordinate transformation for this lens:

$$x'=\frac{x}{x^2+y^2}; y'=\frac{-y}{x^2+y^2}; z'=z \qquad \textbf{(1.19)}$$

Equations 1.19 satisfy equations 1.18, therefore this transformation is a conformal mapping. Then, expressions for relative permittivity and permeability are quite reduced [48] and shown in Equation 1.20, where a is used only as scaling factor.

$$\bar{\bar{\varepsilon}}=\bar{\bar{\mu}}=\frac{AA^T}{|A|}=diag\left\{1,1,\frac{1}{|A|}\right\}=diag\left\{1,1,((ax)^2+(ay)^2)^2\right\} \qquad \textbf{(1.20)}$$

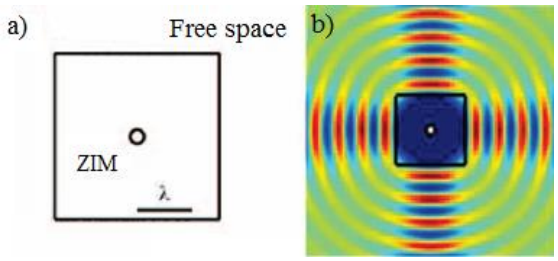


Figure 1.19 Transformation electromagnetics lens by a TE- mode dipole feed at the origin; square lens, a) Geometry and b) Field pattern with four high directive beams [65].

The coordinate transformation is used to convert an isotropic dipole radiation into four directive beams as in Figure 1.19 with homogeneous and anisotropic material parameters. It ensures impedance matching to realise a quad beam radiation in a broad bandwidth.

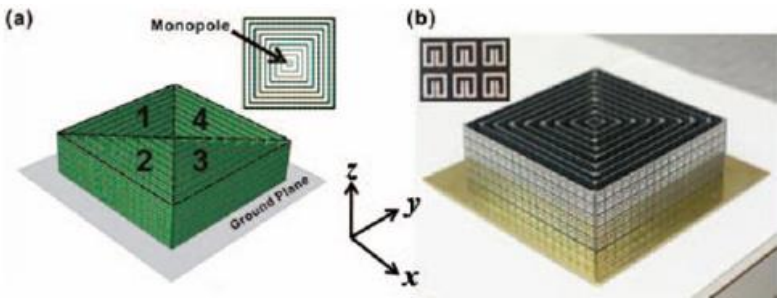


Figure 1.20 a) Configuration of the metamaterial for TE lens as HFSS model. b) Photograph of the fabricated quad-beam TE lens. The length of the outer edge is 102 mm (at 4.8 GHz is 1.632λ) [65].

Transformation is designed to work in G band, as Figure 1.20-a shows, and radiates in its H plane, for Transverse Electric polarisation. The monopole surrounded by four triangular lenses, composed of SSRRs (Single Split Ring Resonator) arrays is also presented. SSRRs are commonly used for their diminished size (compared to SRR) and magnetic behaviour.

Measured and simulated S parameters are presented in Figure 1.21-a. Values are quite similar between measurement and simulation. It is also noticed that the four lobes in Figure 1.21-b and Figure 1.21-c are formed in far field radiation pattern at two frequencies.

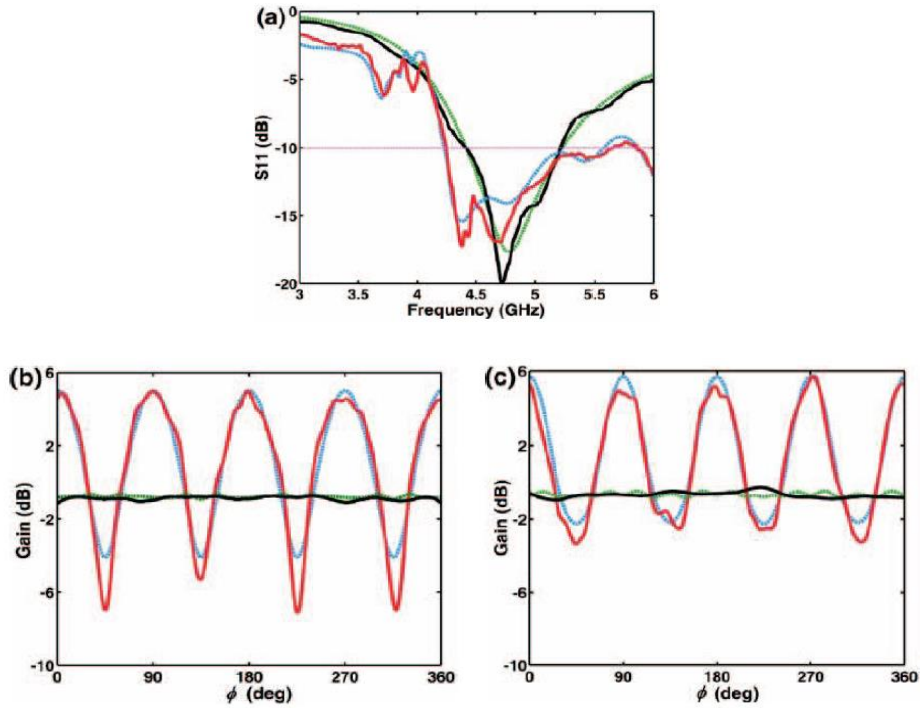


Figure 1.21 a) Comparison of input reflection coefficient for the monopole with and without the TE lens. Results of farfield pattern from the monopole with and without the TE lens at b) 4.5 GHz, and c) 5.2 GHz. Red and black measurement results, blue and green simulation results [65].

3.3. Limitations and drawbacks of Transformation Electromagnetics applications

Several applications were explored in order to summarize the advantages and limits of the TE design methodology. As advantage, it is possible to summarise flexibility in design rarely seen before. It means, wave propagation can be modified, turned, focalized, de-focalized, etc. The designer has in his hands the theoretical tools to manipulate the waves, as he wishes.

However, limitations in the current applications of TE are also present such as bandwidth, size in terms of wavelength, complex materials, high variations in constitutive parameters, difficult realization, etc.

The main disadvantage comes from the realisation process, which is inherent to the use of Metamaterials. Resonant unit cells compose Metamaterials. Resonant structures are very narrow bands compared to standard materials. This disadvantage can limit the use of TE in application for industry.

Another disadvantage is the size of the TE device compared to the wavelength. In all the summarized applications, the size of the TE device is greater than one wavelength. If the size of the TE device is smaller, the TE behaviour disappears.

In Table 1.1 is presented a summary of applications of TE found in literature and their main characteristics in terms of design and realisation process.

Application	**Approach**	**Size in λ**	**Material**	**MP**
Cylindrical Cloaking[1],[3],[7],[8],[17],[19]	Analytical	5-11	Metamaterial	Dispersive
Invisibility carpet[10],[41]-[45]	Conformal Mappings	2	Dielectric	Non-Dispersive
Antenna cloaking [8],[46]-[49]	Both	3	Only simulation/ Dielectric	Both
High directivity [52]-[60]	Both	2.5, 5, 10	Metamaterial/ Dielectric	Dispersive
Multibeam Antenna [64]	Analytical	5	Metamaterial	Dispersive
Multibeam Lens[48],[65][66]	Conformal	2	Metamaterials	Dispersive

Table 1.1 Summary of performances and characteristics of TE applications

4. Conclusions

In this chapter, a detail view of the principle and some the most interesting applications were presented in order to clarify concepts and highlight some limitations inherent to the TE technique.

The invisibility cloak is used to describe in detail the design process, passing through the different steps of the design. Each step allows to visualize some issues and limitations that the technique presents such as: using Metamaterials for the realisation of the devices, or the narrow bandwidth that current works on invisibility present, or size of the device in relation to the wavelength which is important.

Many applications on invisibility cloak and carpets, invisibility of antennas, high directivity devices and multibeam antennas presented, were used to compare two interesting approach on the design of TE devices. The analytical approach and the conformal mapping are widely used for different devices presenting some limitations and advantages compared to each other. The desired electromagnetic behaviour, the geometry of the device and the available materials for realisation determine the approach that the designer should use.

While these applications were described, the use of many tools for the design process is also highlighted. Multiple software tools are needed as Mathematica, Comsol Multiphysics, CST Microwave Studio, HFSS, etc,

In the antenna design field, the tendency of achieving directivity using TE is clearly noticed in many contributions. In several cases, the directivity of the antennas is highly improved and in others applications, the emitting source is modified or embedded inside a TE device in order to achieve the directive emission.

All dielectric solutions represent a very interesting solution in terms of simplicity regarding the design and realisation process of TE devices. In order to fulfil the electromagnetic response of TE devices, some efforts in approximations and simplifications are needed, such as tensors components reduction, defining the polarisation, discretizing MP profiles, etc.

Finally, in order to design TE devices, it is needed to take into account all the considerations that have been summarized in this chapter such as: size of the device, material for the realization, bandwidth of the device, approach in design, etc. All these items are going to be useful for the device that is designed in the next chapter. The flat reflector needs to be thin, simple to realise, slightly wideband. It is used to illustrate the technique of TE by replacing a classical beam controlling device such as the parabolic reflector by another device with similar electromagnetic behaviour.

Chapter 2
All Dielectric Flat Reflector

As first application of Transformation Electromagnetics technique, a flat reflector is proposed while keeping an all-dielectric approach for its realisation. This is an interesting application of TE because not only a classical RF device can be replaced by a TE device but also because it offers a reduction in terms of size and shape compared to a parabolic reflector.

As mentioned before, the works of Pendry et al. [1] and Leonhard [2] about Transformation Electromagnetics drew the attention of many research groups all over the world. It was clearly a breakthrough, because their work gave the possibility of controlling electromagnetic waves as it has never been before. As it is mentioned in Chapter 1, this flexibility in electromagnetic design was achieved using metamaterials or composite materials where wide ranges of permittivity and permeability can be synthetized. However, many issues about the performance of the metamaterial device were highlighted such as narrow bandwidth, infinite phase velocities, or excessive dispersive losses. These issues limit the performances of many applications; this is the reason to introduce an all-dielectric approach. The technique is fully described, explaining the required simplifications and reductions of this approach on realization of TE devices.

For a long time, parabolic reflectors are widely used at many frequency bands and for many purposes such as collecting or emitting energy in form of waves. Parabolic reflectors allow increasing the performance of the feeding antenna by improving the gain and decreasing HPBW. Although, they are very convenient and reliable for some applications, the dimensions sometimes could be challenging. If a flat structure could replace this curved structure, it would be an interesting achievement and many potential applications would fulfil their expectations in terms of occupied volume or space.

In this chapter, a flat all dielectric TE-based reflector is theoretically described as in [67] and [68], then we introduce and highlight simplifications that make TE devices feasible and potentially useful, avoiding resonant structures as the ones used in [8],[58]. Followed by a full description of a flat reflector design is presented with the methodology to achieve different permittivity values with a single dielectric. Simplifications that lead to the use of only a single dielectric structure with holes

are also highlighted. The simulations results of different configurations and optimizations for the flat reflector are presented along the chapter and finally conclusions are drawn at the end.

1. TE Principle

As the powerful theoretical tool that is, TE enables the design of new devices in optics and microwaves as never before. In the present case, a flat structure intends to replace a classical parabolic reflector. As it is described in the previous chapter, TE is based on the Fermat's principle concerning the geometrical path of light, which in this case aims to concentrate the wave trajectories towards the focal point of the or to direct the propagation towards the broadside in order to achieve high directivity. The analytical development to design such a structure is presented, as well as the performances of the device.

Further, this work aims to establish a simple methodology, which leads to demonstrate that a flat structure is able to exhibit almost the same electromagnetic behaviour of a parabolic reflector with improvements in terms of dimensions, while keeping simplicity in the realization.

1.1. 2D study

A typical parabolic reflector associated with a source antenna placed at its focal point is a device which enables to achieve high directivity in the broadside direction and small Half Power Beam Width (HPBW).

In [67], the profile of a planar reflector is theoretically calculated using TE. In Figure 2.1, the 2D cross section of reflectors is presented where the dimensions are displayed in both virtual and real spaces. The virtual space is represented by a parabolic structure and the real desired space by the flat one. In Figure 2.1-a, the cross section of the flat structure is presented. The TE material or transformed space is located between the source and the metallic boundaries. In Figure 2.1-b, the cross section in Cartesian coordinates of a metallic parabolic reflector is presented as well.

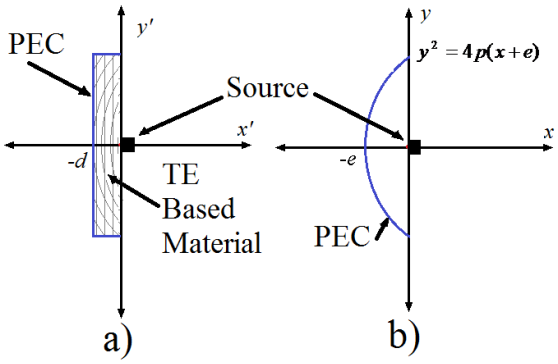


Figure 2.1 Cross section of reflectors: a) TE based flat structure, b) Parabolic reflector. Perfect Electric Conductor (PEC) boundaries in blue.

1.1.1. Analytical transformation

The objective in this application is to design a flat structure while reducing the thickness compared to a typical parabolic reflector. Then, the analytical equations for the transformation need to be established. The electromagnetic behaviour of a parabolic reflector should to be reproduced by a flat structure, in other words a parabolic shape needs to be transformed into a rectangular space equation. Equation 2.1 makes the required transformation. It provides a transformation only in the *x* direction while the other coordinates are unchanged.

$$x' = \frac{4pdx}{4pe - y^2}; y' = y; z' = z \qquad \textbf{(2.1)}$$

Where: *p* is the focal distance; *d* and *e* are the thickness of the flat and parabolic reflector respectively. The values of *d* and *e* are 0.1 m and 0.15 m, which show reduction of the structure's thickness. In this case the *p* is equal to *e*, which is a particular case of a parabolic reflector because it means that the source is located at the same distance as the thickness of the structure.

It's possible to calculate the material parameters of the required structure to achieve the flat structure using Equations 1.5, 1.6 and 1.7 for the transformation. This leads to a material profile expressed in two tensors: ε'_r and μ'_r. After transformation, the resulting tensors are presented in Equation 2.2, and their non-zero components are plotted in Figure 2.2. Considering at this point ε'_r and μ'_r are equals, only the non-zero components of ε'_r are presented.

$$\varepsilon'_r = \mu'_r = \begin{pmatrix} \frac{4pd(4x^2y^2 + (4pe - y^2)^2)}{(4pe - y^2)^3} & \frac{4xy}{4pe - y^2} & 0 \\ \frac{4xy}{4pe - y^2} & \frac{4pe - y^2}{4pd} & 0 \\ 0 & 0 & \frac{4pe - y^2}{4pd} \end{pmatrix} \qquad \textbf{(2.2)}$$

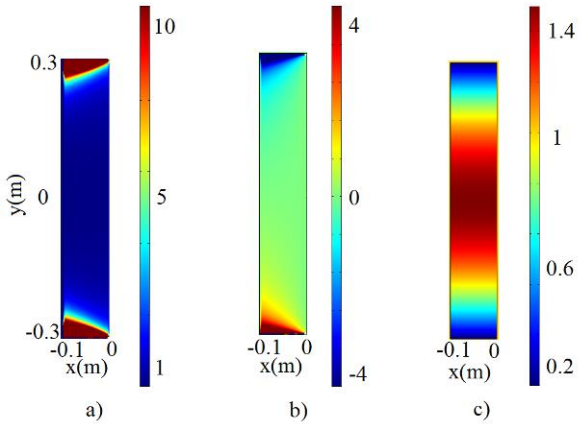


Figure 2.2 TE structure profile: *e* = 0.15 m, *d* = 0.1 m and *p* = 0.15 m, a) ε'_{xx} b)$\varepsilon'_{xy} = \varepsilon'_{yx}$ c) $\varepsilon'_{yy} = \varepsilon'_{zz}$.

As shown in Equation 2.2, the tensors have non-diagonal components and the values of μ'_{yy} are negative. Consequently, some approximations are needed in order to reduce the number of components of the tensors, and thereby making the structure realizable. Thus, one additional step to simplify the MP needed for this structure is to diagonalize these tensors. Diagonalizing allows to reduce the number of components of the tensors by replacing a non diagonal tensor (i.e. $\varepsilon'_r(x,y,z)$) by its diagonal equivalent (i.e. $\varepsilon'_r(u,v,z)$, same is valid for μ'_r) as described in Equation 2.3. It is noticed that diagonalizing using only 2x2 matrix is useful to simplify the calculation. The z component will be included later.

$$\varepsilon'_r(x,y)=\begin{pmatrix}\varepsilon_{xx} & \varepsilon_{xy}\\ \varepsilon_{yx} & \varepsilon_{yy}\end{pmatrix} \Rightarrow \varepsilon'_r(u,v)=\begin{pmatrix}\varepsilon_{uu} & 0\\ 0 & \varepsilon_{vv}\end{pmatrix} \qquad \textbf{(2.3)}$$

However, sometimes the resulting expressions could become more complex. Fortunately, for this case the presented diagonal matrix in Equation 2.4 is slightly easy to calculate.

$$\varepsilon'_r=\mu'_r=diag\left(\frac{A+\sqrt{A^2-(4dpB)^2}}{4pdB},\frac{A+\sqrt{A^2-(4dpB)^2}}{4pdB},\frac{B}{2pd}\right) \qquad \textbf{(2.4)}$$

Where: $B=4pe-y'^2$, $A=B+4(4p^2d^2-x'^2y'^2)$. This allows us to calculate the constitutive parameters profile (ε'_r and μ'_r) that will be used in next steps of the design process. In this case, the simulations will consider μ'_{uu}, μ'_{vv} and ε'_{zz} because of the polarisation choice of the electric field in the source, which will be explained in detail in later sections.

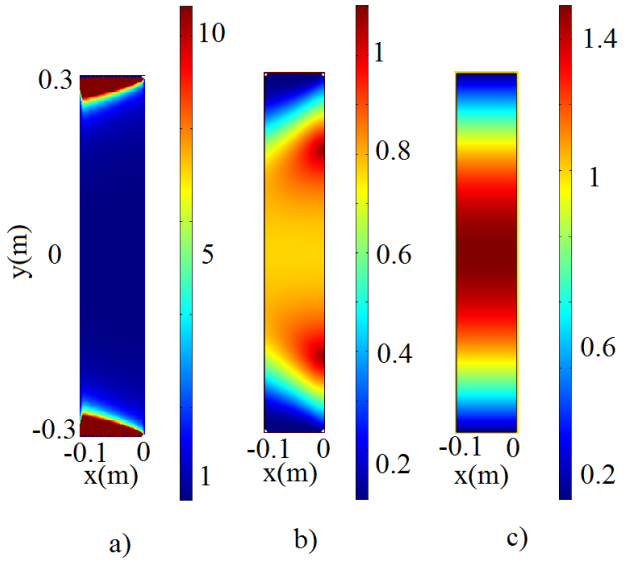


Figure 2.3 Reduced set of tensor components a) μ'_{uu} b) μ'_{vv} c) ε'_{zz}.

The resulting profile of the diagonal values is shown in Figure 2.3. The permeability μ_{vv} varies from values close to 0.7 to 10, μ_{uu} varies from 0.2 to 1 and ε_{zz} varies from 0 to 1.45. As these values for the MP are not found in nature, some approximations and simplifications are needed in order to

achieve a feasible profile for the permittivity and permeability. However, it is important to use the non-diagonalized tensors of permittivity and permeability in the following simulation of the near field, because the different field distributions allow to distinguish the components of tensor that have more impact on the simulation. The diagonalized tensors can be used once this influence of the components are observed. This distinction is also important because we can identify the component that can be reduced or approximated to a constant value.

1.1.2. Near field analysis

As a next step, the complete tensors (non-diagonalized tensors in Equation 2.2) are first included in the simulation, in order to check the electromagnetic behaviour of the structure. Therefore, we consider a polarization with *E* field along the *Oz* axis. Two-dimensional (2D) simulations at 5 GHz of the reflectors were performed with Comsol Multiphysics. The electric field is polarized with a rectangular port in Transverse Electric mode (i.e. polarized along the *z*-axis) used as the source located at the focal point. The simulated distributions of the normalized magnitude of the *z*-component of the electric field *E* of three structures, the classical parabolic reflector, the flat rectangular reflector with metallic boundaries and a perfect electric conductor (PEC) plane reflector are presented in Figure 2.4.

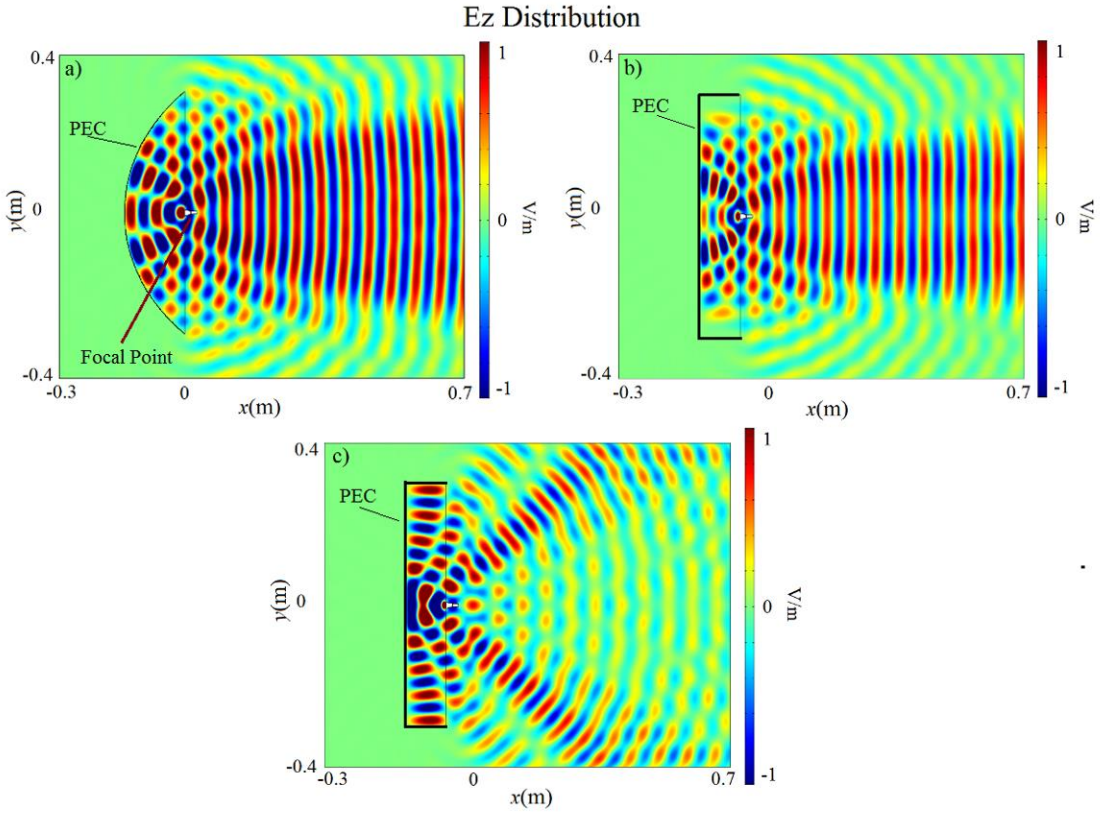


Figure 2.4 Normalized $|E_z|$ distribution at 5 GHz: a) Parabolic reflector b) Flat TE reflector c) PEC flat reflector.

The electric field distributions are quite similar for the two first reflectors demonstrating that the flat reflector can operate as a parabolic one. However, the electric field distribution of the flat reflector is slightly more concentrated toward the broadside direction. The field distribution for the only PEC reflector is not useful as expected, however it is useful to observe what happens if the structure would not contain any transformed material.

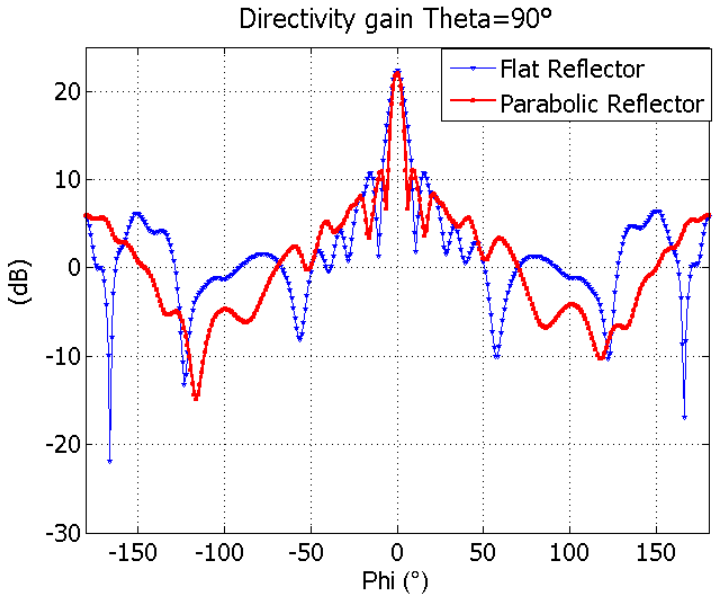


Figure 2.5 Directivity calculated with Comsol Multiphysics at 5 GHz: for both reflectors (Parabolic and Flat TE reflector.

Regarding the farfield in Figure 2.5, both reflectors present a similar behavior, achieving maximal directivity of 22 dB and 22.3 dB for the parabolic and flat TE reflector respectively. From this point, the analysis is strongly oriented towards simplifications of the needed material rather than searching for high or optimized performances in order to prove the concept with a simplified approach, while testing the method of permittivity synthesis for future applications.

2. Synthesis of the structure.

As previously seen, the permeability μ_{vv} varies from values close to 0.7 to 10, μ_{uu} varies from 0.2 to 1 and ε_{zz} varies from 0 to 1.45. These values for the MP are recently achieved using metamaterials as in [60]. However, issues in terms of narrow bands and losses limit the performance of the TE devices. Therefore, all dielectric solutions are reviewed and explored for this application. Thus, the preliminary 2D structure is first designed and simulated and then is extended into a 3D structure to approach the design towards realization. As the values of permeability (both μ_{xx} and μ_{yy}) are difficult to achieve, some analysis are required before to approximate this expressions for MPS to constant values.

2.1. Solutions to synthesise CP values

Transformation Electromagnetics technique requires the use of variant index materials as shown in Equations 2.2 and 2.4. Therefore, potential solutions to synthesise the MP values are presented, such as the use of metamaterials [62], [65] or only dielectric devices [69] using deposition methods or drilling methods as in [63] to synthesize variant values of MPs.

Many contributions deal with the use of metamaterials [62] and how to synthesize a varying permittivity and permeability with these materials using different types of resonators such as Split Ring Resonators SRR [70], Closed Ring CR [71], Complementary Closed Ring CCR [72], Electric LC resonators ELC [62], Z resonator, etc. Although some of them intend to perform in a wide bandwidth [73], they are complex to simulate, time consuming for the design process and hard to handle when realized. As all of performances come from the resonant behaviour, the dispersion losses, bandwidth and the stability of the performances to synthesize the desired MPs values are quite compromised. So it is necessary to use solutions that could be simpler than metamaterials in order to reach a suitable manufacturing method.

2.1.1. All dielectric solutions for TE devices

Current works on full dielectric applications of TE allow to design all dielectric solutions for TE devices, such as graded dielectric invisibility coats [10] using holes to vary ε while keeping the variation of the range of values small. Other dielectric methods of deposition [74] to design multilayered absorbers with nano-particles of CoFe allow to generate the required variation in parameters.

Our approach intends to focus in a non-resonant structure, therefore some solutions are proposed in literature as all-dielectric methods in [10]-[42] and [69]-[73]. Among the solutions, there are interesting contributions such as dielectric deposition. In [69], a powder of micro sized titanate particles was dispersed into a matrix material. This process allows a relative permittivity from 3 to 12.6 to be achieved and used in a planar hyperbolic lens which has focusing properties as a curved lens. The permittivity values in this method depend on the homogeneity and quality of dispersion of the titanate particles inside the matrix. The results of this contribution in terms of gain over the band of [2-7] GHz for the lens combined with a horn antenna are quite stable. Results also show frequency independence for the TE device, as the measured relative permittivity among this operating band is stable as well. Authors claimed that's could be reduced using thin matching layers between the feeding antenna and the TE lens.

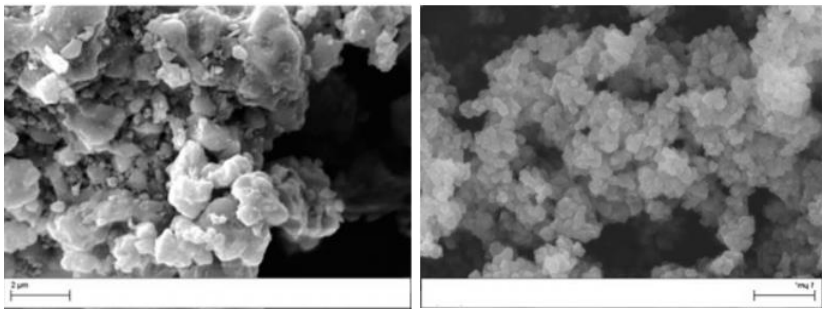


Figure 2.6 Titanate particles from [69] and [52].

Another interesting method for an all-dielectric realisation of TE devices is presented in [10] where invisibility carpets with a ground plane are proposed in 2D and 3D respectively in different regimes, while the one in [10] operates at optical frequencies, in [39] a 3D acoustic version of the carpet is presented. In [42], a study of the performances at many wavelengths of this carpet is presented while in [44] elastic parameters are introduced in the analysis of the device. Real world applications on TE are presented in [75] including some methods of dielectric realisation for devices related to antenna design.

In general, the drilling method used in some contributions as [76], is the simplest because varying permittivity is achieved by varying the quantity of holes inside a homogeneous dielectric, in some cases Teflon, F4B dielectric, silica slabs, silicone rubber, etc.

2.1.2. Graded dielectric methodology

The method of drilling holes is introduced in order to show its advantages. Compared to metamaterials, the simplicity in terms of design, simulation and prototype fabrication is quite attracting.

Then, a small volume of drilled dielectric is studied to illustrate the method. Equation 2.5 enables to calculate the different values of the synthesized permittivity from ε_d and ε_a, the permittivity of the dielectric and the air respectively [76].

$$\varepsilon_{synth} = \varepsilon_d f_d + \varepsilon_a f_a = \varepsilon_d - (\varepsilon_d - \varepsilon_a) f_a \qquad \textbf{(2.5)}$$

The factor f_d represents a volume ratio of the dielectric and f_a represents the volume ratio of the air inside the dielectric. In this case, only air fills the holes but they can be filled with other dielectrics to achieve other ranges of permittivity values. Then, multiple values of permittivity can be synthesized varying the density of holes in the dielectric. In Figure 2.7, the detail view of the drilled dielectric is presented. The layout is simple: the diameter of the holes is kept constant, while the quantity and the location determine the density of holes present in a region.

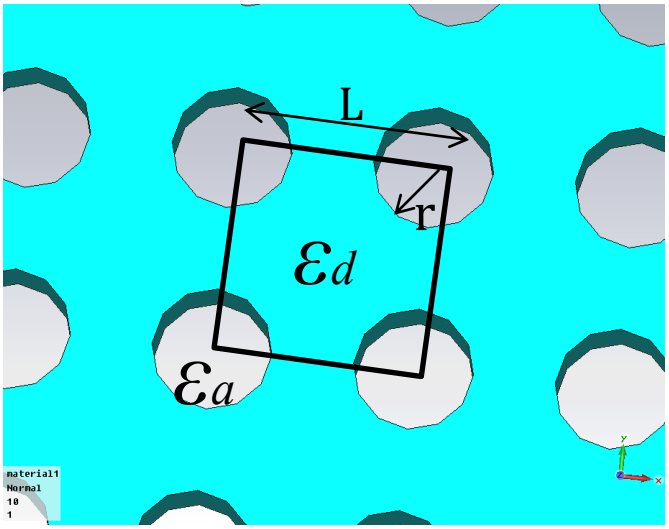


Figure 2.7 Detail view of the drilled dielectric.

2.2. Constitutive parameter simplifications

Simplifications and reductions of the analytical expressions of the MP are needed in order to approach TE devices towards realisation such as calculations of only diagonal tensors for the MP and reductions in the set of tensor components.

In order to simplify the design, Figure 2.8 shows the Ez field distribution along different values of MP tensors with the simplifications and approximations made to them. Although the process of simplification needs the diagonalization process as explained in 1.1.1, the diagonalized components of ε_r' *(u,v,z)* cannot be used as input to the simulation in Comsol Multiphysics, in order to analyze the electric field distribution. The component *u* and *v* of the tensors in diagonalized tensors are transformed coordinates, and Comsol needs expressions in *x* and *y* space. For this simulation MPs tensors in *x*, *y*, *z* are used.

In Figure 2.8-a, all components of the tensors for the permeability and permittivity are used to run the simulation, while in Figure 2.8-b the non-diagonal components of the permeability tensor are avoided. In Figure 2.2-a, the component μ_{xx} is presented and it is possible to observe that, except for some thin zones in the sides, in almost the entire geometry the value of the component is 1. This is the reason to replace μ_{xx} by 1 in the Figure 2.8-c in order to continue the simplifications. All components of permeability are approximated to 1 in Figure 2.8-d to see how the behaviour of the flat reflector is affected. Finally, in Figure 2.8-e and Figure 2.8-f the relative values of μ and ε are approximated to their components μ_{yy} and ε_{zz}.

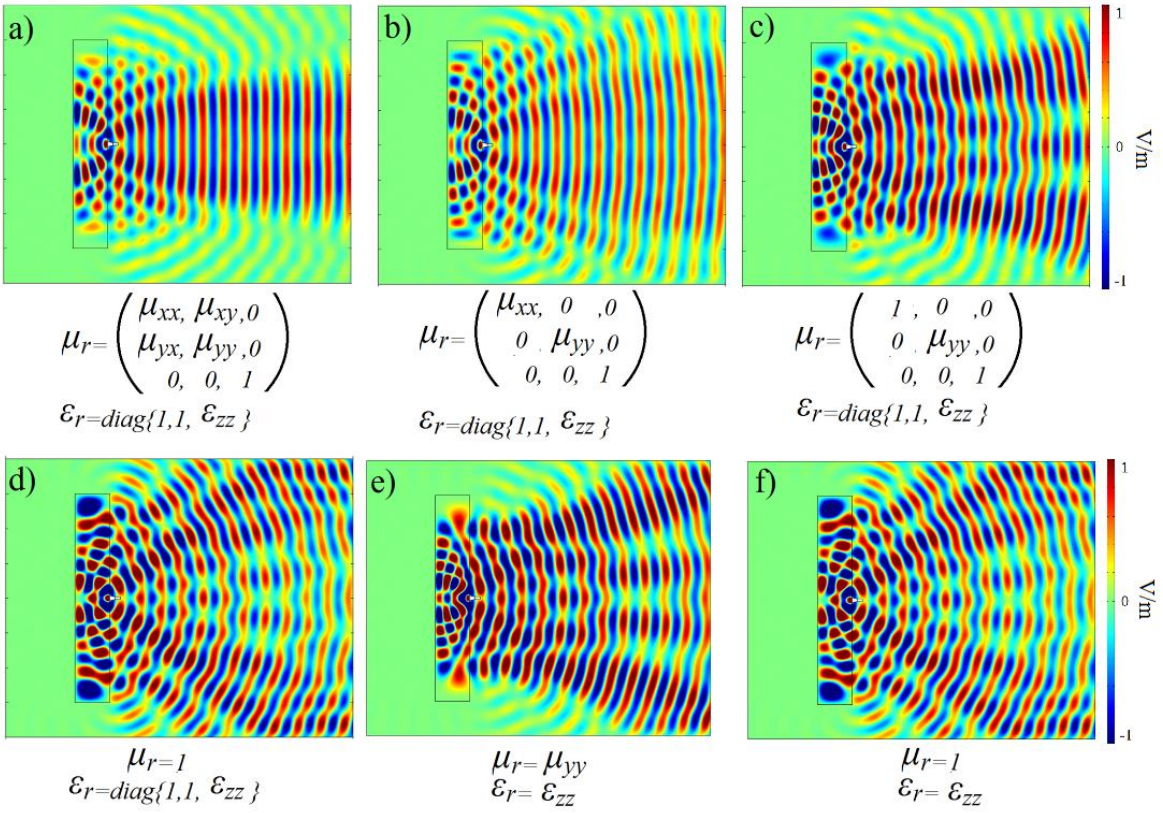


Figure 2.8 Evolution of the E Field distribution through different stages of the approximation.

Through the simplifications, it is noticed that permeability may be approximated to a constant value (in this case μ=1). Because in one side, in the profile presented in Figure 2.2 the values of its components are close to this constant value among all the geometry. In the other side, the results presented in Figure 2.8-f the reflector is defined by only permittivity, although the electric field distribution shows some degradations or reflections, the fact that only one component could define a TE structure is enough to compromise the performances of the device. Therefore, a structure that depends only of the permittivity is achieved. Although Figure 2.8-e and Figure 2.8-f are interesting even though they are different from Figure 2.8-a. The final flat reflector in Figure 2.8-f keeps the electric field distribution very different from the plate mirror made of PEC sheets (in Figure 2.4-c), and the fact that only varying permittivity is needed is a quite improvement in order to have a realistic structure.

2.3. Influence of varying constitutive parameters

A study of the influence of varying MPs values in the performance of device is described in this section. It is necessary to find the limits of MPs in order to keep the desired behaviour and simplify the realisation. An important issue in this flat reflector is that it requires dispersive values of permittivity (permittivity below one). Such values of permittivity are not available among natural materials.

As dispersive values of permittivity need to be avoided, it is necessary to analyse the case where they are approximated by one. Then, in Figure 2.9 values of permittivity are shifted to upper values and lower values in order to observe the influence of varying permittivity or permeability. Four cases are explored in Figure 2.9: *ε +1, ε +2, ε+1* and *ε+2* aiming to find the limits for the variation of ε. It is possible to notice that the electric field distribution is degraded when the values of permittivity are increased, however the electromagnetic behaviour can also be studied looking at the farfield to observe other important parameters such as realized gain and HPBW, these result are presented in the following sections.

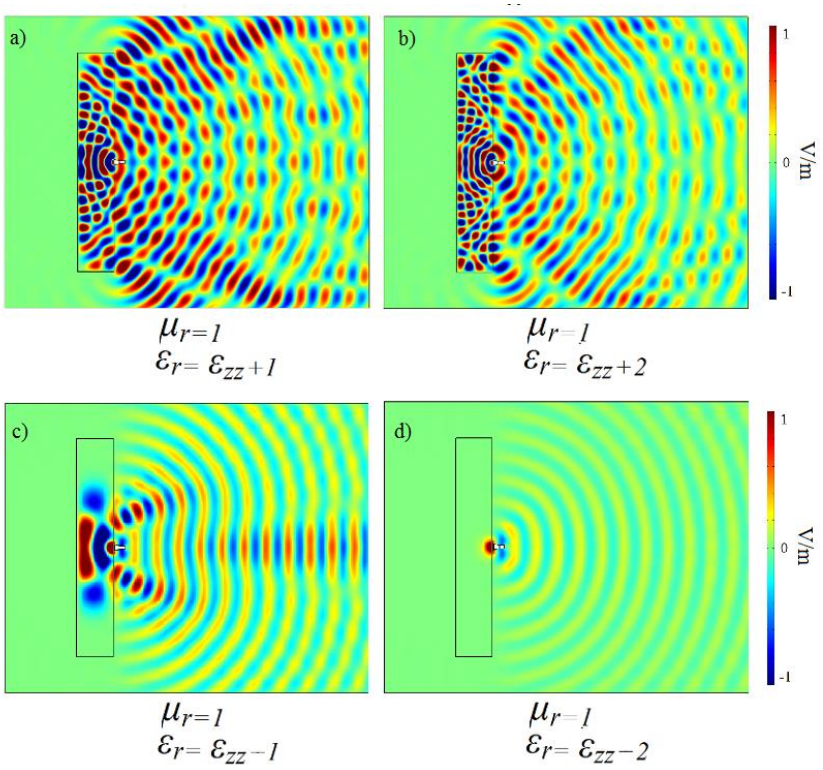


Figure 2.9 Comparison of E Field Distribution through permittivity variation.

In the cases presented in Figure 2.9-c and Figure 2.9-d, the permittivity is decreased by -1 and -2 in order to explore the influence of varying ε. This results in an interesting reflecting behaviour because it shows three lobes appearing, in the case where permittivity is decreased by one, however this behaviour is very far from the expected. In the case of the permittivity decreased by -2, the structure also reflects the waves in a quasi isotropic way. The intensity of the electric field is highly attenuated in the plane by passing through the reflector because of the negative values of permittivity. Although, it is interesting because a directive antenna is transformed into a quasi omnidirectional antenna

In order to evaluate the radiation pattern of the antenna and to continue with the simplifications, CST Microwave Studio simulation results are presented (copolarisation component with transient

solver) at 5 GHz and shown in Figure 2.10. At this point the influence of the dispersive (ε<1) values are analysed. The structure where the values of the permittivity below to one are replaced by one, this reason behind this modification is to study the influence of avoiding these dispersive values. As source, a small horn antenna linearly polarized along z-axis is located at the focal point. A process of discretization of the flat reflector profile for the values of permittivity is used for simulation and it is described in detail in next section. The next approximation that needs to be explained is a comparison between the results obtained with the structure with dispersive parameters and the other one with non-dispersive parameters in order to see how the dispersive values affect the performances and if it is possible to avoid them. The structures simulated are obtained by rotating the 2D profile as it is shown in detail later.

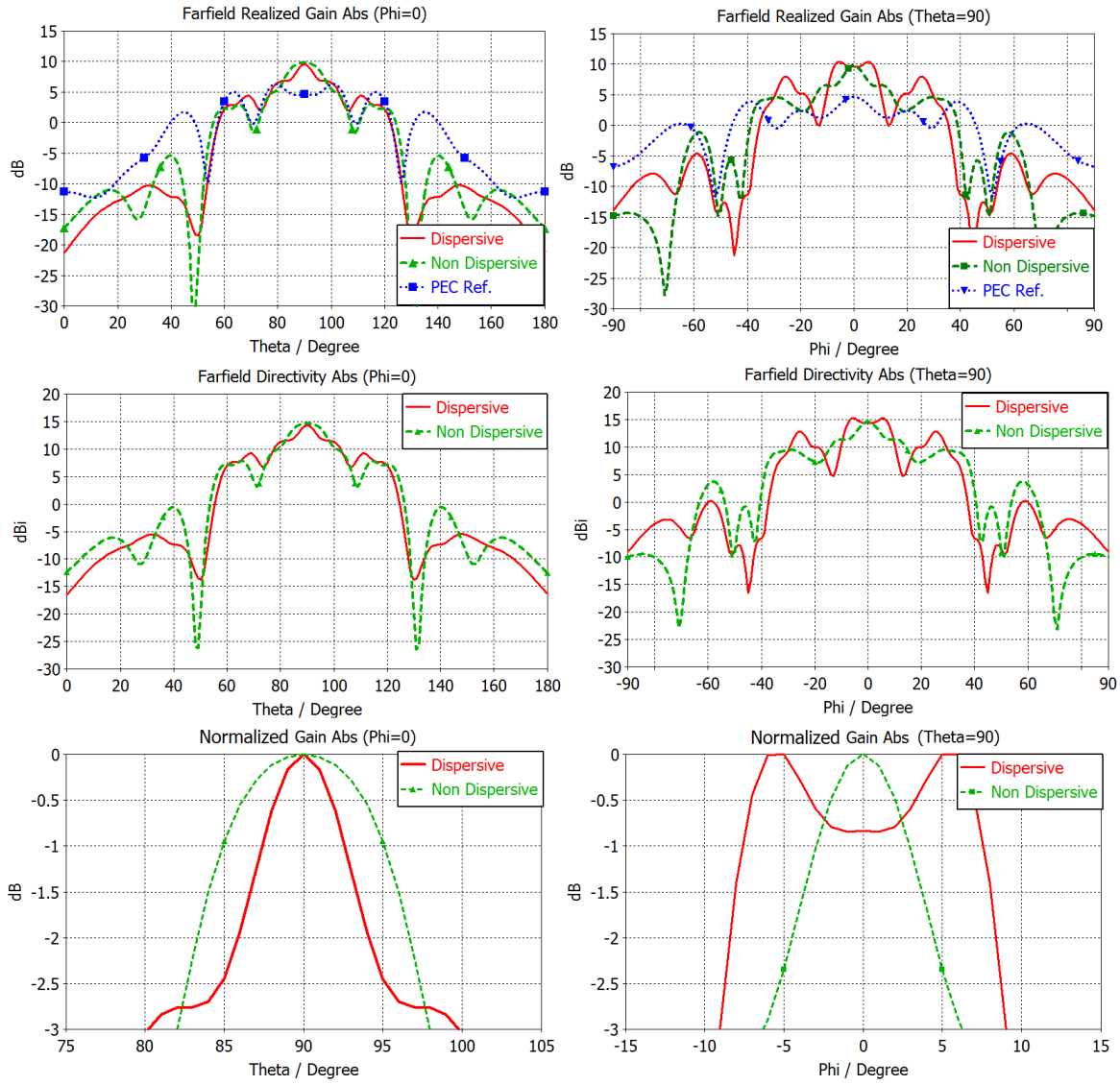


Figure 2.10 Comparison of Realized Gain RG (Figures above), directivity (Figures middle) and HPBW (Figures below) of dispersive and non-dispersive reflectors at 5 GHz.

As the transformation is performed in the *XOY* plane and the direction of propagation is *OX*, the representation of the radiation patterns is presented in the planes $\varphi=0°$ (*XOY* plane) with θ variable for the E plane and $\theta=90°$ (*ZOX* plane) with φ variable for the H plane.

A slightly better performance in terms of gain and Half Power Beamwidth (HPBW) of the dispersive structure is shown while the non-dispersive structure presents some degradation like higher levels of side lobes. However, the performance is quite acceptable.

The gain obtained with the PEC surface as reflector is low as expected. In terms of maximum gain, the dispersive structure's one is 10.4 dB, which is 5dB greater than the gain obtained with the PEC reflector. The non-dispersive structure presents a maximal gain of 9.8 dB, which is slightly lower than the dispersive reflector, because of the higher values of permittivity used in the non dispersive structure. It is also possible to see that the directivity raises up to 14.1 dBi, 14.3 dBi and 15dBi for the dispersive, non dispersive and drilled structures respectively in the phi=0° plane while in other plane (theta=90°) directivity is 15.2 dBi, 14.6 dBi and 15.1 dBi respectively. It is also noticed that due to the material (Teflon) losses are introduced of about 4.5dB comparing RG and directivity results.

Then, HPBW is presented in Figure 2.10-b. The HPBW of the dispersive structure is 20°, which is larger than the non-dispersive one (16°) in phi=0 plane. The difference is small and quite acceptable for the modification that was performed.

2.4. Profile discretization

A discretization process is needed because obviously, it is hard to fabricate a material where both MPs could vary continuously along the geometry of the structure, or even only one of them. Although, there are some efforts to realize this type of materials, at the moment the best choice is to discretize the profile in blocks of constant value of MPs. This discretization process that allows keeping performances while discretizing is described here, as well as its advantages and drawbacks.

As it is previously mentioned, the component ε_{zz} is used as a relative permittivity. Let us focus now on the process of discretization. In Figure 2.11, the discretized profile into 256 blocks of constant value is presented, each block size being 18.75x12.5 mm². The average values of the permittivity ε_{zz} inside each block are taken as relative permittivity. Then, a second discretization is also performed, this time 64 blocks with the average values. The farfield from the two discretizations is calculated and plotted using CST Microwave Studio.

Figure 2.11 in 2D is rotated around *x* axe, in order to extend the profile to a 3D structure as in [77]. The flat reflector (3D structure) is illuminated by a horn antenna placed at the focal point of the structure. The 3D structure is presented in Figure 2.12 and the farfield simulations are presented in Figure 2.13

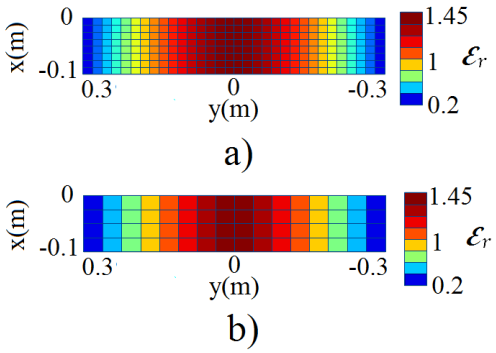


Figure 2.11 TE structure profile with discretized values of permittivity a) 256 blocks: 32 horizontal and 8 vertical regions. b) 64 blocks: 16 horizontal and 4 vertical regions.

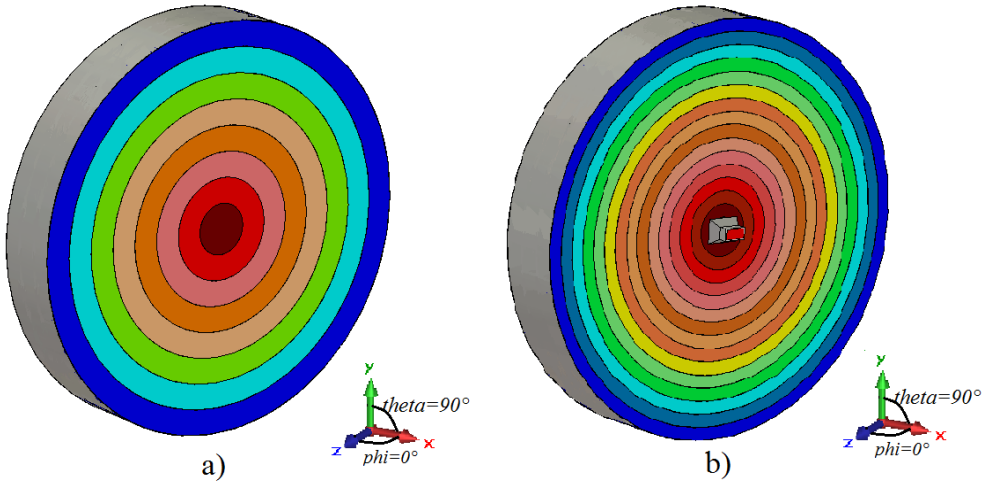


Figure 2.12 Front view of multilayered structure for the flat reflector.

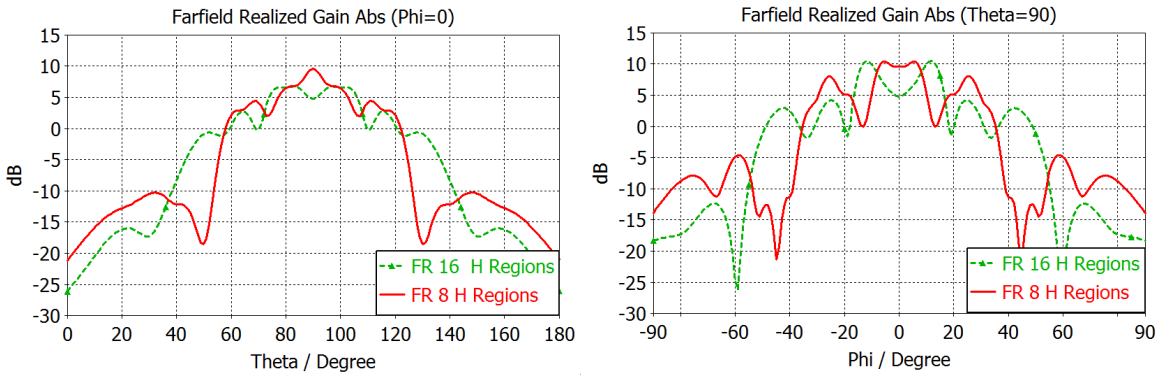


Figure 2.13 Farfield pattern comparison at 5 GHz between two structures with different discretizations: 8 horizontal regions (same dispersive reflector from Figure 2.10) and 16 horizontal regions of constant value of permittivity.

A difference around 3 dB to 5 dB in terms of RG in the broadside direction is highlighted in Figure 2.13. The RG is 9.5 dB for the structure of 16 regions and 6.7 dB for the structure with 8

regions for the phi=0 plane while 10.4 dB and 10.5 dB for the theta =90° plane respectively. However, in terms of HPBW the difference is less pronounced because the 16 regions reflector has 7.2° and 6° for the 8 regions reflector. Finally, the 8 regions structure is kept for realization purposes because of the blocks size, while the 16 regions structure is slightly more complicated. As it is possible to see in Figure 2.11, there is not vertical variation in the values of the profile, then there is no need to have different vertical regions.

2.5. Permittivity synthesis

The process of achieving different values of permittivity using only simple materials is presented. Although it was already explored before, the all-dielectric solution is chosen to approach this application towards a feasible realisation as in [78].

In order to summarize all previous analysis: the use of only standard dielectric materials is needed in order to simplify the realization. In this way, additional approximations are also applied to set a constant value of permeability ($\mu_r=1$, as seen in 2.2) and to have a structure only defined by a variable permittivity. This approximation is justified as the value of μ_r is near 1 in the central region of the structure where the field is concentrated. The next step is the discretization of the material in 64 dielectric blocks (concentric rings) as shown in Figure 2.11-b. The discretized values of permittivity are taken from the profile of ε_{zz} in Figure 2.3-c. Relative permittivity values range from 0.2 to 1.45. It is noticed that some values are below one (dispersive values), which does not correspond to standard materials. Therefore, the case where dispersive values are replaced by a relative permittivity of one is analyzed in 2.3. As the values of permittivity below 1 occur only at the edges of the structure where the field is weak.

As previously mentioned, the profile in Figure 2.11 is rotated around x axis to obtain a 3D flat reflector as in Figure 2.12. As a result, the flat reflector is a cylindrical structure of 60 cm diameter with different annular regions. Furthermore, the realization of the structure is possible using a drilling technique explained in 2.1.2, which involves drilling holes in standard materials to achieve a variable permittivity structure. The density of holes determines the value of the relative permittivity as established in [76]. Density varies by changing the angular distance d_a between holes and keeping the radial distance d_r constant (see Figure 2.14). The diameter of the holes is 4 mm, which represents 0.067λ at 5 GHz. This size for the holes is chosen basically, for making the drilling more easily. Equation 2.6 allows to calculate the different values of the synthesized permittivity from ε_d and ε_a, the permittivity of the Teflon and the air respectively.

$$\varepsilon_{synth} = \varepsilon_d f_d + \varepsilon_a f_a \Rightarrow f_a = N_h * \frac{V_{air}}{V_T} \qquad \textbf{(2.6)}$$

Where: N_h is the number of holes, V_{air} is volume of air and V_T is the total volume of the structure. To build up the first prototype of the reflector, the only dielectric used is Teflon, which has a permittivity of 2.2. Then, the range of relative permittivity values [0.2-1.45] is shifted to [1.6 to 2.2], because Teflon is used for this structure, and it presents relative permittivity of 2.2. Therefore, the numbers of holes for each region need to be calculated under Equation 2.6 using the known values of the permittivity for each region.

	1	***2***	***3***	***4***	***5***	***6***	***7***	***8***
ε_{synth}	2.2	2.15	2	1.89	1.77	1.72	1.66	1.61
No.Holes	0	4	74	155	210	390	490	760
fa	0	0.04	0.16	0.25	0.35	0.4	0.44	0.49

Table 2.1 Synthesized values of permittivity required for the flat reflector with the number of holes needed in each region.

As shown in Figure 2.14, only one layer of Teflon with holes is used to construct the different regions. It is noticed that the centre of the structure has lower density of holes, which indicates that higher values of permittivity are present in the centre. For the purpose of increasing directivity, it is possible to highlight that waves concentrate trough the centre of the reflector thanks to higher values of permittivity that located in this region. This is also possible to see in the original profile for this application and other contributions as [66].

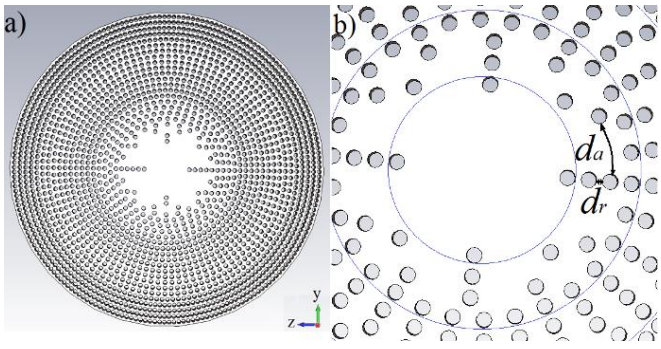


Figure 2.14 a) Front view of dielectric structure. b) Front view in details: d_a angular distance and d_r radial distance between holes.

3. Complete structure

3.1. Geometry and performance of the device

A 2D structure of the permittivity profile has been extended to 3D shown in Figure 2.11. As it is previously mentioned, the profile is rotated to construct a flat reflector of 8 regions. This method is

also used in some other contributions such as [69], [78] and it involves some approximations described in [77].

The geometry of the flat reflector is presented in Figure 2.15, the farfield results at 5 GHz from simulations with CST Microwave Studio are presented in Figure 2.16. At this frequency, the size of the structure compared to the wavelength is 10λ for the diameter and 1.5 λ for focal distance, which gives a maximal directivity of 29 dBi ($4\pi R^2/A$). In terms of *f/D* ratio (focal distance/diameter) makes 0.175, which it makes a very interesting size for a reflector (typical ratio in parabolic reflector is 0.25).

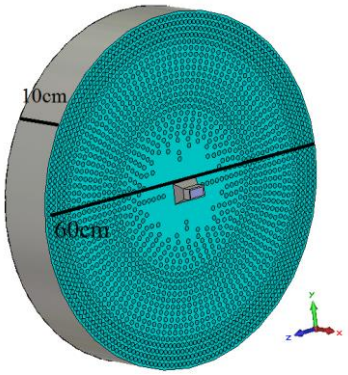


Figure 2.15 Front view of multilayered structure for the flat reflector.

In Figure 2.16, the radiation pattern of the structure with holes is shown, in order to be compared with the dispersive and non-dispersive structures presented earlier. The Teflon reflector is positioned 5 mm from the horn antenna in order to minimize the oscillations in the radiation pattern, which occur when the reflector is in contact with the horn antenna. Results are relatively close among the three reflectors, the HPBW are 20°, 16° and 21° for the dispersive, non-dispersive structure and the drilled structure respectively. The maximal RG in the broadside direction is 12.2 dB for the drilled reflector, which is higher than the other reflectors. This can be explained by the fact that the considered values of permittivity are higher than in the other cases. The side lobe level is higher in the case of the Teflon with holes (-9.2 dB below the maximum RG) than in other cases (-6.8 dB and -5.1 dB) which means that the side lobes decrease for the case of the drilled structure, although it is still 1.7 dB which is challenging for a reflector. The variation can be caused by the separation of 5 mm between the horn antenna and the drilled dielectric.

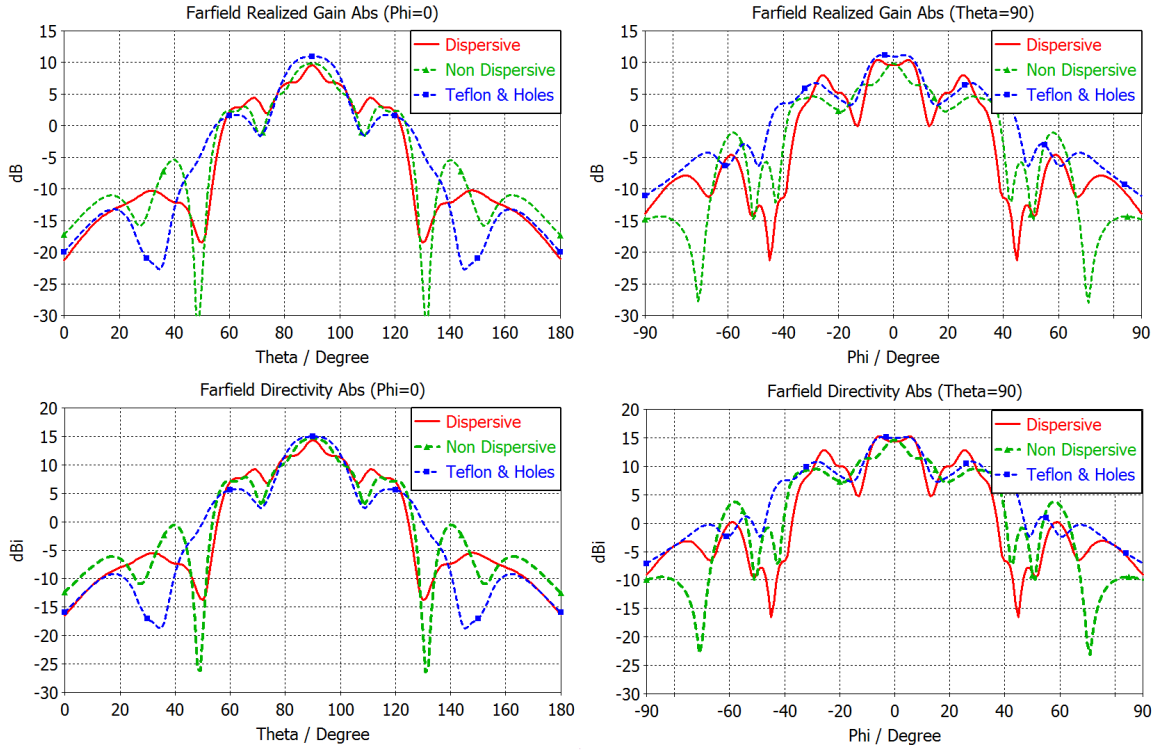


Figure 2.16 Radiation patterns comparison (RG and Directivity) between the dispersive (8 horizontal regions) and non-dispersive reflectors and the drilled one at 5 GHz.

Finally, the co-polar and the cross-polar components of the farfield are presented in Figure 2.17 for both planes. In the phi=0 plane the co polar component is very strong compared to the cross polar component. The maximum value for the co-polar component is 10.9 dB while the cross-polar is 100db lower, which is normally expected because of the perfect rectangular port that illuminates the reflector through the horn antenna. In the other plane theta=90, the case is different.



Figure 2.17 a) Farfield components (Co-polar and Cross-polar).

3.2. Optimisations in size and performance

Optimizations in order to find the most performing device in terms of specifications are presented. One interesting method of fabrication is 3D printing. Then, an effort to approach this design towards

a 3D printing realisation is introduced. The most suitable device to be 3D printed in order to validate the principle of the flat reflector is explored.

3.2.1. Optimizations in size

Considering the size of Teflon reflector, the weight of the device could be a problem. Therefore, a small version of the device is proposed. In Figure 2.18, a WR90-SMA adaptor feeds this small version of the flat reflector, in order to analyse the bandwidth behaviour of the drilled structure in a realistic situation and also in order to keep the conditions of the simulation made in Comsol Multiphysics (dimensions). As the 3D printer has a limit of 250 mm for the maximum diameter, therefore both thickness and diameter have been scaled to 0.41, keeping the *f/D* ratio in 0.17. At 10 GHz, the diameter is 8.3 λ and the thickness is 1.367 λ.

Teflon is very interesting as a dielectric material for TE device because its low value of permittivity. However, other materials with low values of permittivity can also be used, and some of them are used in 3D printers such as FullCure. FullCure has 2.9 as relative permittivity and $tan\delta$=0.0862, therefore a Fullcure version of the flat reflector is analysed and approached towards a feasible realisation.

In the previous version, the flat reflector made of Teflon operates at 5 GHz with 60cm of diameter, the reflector presented in Figure 2.18 made of Fullcure as dielectric with 25cm of diameter is simulated at 10 GHz. As the volumetric factors are kept, the values of permittivity can be easily calculated with them. The values are obviously scaled in their range from [1.6 -2.2] to [2-2.9]. However, this allows to analyse the flat reflector in a much realistic situation.

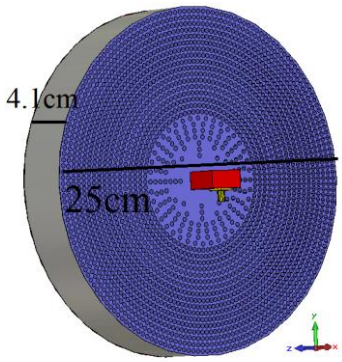


Figure 2.18 Front view of Flat Reflector and W90-coaxial adaptor.

The polar plots of the farfield of the horn antenna with and without the reflector are presented in Figure 2.19. The simulated maximum directivity for the horn is 6.5 dBi with a 62.6° of HPBW for one plane (φ=0°) and 124.9° in the other plane (θ=90°). The horn combined with the FullCure reflector has 6.94 dBi of RG and 17.1° of HPBW in one plane (φ=0°) and 16.2° in the other (θ=90°). In terms of sidelobe levels in the φ =0° plane; the horn presents -8.4dBi and -12.1dBi for the complete

structure, while the sidelobe is -8.4dBi for the horn only and -12.1dBi for the complete structure in the θ=90°. If the performance of the device is only judged by Figure 2.19, it can be said that the flat reflector satisfy the purpose of a parabolic reflector because a 71% of decrease in HPBW (in one plane) and 0.6 dBi of RG increasing are quite interesting for any directive reflector.

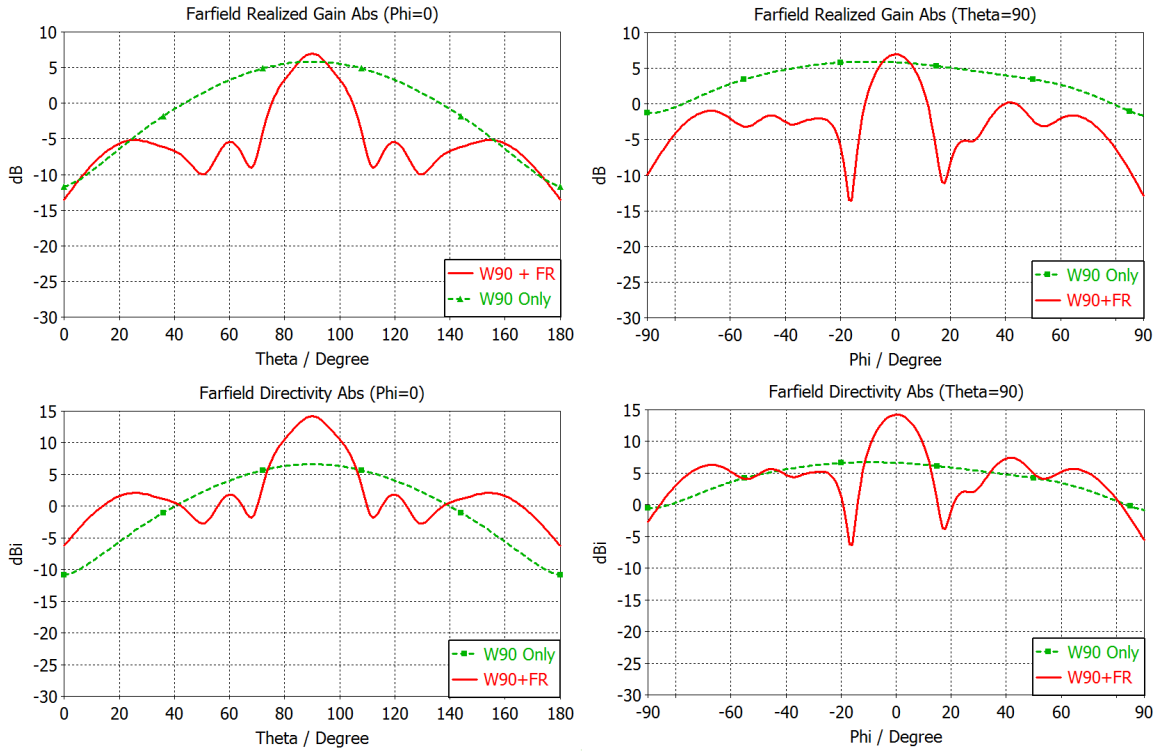


Figure 2.19 FullCure reflector radiation patterns at 10 GHz. Horn antenna only (Blue curve), and Horn combined with the flat reflector (Red curve)

3.2.2. Farfield analysis at different frequencies

Performances of the device at multiple frequencies are studied in order to show the response of the device for a large bandwidth. The horn antenna with flat reflector is simulated and the S_{11} parameter is presented in Figure 2.20. Originally the w90 to SMA adaptor (horn antenna) operates between [9-10.5] GHz and [11.05-13] GHz. However, the horn combined with the flat reflector became quasi wideband, which is ideal for analysing the device at various frequencies. Seven markers are set for calculating the farfield in Figure 2.21.

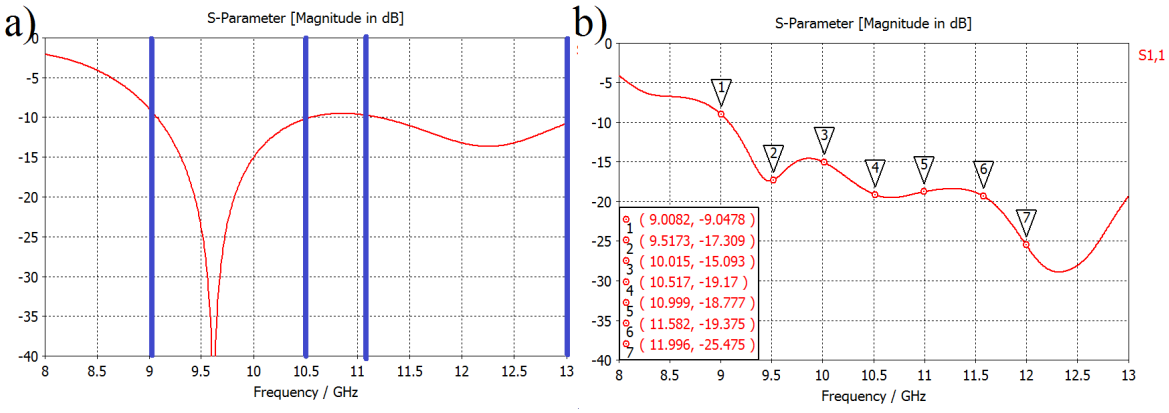


Figure 2.20 S_{11} parameter of the complete structure a) Horn antenna, b) Horn antenna+TE Flat Fullcure reflector)

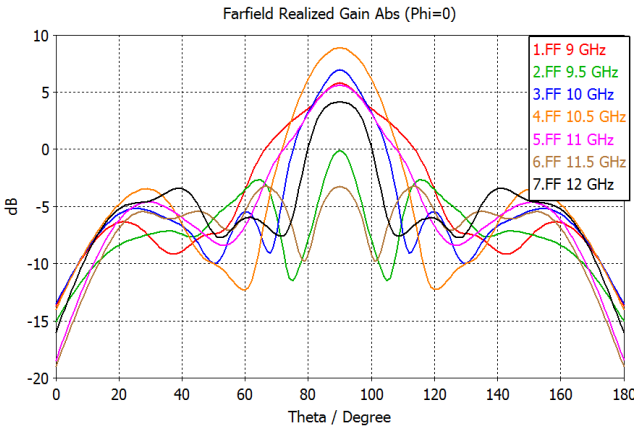


Figure 2.21 Fullcure reflector radiation patterns from 9 GHz to 12 GHz.

The farfield comparison at different frequencies allows seeing the RG evolving along the bandwidth of the device. There is no tendency of better performances at lower frequencies, as well as the upper frequencies. There is overall, an oscillation of the maximum RG among the bandwidth. There are two frequencies where the maximum RG are below 0dB and the other 5 frequencies present an interesting RG between 3 to 9 dB.

2.2.3. Comparison with similar devices

Other flat reflectors in literature as flat parabolic reflectors [79] and reflectarrays [80] proposes interesting performances while keeping the shape of the structure thin. This is an interesting advantage in terms of geometry. Many other advantages come from these devices such as beam shaping, low cost and simple realisation process. However, they present some limitations also in terms of bandwidth and reduced aperture efficiency. Comparing these devices to the flat reflector proposed in this chapter, the main advantage noticed is that these reflectarrays (as typical parabolic reflectors) require also an important distance between the source and the reflecting surface while in the proposed flat reflector this distance can be controlled and drastically reduced. In terms of the *f/D*

factor for example; usually in reflectarrays and other parabolic reflectors 0.5 of f/D is considered as good while our flat reflector the factor f/D is 0.17. Other parameters of the device can be discussed also but in terms of size this drastic reduction of the thickness of the device is very interesting in our flat reflector.

Another contributions of Transformation Electromagnetics on flat reflectors are quite interesting as well. The analytical approach of TE is used in [81] to design a low profile reflector with a planar conducting sheet and a linear coordinate transformation. However, the shape of the reflector is triangular which as the parabolic reflector could be a challenge for applications that requires conformability. Another interesting contributions are presented in [82], [83], both interesting variations of all dielectric flat reflectors. They explore beam steering in their flat reflectors, one analyses different variations in the farfield simulations while the source antenna is being moved along the diameter direction. The other contributions explore the beam steering by shifting the values of the permittivity inside the profile to the sides of the device. The distance between the antenna and the reflecting surface is not studied as it is studied in our device.

4. Conclusions

In this chapter, we have proposed a method to design a flat reflector in order to reduce the thickness of the structure, based on TE principle and using dielectric materials only. Thickness reduction and an all dielectric approach allow to highlight the device as suitable for applications where the shape and simplicity realization are important.

Choosing carefully the approximations and simplifications to be made in the different components of the permeability and the permittivity tensors of the material is important in order to achieve a feasible structure. A comparison between dispersive and non-dispersive flat reflector has demonstrated that the performances are not compromised.

Furthermore, while reviewing of some all-dielectric methods, we have also demonstrated that the method of drilling to achieve different values of permittivity in the different regions of the structure can be successfully used in the design of TE devices. This all-dielectric approach is highly preferred, instead to the use of metamaterials because of its simplicity and wideband behaviour.

As the frequency is not taken into account in the profile calculation, theoretically this method can be used at other frequencies however the dielectric material and the source will define the operating band of the device. As shown, this TE device can work at different frequencies showing an interesting wideband behaviour.

In order to approach the device towards two versions of the device are presented. The 60cm diameter flat reflector is used to carefully describe all the design steps required for this application. Then, once the design is completed and all the performances analyzed and keeping all the previous work in the design process; a 250 mm diameter flat reflector is presented. This smaller version of the device is used to perform in a much realistic setup. A different frequency is used and wideband behaviour of the flat reflector is validated.

Chapter 3
All Dielectric Superstrate to Increase HPBW of an antenna

In this chapter, an all-dielectric superstrate is presented. This second application aims to control the HPBW of a low profile GPS antenna. While the previous chapter deals with increasing directivity using a flat reflector, this chapter intends to increase the HPBW of a patch antenna using a superstrate. Therefore, the major objective of this work is to design a TE inspired superstrate to be fabricated in order to prove the concept.

This superstrate is designed to work over a GPS patch antenna. This GPS antenna is necessary for airborne applications. It implies that in order to work properly, a very large angular beam width is required to maintain the link with the satellites all the time, no matter the position or orientation of the plane.

These studies have been carried on the framework of the Work Package 4 of the MIMiCRA project. This work package is intended to explore new concepts of devices inspired by Transformation Electromagnetics in order to improve performances of a regular antenna.

It is always necessary to compare the performances of the proposed device to a reference one. The antenna chosen to be the reference antenna for these studies is the MIMiCRA Case 1 antenna whose performances are presented at the end of this manuscript (Appendix A). More precisely, two versions of this antenna with different ground planes are presented in this appendix. The version with the bigger ground plane is used in the final set up for measurement of the realized prototype.

Another objective of this work is to explore the different steps of the design process and the optimizations of the prototype in order to achieve best performances. However, it is necessary to mention that for the realized structure, performances are modified in order to focus the validation of the principle by using a simple approach. A 3D printer is used to realize the prototype of this device.

This application is inspired by a conformal mapping application of TE [84] to achieve higher directivity. The full explanation of the process for increasing Half Power Beam Width from the original application is described in this section.

1. TE Inspired superstrate

The purpose of this superstrate is to achieve a larger beamwidth without deteriorating the performances of the original antenna such as the bandwidth, gain, etc. The bandwidth defined (defined by $|S_{11}|$<-10dB) in the reference antenna is 6.7%. Therefore, as it was explained before, an all dielectric solution is more suitable than resonant structures based solution such as: Split Ring Resonators, single Split Ring Resonator, etc. For simplicity reasons in terms of calculation time, avoiding high losses and other issues related to the realisation, the all-dielectric approach is used for this application.

As mentioned previously, our work is inspired from a flat TE device designed to achieve high directivity [84]. This flat TE device achieves directivity by focussing waves towards the centre of its structure. Basically, this superstrate acting as a lens was designed as a flat parabolic reflector with performances similar to the flat reflector designed in the previous chapter of this manuscript. The resulting profile of the transformation used for this device is shown in Figure 3.1.

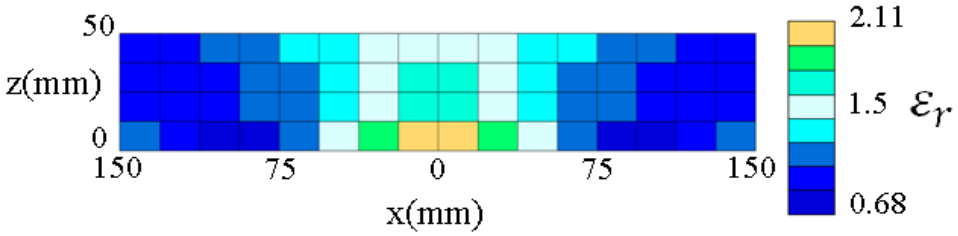


Figure 3.1 Initial TE structure profile, values in colour represent different values of relative permittivity [84].

Several modifications (Figure 3.2) to this profile are made in order to achieve the opposite behaviour, it means to enlarge or increase the angular beam width of the farfield by changing the configuration of permittivity blocks inside the profile while keeping the permeability unchanged (μ_r =1). These cases are compared in order to find the one where the beamwidth is larger than the original reference antenna.

In this application, a dual polarized patch antenna is used for reference. This dual-port patch antenna works in the GPS L5 and L2 bands [1.164-1.239] GHz with dual polarization. The antenna substrate is a 100*100 mm² square with 14.03 mm of thickness and the size of the patch is 68.5*68.5 mm². The substrate is Arlon AD 250 (ε_r =2.5), and the ground plane has the same size as the substrate's one.

The different cases are:

Case a: The reference antenna without any superstrate (Figure 3.2-a).

Case b: The original structure designed for the directivity improvement [84] is put above the reference antenna. This case aims to demonstrate that the TE works despite a change of the frequency and the distance between the source and the superstrate (Figure 3.2-b).

Case c: The values of permittivity are horizontally inversed compared to case b, i.e. the values in the center of the structure have been moved at the outer sides (Figure 3.2-c).

Case d: The permittivity values are vertically inversed compared to case b (Figure 3.2-d).

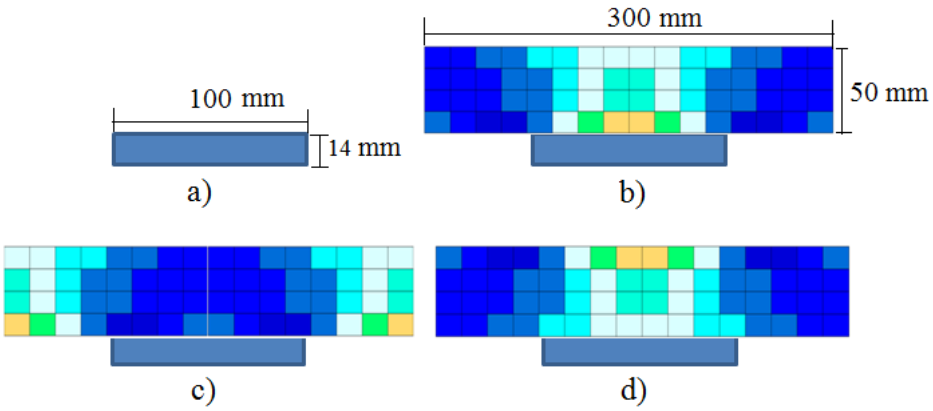


Figure 3.2 Four explored cases, a) Patch Only, b) Patch with directive structure, c) Patch with modified structure (horizontally inversed case), d) Patch with modified structure (vertically inversed case), quantities in mm.

In the next step, these profiles need to be extended to 3D structures in order to perform 3D electromagnetic simulations to verify our hypothesis. This means to find a proper method to extend the profile to a 3D structure that could be able to increase the HPBW of the reference antenna.

1.1. From permittivity profile to superstrate (2D to 3D extension)

A 2D permittivity profile is extended to 3D shown in Figure 3.3. The profile is extended to construct a multi-layered structure, as explained in previous chapters. The method used in [69], [77] and [78], explains how a 2D profile can be extended into a 3D structure by rotating the profile. However in this section, two approaches are described and compared in order to show their advantages and limitations. One of these approaches consists in rotating the profile whereas in the other one, the profile is directly extended into 3D as shown in Figure 3.3.

Then, the normalized radiation pattern results from the 4 different cases are analysed in order to find the most performing result. The HPBW is increased in one of the versions of the extended profile, and the following analysis justifies the choice of the rotated structure.

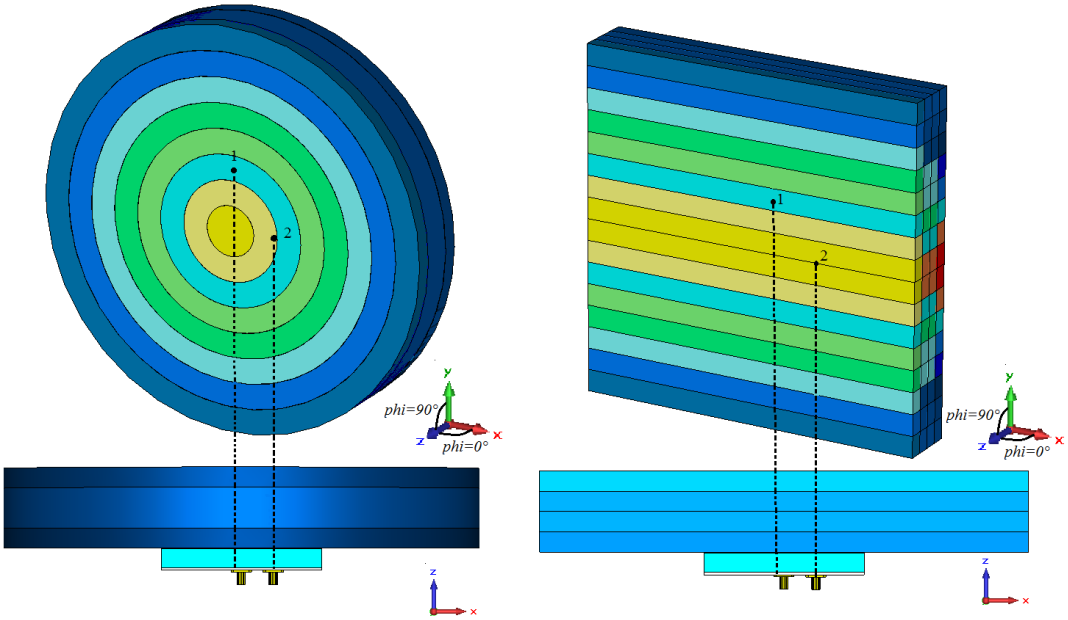


Figure 3.3 a) 2D Profile rotated into a 3D structure, b) 3D structure obtained by adding height to the 2D profile. In this case the profile for this picture is the one in Figure 3.2-b.

1.1.1. Profile Rotation

The radiation pattern of the four cases of Figure 3.2 with rotated profile (Figure 3.3a) for both linear (port 1, E field in *yz* plane) and circular polarisation are presented in Figure 3.4 and Figure 3.5, for both planes. The reason to present and analyse both polarisations is because the antenna used for this application aims to work on RHCP (Right Hand circular polarization) and over a GPS L2 band. The normalized gain is plotted between 0 and -3 dB, so only the main lobe is depicted and the HPBW easily calculated and analysed.

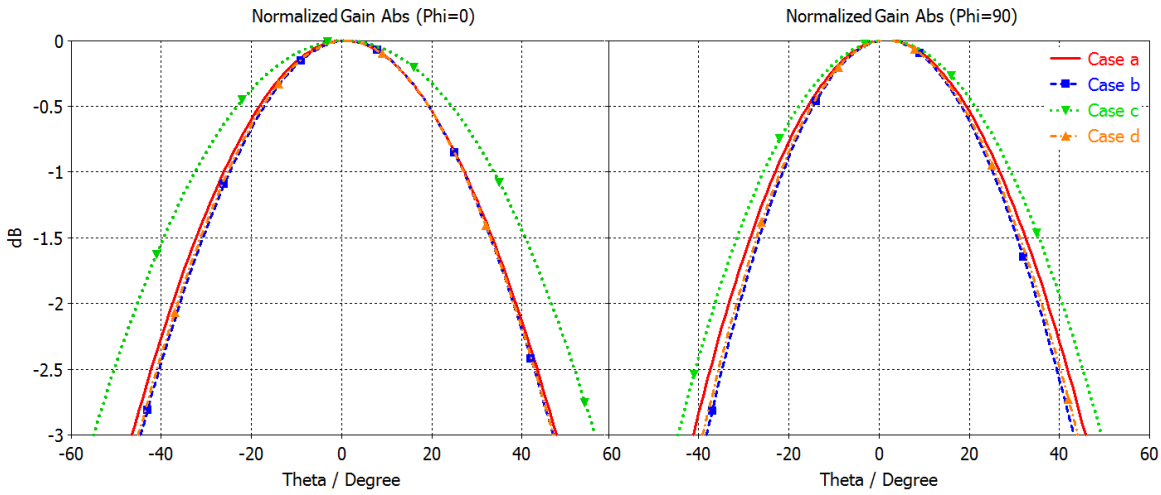


Figure 3.4 Normalised gain at the center frequency of the band (1.2 GHz), both planes for the different cases with linear polarization.

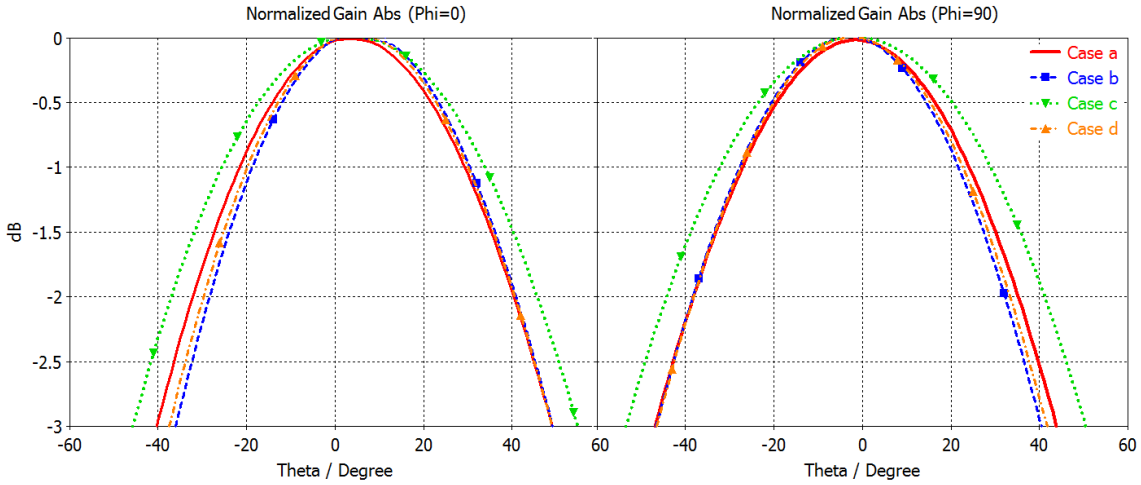


Figure 3.5 Normalised gain at the center frequency of the band (1.2 GHz), both planes for the different cases with RHCP.

In general for case b, simulation results demonstrate the capability of TE device to work at other frequencies than those it was initially designed. In the other two cases (c and d), the superstrate is modified to explore the potential solution to increase HPBW in the antenna.

At 1.2 GHz, the diameter of the structure (300 mm) is greater than one wavelength and TE can operate because in order to achieve the desired behaviour it is important to keep a size that allows waves interact with the geometry. Same effects are observed in linear polarisation as well as in RHCP.

As Figure 3.4 and Figure 3.5 show, it can be seen that case c seems an interesting option to enlarge Half Power Beam Width (HPBW) for the reference antenna. Regarding the case b, as expected, a slight decrease in the HPBW is clearly observed.

In the case of the linear polarization, the effect of increasing HPBW is clearly more noticeable in the phi=0° plane, the feeding port being located in the other orthogonal plane. Indeed, in this plane, the HPBW is increased from 93° for the reference antenna to 112° for case c, while in the other plane, it goes from 86° to 93°. In the case of circular polarization, the value of HPBW increase is less appreciable, however it is almost similar for both planes as expected; the HPBW goes from 89° to 100° in one plane and in the other plane from 91.1° to 103°.

1.1.2. Rectangular blocks

The second possibility of extending the profile into 3D is to extrude the profile directly as in Figure 3.3-b. As previously, the farfield radiation patterns are presented in Figure 3.6 and Figure 3.7 for the 4 cases and both polarizations in the two main planes.

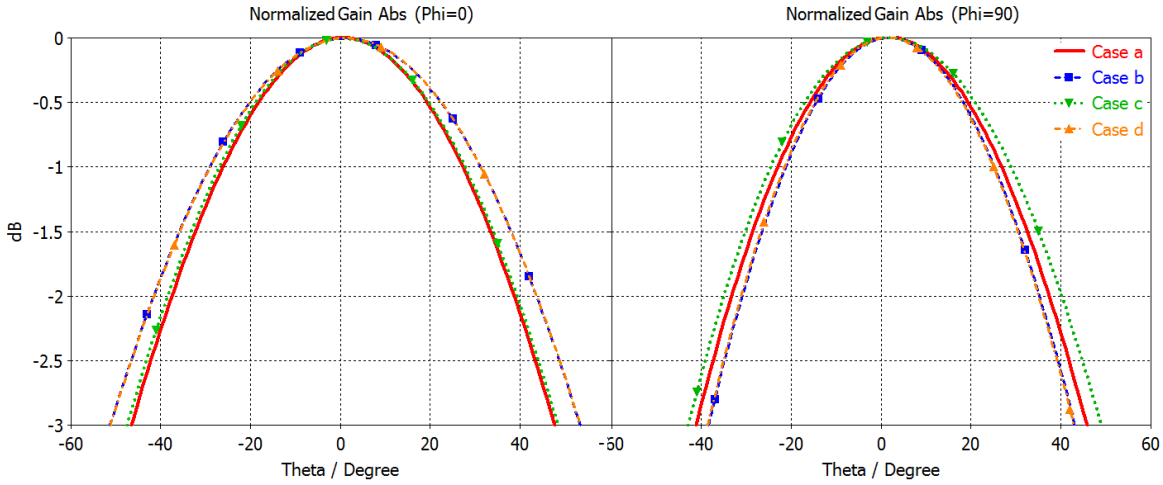


Figure 3.6 Normalised gain at the center frequency of the band (1.2 GHz), both planes for the different cases with a linear polarization

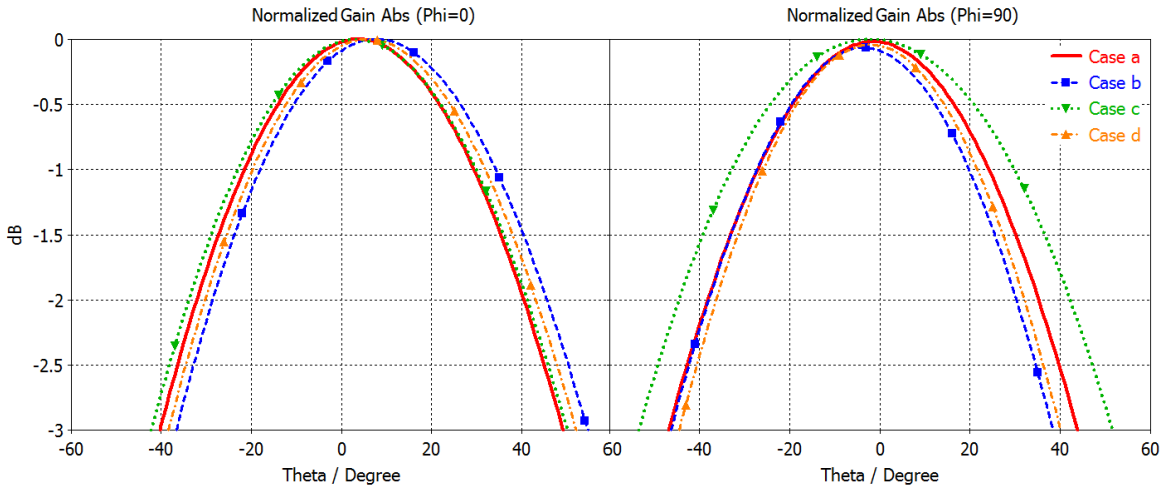


Figure 3.7 Normalised gain at the center frequency of the band (1.2 GHz), both planes for the different cases with a RHCP.

In this version of the 3D structure, from the four cases it is not possible to extract any particular or interesting behaviour among the results presented in Figure 3.6 and Figure 3.7, because results do not show a coherent variation in HPBW among the four cases. The case b, in the linear polarisation does not decrease HPBW because in one plane the HPBW is increased while in the other is decreased. For case c, along the linear polarisation, the HPBW does not change much. In one plane the HPBW goes from 89.9° to 92.2°, then in the other goes from 91.1° to 105.1°, the feeding port being located in this plane. In the case d, the superstrate behaves as in case b in the linear polarisation for both planes while in the circular polarisation in one plane the HPBW is increased and in the other is decreased.

Summary

It is possible to derive two main conclusions for case c with the rotated profile which fits perfectly to our needs. First, the results for the rotated structure in the case c present an enlargement of the beam of about 20% (HPBW = 112.5° for linear polarisation and 105° for RHCP) which justifies the use of this method to extend the 2D profile. Secondly, the highest values of the permittivity have been shifted to the outer layers. This enables to enlarge the radiation beam and helps waves to go to the outer sides instead of going towards the centre of the structure. This modification made to the original structure turned it into an un-focussing superstrate by changing the index of the different regions. In case d, the TE structure does not seem to have any effect on the radiation because the angular width remains relatively equal to the reference case.

In Figure 3.8, the 3D farfield patterns for the reference case and the case c (the case showing the interesting behaviour) with the rotated profile are plotted in order to see the full pattern. Only the linear polarisation is presented because the pattern does not vary too much for the circular polarisation in terms of shape.

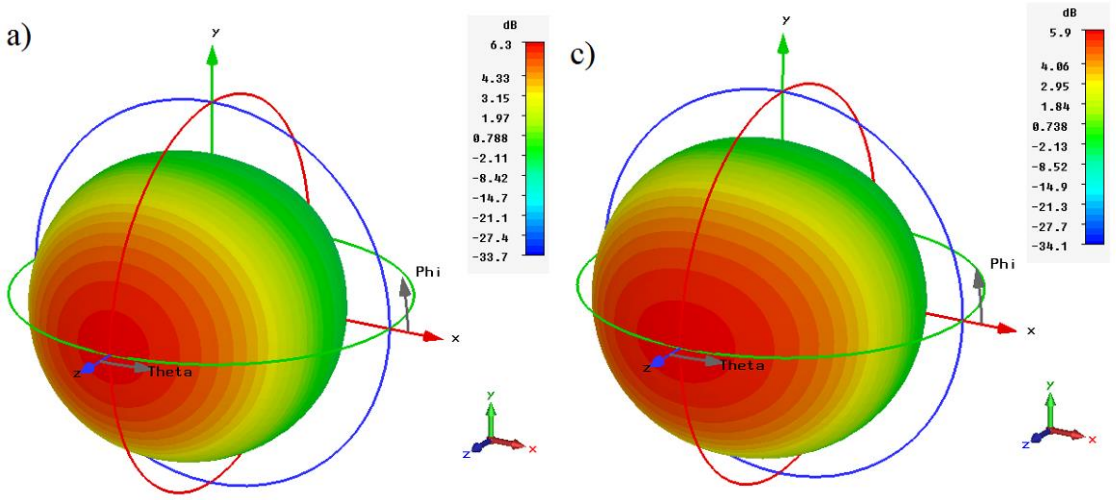


Figure 3.8 RG for Case a (left) and Case c (right) at 1.2 GHz for linear polarisation (Port 1 fed).

The 3D farfield in Figure 3.8 shows a typical pattern for a patch antenna and the reference antenna combined with the modified superstrate. It is possible to observe that HPBW is quite increased in one plane if a linear polarization is applied. It is also possible to observe that the gain decreases from 6.3 dB in the reference antenna to 5.9 dB for the antenna with the superstrate.

1.2. Influence of dispersive values of permittivity

As the case c has been chosen, the next step is to simplify the structure in order to take this design towards a practically realizable one while keeping the performances coherent to our needs. The next step in the process is to reduce the range of permittivity values, because some of them are below one,

in other words they are dispersive values. If the structure is realized using these values, some resonant structures such as metamaterials might be needed in order to synthesise these values of permittivity. Therefore, to avoid this, the values below one are replaced by one as shown in Figure 3.9 and the impact of this modification is studied in Figure 3.10 and Figure 3.11 by calculating the normalized farfield radiation pattern for both types of polarisation as well.

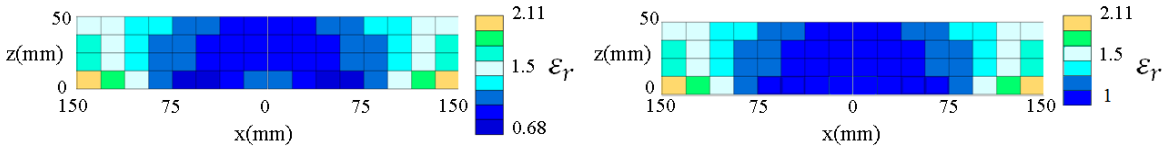


Figure 3.9 Case c profile with dispersive values of permittivity (left), Case c with non dispersive values of permittivity (right).

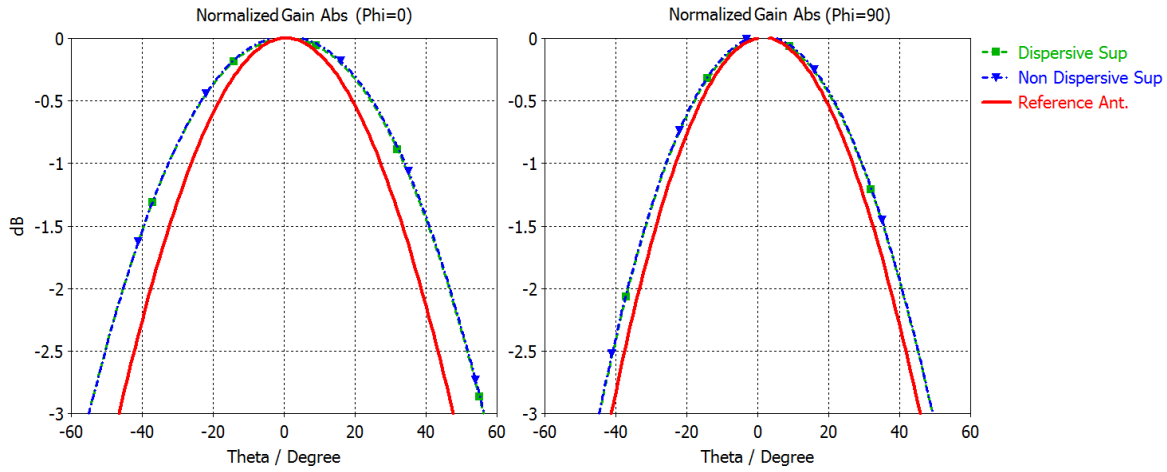


Figure 3.10 Normalized gain at 1.2 GHz for both planes for the different configurations with or without superstrate with linear polarisation.

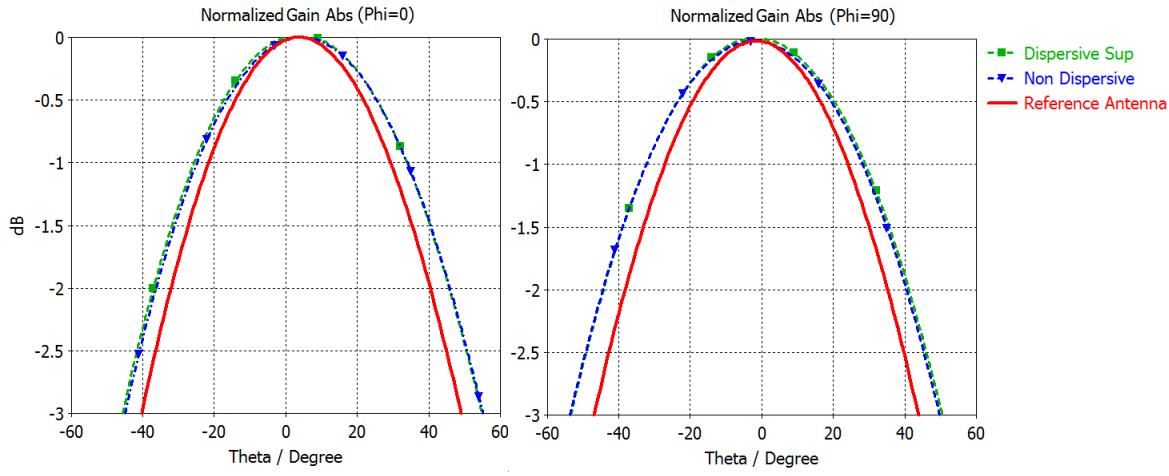


Figure 3.11 Normalized gain at 1.2 GHz for both planes for the different configurations with or without superstrate with RHCP.

As a result, it does not show high changes in terms of performance for both polarisations and two planes. Therefore, it is possible to use the profile of permittivity without any dispersive values, which simplifies the realisation process. This result is important because it implies that we do not need metamaterials to realize this superstrate.

As the values of permittivity are changing in the device, the wave impedance Z also changes according to Equation 3.1. The permittivity is discretized (non continuous) in 8 concentrated rings, which implies that the impedance has 8 values also. Using values of the permittivity in Table 3.1 at boundary face to the patch antenna, it is possible to calculate the average value of impedance wave, in order to see the effect of varying permittivity along the profile.

$$Z = \sqrt{\frac{\mu}{\varepsilon}} \qquad \textbf{(3.1)}$$

ε_{r1}	ε_{r2}	ε_{r3}	ε_{r4}	ε_{r5}	ε_{r6}	ε_{r7}	ε_{r8}
1	0.92	0.84	0.69	0.98	1.37	1.74	2.11

Table 3.1 Permittivity values at boundary of the original superstrate facing the patch antenna. The values are presented in the geometrical position. It means ε_1 is located in the center of the superstrate and ε_8 at the boundaries.

Using Equation 3.1 and the values of relative permittivity, the arithmetic average value of the impedances at the boundaries are calculated for the original dispersive superstrate is 360 Ohms, while in the case of the non-dispersive structure, it is 343 Ohms. These average values of impedance present a variation of 4.5% and 9%, compared to the wave impedance in free space 377 Ohms. The difference between both values is not drastic which could also explain why both superstrate performances are not much different.

1.3. Influence of permittivity variation

The variation of the permittivity is studied more precisely in order to establish the limits of the design so that appropriate materials can be used for realisations. Thus, the range of permittivity values is shifted adding one and two to them. Therefore, in the original dispersive set of values for permittivity, values goes from 0.68 to 2.11 and for the first modified range of permittivity goes from 1.68 to 3.11 and in the second modified range goes from 2.68 to 4.11. The normalized RG is analyzed for every case for linear polarisations. Regarding the wave impedance, the changes made to the permittivity affect the matching between the antenna and the superstrate. Using Equation 3.1 and the values of Table 3.1, it is possible to calculate the average impedance for the modified cases studied. For the first modification (ε_r+1), the average impedance is 253 Ohms and for the second modification (ε_r+2) is 211 Ohms, which indicates that some intermediate material could be needed to match the antenna and the superstrate.

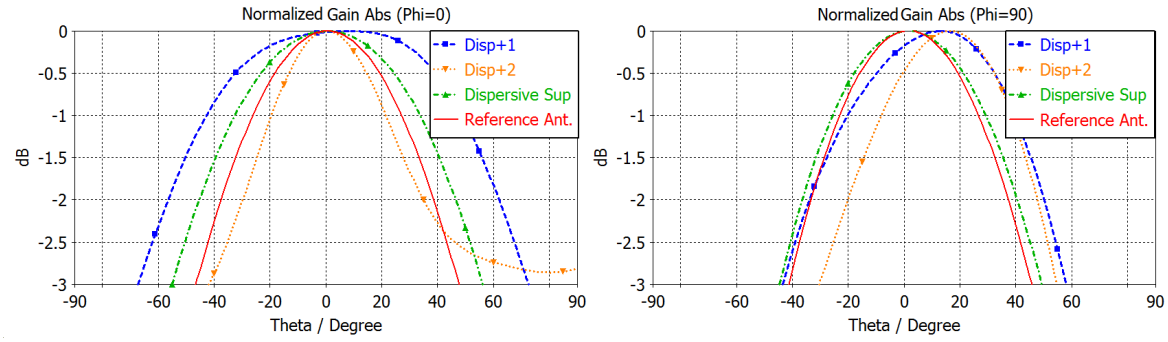


Figure 3.12 Normalized gain at 1.2 GHz for both planes for the different configurations with permittivity variation.

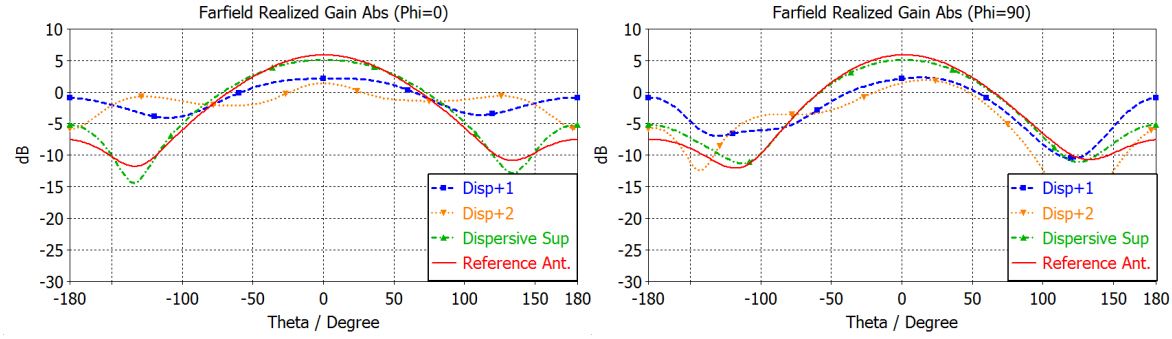


Figure 3.13 RG at 1.2 GHz for both planes for the different configurations with permittivity variation.

Comparing the different cases in Figure 3.12, it is noticed that if the range of values of permittivity is increased by one (range 1.68 to 3.11), the results in terms of HPBW are very interesting because it increases even more the HPBW from 94° for the reference antenna to 139° in the phi=0° plane. It can be recalled that the modified profile (or case c) with the range of values between 0.68 to 2.1 increases the HPBW from 94° to 111.2°. Thus, using the range from 1.68 to 3.11 enables to increase the HPBW of about 47%. In terms of broadside RG (Figure 3.13), it is reduced to 2.2 dB instead of 5.8 dB for the reference antenna. In the other hand, the profile with the range from 2.68 to 4.11 increases the HPBW also. However as Figure 3.13 shows, the radiation pattern is also modified: the gain is strongly reduced, many beams or ripples have appeared and the backside lobes levels have also increased. It is also noticed that the farfield becomes asymmetric while the permittivity increases, especially in the phi=90° plane, this could be explained in the fact that the antenna with the modified superstrates (ε_r+1, ε_r+2) are not matched, as it is shown in Figure 3.14.

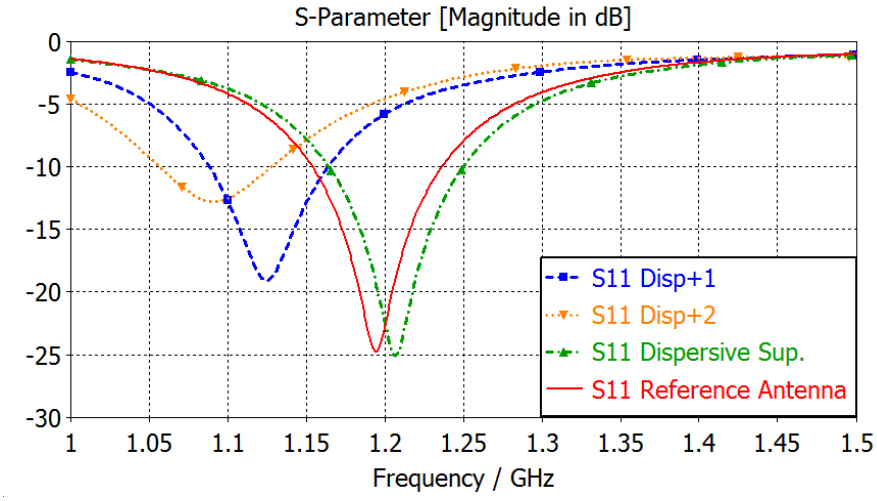


Figure 3.14 Reflection coefficient versus frequency for 4 explored cases

Once these limits in terms of permittivity have been tested, it is possible to say that if the range of permittivity goes from 1.68 to 3.11, the designed structure will increase significantly the HPBW (only one plane in linear polarisation). This also is remarkably adequate for our purpose of realisation, because some interesting dielectric materials with low permittivity can be used such as Teflon (ε_r=2.1), FR4 (ε_r=4.3), FullCure (ε_r=2.9), etc. It also means that the reference antenna has to be rematched or inserting an intermediate layer between antenna and superstrate.

1.4. Permittivity synthesis

The previous analysis concluded to a multi-layered structure resulting from a rotated profile. It was also seen that if values of permittivity are increased above 3.5, the radiation pattern of the antenna is deteriorated. The structure must be synthesized with a dielectric material with a relative permittivity near to three as we intend to use the method of drilling holes to achieve the variation in permittivity required. This structure must be cylindrical and must have multiple layers.

As it is previously mentioned, the all-dielectric superstrate is designed using the method of drilling holes in a dielectric explained in the previous chapter (all-dielectric flat reflector) which is inspired from [76]. However, the range of values of the relative permittivity (1-2.11) is shifted in (1.6 to 2.2) to be able to use only one dielectric material to realise the final prototype of the superstrate. As Teflon is used, then the maximum value for the variation of permittivity when there is not holes inside a specific region is 2.2, then the minimum value that can be obtained by drilling holes is 1.6 as it was shown in equation 2.6. In this regard, the same variation is kept; it means that every value in the range of 1 to 2.11 has a corresponding value in the range of 1.6 to 2.11.

In this case, three stacked layers of Teflon (ε_r=2.2) are used to construct the different regions. The first and third layers have the same thickness (12.5 mm) and the second layer is twice thick (25 mm)

(see Figure 3.15 and Figure 3.16) for a total thickness of 50 mm. Finally, every layer has 8 horizontal regions of different permittivity.

In the process, for the 3 types of layers, 9 different values of permittivity are calculated and shown in Table 3.2. The process takes into account the Equation 2.6, where different values can be obtained using two materials of different permittivity. In this case, the relative permittivity for the dielectric is ε_r=2.2 and for the air ε_r=1, for the holes. The diameter of the holes is 3.34 mm, which is about 0.013λ at 1.2 GHz. The size of the hole was chosen arbitrary small, in order to facilitate the drilling realization.

ε_{r1}	ε_{r2}	ε_{r3}	ε_{r4}	ε_{r5}	ε_{r6}	ε_{r7}	ε_{r8}	ε_{r9}
1.6	1.62	1.7	1.72	1.79	1.84	1.9	2.12	2.2

Table 3.2 Synthesized permittivity values required for the superstrate.

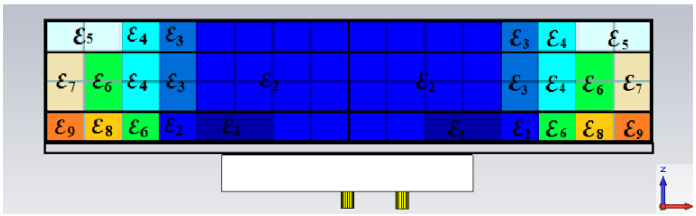


Figure 3.15 Profile view of the structure: Antenna and superstrate with different horizontal and vertical regions.

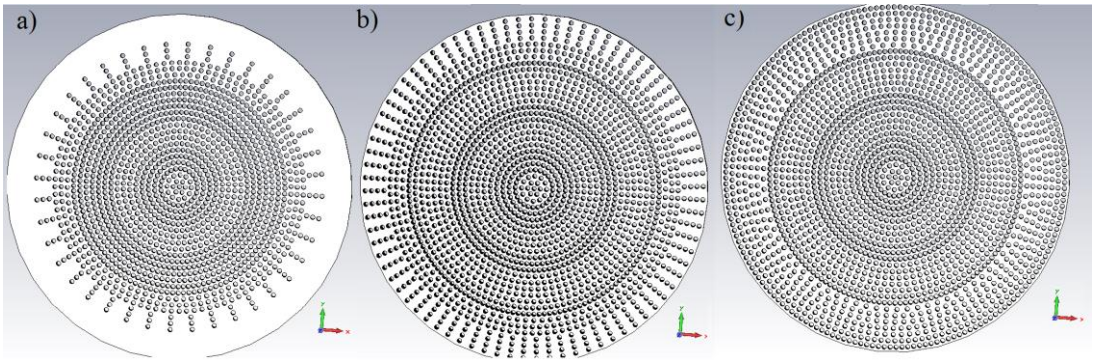


Figure 3.16 Front view of variant permittivity superstrate, a) 1st Layer (bottom), b) 2nd Layer (middle), c) 3rd Layer (upper).

In order to put things in perspective, all significant cases until this point are summarized and analysed in Figure 3.17, which presents the normalized gain (main lobe of the far field radiation pattern in two orthogonal planes) of the superstrate with different configurations at 1.2 GHz. The first configuration is the antenna without any superstrate; the second and third configurations are the theoretical material with dispersive and non-dispersive values of permittivity. The last one is the drilled superstrate made of Teflon.

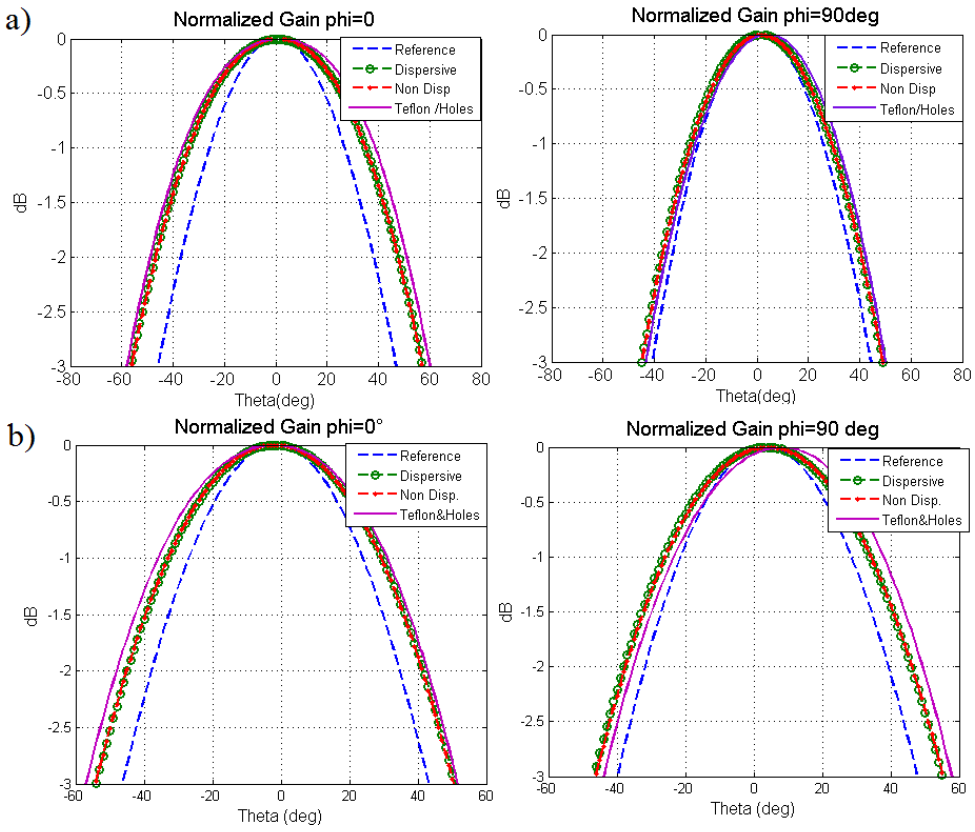


Figure 3.17 Normalized gain at 1.2 GHz for both planes for the different configurations with or without superstrate. a) Linear polarisation, b) RHCP.

As it was explained before, the superstrate increases the HPBW of 20 % with and without dispersive values compared to the reference antenna. The solution with periodic holes shows a very interesting increase of 26% and 16% in HPBW for linear and circular polarisation respectively. This can be explained with the fact that we have changed the original values of the permittivity, and higher values were used as it was explained in Section 1.3, when the values of permittivity were increased until 4.11 the HPBW was largely increased. As high values are used, the band is lightly shifted to upper frequencies. The fact that replacing the smaller dispersive permittivities ($\varepsilon_r<1$) by air ($\varepsilon_r=1$) does not affect the pattern, is the reason why it is possible to use only one material for the 3 layers.

Figure 3.18 shows the axial ratio evolution of the same 4 structures as Figure 3.17. The minimum AR at the broadside is 0.4 dB, 0.2 dB, 0.21 dB and 0.42 dB for the four structures.

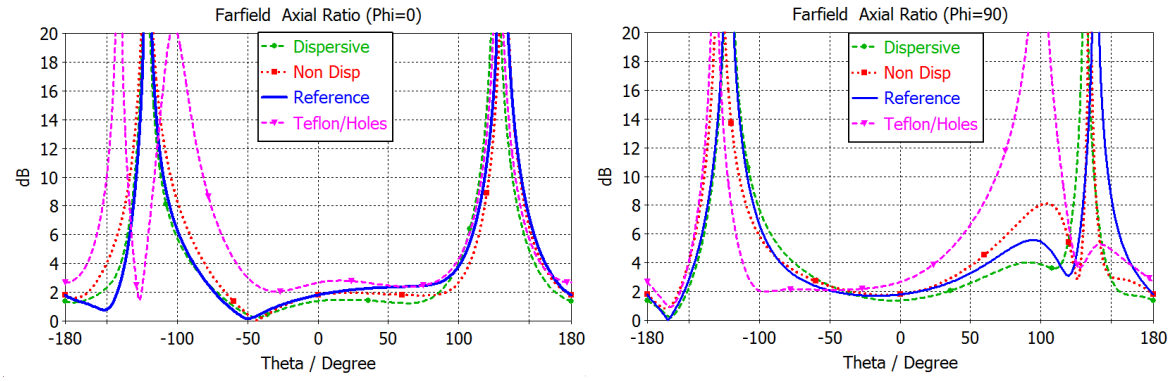


Figure 3.18 Cartesian plot for the axial ratio of the dispersive superstrate, non dispersive superstrate and the drilled superstrate at 1.2 GHz, for both planes (*phi= 0°* and *phi=90°*).

1.5. Comparison with classical superstrates

Devices such as non-drilled superstrates or radomes could also increase HPWB. However, if these devices are compared in terms of performances with our device, some limitations are highlighted in terms of shifting the operating band. Usually dielectrics with small values of permittivity are used. They are included in the design process of the antenna in order to take into account their influence on the resonant frequency of the antenna. The difference with our device is that TE inspired superstrate can potentially work with different planar antennas, the only parameter to be adjusted to preserve the matching is the distance between the antenna and the superstrate.

a) Principles

The approach of using TE to design electromagnetic devices is to transform the space around a radiating element while keeping the wave impedance and avoiding mismatching. Thus, the transformation in the boundaries of the device assures a smooth transition the between regular space and the transformed one. For example in this case, when the impedance is observed at the boundaries of the original superstrate [84], it is possible to notice that the values are not very far from the 376 ohms in the vacuum. The superstrate with the original values comes from the theoretical transformation, but the mismatches appear during the process of approaching to a practically realizable structure. However some compromises are clearly justified in order to prove the concept.

b) Homogenous dielectric comparison

In this comparison, the drilled superstrate of 300 mm diameter and 50 mm thickness and the reference antenna are compared to similar structure. A homogeneous dielectric (ε_r=2.1), this value is used because it is the same value used in the dielectric superstrate made of Teflon. The homogeneous dielectric is put over the reference antenna and is simulated in CST Microwave Studio as it is possible to see in Figure 3.19 as well as S_{11} parameters variations for the different cases presented.

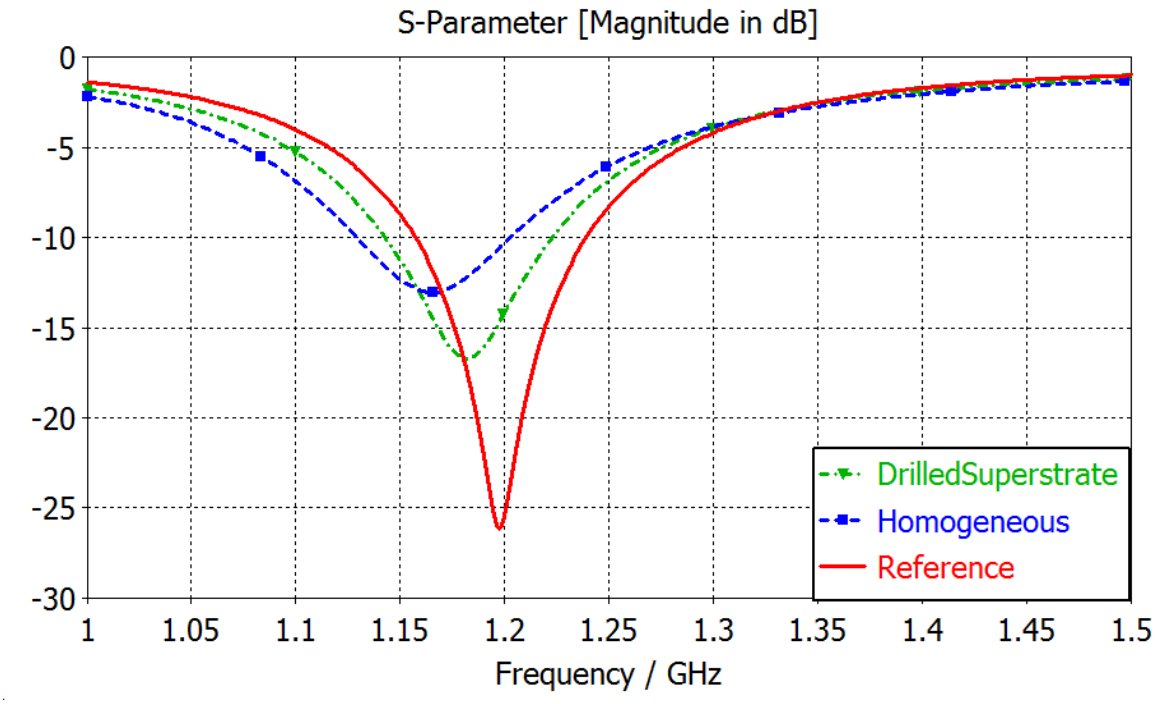


Figure 3.19 S_{11} parameters comparison for 1 layer, 2 layers and 3 layers of non drilled dielectric (below).

It is possible to see how adding a non-drilled homogeneous layer affects clearly the matching in the operating band towards lower frequencies. The operating band moves from [1.16-1.24] GHz to [1.13-1.20] GHz, while in the case of the drilled superstrate, it is [1.14-1.22] GHz.

In Figure 3.20, the farfield pattern is plotted in order to show the evolution of the normalized gain when the homogeneous dielectric is placed over the antenna. Only one plane (phi=0°) in linear polarization is shown because only this plane is relevant for comparison purposes. Indeed, as it is seen in previous normalized farfield patterns, the farfield pattern does not present much variation in the *phi=90°* plane.

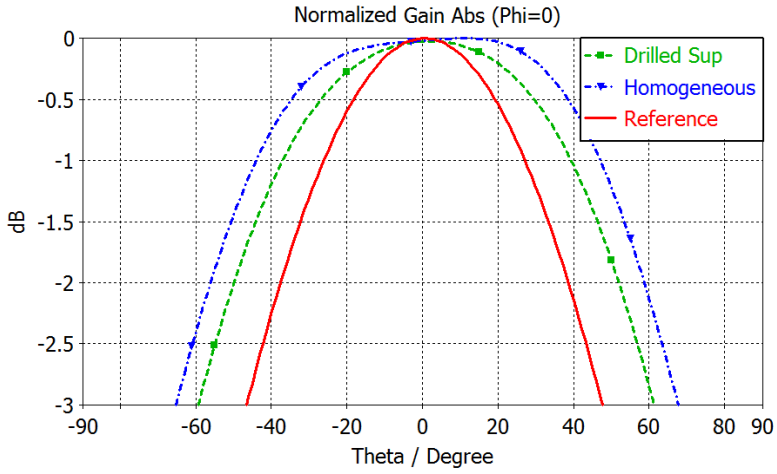


Figure 3.20 Radiation pattern comparison at 1.2 GHz (phi=0°).

From Figure 3.20, we observe an evolution of the HPBW among these different cases. In general, it is possible to see how adding a homogeneous dielectric allows to increase the value of the HPBW to 132°. Although this values is interesting, the mismatching of these structures is quite inacceptable. The drilled superstrate presents a HPBW of 121°, while keeping the operating band almost matched in the required frequency band. Then, the use of the TE drilled approach is justified it presents a spatial variation of permittivity that does not highly compromise the matching

2. Optimisation of size and performances of drilled structure

In this part, a new version of the device is described and FullCure is used as dielectric material to synthesise the permittivity values using the 3D printer. In the MIMiCRA project framework, it has been possible to work with a 3D printer, which is very suitable for this application, because it will not be necessary to perform holes in a homogeneoous material, instead the drilled geometry will be directly printed using a dielectric material (FullCure).

Also, all the optimizations that led to the best performing device and the most suitable to fabricate are presented. The size of the superstrate is 300 mm in diameter and 50 mm in the thickness. Full performance of the device is presented in this section.

2.1. Geometry and performance of the device

The set up for this device is the superstrate and the patch antenna as source as in Figure 3.21. As previously mentioned, a dual polarized patch antenna is used as a reference. The ground plane has the same size of the substrate. The size of the patch is 68.5*68.5 mm² with 14.03 mm of thickness. The substrate is Arlon AD 250 (ε_r =2.5). This antenna has up to 6 dB of RG, and its isolation level is better than 15dB. The maximum HPBW is 93 degrees for both planes in linear polarisation and 87° for a RHCP, for more details see the appendix A at the end of the document.

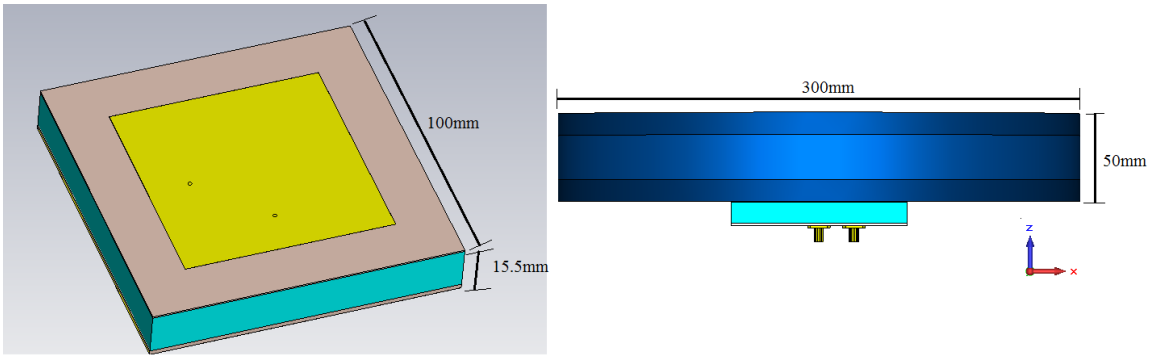


Figure 3.21 Two port reference patch antenna (left), side view of the final set up, antenna and superstrate (right).

In order to summarize the design process until this point, a fast recapitulation of the previous work is necessary. The method of extending a 2D profile of permittivity into a 3D structure is justified in Section 1.1. The profile that corresponds more adequately to our needs was set (Case c, horizontally inverted profile). Results from simulation in linear and RHCP polarisation were presented in order to analyse the farfield of this intermediate structure. In, Figure 3.17 the normalized gain (main lobe of the far field radiation pattern in two orthogonal planes) of the superstrate with different configurations at 1.2 GHz is presented, where the influence of avoiding the use of dispersive values of permittivity is analysed. The fact of replacing dispersive values below one by one did not affect the results in terms of HPBW, which is the reason that makes it possible to use only one material for the 3 layers. Followed by the structure made of Teflon, exhibiting its performances. A 26 % increase of HPBW is shown for the solution with periodic holes for both linear and circular polarisation. As high values are used, the band has shifted lightly to upper frequencies.

However, from this point FullCure is used as dielectric material for the superstrate. FullCure is a material used in 3D printers which has a relative permittivity ε_r =2.9 and ε_r'=0.25 and which is appropriate for our design. The values of permittivity are shifted and recalculated in Table 3.3 using the same methodology as for the Teflon superstrate keeping the volumetric factors for the air and the dielectric as in chapter two. The new range of permittivity goes from 2.1 to 2.9 and it is distributed along the structure as in Figure 3.16.

ε_{r1}	ε_{r2}	ε_{r3}	ε_{r4}	ε_{r5}	ε_{r6}	ε_{r7}	ε_{r8}	ε_{r9}
2.1	2.18	2.25	2.28	2.37	2.45	2.52	2.8	2.9

Table 3.3 Synthesized relative permittivity values required for the superstrate with FullCure.

The commercial software package CST Microwave studio is used to simulate the performances of the drilled device using FullCure as dielectric material. In Figure 3.22 the S parameters are presented, in order to observe the operating band, matching level and isolation in the structure.

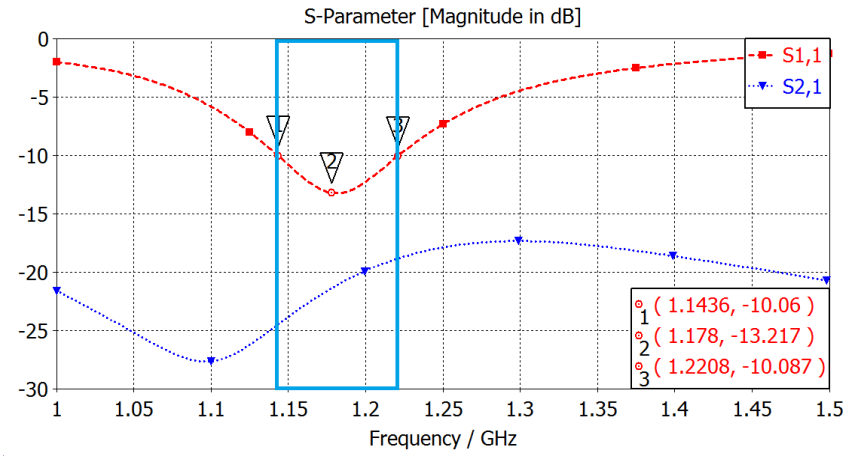


Figure 3.22 Reflection coefficient versus frequency for the FullCure superstrate.

The operating band in this structure is [1.14-1.23] GHz, which is slightly shifted from the original operating band of the reference antenna [1.16-1.24] GHz. This shift can be overcome by changing the distance between the antenna and the superstrate. Moreover, a variation of the ground plane can also be helpful to recover the operating band as we will see in the following sections.

The Figure 3.23 presents the radiation patterns in two orthogonal planes (phi = 0°and phi = 90°) at three frequencies (min, centre, max) of the operating bandwidth of the device when one port is fed (linear polarisation).

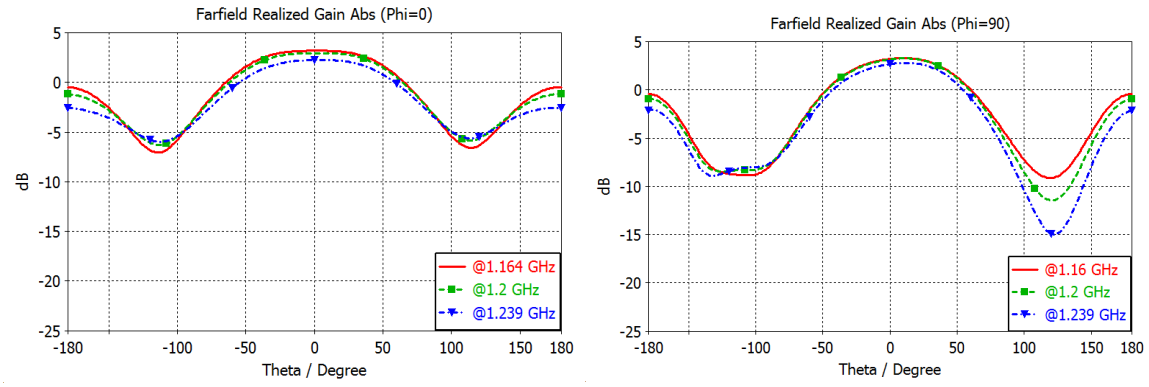


Figure 3.23 Radiation pattern at [1.164-1.239] GHz for phi=0° and phi=90°.

In terms of HPBW, the results do not change drastically: in the phi=0° plane, it goes around 126° to 127° while in the phi=90° plane, result goes from 103.4° at 1.24 GHz to 100.1° at 1.16 GHz. In the case of the RG, the results in the broadside direction show a variation of less than 1 dB in the phi=0° plane and less than 0.5 dB in the phi=90° plane along the different frequencies analyzed.

In order to summarize the results of the structure are as follows:

The structure has the following relevant dimensions: Thickness = 50 mm; diameter=300 mm

Bandwidth covered (VSWR < 2): [1.14-1.22] GHz.

Isolation: less than -15dB.

RG (φ=0°plane) from 2.92 to 3.34 dB

HPBW (φ=0°plane) from 125.2° to 126.3° and 100° to 102.6° for the other plane.

The radiation pattern performances are presented in Table 3.4:

	@1.164 GHz		@1.2 GHz		@1.239 GHz	
	φ=0°	φ=90°	φ=0°	φ=90°	φ=0°	φ=90°
Main Lobe Magnitude (dB)	3.3	3.3	3.3	3.4	2.9	3.0
HPBW	126.3	102.6	125.6	101.3	125.2	100

HPBW of Ref. Antenna.	95	88	94	87	93	85.7

Table 3.4 Radiation pattern performances in the operating bandwidth.

2.2. Optimisations in size and performance

Furthermore, the superstrate has considerable dimensions: at 1.2 GHz, the diameter is equal to 1.2 λ and the thickness is 0.2 λ. To evaluate if it's possible to reduce the size of the superstrate, the diameter and thickness are decreased and the resulting effect is studied. At 1.2 GHz, the wavelength λ is 250 mm so the superstrate diameter is decreased to this value, and a proportional reduction in thickness; hole diameter and radial distance.

2.2.1. Influence of diameter and thickness.

Influence of diameter

Many sizes were studied in order to find the limitations of the device in terms of performances while fulfilling the 3D printer specifications. In this section, the influence of varying the diameter is studied by performing simulations with three different structures where the diameter is decreased from 300 mm to 250 mm and 200 mm. In Figure 3.24 and Figure 3.25, the realized and normalized gain are presented in two orthogonal planes with a linear polarisation at 1.2 GHz.

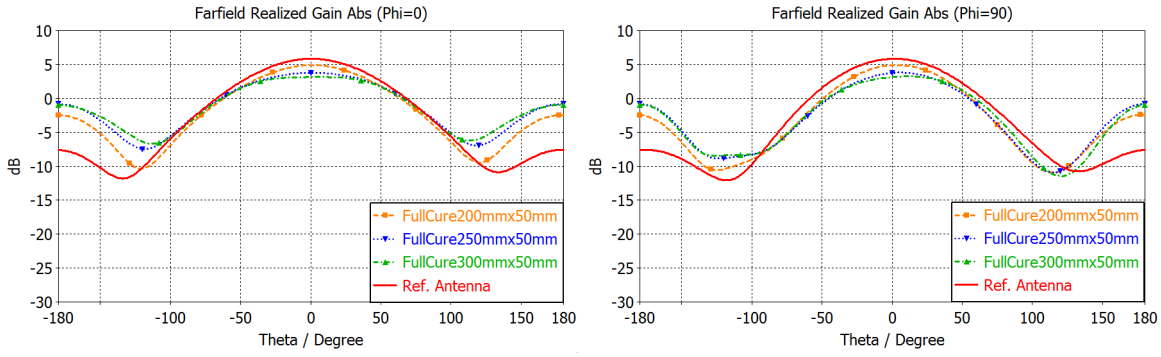


Figure 3.24 RG at 1.2 GHz for both planes for the different configurations with diameter variation of the superstrate.

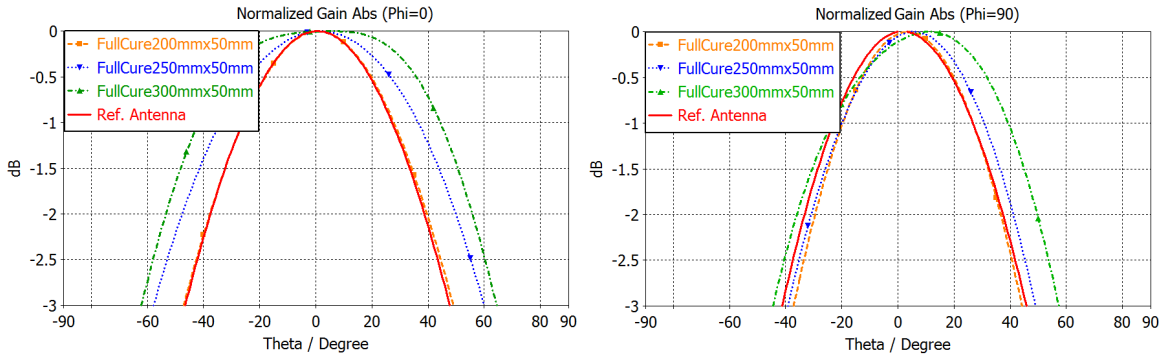


Figure 3.25 Normalized gain at 1.2 GHz for both planes for the different configurations with diameter variation of the superstrate.

Figures above show a small variation of the RG of less than 0.5 dB in cases where the structure has a diameter of 300 mm and 250 mm for both planes. In the case where the diameter is decreased to 200 mm, the gain increases almost of 1.5 dB compared to the 300 mm diameter structure, (reaching 4.9 dB of RG in the broadside direction). However, in terms of the HPBW, decreasing the diameter results in decreasing the HPBW: for example, in the 300 mm diameter structure, the HPBW is 126° and it decreases to 116° for the 250 mm diameter superstrate and even to 96° for the 200 mm diameter superstrate in the phi=0° plane. Results in the phi=90° plane have the same tendency for both RG and HPBW. Thus, it is possible to say that the diameter can be decreased until 250 mm (which is coincidentally the size of λ at 1.2 GHz) without a drastic change in HPBW (10°), which is our main concern for this application, considering the fact that 250 mm is the maximun size for an object that the 3D printer is able to produce.

Influence of thickness

Once the influence of varying the diameter of the device was studied, the same analysis is performed for the thickness of the superstrate. In Figure 3.26 and Figure 3.27, the realized and normalized gain at 1.2 GHz (linear polarization) for both planes are also presented keeping the diameter constant, the thickness is varied from 50 mm to 40 mm and to 30 mm.

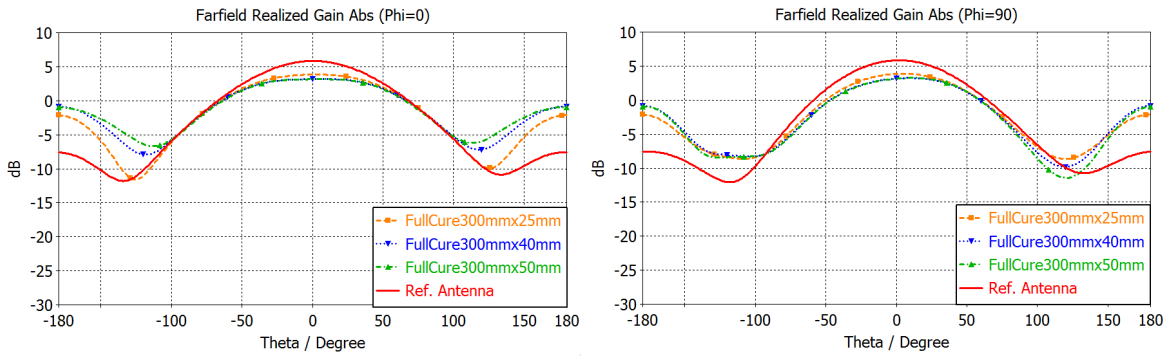


Figure 3.26 RG at 1.2 GHz for both planes for the different configurations with thickness variation.

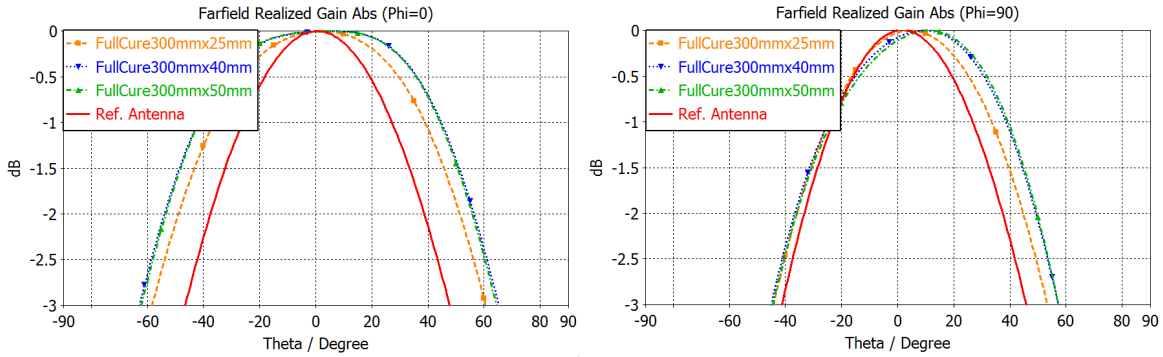


Figure 3.27 Normalized gain at 1.2GHz for both planes for the different configurations with thickness variation.

When the thickness is decreased, it is possible to notice a small variation of the RG (about 0.6 dB) between the three structures. Looking at the HPBW, the variation is pronounced. For the structure with 50 mm thickness, the HPBW is 126° in the phi=0° plane while the structures with 40 mm and 25 mm have 128° and 118° of HPBW respectively. The variation for both RG and HPBW have the same tendency in the plane phi=90°. It is interesting to notice that the structure with 40 mm thickness increases the HPBW of 2° compared to the original case (50 mm thickness), then, a structure with 40 mm thickness can become an interesting optimization.

Through this analysis (diameter and thickness variation) it is possible to notice that the best performing device is the original one, it means the structure of 300x50 mm². However in terms of performances, the structure with 40 mm of thickness is interesting because it presents a 20% reduction of the thickness while keeping the HPBW almost unchanged. In the other hand, the structure with 250 mm diameter is also interesting as it presents a 17% reduction of the diameter while a decrease of 7% of the HPBW. A structure with 40 mm of thickness and 250 mm of diameter can be very appropriate in order to reduce the size of our device regarding the realization of the final prototype.

2.2.3. Influence of ground plane

In this section the structure with 40 mm of thickness and 250 mm of diameter with a 100 x 100 mm² square ground plane is presented and compared to the case where the ground plane of the reference antenna is replaced by a circular plane of 600 mm diameter. This particular diameter is chosen keeping in mind the final size of the structure. This comparison is performed in order to analyse the influence of the ground plane in the device.

The circular ground plane of 600 mm diameter is analysed in this section because the set up for measurement of the device is close to this configuration. In addition, as this device aims to operate in airborne application, it needs to be simulated in a realistic environment because the supporting

structure of this device will be metallic surfaces of planes, aircrafts or fuselage. A circular metallic ground plane emulates perfectly this situation.

The comparison of the S parameters of both cases is presented in Figure 3.28. The influence of the circular plane is clearly observed, because a shift in the operating band is noticed. This shift in the frequency brings the operating band to the targeted band [1.16-1.22] GHz, however the matching level is slightly deteriorated.

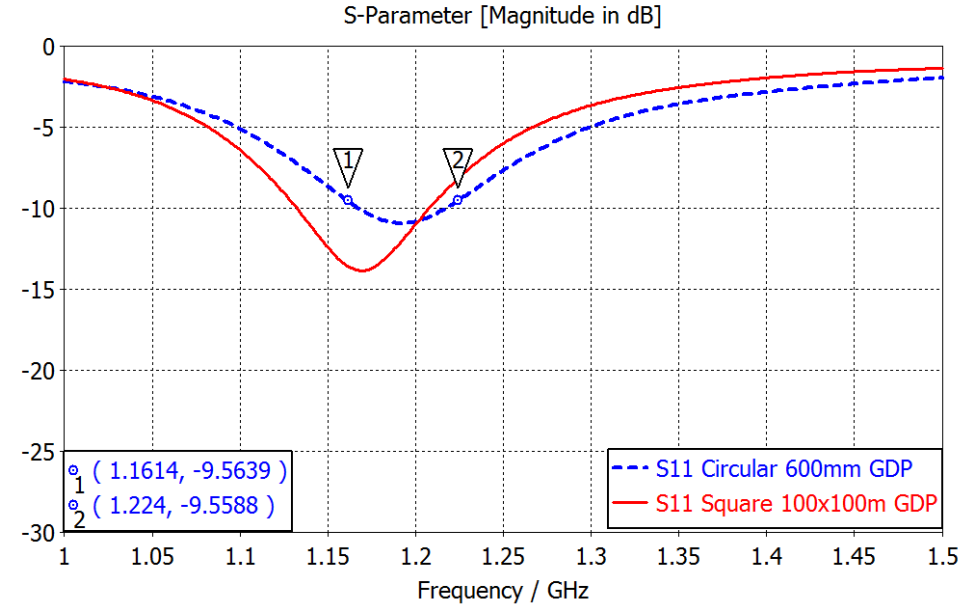


Figure 3.28 Reflection coefficient versus frequency for the FullCure superstrate both 600 mm diameter and 100x100 mm² ground planes. Linear polarization.

The radiation pattern is also compared in Figure 3.29 and Figure 3.30 for two orthogonal planes respectively. The farfield is clearly affected by the presence of the large ground plane, because a ripple appears in the broadside direction for both planes. In terms of the maximal gain, the difference is small (around 1dB) between the devices with the small square ground plane and with the 600 mm diameter circular ground plane. However, regarding the HPBW, the variation is more notable, the HPBW with small square ground plane goes from 113° to 120° while in the case where the circular ground plane is used HPBW decreases the range from 101° to 108° in the phi=0° plane. In phi=90° plane, the variation is similar in terms of gain and HPBW.

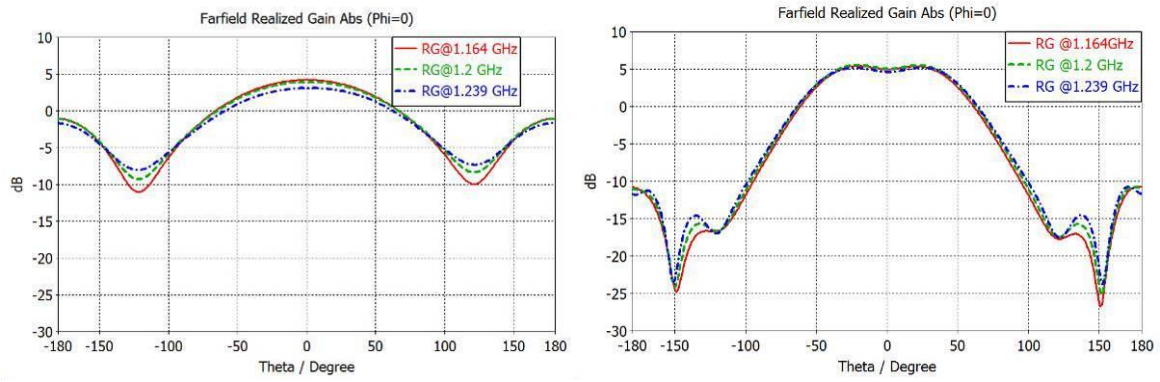


Figure 3.29 RG along the operating band [1.16-1.23] GHz (phi=0°) for both cases: with the 600 mm circular ground plane (left) and with the 100x100 mm² square ground plane (right).

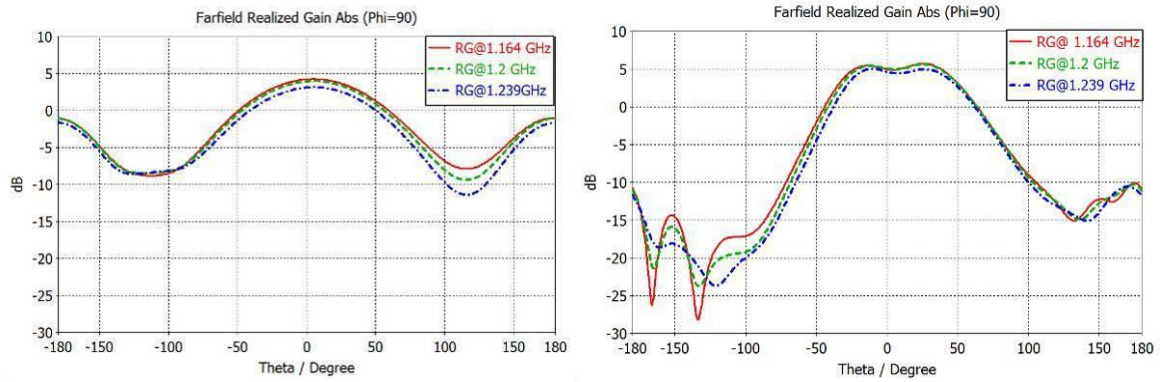


Figure 3.30 RG along the operating band [1.16-1.23] GHz (phi=90°) for both cases with the 600 mm circular ground plane (left) and with the 100x100 mm² square ground plane (right).

The HPBW of the antenna with the superstrate and the circular ground plane is increased by a maximum of 15% compared to the reference antenna, which is slightly lower than the case where the ground plane is a square of 100 mm x 100 mm. A bigger ground plane affects the contribution of the superstrate and results in a decrease of the HPBW.

3. Validation by measurements

As it was mentioned in the previous section, a validation with measurement results is presented. The objective of this validation is not to obtain the best performances otherwise to be used as proof of the concept. In this regard, a new superstrate has been designed, in order to reduce the overall size, with an external diameter of 250 mm and a thickness of 40 mm instead of a diameter of 300 mm and a thickness of 50 mm for the optimal design. This diameter (250 mm) has been chosen because it's the maximum allowed to be fabricated by the 3D printing machine and also because among the optimizations in size and performances this structure offers the best trade-off. The geometry of the updated superstrate is presented in Figure 3.31. In order to keep the antenna well matched, the gap

between the antenna and the superstrate is 5 mm and it is filled with a honeycomb layer with 300 mm of diameter. This is the final set up of the structure for measurement.

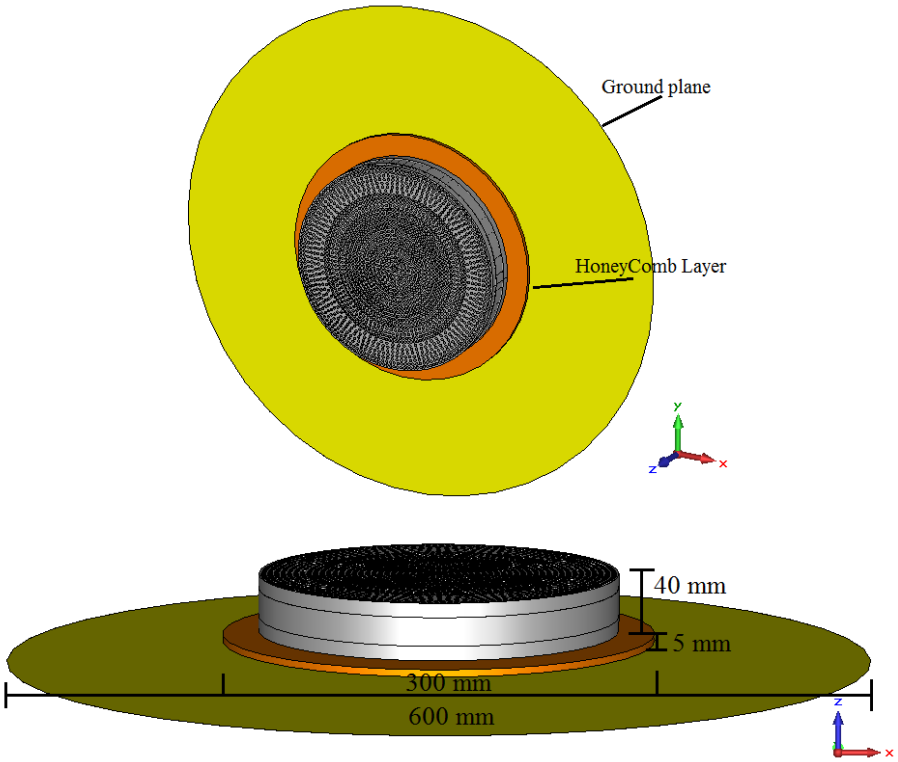


Figure 3.31 Perspective view and side view of reference antenna with 250 mm diameter FullCure superstrate and the honeycomb interlayer of 5 mm of thickness and 300 mm of diameter.

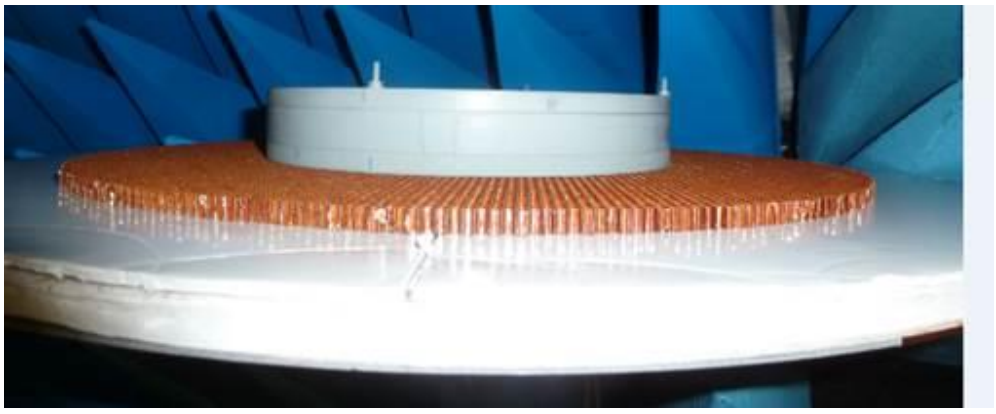


Figure 3.32 Realized reference antenna with the manufactured superstrate.



Figure 3.33 Superstrate composed by 3 printed dielectrics.

3D printing is an incredible versatile method for many mechanical applications; a design could be directly printed in 3D without the need of complex and heavy mechanical operations. The picture of the complete structure and the set up for measurement is presented in Figure 3.32, this structure was fabricated and measured at Airbus group innovation facilities in Suresnes Paris in March 2014.

3.1. S parameters

In this section, results are presented from measurement and simulation of the prototype described above. The simulated performances of the reference antenna with 250 mm diameter FullCure TE inspired superstrate have been obtained with CST Microwave Studio (Transient solver).

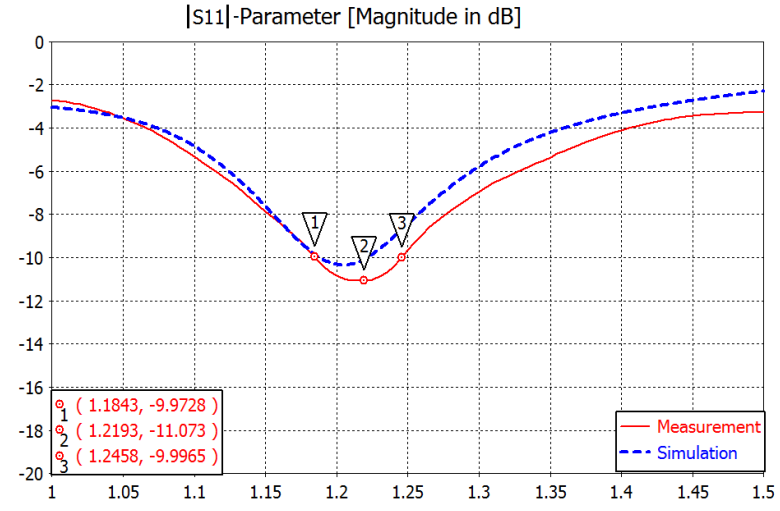


Figure 3.34 Reflection coefficient versus frequency using a -3dB coupler with a 90° shift.

The $|S_{11}|$ parameter comparison in Figure 3.34 shows a variation between measurement and simulation results. In the simulation results, the operating band is strongly reduced to [1.18 - 1.22] GHz while in the case of the measured structure the operating band goes from [1.18-1.24] GHz. There is some disparity between measurement and simulation results, this can be due to measurement set up. These values of minimum and maximum frequency are taken into account for the measurement of the farfield including 1.21 GHz as central frequency.

3.2. Farfield pattern analysis

The radiation patterns are presented in two orthogonal planes (phi = 0° and phi = 90°) at three frequencies (1.184 GHz, 1.21 GHz, 1.245 GHz) of the required bandwidth for every component of the radiation pattern E_{theta} and E_{phi}. The results from both measurement and simulation are normalized and compared in Figure 3.35 to Figure 3.40. Two planes are compared for E_{theta} and E_{phi}. The structure was simulated with a feeding in both ports and a 90° shift between them and the measured results used a -3 dB coupler with the same shift between the 2 ports.

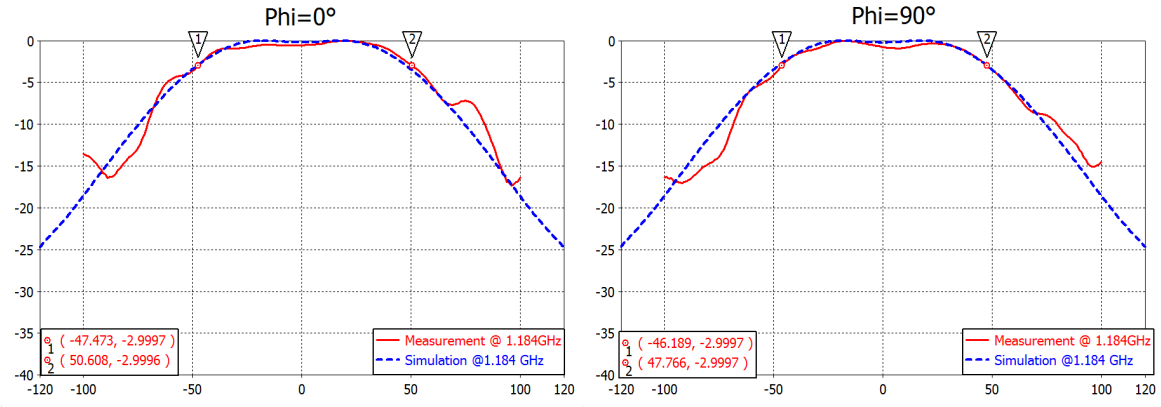


Figure 3.35 $|E_{phi}|$ Measurement vs Simulation at 1.184 GHz.

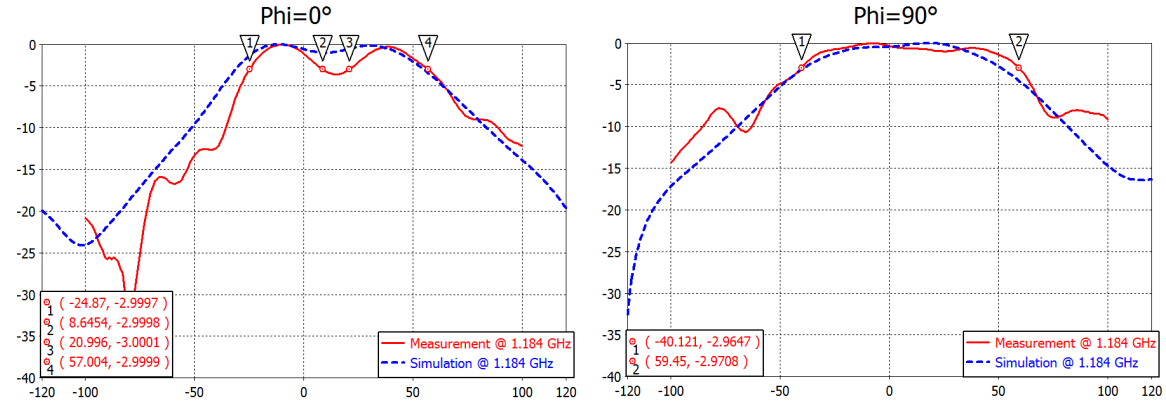


Figure 3.36 $|E_{theta}|$ Measurement vs Simulation at 1.184 GHz.

At the minimum frequency (1.18 GHz), there is an interesting agreement between simulation and measurement for both components. Only in the phi=0° plane for the E_{theta} component, an unexpected

ripple appears in the measurement results, even though the HPBW does not present a big variation (around 4° at best).

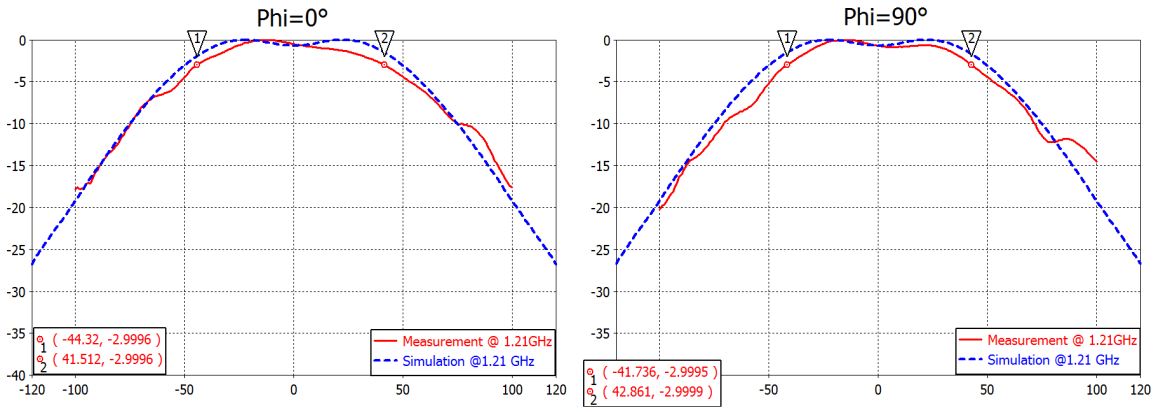


Figure 3.37 |E_{phi}| Measurement vs Simulation at 1.21 GHz.

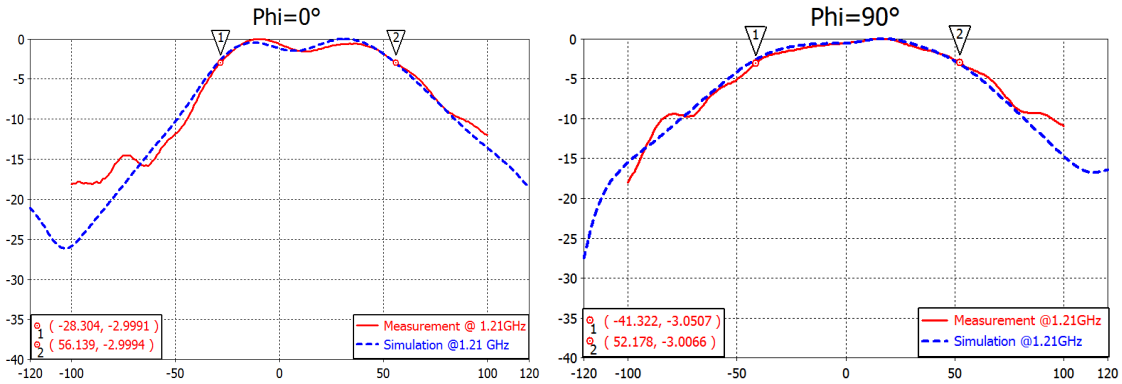


Figure 3.38 |E_{theta}| Measurement vs Simulation for 1.21 GHz.

At the central frequency, the HPBW is 99° for the E_{phi} component in the two orthogonal planes and 84° and 94° for the E_{theta} component for phi=0° and phi=90° planes respectively. In terms of variation between results of measurements and simulations, the difference does not exceed 3°. For the 4 plots, the resemblance in HPBW is quite remarkable.

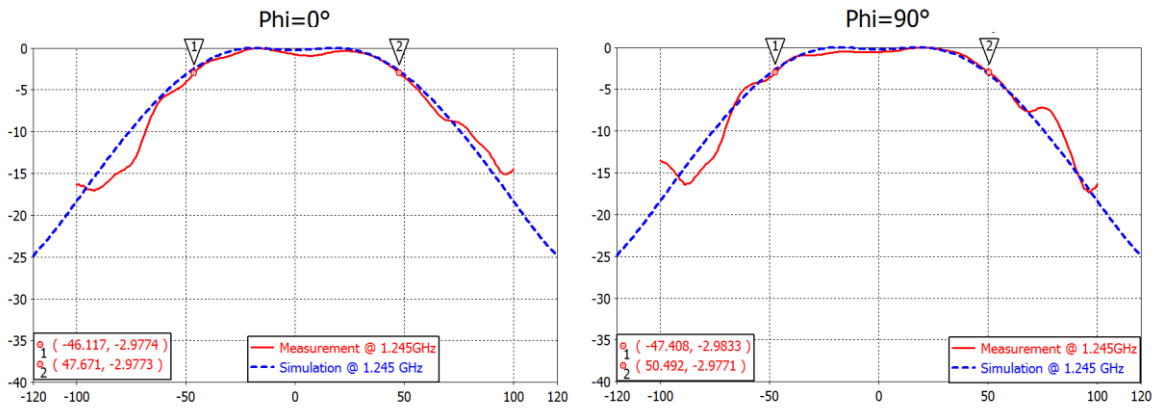


Figure 3.39 |E_{phi}| Measurement vs Simulation for 1.245 GHz.

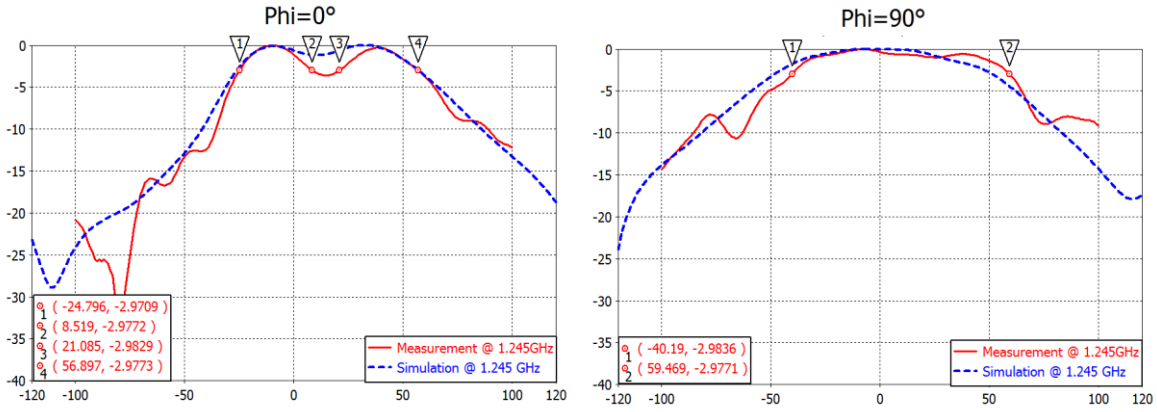


Figure 3.40 $|E_{theta}|$ measurement vs simulation for 1.245 GHz.

Finally, at the maximum frequency of the operating band, results from the four figures show nice agreement between measurement and simulation. Normalized gain results are quite similar between measurement and simulation. Moreover, in terms of HPBW, both results present almost the same values, maybe except the values of E_{theta} in phi=0° and phi=90° where the values from measurement present lower values of HPBW. Regarding the RG, this difference of 2 dB is always observed between measurement and simulation results in the operating band [1.184-1.245] GHz.

The HPBW is increased by 18% compared to the reference antenna, which is very promising for a structure that does not have the optimum size and also because it validates the principle of the design.

Although the superstrate is a complex structure, a nice agreement between simulation and measurement results is visible. The simplicity and compatibility of using CST simulation layout in the 3D printer is quite remarkable. The geometry files are accepted as input in the 3D printer.

4. Conclusions.

To summarize the work discussed in the chapter, an all-dielectric superstrate is proposed in order to increase the HPBW of a low profile planar antenna. This superstrate is a modification of another TE application that aims to increase directivity. Once the modified profile was extended into a 3D structure, the influence of the dispersive values in the performance of the device was analysed. The influence of varying the values of permittivity was analysed as well. A first objective was to synthesize a drilled structure made of Teflon to show a varying permittivity to obtain the desired performances. A second objective was to show the feasibility of this structure with a 3D printer and adapting the design to the requirements of the printer. The influence of varying dimensions and ground plane over the performances of this FullCure superstrate made it possible to carry out optimisations. Finally a 250x40 mm² superstrate was realized on a 3D Printer and was measured to prove the validity of the concept. A nice agreement between measurement and simulation results was observed.

An All-dielectric superstrate can be designed by using modified structures inspired by Transformation Electromagnetics. An increase of about 26% of the HPBW has been demonstrated for the latest prototype.

Then, a key point is the reduction of the size in TE devices. The TE devices lost their behaviour when the size is near or under a wavelength. An important challenge is to search for methods of reducing the size.

The all-dielectric structures are an interesting alternative when the bandwidth is important. The method of drilling holes is quite efficient in order to achieve the range of permittivity values needed for the TE design. However, this method can be improved by taking into account other parameters such as elastics deformations and other techniques of permittivity synthesis in [44].

Many optimizations have been performed to enable realization, and the comparisons of all performances are performed in order to find the best performing device, which is simple to fabricate as well.

The major objective of this work was to design a TE inspired superstrate that will be fabricated in order to proof the concept. The objective was not to obtain the best performances, however for the 40x250 mm² structure it's possible to conclude that:

- TE inspired superstrates can increase the HPBW of an antenna.
- Increasing the thickness of the superstrate to 50 mm slightly leads to band shifting towards lower frequencies. However, the superstrate of the 40 mm thickness is more interesting due to the reduction in size while keeping good performances.

- Increasing the gap between the patch and the superstrate from 2 mm (Teflon superstrate) to 5 mm (FullCure superstrate with honeycomb layer) enables to minimize the frequency band shift due to the change of permittivity from 2.2 to 2.9 (FullCure).
- A large ground plane affects the performances of the antenna with superstrate.
- The 600 mm diameter circular ground plane reduces the operating band from [1.133-1.21] GHz to [1.16-1.22] GHz (Linear polarisation).

The circular ground plane also affects the radiation pattern in the broadside direction of the antenna: the realized gain is increased and consequently the contribution of the superstrate is minimized.

For optimal performances, the optimisation of the device should be done on the entire antenna, i.e. with the superstrate and the large ground plane

Chapter 4
Antipodal Radiation from Superstrate and a Patch Antenna

The two previous applications aimed to control the radiation pattern of an antenna by improving directivity in the case of the flat reflector and increasing the HPBW in the case of the dielectric superstrate. These applications kept a simplistic approach towards fabrication. In this chapter, another attempt to control the propagation of a radiating element is presented. This time, the application aims to create an antipodal radiation using a patch antenna and a planar superstrate.

This application is oriented to work in airborne applications, where the geometry is crucial. Low profile antennas are highly appreciated in this domain because of their trail reduction and consequently decreasing consumption. Antennas on an aircraft have to respect the aerodynamics of the supporting structure and they need to be as conformal as possible, trying to not be protruding. But conventional planar conformal antennas present a broadside radiation as an intrinsic characteristic. Therefore, it could be very interesting if these antennas could radiate in directions other than the broadside. Transformation Electromagnetics is a powerful technique that can be employed to control wave propagation. In this regard, the antipodal radiation can be achieved by using TE, in other words to make the antenna radiate towards the side of the antenna (±90° direction).

This work aims to show the design and performances of a flat superstrate placed above a patch antenna that operates between [1.16-1.24] GHz (L band). Obtained from the Transformation Electromagnetics (TE) technique, this superstrate enables to produce an antipodal radiation with a quasi-null radiation in the broadside direction while keeping the original antenna performances almost unchanged. From the analytical transformations used for the calculation of the constitutive parameters, both permittivity and permeability profiles of the superstrate can be deduced. The field distribution and radiation patterns of the whole structure confirm the antipodal radiation behaviour.

First, the principle of the design of the superstrate and the analytical transformations are shown. Then the description of the 2D and 3D designs and the corresponding simulations results are presented for discussion and analysis. Finally conclusions are drawn at the end of the chapter.

1. Device description

In this section, it is necessary to start with the analytical transformations which are presented on a 2D structure in order to simplify the design process. Then, as it was studied in the previous chapters, this 2D structure is rotated around *x* axis to create the complete 3D structure that is used for simulations.

1.1. Analytical Transformations

The design principle for the 2D superstrate is presented in Figure 4.1. Two spaces are described. We notice that the virtual space is divided in two symmetrical parts. Each one of these parts transform the flat rectangular space in Figure 4.1-a into a shifted elliptical curved space in Figure 4.1-b.

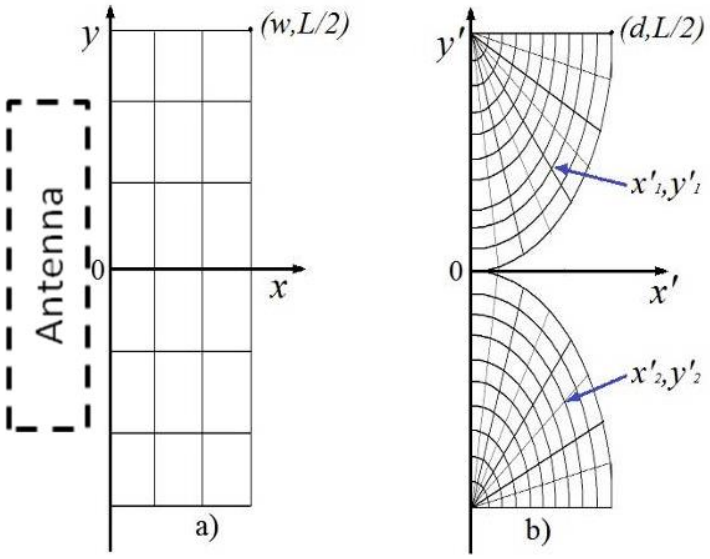


Figure 4.1 *L* = 200 mm, *d* = 37.5 mm, w = 37.5 mm, *a* = 2 (compression factor). a) Real space. b) Virtual space.

Equation 4.1 describes the transformation, both *x* and *y* coordinates are transformed. The Figure 4.1 indicates that a flat rectangular space is transformed into two semi elliptical spaces which direct the wave propagation towards the sides of the structure.

$$x'_{1,2} = \frac{w}{d}\sqrt{(ax)^2 + \left(y \mp \frac{L}{2}\right)^2}\ , \quad y'_{1,2} = \frac{L}{\pi}\tan^{-1}\left(\frac{y \mp \frac{L}{2}}{ax}\right) \qquad \textbf{(4.1)}$$

These two shifted semi elliptical transformations are proposed as a modification of two opposed semi circles compressed in *x* direction. The centre of these compressed circles are located at $y=\pm L/2$. Each semi elliptic structure has $L/2$ as a semi major axis and *d* as a semi minor axis while the thickness *w* and the length *L* define the flat structure. The length is kept equal to the major axis (twice

the size of the semi major axis) along the two spaces in order to simplify the process. The factor *a* is used to adjust the compression of the semi circles. This compression is performed and described in more detail in [85].

The calculations for the constitutive parameters are performed using Transformation Electromagnetics technique. The expressions in Equation 4.2 for the permittivity and permeability allow calculating the tensors for both parameters, where *A* represents the Jacobean matrix for the transformation.

$$\varepsilon'_{1,2} = \frac{A\varepsilon_0 A}{\det(A)}; \qquad \mu'_{1,2} = \frac{A\mu_0 A}{\det(A)} \tag{4.2}$$

$$A = \begin{pmatrix} \frac{\partial x'}{\partial x} & \frac{\partial x'}{\partial y} & \frac{\partial x'}{\partial z} \\ \frac{\partial y'}{\partial x} & \frac{\partial y'}{\partial y} & \frac{\partial y'}{\partial z} \\ \frac{\partial z'}{\partial x} & \frac{\partial z'}{\partial y} & \frac{\partial z'}{\partial z} \end{pmatrix} \tag{4.3}$$

The resulting tensors for both MPs are presented in Equation 4.4 and 4.5. At this point of the design process, both MPs tensors have all components, except the components related to *z* coordinate which is logical due to fact that z keeps untransformed.

$$\varepsilon'_{1,2} = \begin{pmatrix} \varepsilon_{xx}^{1,2} & \varepsilon_{xy}^{1,2} & 0 \\ \varepsilon_{yx}^{1,2} & \varepsilon_{yy}^{1,2} & 0 \\ 0 & 0 & \varepsilon_{zz}^{1,2} \end{pmatrix} \tag{4.4}$$

$$\mu'_{1,2} = \begin{pmatrix} \mu_{xx}^{1,2} & \mu_{xy}^{1,2} & 0 \\ \mu_{yx}^{1,2} & \mu_{yy}^{1,2} & 0 \\ 0 & 0 & \mu_{zz}^{1,2} \end{pmatrix} \tag{4.5}$$

Moreover, if an Ez-polarized incident wave is used to illuminate the designed flat structure (electric field along the *z* direction), only the components μ'_{xx}, μ'_{yy} and ε'_{zz} contribute to the design which by the way only depends on *x'*. In that case, the permittivity and permeability become as Equations 4.6.

$$\mu_{xx}^{1,2} = \frac{\pi . x'_{1,2}}{L} \qquad \mu_{yy}^{1,2} = \frac{1}{\mu_{xx}^{1,2}} \qquad \varepsilon_{zz}^{1,2} = a\frac{d\pi}{wL}x'_{1,2} \tag{4.6}$$

It is also needed to simplify the permittivity and the permeability tensors in order to achieve a realistic material profile as in [20], [60] and [68]. Considering a=2 and d=w, the reduced set of components of the permittivity and permeability tensors is shown in Equation 4.7.

$$\mu_{xx}^{1,2}=1 \qquad \mu_{yy}^{1,2}=\left(\frac{L}{\pi.x_{1,2}^{'}}\right)^2 \qquad \varepsilon_{zz}^{1,2}=4\left(\frac{\pi}{L}x'_{1,2}\right)^2 \quad \textbf{(4.7)}$$

Finally these expressions for permittivity and permeability are used for the next step of our design, simulations with Comsol Multiphysics to determine the electromagnetic behaviour.

1.2. 2D structure

As previously mentioned, the components of the tensors of constitutive parameters are reduced to $\mu'=diag(\mu_{xx}, \mu_{yy}, 1)$ and $\varepsilon'=diag(1,1\ \varepsilon_{zz})$ these are the only non-zero values because of the considerations that were taken into account in the design process. The range of values and the spatial variation of MPs are shown in the profile in Figure 4.2. It is noticed that values for permittivity goes from 1 up to 15 and permeability from 0.3 up to 3. In the first preliminary profiles, values went up to 40 for the permittivity and down close to 0 for the permeability, some of these values were truncated in order to keep the values of permittivity realisable [79]. These high values were located in very small regions of the profile, for example the high values for the permittivity were located in a small region in the centre of the left side of the profile; as it is shown in Figure 4.2-a. In the case of the permeability, high values are located in the upper right side of the profile as seen in Figure 4.2-b.

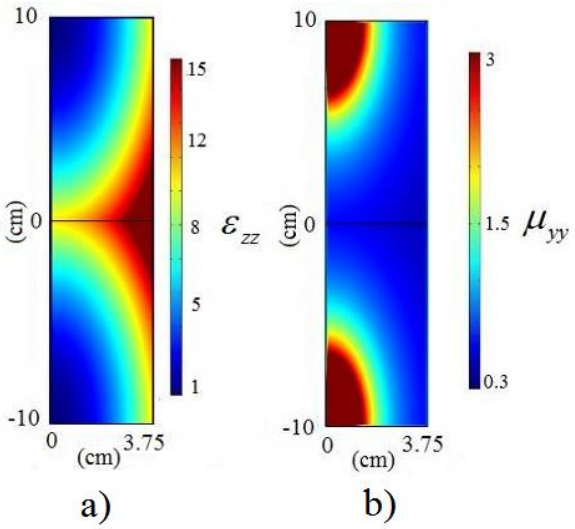


Figure 4.2 a) Component ε_{zz} from permittivity tensor. b) Component μ_{yy} from permeability tensor.

In order to evaluate the electromagnetic behaviour of the device, the electric near field is analyzed at 1.2 GHz. Comsol Multiphysics is used to perform simulations where it is possible to define an anisotropic and inhomogeneous material such this one. Other commercial softwares do not allow to define permittivity and permeability as tensors depending on the coordinate systems.

The antenna is modelled by a distribution of surface currents, a PEC ground plane and a dielectric. The normalized electric field distributions *Ez* for the 2D structure for the antenna model without and with TE based superstrate are presented in Figure 4.3 and Figure 4.4 respectively.

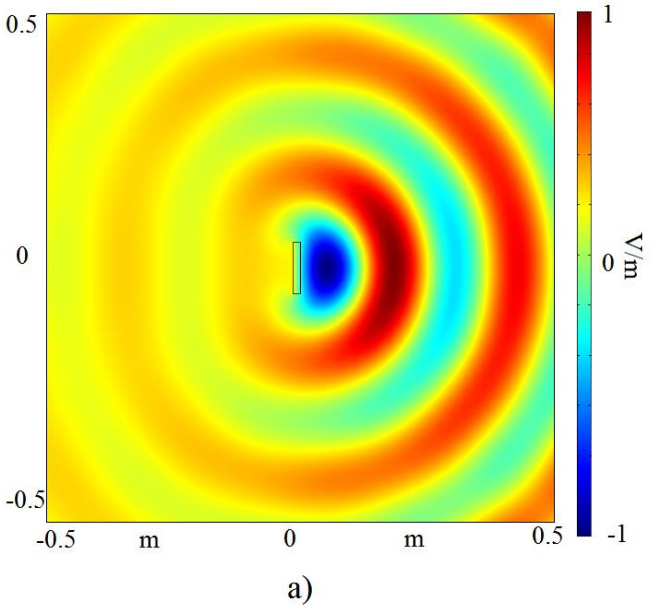


Figure 4.3 2D Simulation of *Ez* field distribution at 1.2 GHz for the antenna model only.

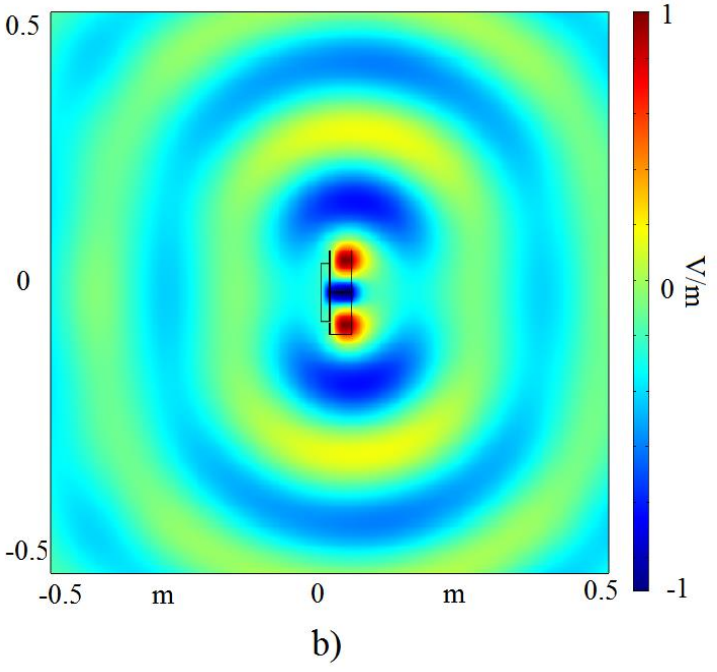


Figure 4.4 2D Simulation of *Ez* field distribution at 1.2 GHz for antenna model with TE based superstrate.

It is observed in Figure 4.3 that the patch antenna, modelled with a distribution of surface currents presents a directive radiation as expected, the electric field propagation being directed towards the

broadside. In Figure 4.4, when the TE based superstrate is placed over the antenna, the electric field is split in two and propagates towards the sides of the antenna exhibiting clearly a nice antipodal radiation.

2. Impedance matching

In order to confirm the performances of the device, the radiation pattern of the antenna obtained with or without superstrate, has been calculated with CST Microwave Studio. A probe fed patch antenna has been designed in order to work in the L band with the superstrate. This low profile antenna is similar to the reference antenna used in chapter three (detailed in appendices) with modifications in the patch size in order to keep the operating band of the antenna in the targeted frequency. In this case, the antenna substrate is a 100*100 mm² square with 15.5 mm of thickness and the size of the patch is 65.5*65.5 mm². The substrate is Arlon AD 250 (ε_r = 2.5) and the ground plane has the same size as the substrate.

The 3D TE based structure with the patch antenna is simulated using the discretized values of the constitutive parameters ε_{zz} and μ_{yy} shown in Figure 4.5. It means that the profiles for both permittivity and permeability are divided into blocks of constant value (the average value of ε_{zz} and μ_{yy}), and these 2D blocks are then converted into 3D concentric rings. Therefore, three multi-annular layers constitute the superstrate using the method presented in section 1.1.1 of chapter 3.

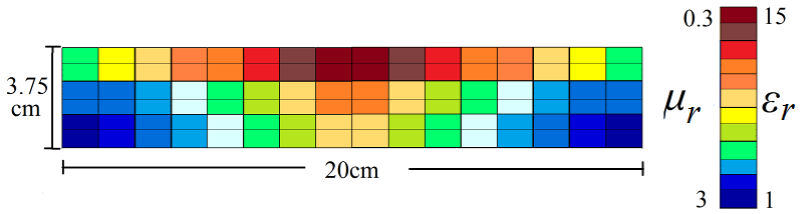


Figure 4.5 Discretized profile for relative permittivity and permeability.

Next, this superstate is placed above a patch antenna and different configurations are explored in order to obtain a adequate impedance matching between the patch antenna and the superstrate in the desired frequency band [1.16-1.2] GHz which is reduced (compared to the original band [1.16-1.24] GHz) because of the influence of the superstrate as it is explained later. In Figure 4.6, the magnitude of the input reflection coefficient of the complete structure is presented for these different configurations. The reference antenna is presented with other configurations for the superstrate combined with the antenna, such as: the antenna and the superstrate in direct contact (no intermediate layer); the antenna and the superstrate with 10 mm of spacing in between; the antenna with the superstrate with an intermediate layer of 5 mm and 10 mm of thickness.

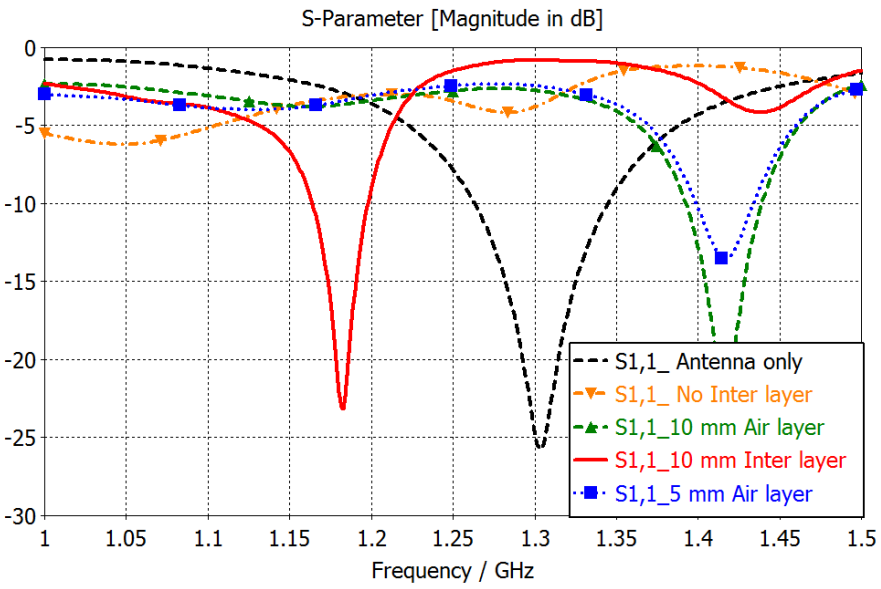


Figure 4.6 Magnitude of reflection coefficient of the complete structure with different configurations.

First, we observe that the antenna without superstrate is matched around 1.3 GHz exhibiting an operating band between [1.26-1.34] GHz. It is noticed that the impedance matching of the complete structure without any inter layer is clearly affected in the operating band by two major causes. The first one is that there are high values of permittivity and low values of permeability in direct contact with the radiating surface. The second factor is the discretization of the continuous values of the constitutive parameters (ε and μ) that introduces reflections between each layer. If the full continuous expression for the permittivity and permeability tensor would have been used without any approximation and reduction, the impedance matching would not be compromised.

Adding an air layer between the antenna and the superstrate helps to recover an operating bandwidth but it is shifted to higher frequencies than the targeted one. Finally, a transition layer of 10 mm thickness and a relative permittivity ε_r = 4 is placed between the patch antenna and the superstrate to obtain the desired frequency band. This layer increases the thickness of the whole device from 53 mm to 63 mm for the final structure.

3. Complete structure study

In Figure 4.7, the *Ez*-Field distributions of the patch alone and of the complete structure are presented in their operating frequency band. It is observed how the electric field travels towards the side of the structure thanks to the superstrate, instead of travelling in axial direction.

The radiation pattern performances and electric field distribution of the antenna at 1.3 GHz are presented because it is the resonance frequency of this antenna, while in the antenna combined with

the superstrate is studied at 1.2 GHz because this frequency corresponds to the targeted operating band [1.16-1.2] GHz.

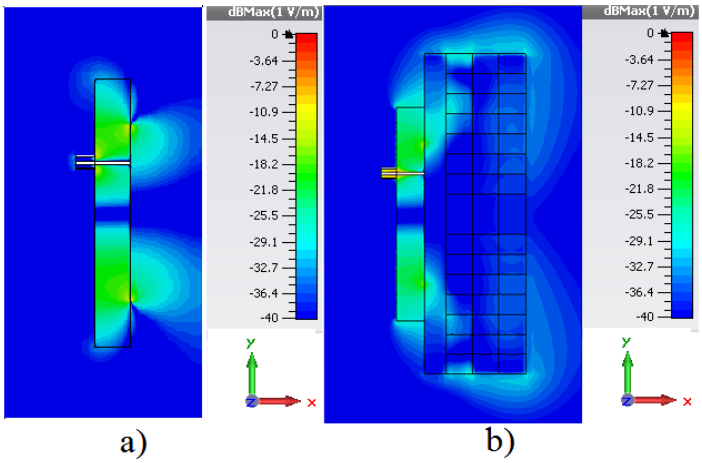


Figure 4.7 a) *Ez* Field Distribution at 1.3 GHz for the patch only and b) *Ez* Field Distribution at 1.2 GHz for the complete structure.

3.1. Radiation Pattern Analysis

In order to highlight the performances of the complete structure, the 3D radiation patterns obtained from CST Microwave Studio are presented in Figure 4.8 with and without superstrate. In Figure 4.8-a, the radiation pattern of the patch antenna calculated at 1.3 GHz shows that the radiation pattern is maximum at 0° (broadside) with a RG of 4.2 dB and -8.5 dB at ± 90°.

In Figure 4.8.b, the antenna and the TE device produce an antipodal radiation pattern at 1.2 GHz with two main beams along the sides, with a maximum RG of 3.5 dB at ± 89° and -14.9 dB in the broadside direction.

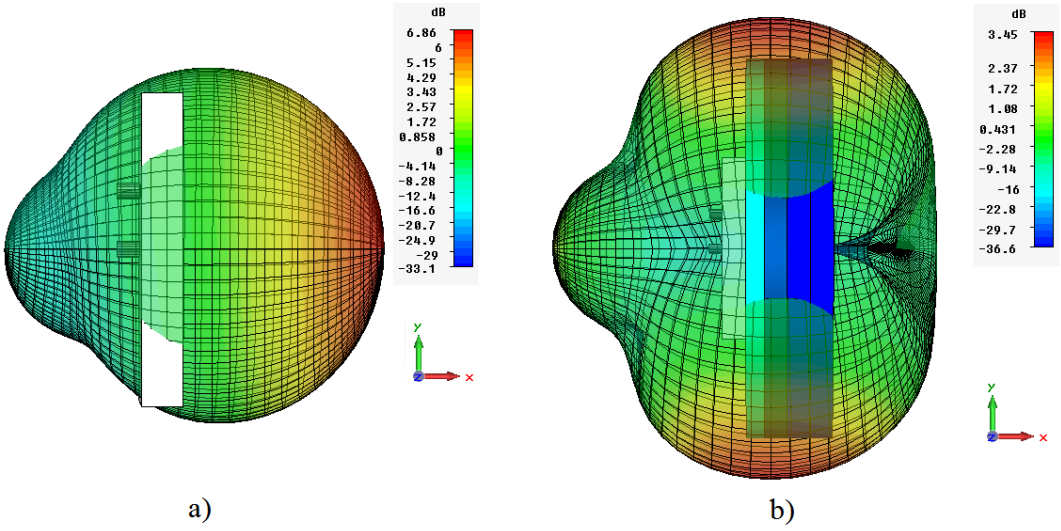


Figure 4.8 Magnitude of the RG for: a) Patch only at 1.3 GHz and b) Patch with TE based superstrate at 1.2 GHz.

The co-polar and cross-polar components of the RG in the two main planes of the antenna (*phi*=0° and *theta*=90°) are presented in Figure 4.9. In the plane *theta*=90°, the two main lobes are close to the antipodes and a third lobe in the *phi*=180° direction is also present with a lower level (-2.2 dB compared to the main lobes).

In the other plane *phi*=0°, the radiation pattern is strongly directed backwards. It presents 1.3 dB of RG in the main direction (*theta* =274°). Two other lobes are directed to 12° and 133°. They are quite asymmetrical compared to the ones in the other plane, this can be due to the position of the port in the antenna feeding. The level of cross-polar component is very low for both planes.

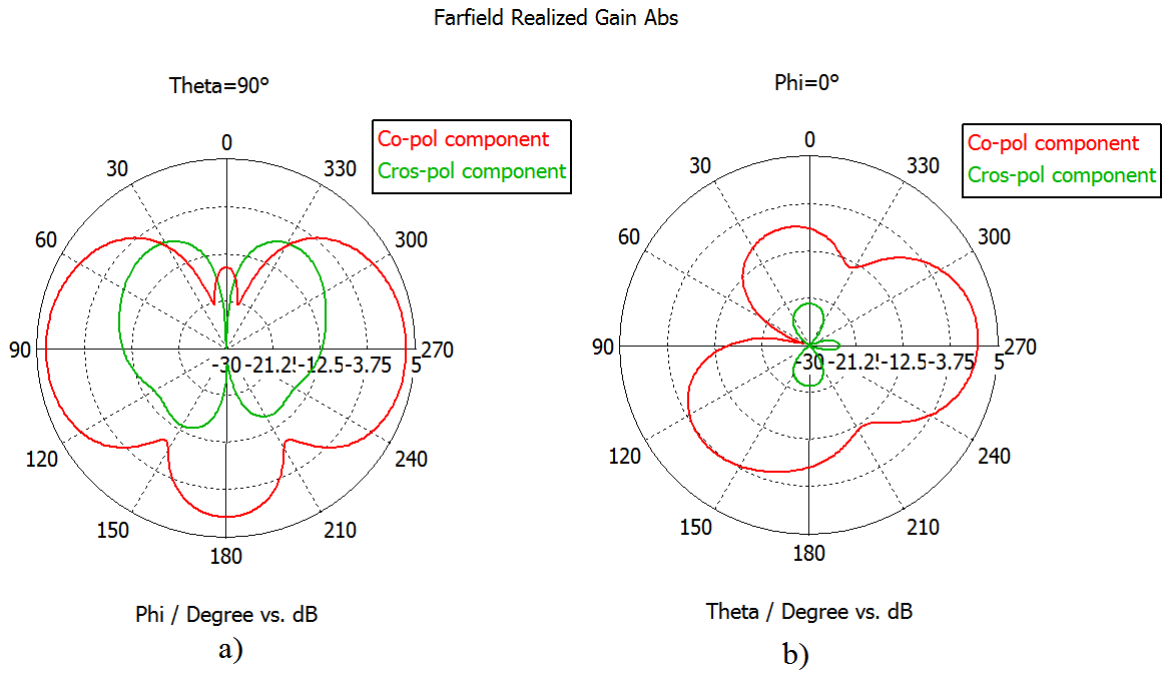


Figure 4.9 Co-polar and cross-polar components of the RG in the two main planes of antenna at 1.2 GHz (centre frequency). a) *theta=90°*. b) *phi=0°*.

3.2. Influence of the feeding configuration.

The performances presented in the last section were calculated with a linear polarisation and these performances shown the possibility to obtain an antipodal farfield pattern in one plane. However, the antenna can be fed with two ports. It could be quite interesting to feed the antenna using the two ports in order to achieve an omnidirectional radiation. In this regard, it is possible to follow two approaches: First, the two ports of this antenna are fed simultaneously in phase (linear polarisation). Then, the ports are fed with a 90° phase and a hybrid coupler. As previously mentioned, the antipodal radiation is very clearly observed in only one plane (*theta=90°*) when the antenna is fed only by one port and the other being connected to a 50 Ohms load. With these different feeding configurations, both ports may produce an antipodal radiation in both planes (*theta=90°* and *phi=0°*).

Simulations are performed to calculate the S_{11} parameters and presented in Figure 4.10 to analyze the effect of the different feeding configurations over the operating band and the resonant frequency of the device.

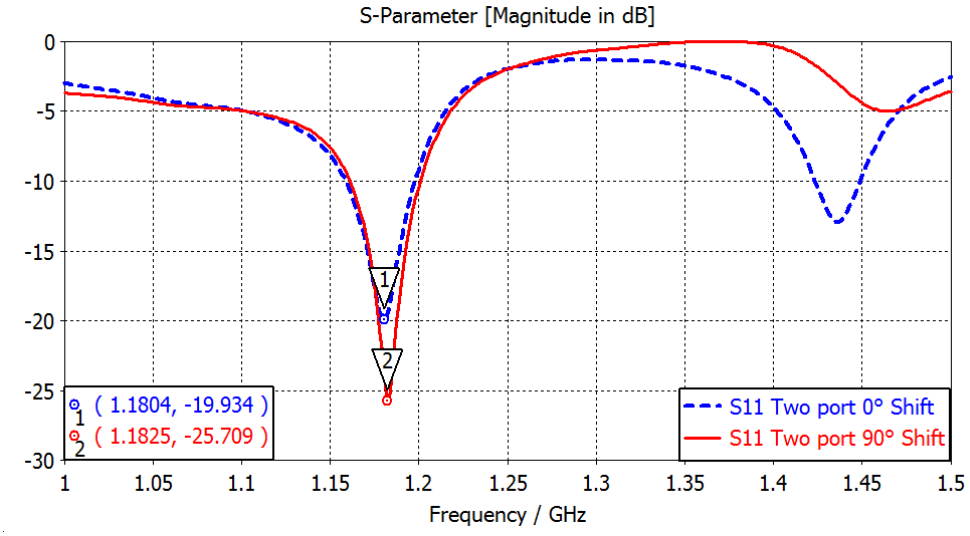


Figure 4.10 Magnitude of the input reflection coefficient of the structure with different feeding configurations.

As expected the operating band is almost the same for both cases. From the S parameter results, it is possible to obtain the resonant frequency: 1.18 GHz, then this frequency can be used in the calculation of the farfields shown in Figure 4.11.

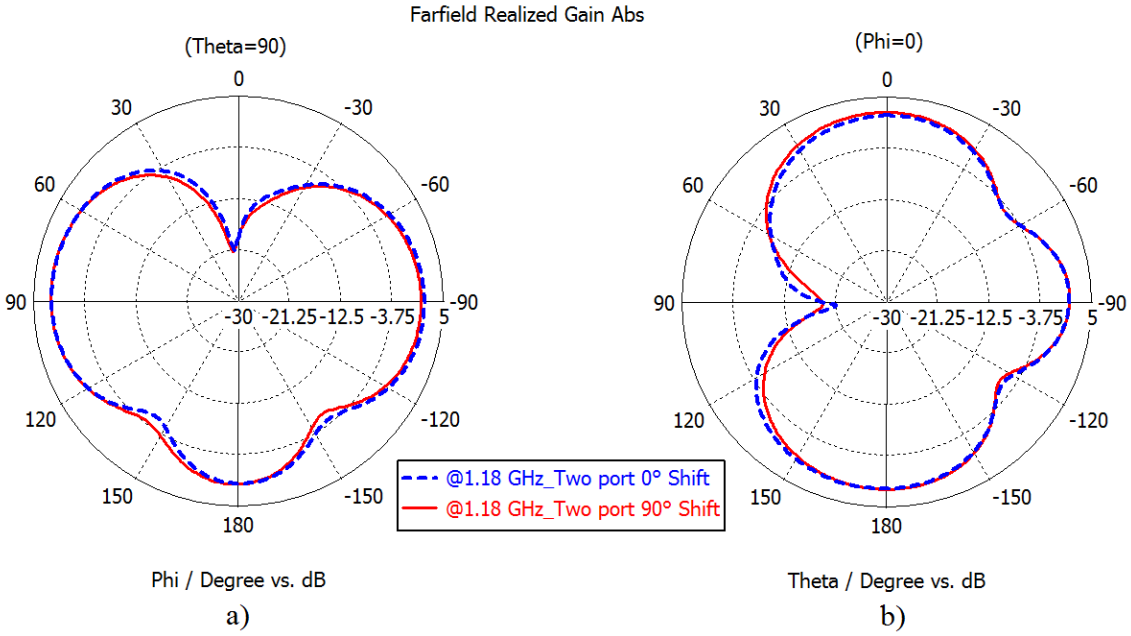


Figure 4.11 RG in the two main planes of the antenna and the superstrate for different feeding configurations at 1.18 GHz. a) *theta=90°*. b) *phi=0°*.

For both planes, the antipodal radiation is clear in the two feeding configurations that were calculated. In the *theta=90°* plane, the RG towards ±90° direction is 2.0 dB for the configuration with 90° shifting meanwhile it is 1.9 dB for the 0° shifting configuration. Although the shape of the farfield still includes 3 beams (one backward) and the antipodal radiation exhibits quite nicely, the real difference between these configurations is observed in the phi=*90°* plane in Figure 4.12.

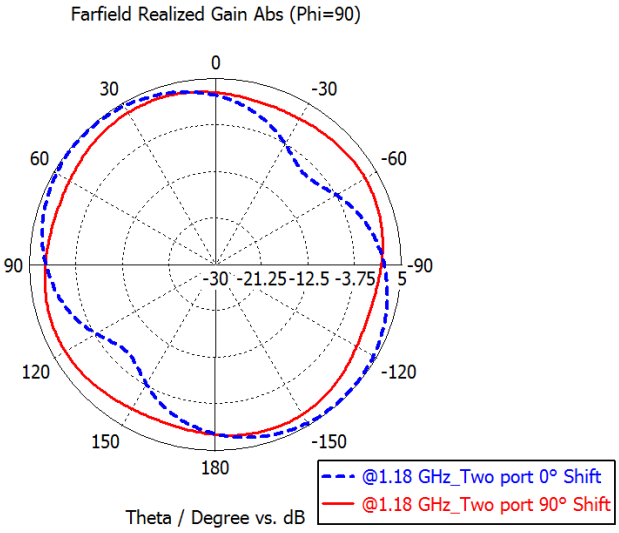


Figure 4.12 RG in the *phi=90°* plane of the antenna and the superstrate for different feedings configurations at 1.18 GHz.

The 90° shifting configuration exhibits a quasi isotropic radiation in this plane formed by four small beams and presenting a maximum RG of 3 dB at *theta=23°* direction. Two main beams are formed in the configuration with 0° shifting, presenting a maximum RG of 4.7 dB in *theta =46°* direction. For more detail the 3D radiation is presented in Figure 4.13.

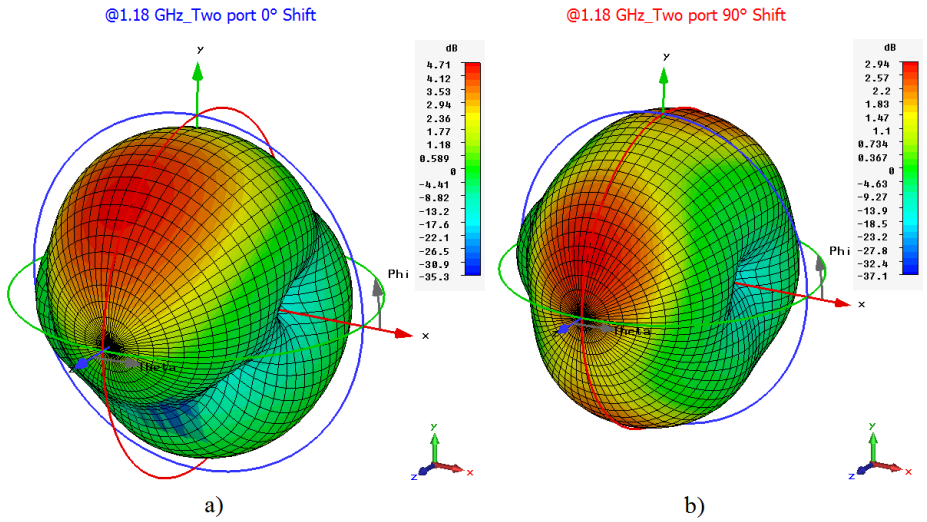


Figure 4.13 3D Farfield pattern at 1.18 GHz for: a) Device fed in two ports without shift, and b) Device fed in two ports fed with 90° shifting.

As it becomes clearer in Figure 4.13, the configuration without any shift exhibits an antipodal radiation shifted at 46° compared to the original case, while the configuration with the 90° shifting disperses the antipodal radiation in 4 small beams achieving a radiation pattern that slightly resembles a dipole pattern.

4. Sensitivity to the value of the maximal relative permittivity

As a large range of values of permittivity are needed for this application, a study of their influence on the performance of the device is presented, with restrictions and reductions applied. The first parameter to study in this case is the permittivity, two variations to the original device are proposed. The first study is when the range of relative permittivity values is truncated from 15 to 12.5; it means that the range of values is changed. Instead of [1-15] in the original profile, the new range of values for the first modification is [1-12.5] (max-1 in Figure 4.14). The same logic assumption is made for the second study using the maximum permittivity allowed in the device to be 10(max-2 inFigure 4.14). All values of permittivity over 12.5 or 10 in the profile are replaced while keeping the values of permeability unchanged.

Higher values of permittivity are a problem for the realization of this device, because in nature it is very difficult to find materials with high values for the permittivity. Even if they are found, it is very complicated to work with these materials. This is the reason to truncate the higher values of permittivity.

First, to observe the effect of these variations on the performances of the TE device, we start with the S parameters in Figure 4.14 to observe the operating band and the resonance frequency.

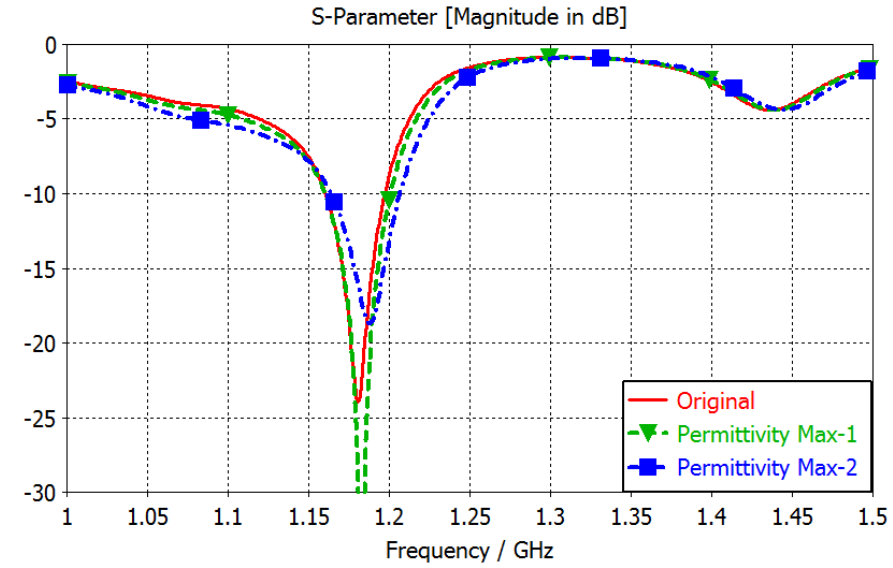


Figure 4.14 Magnitude of input reflection coefficient of the structure with different configurations of permittivity variation.

The resonant frequency is slightly shifted towards upper frequencies for both of the variations in the profile, while the operating band presents the same effect. However, these variations in the profile are not changing the performances of the antenna drastically. For example, the bandwidth in the original device is 39.2 MHz while for the first and second variation, it is slightly increased to 43 MHz and 46.2 MHz respectively. This can be explained because of the range of lower values of permittivity used in these modified devices.

In Figure 4.15, the farfield results for both modifications are presented at 1.18 GHz, the RG presented in this figures are absolute values which is different from Figure 4.9 where the components of the farfield were plotted.

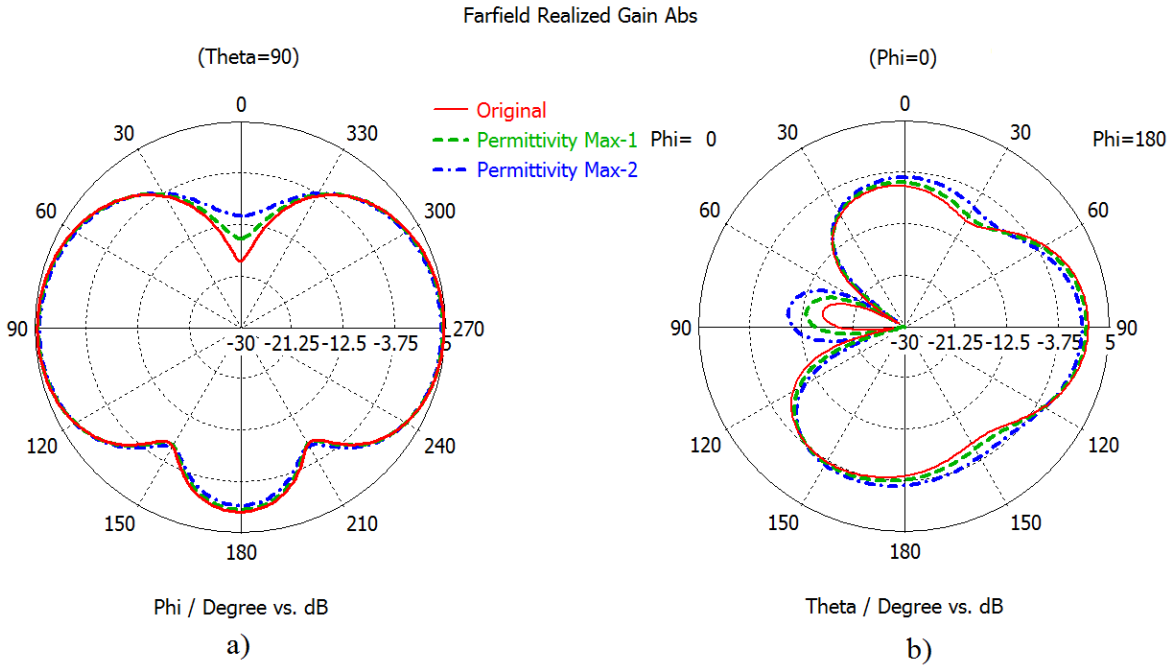


Figure 4.15 RG in the two main planes of antenna at 1.18 GHz for different ranges of the permittivity. a) *theta=90°*. b) *phi=0°*.

For both planes the radiation pattern has not changed greatly, however some of the effects are visible in both planes. For example in the *theta=90°* plane, the gain in the broadside is increased with each modification, from -18.6 dB to -14.8 and -11. In the *phi=0°* plane, the small beam in the 85° direction is also increased for each variation from -16 dB in the original configuration to -13.3 dB in the first variation and -10.1 dB in the second variation.

The absolute RG in the antipodal beams is not greatly compromised by these variations, because from the 4.5 dB in the original device, it only decreases of 0.5 dB to the second configuration which is quite acceptable for this modification.

Usually materials with values of permittivity up to 10 are relatively easy to find in the market, they present some constraint as weight or robustness. However, the fact that it is possible to reduce high values of permittivity is an important step towards a fabrication.

In general terms, the performances of our device are not compromised when some constraints in the range of values for the permittivity are applied. This fact would be very useful for realization process and synthesis of these values of permittivity.

5. Sensitivity to the value of the minimal relative permittivity

The same approach is applied in the case of the permeability, however in this case the lowest values are the ones that present problems when it comes to fabrication. Values below 1 are dispersive and the only materials capable of achieving these values are metamaterials. As it was clearly explained before, these materials present some characteristics such as high losses, very narrow bandwidth, etc. These characteristics that make them difficult to work with, in terms of design and practical realization.

In this regard, this study aims to find if it is possible to avoid these dispersive values of permeability. Two modifications are proposed in the original profile where the permeability values goes from 0.3 to 3. In the first modification, the lower values are truncated to 1 and in the second configuration the lower values were truncated to 0.7. Then, the range of permeability is [1- 3] in the first configuration avoiding all dispersive values and [0.7-3] in the second configuration keeping some of these dispersive values.

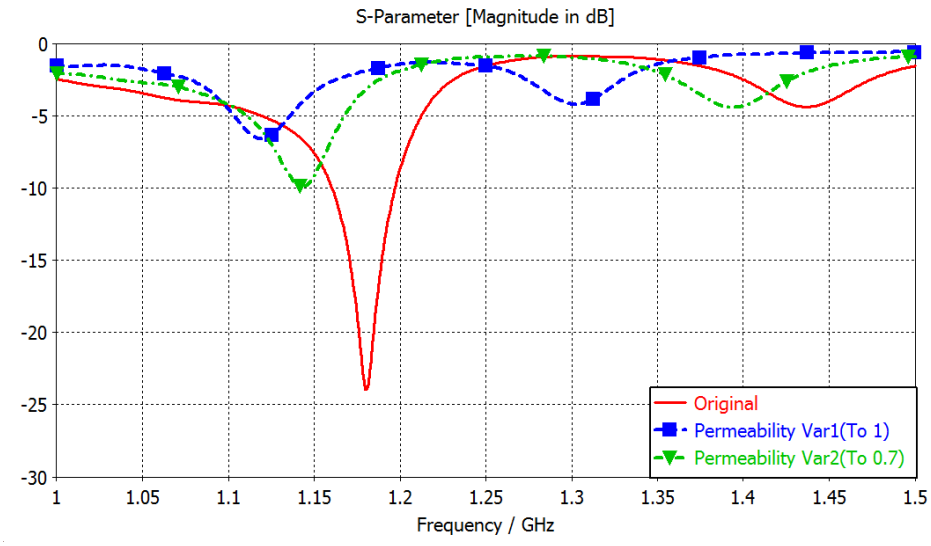


Figure 4.16 Magnitude of reflection coefficient of the structure with different configurations of permeability range.

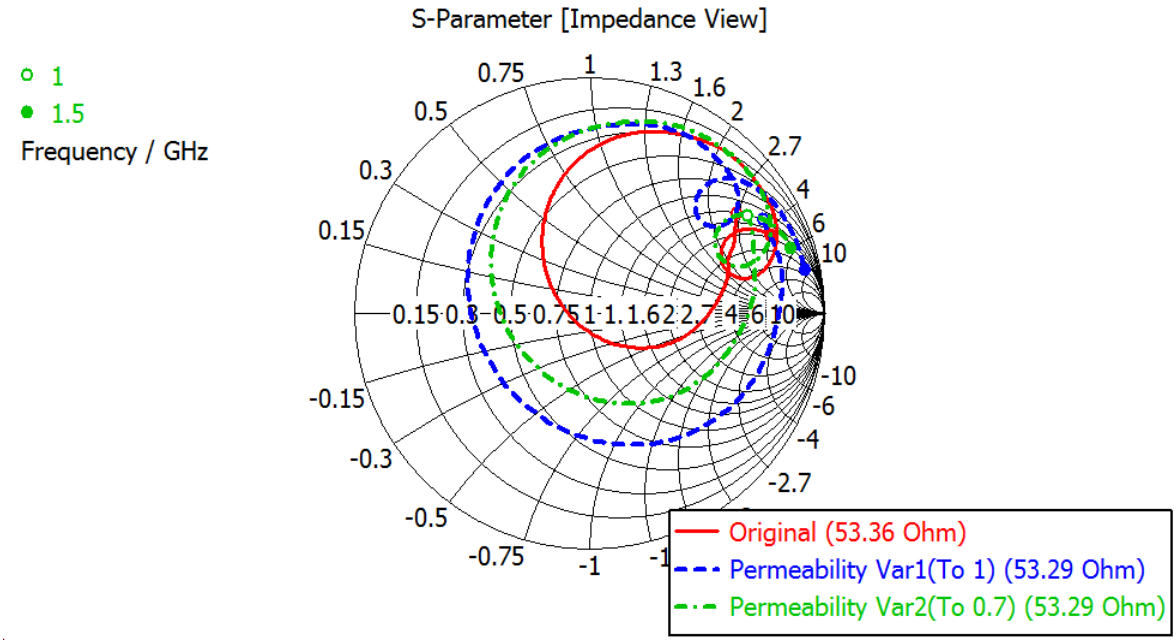


Figure 4.17 Impedance view of the smith chart of the structure with different configurations of permeability variation.

From the S parameters calculation presented in Figure 4.16, it is possible to remark that changing the values of permeability clearly affects the performance of the device. In other words, the lower values, for this case the dispersive values of permeability, are crucial to the performance of the device. For both modifications, the operating band is completely lost; while in the first case is more drastic; in the second case, a shifted narrow band appears because some of the dispersive values are kept.

As the bandwidth is lost due to these modifications, there is no point in calculating the farfield pattern in these cases, because in order to operate correctly our device must be well matched first.

6. Conclusions

This application demonstrates the performances of a superstrate based on TE technique. This flat device produces an interesting electromagnetic behaviour with a L-band patch antenna, as there is an antipodal radiation with a RG equal to 3.5 dB at ± 89 °, then dropping off to the minimum in the broadside direction which is slightly similar to a dipole pattern.

Using the designed TE device decreases the maximum RG of the patch antenna which results of the creation of the two lobes. In linear polarisation, these two lobes indicate that the antipodal radiation is present in only one plane of the farfield.

In addition, as this superstrate is flat, it can be used for some applications, where shape and conformability are highly important. Thickness of the superstrate is 37.5 mm, which corresponds to 0.15 wavelength at 1.2 GHz.

When different feeding configurations with different phases are applied, antipodal radiation appears for both planes (*theta=90°* and *phi=0°*). However the difference appears in the plane perpendicular to the broadside direction, while in one case the two shifted lobes appear in the other, four lobes became a quasi-isotropic radiation.

Exploring the sensitivity to MPs variations allow to simplify the profile towards realisation. In the case of the permittivity, the results of the reduction in the range of values keep the performances of the device interesting. The bandwidth and farfield do not change drastically. In the case of the permeability, any change in the range of values strongly compromises the performances of the device.

Conclusions and Future Work

Conclusions

The TE technique is a powerful and performing way to control wave propagation. However, to obtain the best performances, it is mostly needed complex materials or materials not available in nature (metamaterials) and also to define a space to perform the transformation whose size is bigger than the wavelength. This characteristic on the size of the device is not much attractive in antenna design where solutions must be small compared to the wavelength.

The present work has two objectives. The first one is to verify that it is possible to reduce the space of the transformation while trying to keep the TE behaviour attractive for an antenna design. The second objective is to propose different modifications to the material by taking action on the permittivity and permeability in order to facilitate the fabrication of prototypes with standard materials.

In this thesis, a detail view of the principle and some of the most interesting applications were presented in order to clarify concepts and highlight some limitations inherent to the TE technique. The invisibility cloak was used to describe in detail the design process, passing through the different steps of the design. Each of these steps enables to visualize some issues and limitations that the technique presents. Applications on invisibility cloak and carpets, invisibility of antennas, high directivity devices and multibeam antennas were presented in order to compare two interesting approaches on the design of TE devices such as: the analytical transformation and conformal mappings. The potential solution for synthesizing variant values of MP was also presented in order to explore actual issues on complexity on fabrication.

All dielectric solutions represent a very interesting solution in terms of simplicity regarding the design and realisation process of TE devices. We have proposed a method to design a flat reflector in order to reduce the thickness of the structure, based on TE principle and using dielectric materials only. Thickness reduction and an all dielectric approach allow to obtain a device suitable for applications where the shape and simplicity realization are important.

Choosing carefully the approximations and simplifications to be made in the different components of the permeability and the permittivity tensors of the material is important in order to achieve a feasible structure. We have also demonstrated that the method of drilling holes to achieve different values of permittivity in the different regions of the structure can be successfully used in the design of TE devices.

In this regard, a 3D printing realization can be an interesting and useful contribution. In the case of the superstrate used to increase HPBW, a drilled superstrate made of FullCure brought the device closer to a 3D print realisation. Studying the influence of varying dimensions and ground plane sizes on the performances of this FullCure superstrate is important to carry out the prototype to be fabricated and measured. Finally the superstrate was realized on a 3D Printer and was measured to prove the validity of the concept. A nice agreement between measurement and simulation results was observed.

In the last application, a superstrate was completely defined, from the analytical transformation to all constitutive parameters, to modify the broadside radiation pattern of a dual polarized patch antenna to an antipodal radiation pattern. Then, different feeding configurations with different phases were applied, antipodal radiation appears for both planes (*theta=90°* and *phi=0°*).The sensitivity to MPs variations were studied and it allowed to simplify the profile towards a realisation. In the case of the permittivity, the results of the reduction in the range of values keep the performances of the device interesting. However, in this case the structure needs imperatively a varying permeability which is different than the previous applications shown in this manuscript where only permittivity needed to be variant.

To summarize, three applications aiming to control or modify the radiation pattern of a regular antenna were presented. Either concentrating the radiation towards the broadside direction, or increasing the HPBW or even creating two lobes radiation towards the antipodes, the present work aimed to approach these applications towards a simple methodology. This methodology is also compatible with industrial process in order to be applied or used in fields such as airborne applications.

Future Work

In this manuscript, the approach of only permittivity variation was kept along the different applications to keep a simplistic approach. Avoiding resonant structures was important to reduce computing time in the simulations and also to decrease the complexity in both design and fabrication. However, for other applications, it could be very interesting to include the use of techniques of permeability variation such as [61], using the non-resonant part of the response of the SRR behaviour as metamaterial to obtain a larger wideband response. In the same way in chapter 4, the superstrate needs both permittivity and permeability variation, otherwise the antipodal radiation is not possible

The method of drilling holes is quite efficient in order to achieve the range of permittivity values needed for the TE design. However, this method can be improved in the future by taking into account other parameters such as elastics deformations and other techniques of permittivity synthesis in [44].

Combining these applications with other beam controlling techniques such as AMC reflectors to study the effect of both methods and the influence on each other could be a quite interesting contribution. AMC can be used as a beam controlling device, then using also a TE device such as the applications presented in this manuscript could increase the electromagnetic performances of the resulting device or or improve the compactness of the device.

In the case of the antipodal antenna, a square patch was used as radiating element, other geometry of radiating element could be used to form a 4 beam antenna or even to increase the gain of the antipodal radiation. Other types of radiating element with complex geometries that affect beam of the antenna could also work with the TE device. The influence of the TE device on the performances of the antenna could be quite interesting to evaluate and analyze.

In the last case (antipodal radiation pattern) the case where the same phase is applied to the two input ports is applied to the two port antenna which led to a quasi omnidirectional radiation is a quite interesting result. It deserves to be studied in more detail in order to design a flat superstrate that could turn a low profile antenna into an omnidirectional antenna.

References

[1]. J. B. Pendry, D. Schurig, and D. R. Smith, Controlling electromagnetic fields, Science, Vol. 312, pp. 1780–1782 (2006).

[2]. U. Leonhardt and T. G. Philbin, Transformation optics and the geometry of light, Prog. Opt., Vol. 53, pp. 69-152 (2009).

[3]. D. Schurig, J. J. Mock, B. J. Justice, S. A. Cummer, J. B. Pendry, A. F. Starr and D. R. Smith, Metamaterial electromagnetic cloak at microvave frequencies, Science, Vol. 314, pp. 977-980 (2006).

[4]. U. Leonhardt and T. Philbin, Geometry and Light: The Science of Invisibility (Dover Books on Physics, (2010)

[5]. P. Zhang, Theory of transformtion optics and invisibility cloak design, PhD Thesis, KTH Royal Institute of Technology, Stockholm (2011).

[6]. P. H. Tichit, Transformations d'espaces et applications électromagnétiques dans les domaines optiques et micro-ondes, PhD Thesis, Université Paris-Sud XI, (2012).

[7]. A. De Lustrac, Invisibilité transformation d'espace et applications, Techniques de l'ingénieur Optique physique, ref. art. af3714, (2010).

[8]. D. H. Kwon and D. H. Werner, Transformation electromagnetics: an overview of the theory and its application, IEEE Antennas Propag. Mag., Vol. 52, pp. 24–45 (2010).

[9]. Y. Liu and X. Zhang, Metamaterials: a new frontier of science and technology, Chem. Soc. Rev. Advance Article, (2011).

[10]. J. Li and J. Pendry, Hiding under the carpet: A new strategy for cloaking, Phys. Rev. Lett., Vol. 101, No. 20, pp. 203901 (2008).

[11]. N. Kundtz, D. R. Smith, Extreme-angle broadband metamaterial lens. Nat Mater. Vol. 9, pp.129–132 (2009).

[12]. W. X. Jiang, J. Y. Chin, S. Li, Q. Cheng, R. Liu and T. J. Cui, Analytical design of Conformally invisible cloaks for arbitrarily shaped objects, Physical Review E, Vol. 77, pp. 066607/1-6 (2008).

[13]. U. Leonhardt and T. Tyc, Broadband invisibility by non-Euclidean cloaking, Science 323, pp.110 (2009).

[14]. U. Leonhardt, Notes on conformal invisibility devices, New J. Phys., Vol. 8, pp. 118 (2006).

[15]. H. Chen, B. Wu, B. Zhang, and J. Kong, Electromagnetic wave interactions with a metamaterial cloak, Phys. Rev. Letters, Vol. 9, pp. 063903 (2007).

[16]. Z. Ruan, M. Yan, C. W. Neff, and M. Qiu, Ideal cylindrical cloak: Perfect but sensitive to tiny perturbations, Phys. Rev. Letters, Vol. 99, pp. 113903 (2007).

[17]. Z. Liang, P. Yao, X. Sun, and X. Jiang, The physical picture and the essential elements of the dynamical process for dispersive cloaking structures, Appl. Phys. Letters, Vol. 92, 131118 (2008).

[18]. B. Zhang, H. Chen, B-I. Wu and J. A. Kong, Extraordinary surface voltage effect in the invisibility cloak with an active device inside. Phys. Rev. Letters, Vol. 100, pp. 063904 (2008).

[19]. B. Kanté, D. Germain, and A. De Lustrac, Experimental demonstration of a non-magnetic metamaterial cloak at microwave frequencies. Phys. Rev. B, Vol. 80, pp. 201104 (2009).

[20]. D. H. Kwon and D. H. Werner, Two-dimensional eccentric elliptic electromagnetic cloaks, Applied Physics Letters, Vol. 92, pp. 013505/1-3 (2008).

[21]. M. Rahm, D. Schurig, D. A. Roberts, S. A. Cummer, D. R. Smith and J. B. Pendry, Design of electromagnetic cloaks and concentrators using form-invariant coordinate transformations of Maxwell's equations. Photon Nanostruct Fundam Appl, Vol. 6, pp. 87–95 (2008).

[22]. H. Ma, S. Qu, S. Xu, and J. Wang, Numerical method for designing approximate cloaks with arbitrary shapes, Physical Review E, Vol. 78, pp. 036608/1-4 (2008).

[23]. W. X. Jiang, T. J. Cui, G. X. Yu, X. Q. Lin, Q. Cheng, and J. Y. Chin, Arbitrarily elliptical-cylindrical invisible cloaking, Journal of Physics D: Applied Physics, Vol. 41, pp. 085504/1-4 (2008).

[24]. A. Nicolet, F. Zolla and S. Guenneau, Finite-element analysis of cylindrical invisibility cloaks of elliptical Cross Section, IEEE Transactions on Magnetics, Vol. 44, No. 6, pp. 1150-1153 (2008).

[25]. C. Li and F. Li, Two-dimensional electromagnetic cloaks with arbitrary geometries, Optics Express, Vol. 16, No.17, pp. 13414-13420 (2008).

[26]. C. Li, K. Yao, and F. Li, Two-dimensional electromagnetic cloaks with non-conformal inner and outer boundaries, OpticsExpress, Vol. 16, No. 23, pp. 19366-19374 (2008).

[27]. D-H. Kwon and D.H. Werner, Two-dimensional electromagnetic cloak having a uniform thickness for elliptic cylindrical regions. Appl Phys Lett, Vol. 92, pp. 113502 (2008).

[28]. W. Yan, M. Yan, and M. Qiu, Non-Magnetic simplified cylindrical cloak with suppressed zeroth order scattering, Appl. Phys. Lett. 93, 021909 (2008).

[29]. M. Yan, Z. Ruan, and M. Qiu, Scattering characteristics of simplified cylindrical invisibility cloaks, Opt. Express, Vol. 15, pp. 17772 (2007).

[30]. A. V. Kildishev, W. Cai, U. K. Chettiar, and V. M. Shalaev, Transformation optics: approaching broadband electromagnetic cloaking, New J. Physics, Vol. 10, pp. 115029

(2008).

[31]. H. Chen, Z. Liang, P. Yao, X. Jiang, H. Ma, and C. Chan, Extending the bandwidth of electromagnetic cloaks, Phys. Rev. B, Vol. 76, pp. 241104 (2007).

[32]. H. Hashemi, B. Zhang, J. D. Joannopoulos, and S. G. Johnson, Delay-bandwidth and delay-loss limitations for cloaking of large objects, Phys. Rev. Letters, Vol. 104, pp. 253903 (2010).

[33]. R. Mittra, Lenses, cloaks and transformation optics (TO)—Myths, mysteries and practical realities, Antennas and Propagation Conference (LAPC), 2012 Loughborough, vol., no., pp.1,4 (12-13 Nov. 2012).

[34]. S. A. Cummer, B. I. Popa, D. Schurig, D. R. Smith, J. Pendry, M. Rahm, and A. Starr, Scattering theory derivation of a 3D acoustic cloaking shell, Phys. Rev. Letters, Vol. 100, pp. 024301 (2008).

[35]. M. Farhat, S. Guenneau and S. Enoch, Ultrabroadband elastic cloaking in thin plates, Phys. Rev. Lett., Vol. 103, pp. 024301 (2009).

[36]. S. Brûlé, E. H. Javelaud, S. Enoch, and S. Guenneau, Experiments on seismic metamaterials: molding surface waves, Phys. Rev. Lett., Vol. 112, pp.133901 (2014).

[37]. S. Ping, A Step towards a seismic cloak, Physics, Vol.7, pp 34 (2014).

[38]. S. Zhang, D. A. Genov, C. Sun, and X. Zhang, Cloaking of matter waves, Phys. Rev. Lett., Vol. 100, pp. 123002 (2008).

[39]. L. Zigoneanu, B-I. Popa, S.A. Cummer, Three-dimensional broadband omnidirectional acoustic ground cloak, Nat Mater, 13, 4, 352-355 (2014).

[40]. T. Han, X. Bai, D. Gao, J.T.L. Thong, B. Li, and C.-W. Qiu, Experimental Demonstration of a Bilayer Thermal Cloak, Phys. Rev. Lett.112,5, 054302 (2014).

[41]. R. Liu, C. Ji, J. J. Mock, J. Y. Chin, T. J. Cui and D. R. Smith, Broadband ground-plane cloak, Science, Vol. 323, pp. 366–369 (2009).

[42]. J. Valentine, J. Li, T. Zentgraf, G. Bartal and X. Zhang, An optical cloak made of dielectrics.Nat Mater, Vol. 8, pp. 568–571 (2009).

[43]. W. Zhu, I. Shadrivov, D. Powell, and Y. Kivshar, Hiding in the corner, Optics Express, Vol. 19, Issue 21, pp. 20827-20832 (2011).

[44]. D. Shin, Y. Urzhumov, Y. Jung, G. Kang, S. Baek, M. Choi, H. Park, K. Kim and D. R. Smith, Broadband electromagnetic cloaking with smart metamaterials, Nat Commun, Vol. 3, No. 1213 (2012).

[45]. T. Ochiai, U. Leonhardt, and J. C. Nacher, A novel design of dielectric perfect invisibility devices, J. Math. Phys. Vol. 49, pp. 032903 (2008).

[46]. D. H. Kwon and D. H. Werner, Restoration of antenna parameters in scattering environments using electromagnetic cloaking, Applied Physics Letters, Vol. 92, pp. 113507/1-3 (2008).

[47]. W. Tang and H. Yang, Cloak an underground antenna using transformation electromagnetics, 2011 IEEE International Symposium on Antennas and Propagation (APSURSI), vol., no., pp.2865-2868 (3-8 July 2011).

[48]. J. P. Turpin, A. T. Massoud, S. H. Jiang, P. L. Werner, and D. H. Werner, Conformal mappings to achieve simple material parameters for transformation optics devices, Optics Express, Vol. 18, Issue 1, pp. 244-252 (2010).

[49]. W. Tang, Y, Hao and R. Mittra, Design of a carpet cloak to conceal an antenna located underneath, IEEE Transactions on Antennas and Propagation, Vol. 60, Issue 9, pp. 4444-4449 (2012).

[50]. N. Kundtz, D. A. Roberts, J. Allen, S. Cummer, and D. R. Smith, Optical source transformations, Opt. Express, Vol. 16, pp. 21215 (2008).

[51]. S. A. Cummer, N. Kundtz, and B. I. Popa, Electromagnetic surface and line sources under coordinate transformations, Phys. Rev. A. Vol. 80, pp. 033820 (2009).

[52]. C. Mateo-Segura, A. Dyke, H. Dyke, S. Haq, Y. Hao, Flat luneburg lens via transformation optics for directive antenna applications, IEEE Transactions on Antennas and Propagation,Vol.62, Issue 4,pp 1945-1953 (2013).

[53]. S. H. Sedighy, C. Guclu, M. K. Amirhosseini and F. Capolino, Directive radiation of a line-source inside an anisotropic material slab via transformation electromagnetics, Proceedings of 2013 URSI International Symposium on Electromagnetic Theory (EMTS), vol., no., pp.890-892, 20-24 (2013).

[54]. J. J. Zhang, Y. Luo, S. Xi, H. S. Chen, L. X. Ran, B-I. Wu and J. A. Kong, Directive emission obtained by coordinate transformation. Progress In Electromagnetics Research, Vol. 81, pp. 437–446 (2008).

[55]. D. A Roberts, N. Kindtz and D.R. Smith, Optical lens compression via transformation optics. Opt Express, Vol. 17, pp. 16535–16542 (2009).

[56]. B. Zhang, B-I. Wu, and H. Chen, High directive antenna with virtual aperture, Proceedings of the Antennas and Propagation Society International Symposium 2009, Vol., pp.1–4 (2009).

[57]. J. J. Zhang, Y. Luo, S. Xi, H. S. Chen, L. X. Ran, B-I. Wu and J. A. Kong, Directive emission obtained by coordinate transformation, Progress In Electromagnetics Research, PIER, Vol. 81, pp. 437–446 (2008).

[58]. P. H. Tichit, S. N. Burokur and A. De Lustrac, Ultra-directive antenna via transformation optics, Journal of Applied Physics, Vol.105, No.10, pp.104912-104912-6 (2009).

[59]. P. H. Tichit, S. N. Burokur, D. Germain and A. De Lustrac, Design and experimental demonstration of a high-directive emission with transformation optics, Phys. Rev. B, Vol. 83, No. 15, pp. 155108 (2011).

[60]. P. H. Tichit, S. N. Burokur, D. Germain and A. De Lustrac, Ultra-directive emission made by transformation optics, Proceedings of the 5th European Conference on Antennas and Propagation (EUCAP), vol., no., pp.3297-3300 (11-15 April 2011).

[61]. J. B. Pendry, A. J. Holden, W. J. Stewart and I. Youngs, Extremely low frequency plasmons in metallic mesostructures, Phys. Rev. Lett., Vol. 76, pp. 4773 (1996).

[62]. D. Schuring, J. J. Mock and D. R. Smith, Electric-field-coupled resonators for negative permittivity metamaterials, Appl. Phys. Lett., vol. 88, pp. 041109 (2006).

[63]. A. M. Nicolson and G. F. Ross, Measurement of the intrinsic properties of materials by time-domain techniques, IEEE Transactions on Instrumentation and Measurement, Vol.19, No.4, pp.377-382 (1970).

[64]. Y. Yang, X. Shao and T. Wang, Design of multi-beam antennas via optical transformation for anti-collision radar system, 2008 International Workshop on Metamaterials, Vol., No., pp. 240-243 (9-12 Nov. 2008).

[65]. D. H. Werner, S. H. Jiang, J. P. Turpin and P. L. Werner, Transformation optics collimating lenses for multi-beam antenna applications, Proceedings of the 4th IEEE Int. Symp. Microw. Antenna Propagat. EMC Technol. for Wireless Communications, pp. 458-461, Beijing, China (Nov. 1-3, 2011).

[66]. I. Aghanejad, H. Abiri and A. Yahaghi, Design of high-gain lens antenna by gradient-index metamaterials using transformation optics, IEEE Transactions on Antennas and Propagation, Vol.60, No.9, pp.4074-4081 (2012).

[67]. F. Kong, B-I. Wu, J. A. Kong, J. Huangfu, S. Xi and H. Chen, Planar focusing antenna design by using coordinate transformation technology, Appl. Phys. Lett., Vol. 91, pp. 253509 (2007).

[68]. M. Clemente Arenas, A. C. Lepage, X. Begaud, P. H. Tichit and A. De Lustrac, All standard materials flat reflector made by transformation electromagnetics, International Journal of Microwave and Wireless Technologies (2014). doi:10.1017/S1759078714000026.

[69]. O. Quevedo-Teruel, W. Tang, R. C. Mitchell-Thomas, A. Dyke, H. Dyke, L. Zhang, S. Haq, and Y. Hao, Transformation optics for antennas: why limit the bandwidth with metamaterials?, Scientific Reports, Vol. 3, No. 1903 (2013).

[70]. J.B. Pendry, A J. Holden, D. J. Robbins, W. J. Stewart, Magnetism from conductors and enhanced nonlinear phenomena, Microwave Theory and Techniques, IEEE Transactions on , vol.47, no.11, pp.2075,2084 (Nov 1999).

[71]. H. Chen, L. Huang, X. Cheng, and H. Wang, Magnetic properties of metamaterial composed of closed rings, Progress In Electromagnetics Research, Vol. 115, 317-326, (2011).

[72]. A. Dhouibi, S. N. Burokur, A. de Lustrac, A. Priou, Compact Metamaterial-Based Substrate-Integrated Luneburg Lens Antenna, Antennas and Wireless Propagation Letters, IEEE , vol.11, no., pp.1504,1507, (2012).

[73]. Y. Wu, , Y. Lai, Z. Q. Zhang, Elastic metamaterials with simultaneously negative effective shear modulus and mass density. Phys. Rev. Lett., Vol. 107, pp.105506 (2011).

[74]. R. Mittra, Z. Yuda, Real-world design of thin absorbers for RCS reduction of arbitrarily shaped radar targets over a wide band and for arbitrary incident angles and polarization using the concepts of Transformation Optics, Antennas and Propagation (EuCAP), 2013 7th European Conference on , vol., no., pp.3682,3684 (8-12 April 2013).

[75]. H. Ma, W. Jiang, X. Yang, X. Zhou, and T. Cui, Compact-sized and broadband carpet cloak and free-space cloak, Opt. Express,Vol. 17, pp. 19947-19959 (2009).

[76]. L. Schulwitz, L. Mortazawi, A new low loss rotman lens design using a graded dielectric substrate, IEEE Transactions on Microwave Theory and Techniques, Vol. 56, No.12, pp. 2734-2741 (Dec. 2008).

[77]. N. I. Landy, N. Kundtz, and D. R. Smith, Designing Three-DimensionalTransformation Optical Media Using Quasiconformal CoordinateTransformations, Physical Review Letters, Vol 105, pp. 193902 (2010).

[78]. H. F. Ma and T. J. Cui, Three-dimensional broadband ground-plane cloak made of metamaterials, Nature Communications 1 (2010).

[79]. L. J. Sikora, FLAPS reflector antennas, Telesystems Conference, 1993. Commercial Applications and Dual-Use Technology', Conference Proceedings., National , vol., no., pp.233-238 (16-17 Jun 1993).

[80]. S.M. Duffy, S.D. Targonski, Comparison of two flat reflector-type designs for dual-polarization, dual-band operation, Antennas and Propagation Society International Symposium, 2001. IEEE , vol.2, no., pp.288,291 (8-13 July 2001).

[81]. Y. Feng, S. Xiong, B. Zhu, J. Zhao and T. Jiang, Design and realization of planar reflectors through transformation optics, Antenna Technology (iWAT), 2013 International Workshop on , vol., no., pp.187,190 (4-6 March 2013).

[82]. R. Yang, W. Tang, Y. Hao, Wideband Beam-Steerable Flat Reflectors via Transformation Optics, Antennas and Wireless Propagation Letters, IEEE , vol.10, pp.1290,1294(2011).

[83]. T. McManus, Y. Rui, O. Quevedo-Teruel, Y. Hao, Asymmetric flat reflector from transformation optics, Antennas and Propagation (EuCAP), 2013 7th European Conference on , vol., no., pp.1836,1839 (8-12 April 2013).

[84]. W. Tang, C. Argyropoulos, E. Kallos, W. Song and Y. Hao, Discrete coordinate transformation for designing all-dielectric flat antennas, IEEE Trans. on Antennas and Propagation, Vol. 58, pp. 3795-3804 (2010).

[85]. A. Demetriadou, Y. Hao, A Grounded Slim Luneburg Lens Antenna Based on Transformation Electromagnetics, Antennas and Wireless Propagation Letters, IEEE , vol.10, no., pp.1590,1593 (2011)

.

List of Figures

Figure 1.1 a) Cartesian coordinate system and b) Transformed coordinate system. 44

Figure 1.2 Example of Discrete Transformation [11]. 47

Figure 1.3 Maps of index in the physical and virtual spaces [11]. 48

Figure 1.4 a) Wave's trajectory turned around an object. b) Layout for cloaking. Transformed space is the region between R_1 and R_2, the cylinder's section between 0 and R_1 is metallic. 50

Figure 1.5 Comsol Multiphysics simulations at 400MHz, a) Effects of a TM illumination over a PEC cylinder, b) 2D annular cloak 51

Figure 1.6 Experimental devices of invisibility cloak a) 2D microwave cloaking structure from [3] with a plot of the metamaterial cell and dimensions b) Assembling of the cloaking device from [17]. 52

Figure 1.7 Principle of invisibility carpet. 53

Figure 1.8 E-Field distribution at 750 nm. a) Cloacked object with a 45° illumination, b) The object only. 53

Figure 1.9 Two realisations of the carpet cloak: microwave regime (left) and optical regime (right) 53

Figure 1.10 Two antennas A_1 and A_2 with narrow bands cloaks C_1 and C_2. 54

Figure 1.11 Magnetic field distribution of A_1 antenna at 2 GHz [46] in presence of: a) an uncloaked A_2 antenna, b) Cloaked A_2 antenna. 55

Figure 1.12 Transformation needed to achieve directivity from a) Initial to b) Transformed space [59]. 56

Figure 1.13 Normalised Electric Field distribution in Transverse Electric polarisation at different frequencies to test directivity variations [58]. a) 5 GHz, b) 10 GHz and c) 20 GHz. 57

Figure 1.14 a) Schematic of the metamaterial structure with a microstrip path as source. The structure is composed of alternating permittivity and permeability vertical layers. b) Continuous variation of ε_{zz} and μ_{yy}c) Discrete values of MP of ε_{zz} and μ_{yy} [60] 58

Figure 1.15 Detailed view of the assembled metamaterial over the antenna with the succession of permittivity and permeability metamaterial layers. Variations in unit cells is also in detail for SRR

among the structure of the antenna. 5 regions in detail where each magnetic and dielectric layer of the metamaterial is presented along the propagation direction. Details of the resonators used in the magnetic (right) and electric (left) metamaterial layers. Three rows of identical resonators made each level [60]. 59

Figure 1.16 Farfield results at 10.6 GHz: antenna alone (red) and antenna and metamaterial layers (blue), a) Measurements, b) Simulations [60]. 60

Figure 1.17 a) Configuration of the antenna. The green region is the original space and the red one is the transformed space, b) One sector of the multi beam antenna in the Cartesian coordinate system [64]. 60

Figure 1.18 a) E-Field distribution for the four beam antenna, b) E Field distribution for the three beam antenna c) Normalised far field radiation for four beam antenna, d) Normalized far field radiation for the three beam antenna [64]. 61

Figure 1.19 Transformation electromagnetics lens by a TE- mode dipole feed at the origin; square lens, a) Geometry and b) Field pattern with four high directive beams [65]. 62

Figure 1.20 a) Configuration of the metamaterial for TE lens as HFSS model. b) Photograph of the fabricated quad-beam TE lens. The length of the outer edge is 102 mm (at 4.8 GHz is 1.632λ) [65]. 63

Figure 1.21 a) Comparison of input reflection coefficient for the monopole with and without the TE lens. Results of farfield pattern from the monopole with and without the TE lens at b) 4.5 GHz, and c) 5.2 GHz. Red and black measurement results, blue and green simulation results [65]..... 63

Figure 2.1 Cross section of reflectors: a)TE based flat structure, b) Parabolic reflector. Perfect Electric Conductor (PEC) boundaries in blue. 67

Figure 2.2 TE structure profile: e = 0.15 m, d = 0.1 m and p = 0.15 m, a) ε'_{xx} b)$\varepsilon'_{xy} = \varepsilon'_{yx}$ c) $\varepsilon'_{yy} = \varepsilon'_{zz}$. 68

Figure 2.3 Reduced set of tensor components a) μ'_{uu} b) μ'_{vv} c) ε'_{zz}. 69

Figure 2.4 Normalized $|E_z|$ distribution at 5 GHz: a) Parabolic reflector b) Flat TE reflector c) PEC flat reflector..... 70

Figure 2.5 Directivity calculated with Comsol Multiphysics at 5 GHz: for both reflectors (Parabolic and Flat TE reflector. 71

Figure 2.6 Titanate particles from [69] and [52]. 73

Figure 2.7 Detail view of the drilled dielectric. 74

Figure 2.8 Evolution of the E Field distribution through different stages of the approximation. 75

Figure 2.9 Comparison of E Field Distribution through permittivity variation. 76

Figure 2.10 Comparison of Realized Gain RG (Figures above), directivity (Figures middle) and HPBW (Figures below) of dispersive and non-dispersive reflectors at 5 GHz. 77

Figure 2.11 TE structure profile with discretized values of permittivity a) 256 blocks: 32 horizontal and 8 vertical regions. b) 64 blocks: 16 horizontal and 4 vertical regions. 79

Figure 2.12 Front view of multilayered structure for the flat reflector. 79

Figure 2.13 Farfield pattern comparison at 5 GHz between two structures with different discretizations: 8 horizontal regions (same dispersive reflector from Figure 2.10) and 16 horizontal regions of constant value of permittivity. 79

Figure 2.14 a) Front view of dielectric structure. b) Front view in details: d_a angular distance and d_r radial distance between holes. 81

Figure 2.15 Front view of multilayered structure for the flat reflector. 82

Figure 2.16 Radiation patterns comparison (RG and Directivity)between the dispersive (8 horizontal regions) and non-dispersive reflectors and the drilled one at 5 GHz. 83

Figure 2.17 a) Farfield components (Co-polar and Cross-polar). 83

Figure 2.18 Front view of Flat Reflector and W90-coaxial adaptor. 84

Figure 2.19 FullCure reflector radiation patterns at 10 GHz. Horn antenna only (Blue curve), and Horn combined with the flat reflector (Red curve) 85

Figure 2.20 S_{11} parameter of the complete structure a) Horn antenna, b) Horn antenna+TE Flat Fullcure reflector) 86

Figure 2.21 Fullcure reflector radiation patterns from 9 GHz to 12 GHz. 86

Figure 3.1 Initial TE structure profile, values in colour represent different values of relative permittivity [84]. 91

Figure 3.2 Four explored cases, a) Patch Only, b) Patch with directive structure, c) Patch with modified structure (horizontally inversed case), d) Patch with modified structure (vertically inversed case), quantities in mm. 92

Figure 3.3 a) 2D Profile rotated into a 3D structure, b) 3D structure obtained by adding height to the 2D profile. In this case the profile for this picture is the one in Figure 3.2-b. 93

Figure 3.4 Normalised gain at the center frequency of the band (1.2 GHz), both planes for the different cases with linear polarization. 93

Figure 3.5 Normalised gain at the center frequency of the band (1.2 GHz), both planes for the different cases with RHCP. 94

Figure 3.6 Normalised gain at the center frequency of the band (1.2 GHz), both planes for the different cases with a linear polarization..... 95

Figure 3.7 Normalised gain at the center frequency of the band (1.2 GHz), both planes for the different cases with a RHCP. 95

Figure 3.8 RG for Case a (left) and Case c (right) at 1.2 GHz for linear polarisation (Port 1 fed). 96

Figure 3.9 Case c profile with dispersive values of permittivity (left), Case c with non dispersive values of permittivity (right). 97

Figure 3.10 Normalized gain at 1.2 GHz for both planes for the different configurations with or without superstrate with linear polarisation. 97

Figure 3.11 Normalized gain at 1.2 GHz for both planes for the different configurations with or without superstrate with RHCP. 97

Figure 3.12 Normalized gain at 1.2 GHz for both planes for the different configurations with permittivity variation. 99

Figure 3.13 RG at 1.2 GHz for both planes for the different configurations with permittivity variation..... 99

Figure 3.14 Reflection coefficient versus frequency for 4 explored cases 100

Figure 3.15 Profile view of the structure: Antenna and superstrate with different horizontal and vertical regions. 101

Figure 3.16 Front view of variant permittivity superstrate, a) 1st Layer (bottom), b) 2nd Layer (middle), c) 3rd Layer (upper)..... 101

Figure 3.17 Normalized gain at 1.2 GHz for both planes for the different configurations with or without superstrate. a) Linear polarisation, b) RHCP. 102

Figure 3.18 Cartesian plot for the axial ratio of the dispersive superstrate, non dispersive superstrate and the drilled superstrate at 1.2 GHz, for both planes (*phi= 0°* and *phi=90°*)..... 103

Figure 3.19 S_{11} parameters comparison for 1 layer, 2 layers and 3 layers of non drilled dielectric(below). 104

Figure 3.20 Radiation pattern comparison at 1.2 GHz (phi=0°). 105

Figure 3.21 Two port reference patch antenna (left), side view of the final set up, antenna and superstrate (right). 105

Figure 3.22 Reflection coefficient versus frequency for the FullCure superstrate. 106

Figure 3.23 Radiation pattern at [1.164-1.239] GHz for phi=0° and phi=90°. 107

Figure 3.24 RG at 1.2 GHz for both planes for the different configurations with diameter variation of the superstrate. 108

Figure 3.25 Normalized gain at 1.2 GHz for both planes for the different configurations with diameter variation of the superstrate. 109

Figure 3.26 RG at 1.2 GHz for both planes for the different configurations with thickness variation..... 109

Figure 3.27 Normalized gain at 1.2GHz for both planes for the different configurations with thickness variation..... 110

Figure 3.28 Reflection coefficient versus frequency for the FullCure superstrate both 600 mm diameter and 100x100 mm² ground planes. Linear polarization..... 111

Figure 3.29 RG along the operating band [1.16-1.23] GHz (phi=0°) for both cases: with the 600 mm circular ground plane (left) and with the 100x100 mm² square ground plane (right)..... 112

Figure 3.30 RG along the operating band [1.16-1.23] GHz (phi=90°) for both cases with the 600 mm circular ground plane (left) and with the 100x100 mm² square ground plane (right)..... 112

Figure 3.31 Perspective view and side view of reference antenna with 250 mm diameter FullCure superstrate and the honeycomb interlayer of 5 mm of thickness and 300 mm of diameter. 113

Figure 3.32 Realized reference antenna with the manufactured superstrate..... 113

Figure 3.33 Superstrate composed by 3 printed dielectric 114

Figure 3.34 Reflection coefficient versus frequency using a -3dB coupler with a 90° shift..... 114

Figure 3.35 $|E_{phi}|$ Measurement vs Simulation at 1.184 GHz..... 115

Figure 3.36 $|E_{theta}|$ Measurement vs Simulation at 1.184 GHz. 115

Figure 3.37 $|E_{phi}|$ Measurement vs Simulation at 1.21 GHz..... 116

Figure 3.38 $|E_{theta}|$ Measurement vs Simulation for 1.21 GHz. 116

Figure 3.39 $|E_{phi}|$ Measurement vs Simulation for 1.245 GHz. 116

Figure 3.40 $|E_{theta}|$ measurement vs simulation for 1.245 GHz. 117

Figure 4.1 L = 200 mm, d = 37.5 mm, w = 37.5 mm, a = 2 (compression factor). a) Real space. b) Virtual space. 121

Figure 4.2 a) Component ε_{zz} from permittivity tensor. b) Component μ_{yy} from permeability tensor. 123

Figure 4.3 2D Simulation of *Ez* field distribution at 1.2 GHz for the antenna model only..... 124

Figure 4.4 2D Simulation of *Ez* field distribution at 1.2 GHz for antenna model with TE based superstrate. 124

Figure 4.5 Discretized profile for relative permittivity and permeability. 125

Figure 4.6 Magnitude of reflection coefficient of the complete structure with different configurations..... 126

Figure 4.7 a) *Ez* Field Distribution at 1.3 GHz for the patch only and b) *Ez* Field Distribution at 1.2 GHz for the complete structure. 127

Figure 4.8 Magnitude of the RG for: a) Patch only at 1.3 GHz and b) Patch with TE based superstrate at 1.2 GHz. 127

Figure 4.9 Co-polar and cross-polar components of the RG in the two main planes of antenna at 1.2 GHz (centre frequency). a) *theta=90°*. b) *phi=0°*. 128

Figure 4.10 Magnitude of the input reflection coefficient of the structure with different feeding configurations..... 129

Figure 4.11 RG in the two main planes of the antenna and the superstrate for different feeding configurations at 1.18 GHz. a) *theta=90°*. b) *phi=0°*. 129

Figure 4.12 RG in the *phi=90°* plane of the antenna and the superstrate for different feedings configurations at 1.18 GHz. 130

Figure 4.13 3D Farfield pattern at 1.18 GHz for: a) Device fed in two ports without shift, and b) Device fed in two ports fed with 90° shifting. 130

Figure 4.14 Magnitude of input reflection coefficient of the structure with different configurations of permittivity variation. 131

Figure 4.15 RG in the two main planes of antenna at 1.18 GHz for different ranges of the permittivity. a) *theta=90°*. b) *phi=0°*. 132

Figure 4.16 Magnitude of reflection coefficient of the structure with different configurations of permeability range..... 133

Figure 4.17 Impedance view of the smith chart of the structure with different configurations of permeability variation. 134

List of Publications

Publications

- **Journals:**
- M. Clemente, A-C, Lepage, X. Begaud, Antipodal Radiation Pattern of a Patch Antenna Combined with Superstrate Using Transformation Electromagnetics, **Applied Physics A**, Volume 117, Issue 2 (2014), Page 699-703. DOI: 10.1007/s00339-014-8725-4
- M. Clemente Arenas, A. C. Lepage, X. Begaud, P. H. Tichit, A. De Lustrac, All standard materials flat reflector made by transformation electromagnetics, **International Journal of Microwave and Wireless Technologies**, 2014. doi:10.1017/S1759078714000026
- M. Clemente Arenas, A. C. Lepage, G.P. Piau, X. Begaud, All Dielectric 3D Printed Superstrate to Control the Radiation of A Dual Polarized Patch Antenna, Submitting to **Scientific Reports**.
- **Conferences:**
- M. Clemente, A-C, Lepage, X. Begaud, Antipodal Radiation Pattern of a Patch Antenna Combined with Superstrate Using Transformation Electromagnetics, **META'14**, Singapore, May 2014.
- M. Clemente, A-C, Lepage, X. Begaud, A. De Lustrac, P-H. Tichit Réflecteur Plat calculé par la Transformée d'Espace et réalisé avec des matériaux standards, **JNM2013**, Paris, May 2013.
- M. Clemente, A-C, Lepage, X. Begaud, All Dielectric Superstrate to Control the Half-Power-BeamWidth of A Dual Polarized Patch Antenna, **EuCAP 2013**,Goteburg, April 2013.
- M. Clemente, A-C, Lepage, X. Begaud, Superstrat tout Dielectrique Pour le Contrôle de l'Ouverture Angulaire d'une Antenne à Double Polarisation, **JS-URSI**, Paris, Mars 2013

Appendices

Appendix A: Reference Antenna Specifications

1-Introduction

Based on specifications of the MIMiCRA project, the down-selection of some requirements for a multi-purpose L-band antenna is presented in Table A.1.

Parameter	Reference Antenna
Bands to be covered (MHz)	1164-1239
Polarisation	RHCP & LHCP
Maximum Element Gain (dBi)	3 dBiC
Beamwidth (3 dB)	Within 3dB of maximum out 60° off zenith
Direction of maximum gain	Within 60° of the zenith
SWR	<2
Axial ratio	6 dB or better out to 60° off zenith
Polarisation Isolation	> 15dB
Rx/Tx	Rx only
Power handling (W)	1 W (ESA spec.)
Thickness (mm)	<15 mm (excluding connector)
Diameter (mm)	>80mm

Table A.1 Summary of finally agreed requirement for case 1 antenna

The important point on this antenna is that is generic which allows to make valuable comparisons with the different versions of this antenna combined with the TE applications.

2-Description of Case 1 antenna

Geometry

The overview of the profile of the reference antenna is summarized in Figure A.1

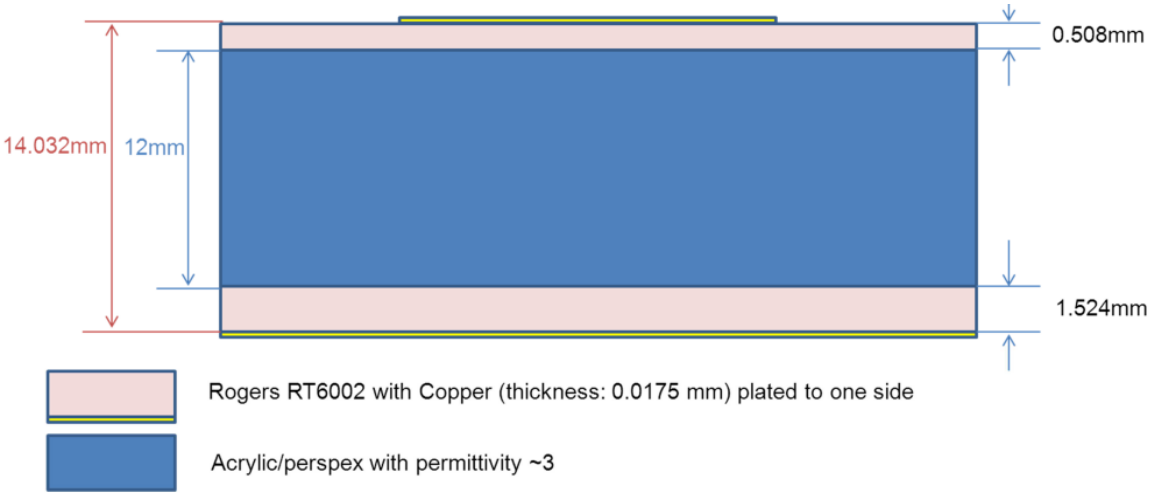


Figure A.1 Reference antenna. Proposed manufacture method.

The inner conductor of coaxial connector is only passing through the substrate to the patch (without the PTFE shield). SMA connector is detailed in: http://uk.rs-online.com/web/p/connector-rf/5463181.

This reference antenna has been modelled with materials information and dielectric data (for Perspex material) provided/measured by BAE and EADS, and with alternative ground planes (square 100 mm^2, circular 600 mm^2 see later). Permittivity of the acrylic/Perspex is: real part is 2.67 and imaginary part is 0.021.

An antenna with square 100 mm² ground plane overview is presented in Figure A.2.

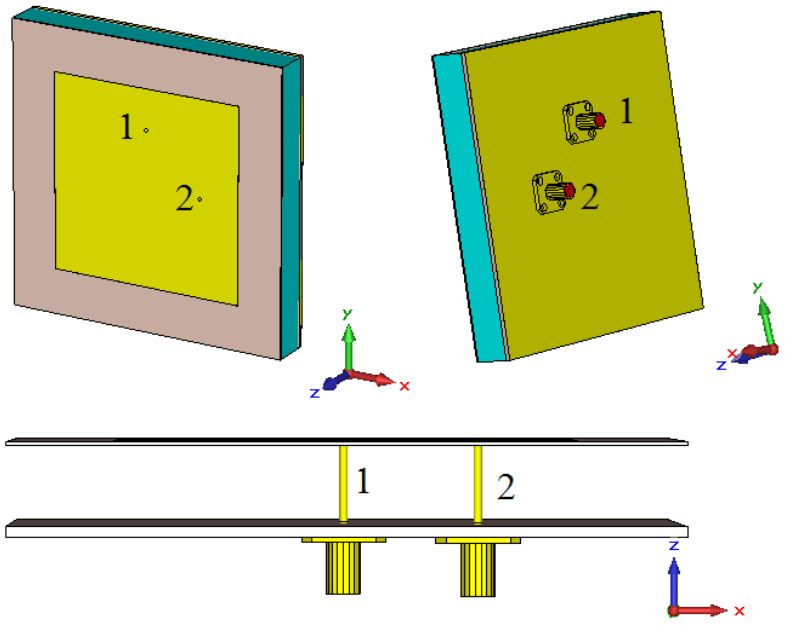


Figure A.2 Front, rear view and details of connectors of optimised design.

The antenna is composed of five layers: ground plane/substrate1/substrate2/ substrate3/radiating element (Figure A.2).

The Ground plane and radiating element are made of Copper (thickness: 0.0175 mm, Electric conductivity: 5.96e+007 S/m)

Substrate1 and substrate3 are composed of Rogers RT 6002 (Permittivity: 2.94, Tan $\delta = 0.0012$).

Substrate2 is composed of acrylic/Perspex (Permittivity is: real part is 2.67 and imaginary part is 0.021).

The dimensions are:

- Ground plane: square 100*100 mm²
- Patch (radiating element): square 68.5*68.5 mm
- Substrate1: Square 100*100 mm² - Thickness: 1.524 mm
- Substrate2: Square 100*100 mm² - Thickness: 12 mm
- Substrate3: Square 100*100 mm² - Thickness: 0.508 mm

Two coaxial feeding probes are used to generate two orthogonal linear polarizations.

The distance from the centre of patch to the probe: 20 mm

Dimensions of the coaxial connectors:

- Outside diameter of inner conductor, d = 1.27 mm
- Inside diameter of the shield, D = 4 mm
- Dielectric insulator: Teflon, Permittivity: 1.9

NB: Circular polarization will be generated with 90 Degree Hybrid Couplers.

3-Simulated performances of Case 1 Antenna with square 100 mm² ground plane results

All these results have been obtained with CST Microwave Studio (Transient solver).

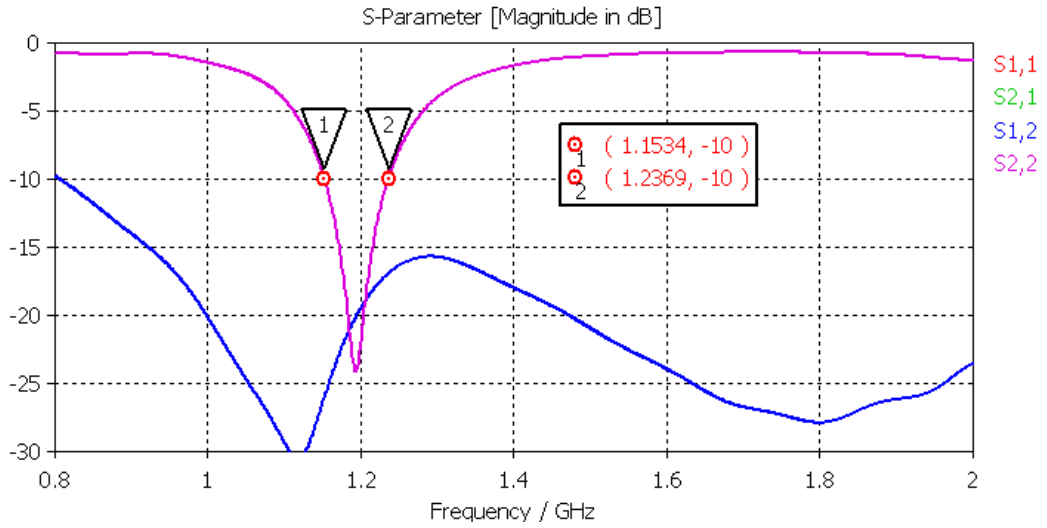


Figure A.3 Reflection coefficient versus frequency.

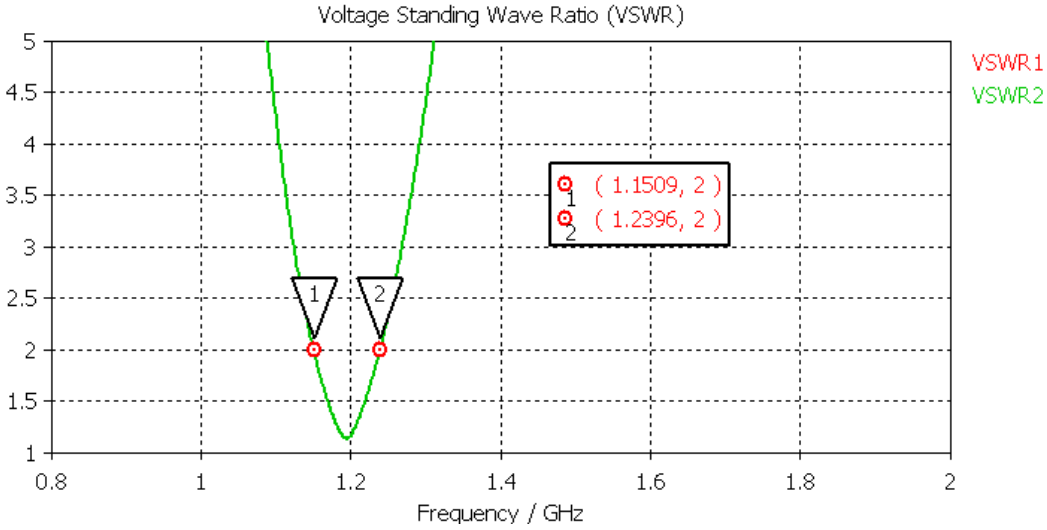


Figure A.4 VSWR versus frequency.

The radiation pattern are presented (Figure A.5-Figure A.10) in two orthogonal planes (phi = 0° and phi = 90°) at three frequencies (min, center, max) of the required bandwidth (see table 1).



Figure A.5 Radiation pattern at 1.164 GHz (phi=0°).



Figure A.6 Radiation pattern at 1.164 GHz (phi=90°).

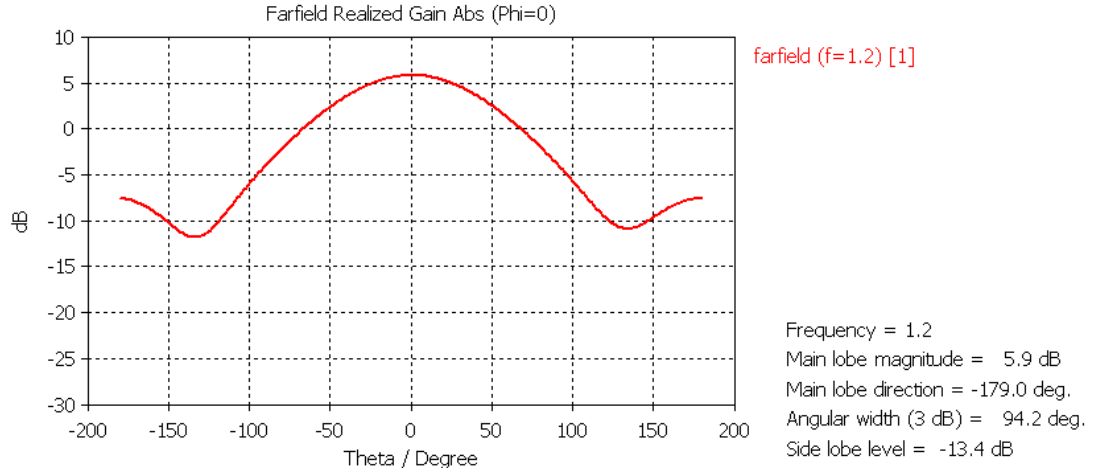


Figure A.7 Radiation pattern at 1.2 GHz (phi=0°).



Figure A.8 Radiation pattern at 1.2 GHz (phi=90°).

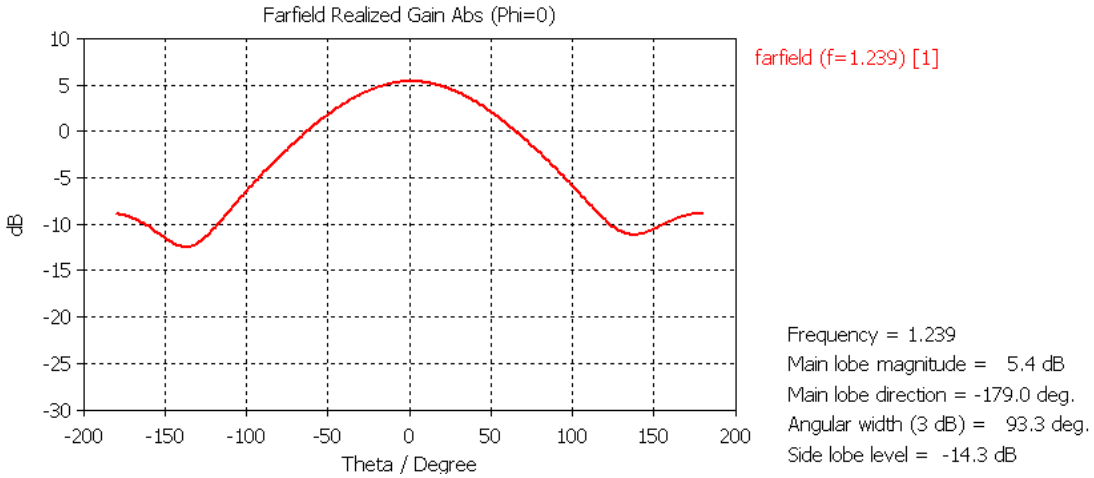


Figure A.9 Radiation pattern at 1.239 GHz (phi=0°).



Figure A.10 Radiation pattern at 1.239 GHz (phi=90°).

Summary of the performances

This work has given the following results:

The bandwidth (defined for VSWR < 2, in dual linear orthogonal polarization): 1.15-1.239 GHz (Figure A.4), for this bandwidth:

Isolation between the two ports is better than 17dB in the bandwidth

	f=1.164 GHz		**f=1.2 GHz**		**f=1.239 GHz**	
Plan phi=	0°	90°	0°	90°	0°	90°
Main Lobe Magnitude(dB)	5.6	5.6	5.9	5.9	5.4	5.4
HPBW (°)	95	88	94	87	93	85
Side lobe level (dB)	-12.6	-12.6	-13.4	-13.4	-14.3	-14.2

The structure has the following relevant dimensions:

Thickness = 14.05 mm (Without SMA connectors).

Size: (100*100) mm^2

4.Simulated performances of Case 1 Antenna with circular 600 mm diameter ground plane

In order to take into account the ground plane used for measurement, we have extended the previous ground plane to a circular ground plane with following diameter: 600 mm (same thickness, other dimensions are kept as the reference antenna). An antenna overview is presented in Figure A.11.

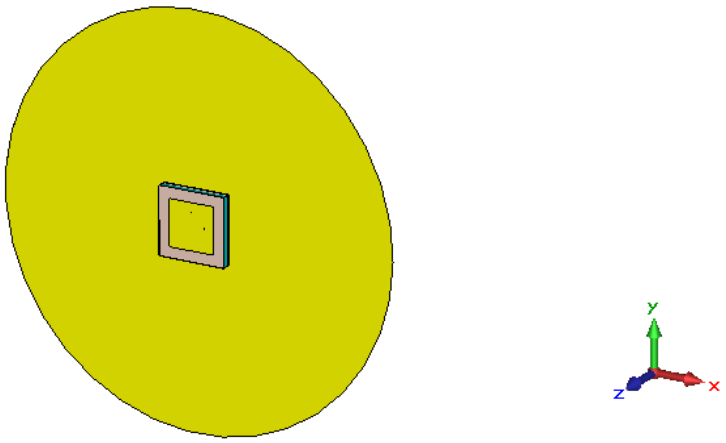


Figure A.11 Front view of case 1 antenna with circular 600 mm diameter ground plane.

All these results have been obtained with CST Microwave Studio (Transient solver).

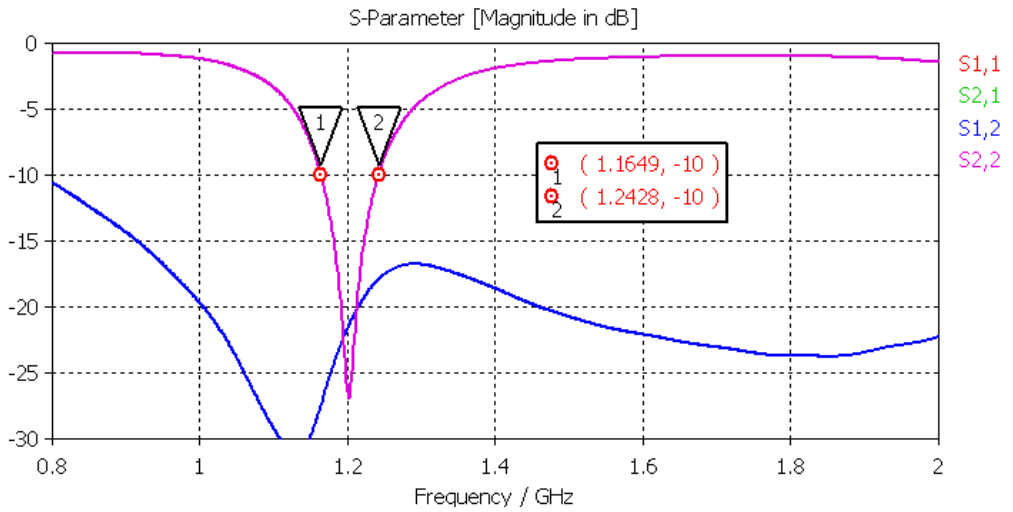


Figure A.12 Reflection coefficient versus frequency.

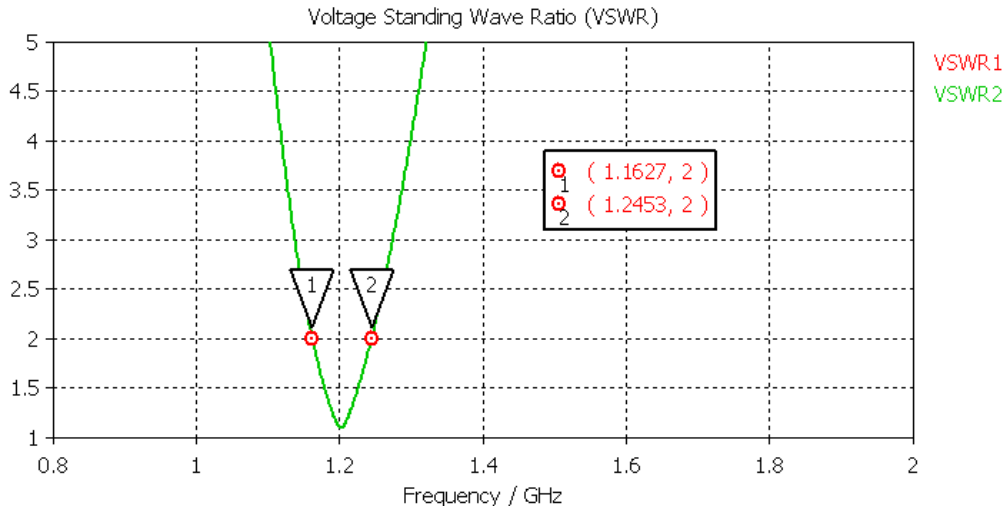


Figure A.13 VSWR versus frequency.

The radiation patterns are presented (Figure A.14-Figure A.19) in two orthogonal planes (phi = 0° and phi = 90°) at three frequencies (min, center, max) of the required bandwidth as in Table A.1.

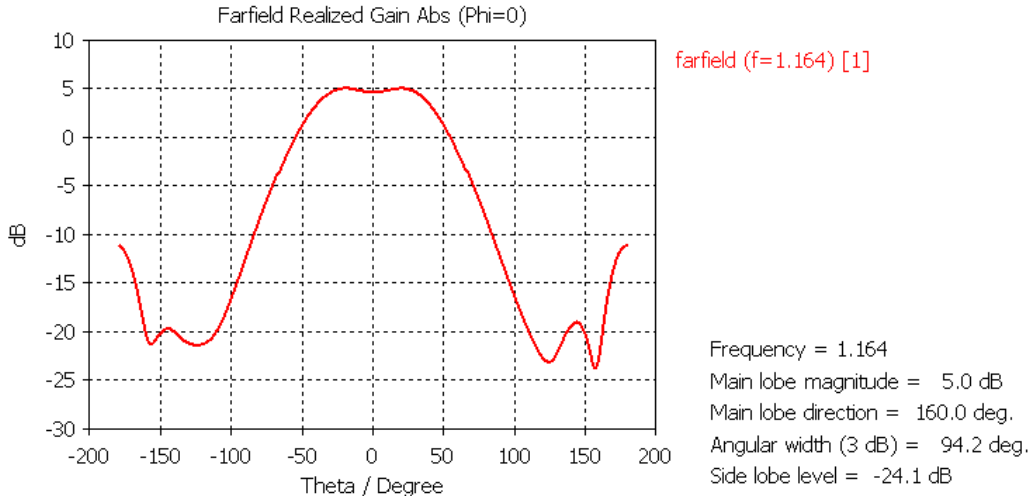


Figure A.14 Radiation pattern at 1.164 GHz (phi=0°).

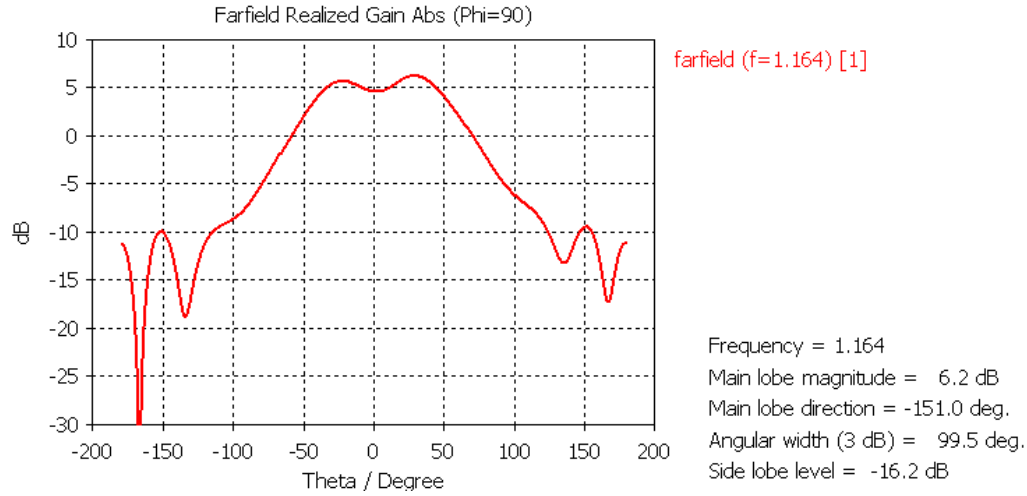


Figure A.15 Radiation pattern at 1.164 GHz (phi=90°).

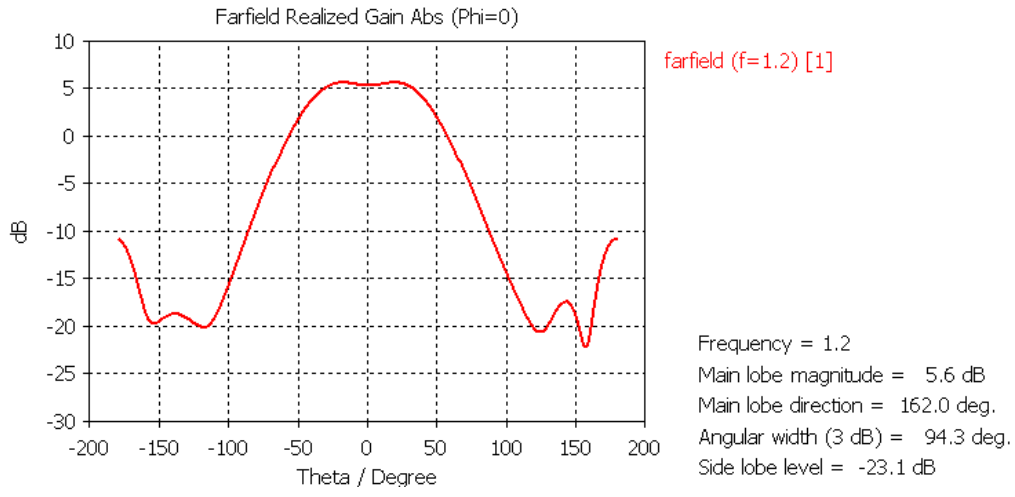


Figure A.16 Radiation pattern at 1.2 GHz (phi=0°).

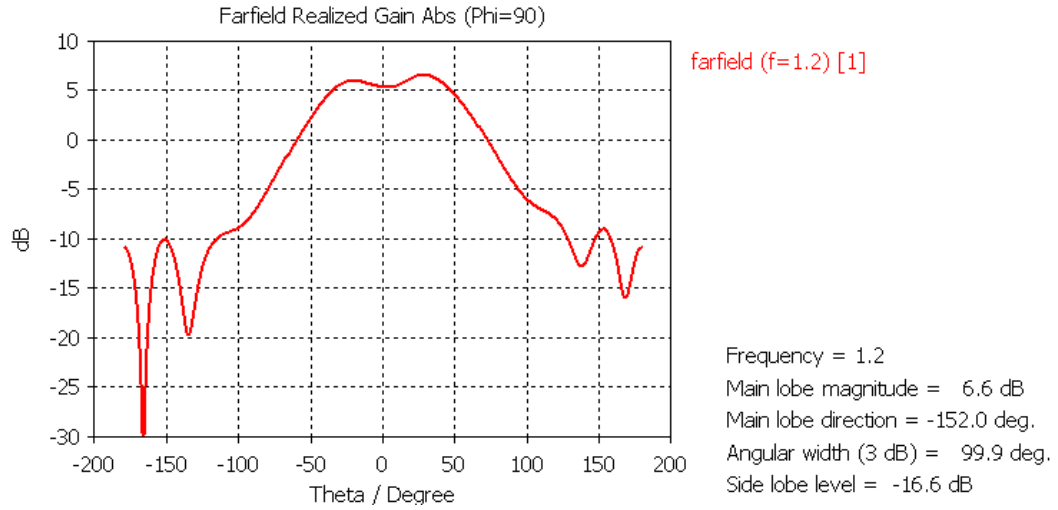


Figure A. 17 Radiation pattern at 1.2 GHz (phi=90°).

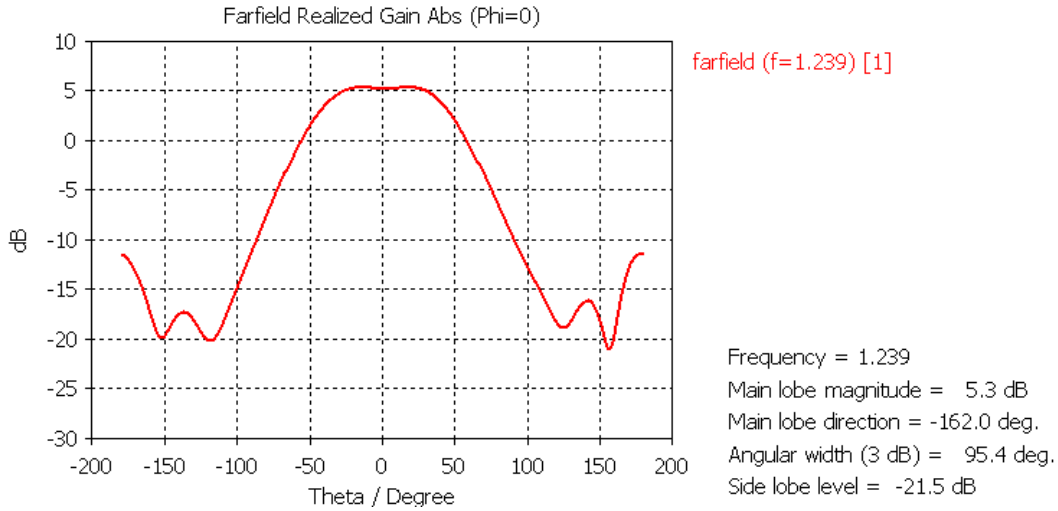


Figure A.18 Radiation pattern at 1.239 GHz (phi=0°).

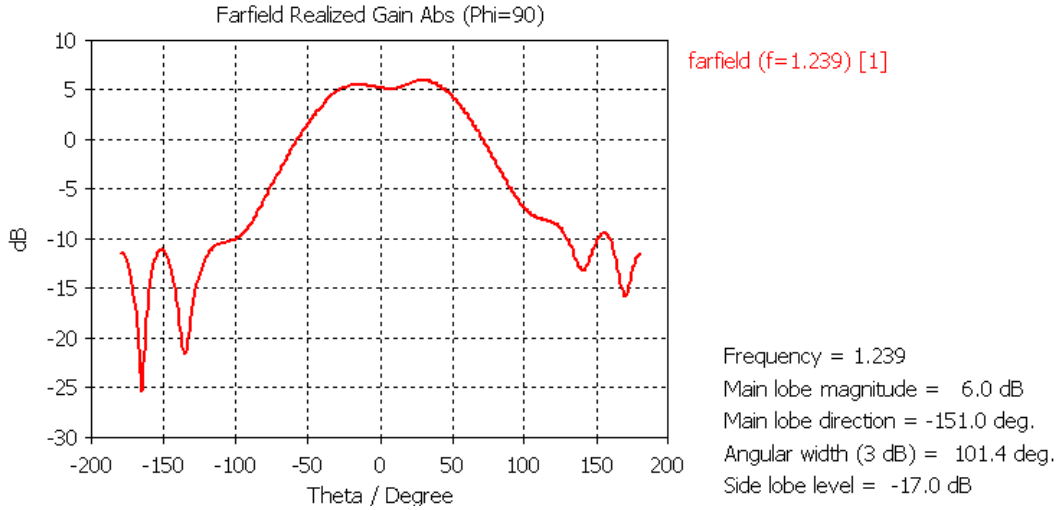


Figure A.19 Radiation pattern at 1.239 GHz (phi=90°).

Summary of the performances

The bandwidth (defined for VSWR < 2, in dual linear orthogonal polarization): 1.163-1.245 GHz.

In this bandwidth:

Isolation between the two port is better than 16dB in the bandwidth

	f=1.164 GHz		**f=1.2 GHz**		**f=1.239 GHz**	
Plan phi =	0°	90°	0°	90°	0°	90°
Main Lobe Magnitude(dB)	5	6.2	5.6	6.6	5.3	6
HPBW (°)	94	99	94	100	95	101
Side lobe level (dB)	-24	-16	-23	-17	-22	-17

The structure has the following relevant dimensions:

Thickness = 14.05 mm (Without SMA connectors).

Size : circular 600 mm diameter.

Appendix B: Design tools

Many simulation tools have been used through this work, as consequence a brief resume of the methodology for the design of TE devices from simulations is presented in this appendix.

As it is defined in the chapter 1, the methodology for designing in TE devices is the following 3 steps:

1-Defining the targeted transformation

This step is basically to create the concept or application needed and it is made by hand. It requires as we can remember to fulfil two points:

- Determining a known wave-material interaction in the real space. For example, changing the trajectory of a plane wave by using a curved geometry.
- Choosing a volume of space in the original system and its associated volume in the transformed system.

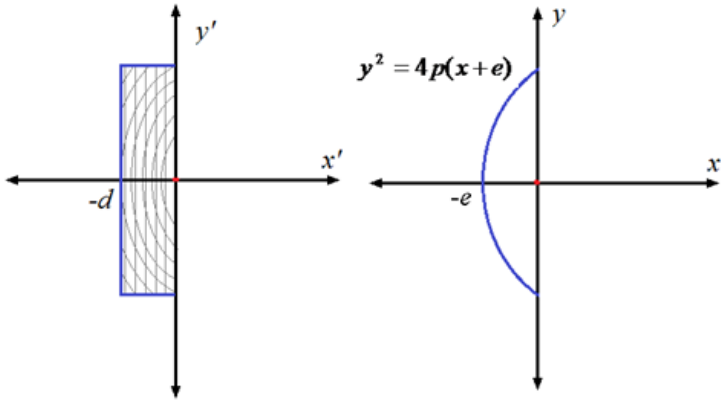


Figure A.20 In the case of the flat reflector the wave geometry interaction of the TE is defined as well as volumes of virtual and real spaces.

2-Defining the mathematical expressions

This step requires a mathematical background, because once the idea for the application is clear, the next step is to take this idea into mathematical expressions. It requires to steps:

- Defining an analytical coordinate transformation that links both spaces (virtual and real).
- Computing the MP in the transformed space using Equations 1.5 and 1.6.

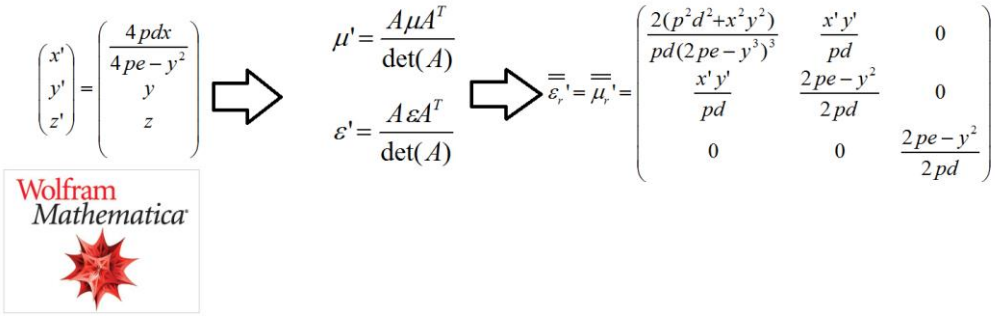


Figure A. 21 MP expressions calculated from the analytical expressions that linked both virtual and real spaces.

The commercial software Mathematica is used to develop this part of the design. Mathematica is a computational software program developed by Wolfram Reasearch used in many scientific, engineering, mathematical and computing fields, based on symbolic mathematics. The mathematical transformation in most of the cases need hard work, because of the analytical tensors are calculated for both MPs. However, sometimes they can be simplified or some components reduced by carefully managing the symbolic equations. Mathematica capabilities suits perfectly for the work needed in TE design. Mathematica allows to calculate the Jacobian matrix, the inverse Jacobian matrix, and the full expression of MP tensors.

3-Testing the electromagnetic behaviour of the device.

As we can remember the next step in the design is:

- Interpreting these MP and obtaining the material profile in the original space. For example, calculated MPs tensor could include some components needing some approximations, reductions or some particular orientation. These intermediate steps are needed to simplify the model and the resulting material.

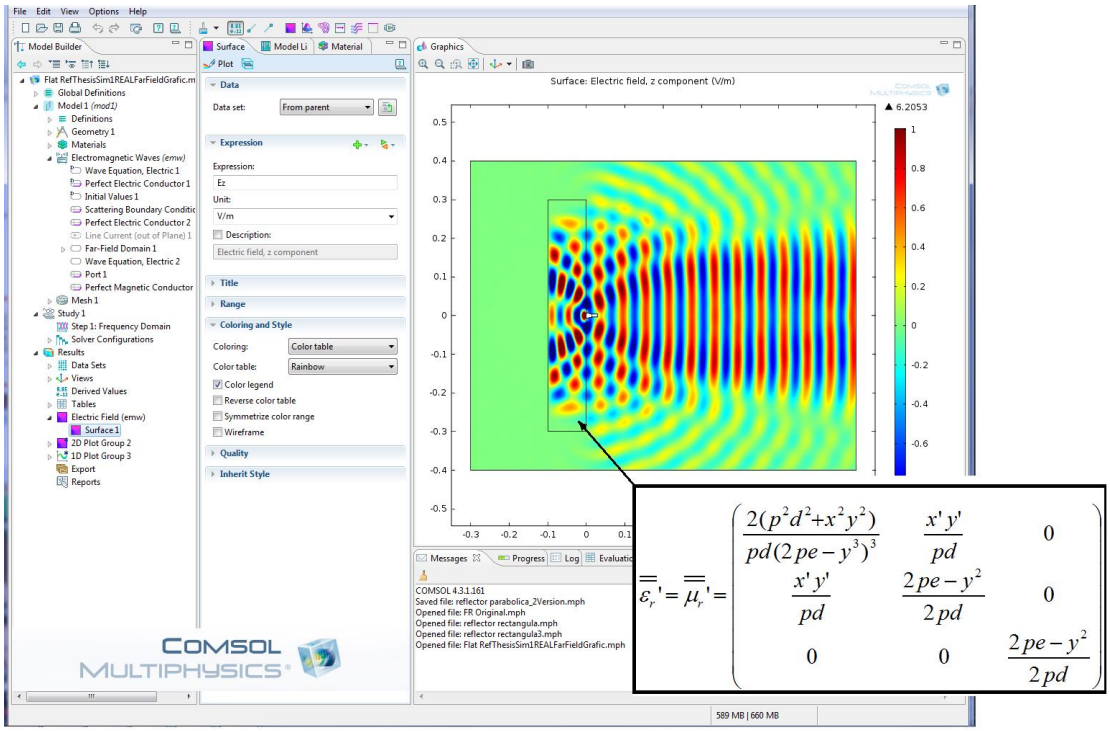


Figure A. 22 Comsol Multiphysics simulation for the flat reflector. The MPs are related to spatial variations in the electromagnetic simulations

Comsol Multiphysics is a commercial software package which is a finite element analysis, solver and simulation software for various physics and engineering applications, especially coupled phenomena, which explains the term multiphysics on its name. In the context of the TE design, Comsol is highly useful, because it allows to link spatial coordinates to the expressions for the permeability and permittivity. In Comsol the electromagnetic behaviour is tested with Electric field distributions, profile plotting, farfield results, etc.

4-Synthesizing the material needed to produce the TE behaviour

The final steps is to chose or synthesize a specific material to fulfil the spatial variation required in the MPs.

- Choosing or designing a material with the desired profile.

In most of cases, this last part of the technique requires, as it was shown along the thesis, some other intermediate steps:

- Profile discretization.
- 2D to 3D extension.
- Synthesizing MP.
- Optimizations.

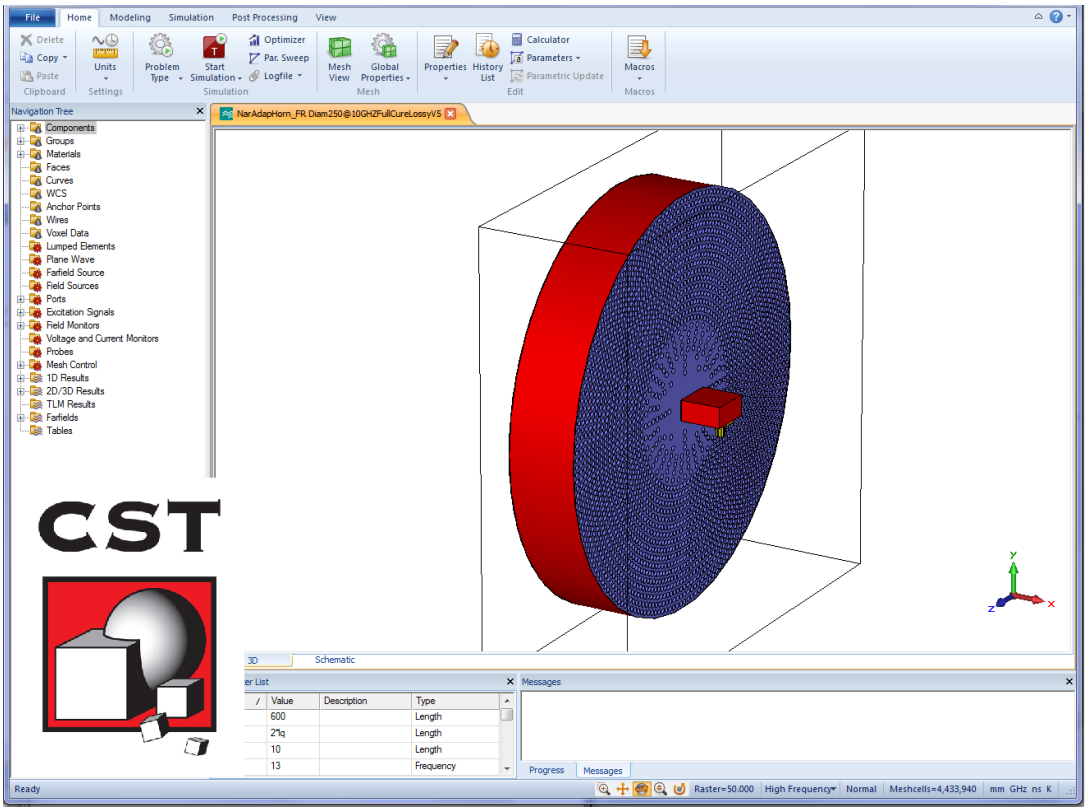


Figure A.23 The flat reflector that has already been discretized and extended to a 3D Structure. The drilling method is used to achieve variant permittivity. Several optimisations are also performed in CST.

All these steps are overcome thanks to several simulations with CST Microwave Studio. CST MS is another commercial software package, which is RF and microwave module of CST STUDIO SUITE. CST MS is finite element method solver used in engineering applications. CST allows to work with more standard materials and performances which can bring the TE design closer to the fabrication of the prototype. In CST we can obtain the S parameters, the bandwidth of the TE device, Electric field distribution and farfield results (directivity, gain, axial ratio, etc).